AWARD NUMBER: W81XWH-17-1-0357

TITLE: Combinational Targeting EZH2 and PARP1 in Prostate Cancer

PRINCIPAL INVESTIGATOR: Qi Cao

CONTRACTING ORGANIZATION: Northwestern University
Chicago, IL 60611

REPORT DATE: Sept 2019

TYPE OF REPORT: Annual

PREPARED FOR: U.S. Army Medical Research and Materiel Command
Fort Detrick, Maryland 21702-5012

REPORT DOCUMENTATION PAGE

Form Approved
OMB No. 0704-0188

1. REPORT DATE	2. REPORT TYPE	3. DATES COVERED
Sept 2019	Annual Report	1 Sep 2018 - 31 Aug 2019

4. TITLE AND SUBTITLE
Combinational Targeting EZH2 and PARP1 in Prostate Cancer

5a. CONTRACT NUMBER

5b. GRANT NUMBER
W81XWH-17-1-0357

5c. PROGRAM ELEMENT NUMBER

6. AUTHOR(S)

Qi Cao

E-Mail: qi.cao@northwestern.edu

5d. PROJECT NUMBER

5e. TASK NUMBER

5f. WORK UNIT NUMBER

7. PERFORMING ORGANIZATION NAME(S) AND ADDRESS(ES) AND ADDRESS(ES)
Northwestern University
Feinberg School of Medicine
303 E Chicago Ave.
Tarry 16-756, 758
Chicago, IL 60611

8. PERFORMING ORGANIZATION REPORT NUMBER

9. SPONSORING / MONITORING AGENCY NAME(S) AND ADDRESS(ES)

U.S. Army Medical Research and Materiel Command
Fort Detrick, Maryland 21702-5012

10. SPONSOR/MONITOR'S ACRONYM(S)

11. SPONSOR/MONITOR'S REPORT NUMBER(S)

12. DISTRIBUTION / AVAILABILITY STATEMENT

Approved for Public Release; Distribution Unlimited

13. SUPPLEMENTARY NOTES

14. ABSTRACT

Most advanced prostate cancer cells have higher levels of EZH2 and PARP1 proteins compared to that in early stage prostate cancer cells, suggesting the importance of these proteins in prostate cancer progression. We found that PARP1 directly interacts with EZH2. In the proposed project, we will identify precisely how EZH2 and PARP1 interact and how these two proteins regulate each other in prostate cancer. Next, we will study how EZH2 and PARP1 work together to decrease the expression of tumor suppressors (genes/proteins that inhibit tumor growth) and increase genetic instability in advanced prostate cancer. Understanding these mechanisms will lead to the future design of new inhibitors of EZH2 and PARP1. Furthermore, our preliminary data strongly suggest that PARP inhibition-resistant tumors have higher levels of EZH2 compared to PARP inhibition-sensitive tumors and that inhibiting EZH2 alone enhances the enzymatic activities of PARPs; thus, overcoming the therapeutic effectiveness of PARP inhibition. Therefore, our work provides a novel rationale to target both PARPs and EZH2, and we predict that the inhibition of both PARPs and EZH2 will kill more cancer cells than inhibiting either PARPs or EZH2 alone. We anticipate that this combination therapy will overcome therapeutic resistance and will substantially benefit the majority of prostate cancer patients, regardless of any DNA repair defects.

15. SUBJECT TERMS

16. SECURITY CLASSIFICATION OF:			17. LIMITATION OF ABSTRACT	18. NUMBER OF PAGES	19a. NAME OF RESPONSIBLE PERSON
a. REPORT	b. ABSTRACT	c. THIS PAGE			19b. TELEPHONE NUMBER *(include area code)*
Unclassified	Unclassified	Unclassified	Unclassified		USAMRMC

Standard Form 298 (Rev. 8-98)
Prescribed by ANSI Std. Z39.18

TABLE OF CONTENTS

1. **INTRODUCTION:** *Narrative that briefly (one paragraph) describes the subject, purpose and scope of the research.*

Most advanced prostate cancer cells have higher levels of EZH2 and PARP1 proteins compared to that in early stage prostate cancer cells, suggesting the importance of these proteins in prostate cancer progression. We found that PARP1 directly interacts with EZH2. In the proposed project, we will identify precisely how EZH2 and PARP1 interact and how these two proteins regulate each other in prostate cancer. Next, we will study how EZH2 and PARP1 work together to decrease the expression of tumor suppressors (genes/proteins that inhibit tumor growth) and increase genetic instability in advanced prostate cancer. Understanding these mechanisms will lead to the future design of new inhibitors of EZH2 and PARP1. Furthermore, our preliminary data strongly suggest that PARP inhibition-resistant tumors have higher levels of EZH2 compared to PARP inhibition-sensitive tumors and that inhibiting EZH2 alone enhances the enzymatic activities of PARPs; thus, overcoming the therapeutic effectiveness of PARP inhibition. Therefore, our work provides a novel rationale to target both PARPs and EZH2, and we predict that the inhibition of both PARPs and EZH2 will kill more cancer cells than inhibiting either PARPs or EZH2 alone. Although pharmacological inhibitors of EZH2 and PARP have been clinically proven to be safe, the combination of these drugs has never been tested and does pose some risks. To decrease the risk to patients, we will preclinically test, in this proposal, the safety and efficacy of this combination therapy. We anticipate that this combination therapy will overcome therapeutic resistance and will substantially benefit the majority of prostate cancer patients, regardless of any DNA repair defects.

2. **KEYWORDS:** *Provide a brief list of keywords (limit to 20 words).*

Polycomb, EZH2, PARP1, protein methylation, PRC2, DNA damage repair, castration-resistant prostate cancer

3. **ACCOMPLISHMENTS:** *The PI is reminded that the recipient organization is required to obtain prior written approval from the awarding agency grants official whenever there are significant changes in the project or its direction.*

What were the major goals of the project?
List the major goals of the project as stated in the approved SOW. If the application listed milestones/target dates for important activities or phases of the project, identify these dates and show actual completion dates or the percentage of completion.

Major Task 1: To characterize the methylation of PARP1 mediated by EZH2 in PCa 50%
Major Task 2: To characterize the unique and common downstream targets of PRC2 and PARP1 in PCa 60%
Major Task 3: To evaluate the combination effect of EZH2 inhibitor and PARP inhibitor, and the new EZH2 inhibitor in cell lines and CRPC xenograft models 60%
Major Task 4: To evaluate the synergistic efficacy of EZH2 and PARP inhibition in PCa bone metastasis xenograft models 20%

What was accomplished under these goals?

For this reporting period describe: 1) major activities; 2) specific objectives; 3) significant results or key outcomes, including major findings, developments, or conclusions (both positive and negative); and/or 4) other achievements. Include a discussion of stated goals not met. Description shall include pertinent data and graphs in sufficient detail to explain any significant results achieved. A succinct description of the methodology used shall be provided. As the project progresses to completion, the emphasis in reporting in this section should shift from reporting activities to reporting accomplishments.

1. **Identification of PARP1 potential methylated sites**

We first overexpressed FLAG-PARP1 in 293FT cells and then pulled down PARP1 by anti-FLAG agarose beads, followed by mass-spectrometry analysis to identify methylated sites.
As shown in table 1

Table 1 All detected methylation on PARP1 protein

Site	Score
K607DiMet+K616DiMet or K607Met+K616TriMet	16.5
R18Met or K22Met or K23Met	16.9
K305Met	19.1
K192Met	33
K653Met	36.9
K486Met	42.8
K486TriMet	47
R173Met	16.4
R841Met or R847Met	18.9
R878Met	30.1
R806Met	55.8

Higher score indicates more methylation detected.

We detected several lysines and arginines were methylated in cells.
Next, we treated the FLAG-PARP1 overexpressed 293FT cells with DMSO (negative control), EZH2 inhibitors GSK126 and EPZ6438 respectively. And then we pulled down FLAG-PARP1 from these 3 conditions, followed by mass spectrometry analysis. As shown in Fig. 1, we detected the methylation levels of 4 lysine sites were altered. Among them, the methylation levels of K337 and K486 were decreased be both GSK126 and EPZ6438, indicating these two lysines are most possible methylation sites by EZH2.

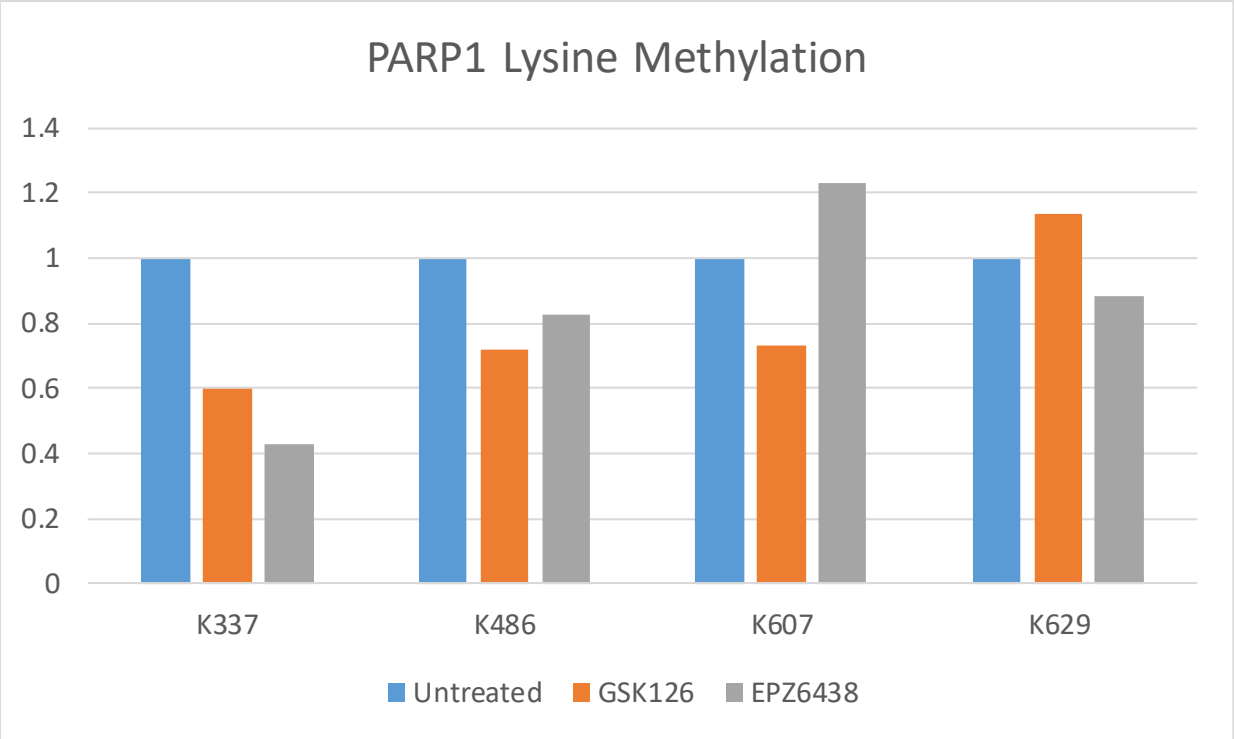

Figure 1. Methylation levels of PARP1 were altered by inhibiting EZH2 methyltransferase activities via its specific inhibitors. Immunoprecipitation by anti-FLAG antibody from the lysates of 293FT cells overexpressing FLAG-PARP1 and treated with DMSO (Vehicle, GSK126 5uM, EPZ6428 5uM for 48 hours), followed by mass-spectrometry analysis to detect the changes of the methylation sites of PARP1.

2. RNA-Seq of EZH2 or PARP1 knockdown cells. To identify the EZH2 and PARP1 commonly regulated genes in PCa cells, we knocked down EZH2 and PARP1 by 2 shRNAs respectively in C4-2 cells. After confirming the knockdown efficacy, we harvested cells and isolated RNA and sent the RNA for RNA-seq analysis. As shown in the Fig. 2, the transcript levels of EZH2 and PARP1 were decreased markedly.

GO pathway analysis showed that knocking down EZH2 or PARP1 dysregulated many genes involved in functional pathways including prostate cancer, cell cycle, and mTOR pathways (Fig 3A and B). More importantly, most EZH2 KD downregulated genes were also downregulated by PARP1, and vice versa (Fig. 3C). Similarly, EZH2 and PARP1 KD dysrgulated genes were involved into similar pathways (Fig. 3D).

We are performing the ChIP-seq in the EZH2 KD and PARP1 KD C4-2 cells to characterize if EZH2 and PARP1 are enriched in the same genome loci, and if knocking down EZH2 could alter the recruitment of PARP1 (or vice versa).

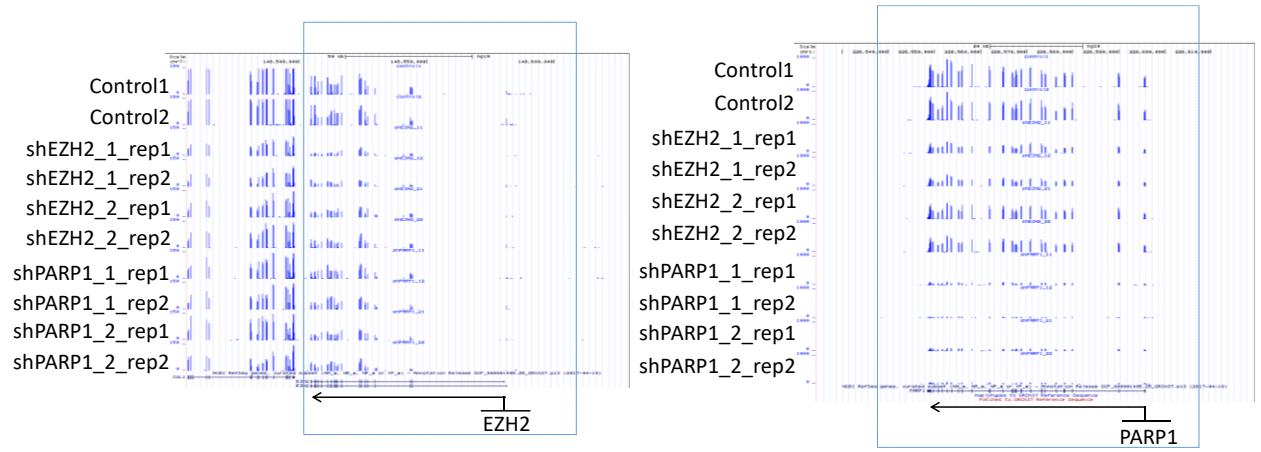

Figure 2. RNA-seq of EZH2 and PARP1 knockdown.
C4-2 cells were infected with control shRNA, EZH2 shRNA-1, -2 and PARP1 shRNA-1, -2 respectively. RNA were isolated and subjected to RNA-Seq analysis. Genome browser views of EZH2 (left panel) and PARP1 (right panel) regions were shown.

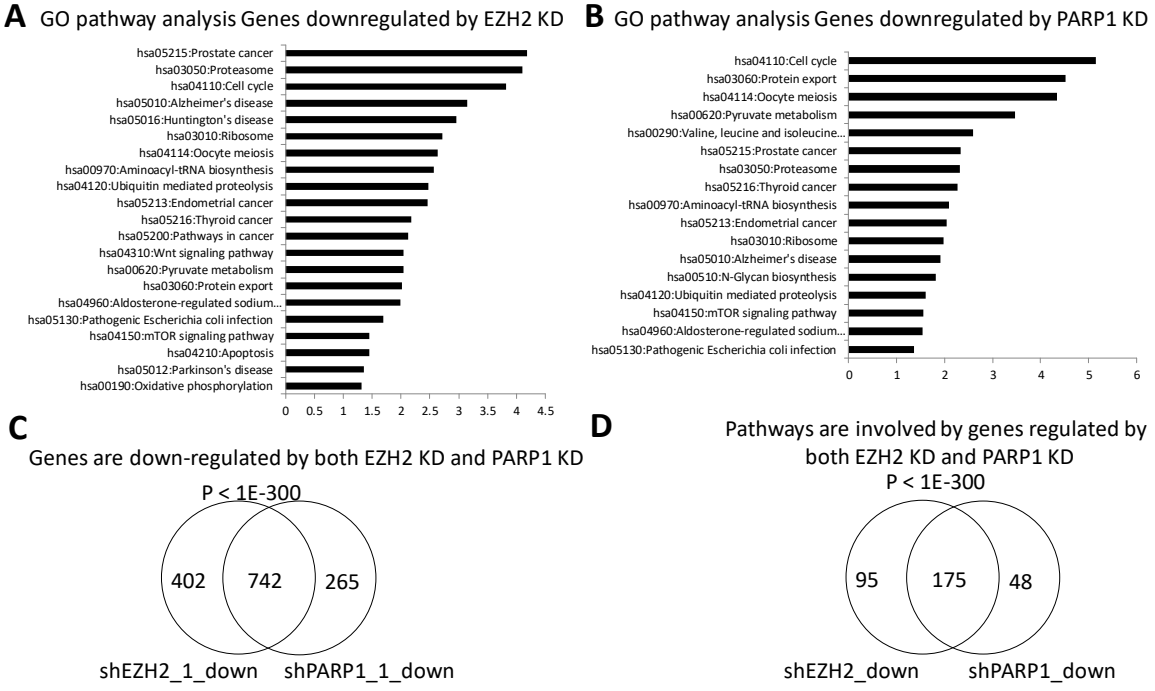

Figure 3. EZH2 and PARP1 have shared downstream targets.
(A, B) GO pathway analysis showed pathways involved by EZH2 KD (A) or PARP1 (B) downregulated genes in PCa C4-2 cells. (C) Venn diagram shows EZH2 KD and PARP1 KD have shared target genes. (D) EZH2 KD downregulated genes involved pathways were also involved by PARP1 KD downregulated genes.

What opportunities for training and professional development has the project provided?
If the project was not intended to provide training and professional development opportunities or there is nothing significant to report during this reporting period, state "Nothing to Report."

Describe opportunities for training and professional development provided to anyone who worked on the project or anyone who was involved in the activities supported by the project. "Training" activities are those in which individuals with advanced professional skills and experience assist others in attaining greater proficiency. Training activities may include, for example, courses or one-on-one work with a mentor. "Professional development" activities result in increased knowledge or skill in one's area of expertise and may include workshops, conferences, seminars, study groups, and individual study. Include participation in conferences, workshops, and seminars not listed under major activities.

Award/grant

2019-2020 Northwestern Univ. prostate cancer SPORE pilot grant
2019-2022 Northwestern Univ. Polski Urological Cancer Institute Research Award
2019-2022 DoD PCRP Idea Development Award

National/International conferences attended

Oct 26-28, 2018 Prostate Cancer Foundation Scientific Retreat, Carlsbad, CA
Mar 3-5, 2018 Multi-institute prostate cancer SPORE annual retreat, Ft Lauderdale, FL
Mar 29-Apr 3, 2019 AACR Annual Meeting, Atlanta, GA

Invited Oral Presentation

Feb 10, 2019 Targeting EZH2 in Advanced Prostate Cancer. Department of Urology Research Retreat. Northwestern University Feinberg School of Medicine, Chicago, IL
Apr 10, 2019 A HMT-independent Role of EZH2 in Prostate Cancer. Prostate Cancer Symposium. Robert H. Lurie Comprehensive Cancer Center, Northwestern University Feinberg School of Medicine, Chicago, IL
Jul 25, 2019 A HMT-independent Role of EZH2 in Prostate Cancer. The 17th SCBA International Symposium, Kunming, China
Aug 1, 2019 The Role of Polycomb Group Proteins in Cancer, Department of Pathology, Shandong University Cheeloo College of Medicine, Jinan, China

How were the results disseminated to communities of interest?
If there is nothing significant to report during this reporting period, state "Nothing to Report."

Describe how the results were disseminated to communities of interest. Include any outreach activities that were undertaken to reach members of communities who are not usually aware of these project activities, for the purpose of enhancing public understanding and increasing interest in learning and careers in science, technology, and the humanities.

Nothing to Report

Describe briefly what you plan to do during the next reporting period to accomplish the goals and objectives.

We are continuously working on this project and pursue the aims. Because we just moved to a new institute, we will obtain the local IACUC and ACURO approval first and then perform the proposed animal work.

4. **IMPACT:** D*escribe distinctive contributions, major accomplishments, innovations, successes, or any change in practice or behavior that has come about as a result of the project relative to:*

What was the impact on the development of the principal discipline(s) of the project?
If there is nothing significant to report during this reporting period, state "Nothing to Report."

Describe how findings, results, techniques that were developed or extended, or other products from the project made an impact or are likely to make an impact on the base of knowledge, theory, and research in the principal disciplinary field(s) of the project. Summarize using language that an intelligent lay audience can understand (Scientific American style).

Nothing to Report

What was the impact on other disciplines?
If there is nothing significant to report during this reporting period, state "Nothing to Report."

Describe how the findings, results, or techniques that were developed or improved, or other products from the project made an impact or are likely to make an impact on other disciplines.

Nothing to Report

What was the impact on technology transfer?
If there is nothing significant to report during this reporting period, state "Nothing to Report."

Describe ways in which the project made an impact, or is likely to make an impact, on commercial technology or public use, including:

- *transfer of results to entities in government or industry;*
- *instances where the research has led to the initiation of a start-up company; or*
- *adoption of new practices.*

Nothing to Report

What was the impact on society beyond science and technology?
If there is nothing significant to report during this reporting period, state "Nothing to Report."

Describe how results from the project made an impact, or are likely to make an impact, beyond the bounds of science, engineering, and the academic world on areas such as:

- *improving public knowledge, attitudes, skills, and abilities;*
- *changing behavior, practices, decision making, policies (including regulatory policies), or social actions; or*
- *improving social, economic, civic, or environmental conditions.*

Nothing to Report

5. CHANGES/PROBLEMS: *The PD/PI is reminded that the recipient organization is required to obtain prior written approval from the awarding agency grants official whenever there are significant changes in the project or its direction. If not previously reported in writing, provide the following additional information or state, "Nothing to Report," if applicable:*

We just moved to a new institute (Department of Urology and Robert H. Lurie Comprehensive Cancer Center, Northwestern University Feinberg University. We are working on the grant transfer. Local IACUC protocol was approved.

Actual or anticipated problems or delays and actions or plans to resolve them
Describe problems or delays encountered during the reporting period and actions or plans to resolve them.

Nothing to Report

Changes that had a significant impact on expenditures
Describe changes during the reporting period that may have had a significant impact on expenditures, for example, delays in hiring staff or favorable developments that enable meeting objectives at less cost than anticipated.

We just moved to a new institute (Department of Urology and Robert H. Lurie Comprehensive Cancer Center, Northwestern University Feinberg University. We are working on the grant transfer, hiring new post-doc and getting the local IACUC and ACURO approval.

Significant changes in use or care of human subjects, vertebrate animals, biohazards, and/or select agents

Describe significant deviations, unexpected outcomes, or changes in approved protocols for the use or care of human subjects, vertebrate animals, biohazards, and/or select agents during the reporting period. If required, were these changes approved by the applicable institution committee (or equivalent) and reported to the agency? Also specify the applicable Institutional Review Board/Institutional Animal Care and Use Committee approval dates.

Significant changes in use or care of human subjects

Nothing to report

Significant changes in use or care of vertebrate animals

We just moved to a new institute (Department of Urology and Robert H. Lurie Comprehensive Cancer Center, Northwestern University Feinberg University. We are working on the grant transfer, hiring new post-doc and getting the local IACUC and ACURO approval.

Significant changes in use of biohazards and/or select agents

Nothing to report

6. PRODUCTS: *List any products resulting from the project during the reporting period. If there is nothing to report under a particular item, state "Nothing to Report."*

- **Publications, conference papers, and presentations**

Report only the major publication(s) resulting from the work under this award.

Journal publications. *List peer-reviewed articles or papers appearing in scientific, technical, or professional journals. Identify for each publication: Author(s); title; journal; volume: year; page numbers; status of publication (published; accepted, awaiting publication; submitted, under review; other); acknowledgement of federal support (yes/no).*

1. Kim J, Lee Y, Zha J, Lu X, Song B, Fong KW, **Cao Q**, Licht J, Yu J. EZH2 transcriptionally activates androgen receptor gene through polycomb- and methylation-independent roles. Cell Reports. 2018; 25(10):2808-2820.e4. PMID: 30517868 PMCID: PMC6342284
2. Long Z, Li Y, Gan Y, Zhao D, Wang G, Xie N, Lovnicki JM, Fazli L, **Cao Q**, Chen K, Dong X. Roles of the HOXA10 gene during castrate-resistant prostate cancer progression. Endocrine-related cancer. 2019; 26(3):279-292. PMID: 30667363
3. Liu Q, Wang G, Li Q, Jiang W, Kim JS, Wang R, Zhu S, Wang X, Yan L, Yi Y, Zhang L, Meng Q, Li C, Zhao D, Qiao Y, Li Y, Gursel DB, Chinnaiyan AM, Chen K#, **Cao Q#**. Polycomb group proteins EZH2 and EED directly regulate androgen receptor in advanced prostate cancer. International journal of cancer. 2019; 145(2):415-426. PMID: 30628724. (#co-corresponding authors).
4. Vantaku V, Putluri V, Bader DA, Maity S, Ma J, Arnold JM, Rajapakshe K, Donepudi SR, von Rundstedt FC, Devarakonda V, Dubrulle J, Karanam B, McGuire SE, Stossi F, Jain AK, Coarfa C, **Cao Q**, Sikora AG, Villanueva H, Kavuri SM, Lotan Y, Sreekumar A, Putluri N. Epigenetic loss of AOX1 expression via EZH2 leads to metabolic deregulations and promotes bladder cancer progression. Oncogene. 2019 Aug 5;. doi: 10.1038/s41388-019-0902-7. [Epub ahead of print] PubMed PMID: 31383940.
5. Zhu S, Zhao D, Li C, Li Q, Jiang W, Liu Q, Wang R, Fazli L, Li Y, Zhang L, Yi Y, Meng Q, Wang W, Wang G, Zhang M, Zu X, Zhao W, Deng T, Yu J, Dong X, Chen K#, **Cao Q#**. BMI1 is directly regulated by androgen receptor to promote castration-resistance in prostate cancer. Oncogene. 2019 Aug 28;. doi: 10.1038/s41388-019-0966-4. [Epub ahead of print] PubMed PMID: 31462713. (#co-corresponding authors).
6. Li F, Yang Yi Y, Miao Y, Long W, Long T, Chen S, Cheng W, Zou C, Zheng Y, Wu X, Ding J, Zhu K, Chen D, Xu Q, Wang J, Liu Q, Zhi F, Ren J, **Cao Q#**, Zhao W#. N6-methyladenosine Modulates Nonsense-mediated mRNA Decay in Human Glioblastoma (#co-corresponding authors). Cancer Res. 2019 Sep 17;. doi: 10.1158/0008-5472.CAN-18-2868. [Epub ahead of print] PubMed PMID: 31530567.

Books or other non-periodical, one-time publications. *Report any book, monograph, dissertation, abstract, or the like published as or in a separate publication, rather than a periodical or series. Include any significant publication in the proceedings of a one-time conference or in the report of a one-time study, commission, or the like. Identify for each one-time publication: author(s); title; editor; title of collection, if applicable; bibliographic information; year; type of publication (e.g., book, thesis or dissertation); status of publication (published; accepted, awaiting publication; submitted, under review; other); acknowledgement of federal support (yes/no).*

no

Other publications, conference papers and presentations. *Identify any other publications, conference papers and/or presentations not reported above. Specify the status of the publication as noted above. List presentations made during the last year (international, national, local societies, military meetings, etc.). Use an asterisk (*) if presentation produced a manuscript.*

no

- **Website(s) or other Internet site(s)**
  List the URL for any Internet site(s) that disseminates the results of the research activities. A short description of each site should be provided. It is not necessary to include the publications already specified above in this section.

N/A

- **Technologies or techniques**
  Identify technologies or techniques that resulted from the research activities. Describe the technologies or techniques were shared.

N/A

- **Inventions, patent applications, and/or licenses**
  Identify inventions, patent applications with date, and/or licenses that have resulted from the research. Submission of this information as part of an interim research performance progress report is not a substitute for any other invention reporting required under the terms and conditions of an award.

N/A

- **Other Products**
  Identify any other reportable outcomes that were developed under this project. Reportable outcomes are defined as a research result that is or relates to a product, scientific advance, or research tool that makes a meaningful contribution toward the understanding, prevention, diagnosis, prognosis, treatment and /or rehabilitation of a disease, injury or condition, or to improve the quality of life. Examples include:
  - *data or databases;*
  - *physical collections;*
  - *audio or video products;*
  - *software;*
  - *models;*
  - *educational aids or curricula;*
  - *instruments or equipment;*
  - *research material (e.g., Germplasm; cell lines, DNA probes, animal models);*
  - *clinical interventions;*
  - *new business creation; and*
  - *other.*

N/A

7. PARTICIPANTS & OTHER COLLABORATING ORGANIZATIONS

What individuals have worked on the project?

Provide the following information for: (1) PDs/PIs; and (2) each person who has worked at least one person month per year on the project during the reporting period, regardless of the source of compensation (a person month equals approximately 160 hours of effort). If information is unchanged from a previous submission, provide the name only and indicate "no change".

Example:

Name: *Mary Smith*
Project Role: *Graduate Student*
Researcher Identifier (e.g. ORCID ID): *1234567*
Nearest person month worked: *5*

Contribution to Project: *Ms. Smith has performed work in the area of combined error-control and constrained coding.*
Funding Support: *The Ford Foundation (Complete only if the funding support is provided from other than this award.)*

Name:	*Qi Cao*
Project Role:	*PI*
Researcher Identifier (e.g. ORCID ID):	
Nearest person month worked:	3
Contribution to Project:	*Conceive the idea, lead the project, design experiments and analyze the data*
Funding Support:	*DoD PCRP IDA, Prostate Cancer Foundation, American Cancer Society, Start-up*

Name:	*Qingshu Meng*

Project Role:	*Post-Doctoral*
Researcher Identifier (e.g. ORCID ID):	
Nearest person month worked:	12
Contribution to Project:	*Perform major experiments and analyze the data*
Funding Support:	*DoD PCRP IDA*

Name:	*Kaifu Chen*
Project Role:	*Co-investigator*
Researcher Identifier (e.g. ORCID ID):	
Nearest person month worked:	1
Contribution to Project:	*analyze the data*
Funding Support:	*DoD PCRP IDA, NIH, Start-up*

Has there been a change in the active other support of the PD/PI(s) or senior/key personnel since the last reporting period?
If there is nothing significant to report during this reporting period, state "Nothing to Report."

If the active support has changed for the PD/PI(s) or senior/key personnel, then describe what the change has been. Changes may occur, for example, if a previously active grant has closed and/or if a previously pending grant is now active. Annotate this information so it is clear what has changed from the previous submission. Submission of other support information is not necessary for pending changes or for changes in the level of effort for active support reported previously. The awarding agency may require prior written approval if a change in active other support significantly impacts the effort on the project that is the subject of the project report.

Nothing to Report

What other organizations were involved as partners?
If there is nothing significant to report during this reporting period, state "Nothing to Report."

Describe partner organizations – academic institutions, other nonprofits, industrial or commercial firms, state or local governments, schools or school systems, or other organizations (foreign or domestic) – that were involved with the project. Partner organizations may have provided financial or in-kind support, supplied facilities or equipment, collaborated in the research, exchanged personnel, or otherwise contributed.

Provide the following information for each partnership:
Organization Name:
Location of Organization: (if foreign location list country)
Partner's contribution to the project (identify one or more)

- *Financial support;*
- *In-kind support (e.g., partner makes software, computers, equipment, etc., available to project staff);*
- *Facilities (e.g., project staff use the partner's facilities for project activities);*
- *Collaboration (e.g., partner's staff work with project staff on the project);*
- *Personnel exchanges (e.g., project staff and/or partner's staff use each other's facilities, work at each other's site); and*
- *Other.*

Nothing to Report

8. SPECIAL REPORTING REQUIREMENTS

COLLABORATIVE AWARDS: *For collaborative awards, independent reports are required from BOTH the Initiating Principal Investigator (PI) and the Collaborating/Partnering PI. A duplicative report is acceptable; however, tasks shall be clearly marked with the responsible PI and research site. A report shall be submitted to* ***https://ers.amedd.army.mil*** *for each unique award.*

QUAD CHARTS: *If applicable, the Quad Chart (available on https://www.usamraa.army.mil) should be updated and submitted with attachments.*

9. APPENDICES: *Attach all appendices that contain information that supplements, clarifies or supports the text. Examples include original copies of journal articles, reprints of manuscripts and abstracts, a curriculum vitae, patent applications, study questionnaires, and surveys, etc.*

Reprints of 6 publications

Article

Cell Reports

Polycomb- and Methylation-Independent Roles of EZH2 as a Transcription Activator

Graphical Abstract

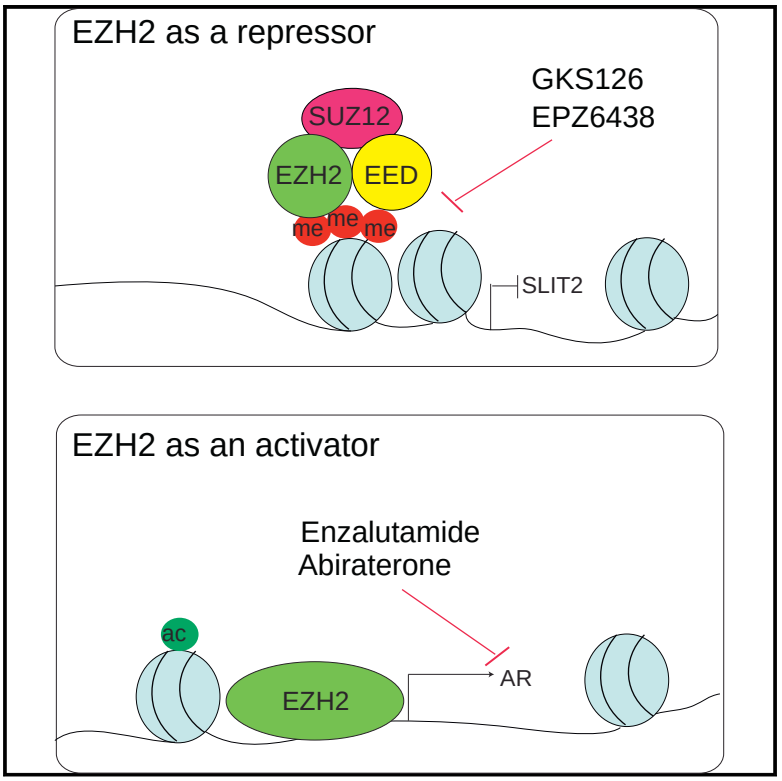

Authors

Jung Kim, Yongik Lee, Xiaodong Lu, ..., Jonathan D. Licht, Jonathan C. Zhao, Jindan Yu

Correspondence

jonathan-zhao@northwestern.edu (J.C.Z.), jindan-yu@northwestern.edu (J.Y.)

In Brief

Kim et al. report EZH2 as a transcriptional activator that directly induces AR gene expression in a Polycomb- and methylation-independent manner, providing a mechanism to escape enzymatic EZH2 inhibitors. Combination of inhibitors with AR-targeted therapies showed a strong synergy in blocking the EZH2 downstream pathways and suppressing prostate cancer progression.

Highlights

- EZH2 directly activates androgen receptor (AR) gene transcription
- EZH2 induces AR through Polycomb- and methylation-independent mechanisms
- Local chromatin environment dictates the roles of EZH2 as an activator or repressor
- Prostate cancer depends on both catalytic and non-catalytic activities of EZH2

Kim et al., 2018, Cell Reports *25*, 2808–2820
December 4, 2018
https://doi.org/10.1016/j.celrep.2018.11.035

CellPress

OPEN ACCESS
CellPress

Cell Reports
Article

Polycomb- and Methylation-Independent Roles of EZH2 as a Transcription Activator

Jung Kim,[1,6] Yongik Lee,[1,6] Xiaodong Lu,[1] Bing Song,[1] Ka-Wing Fong,[1] Qi Cao,[2,3] Jonathan D. Licht,[1,2,4] Jonathan C. Zhao,[1,2,*] and Jindan Yu[1,2,5,7,*]

[1]Division of Hematology and Oncology, Department of Medicine, Northwestern University Feinberg School of Medicine, Chicago, IL, USA
[2]Robert H. Lurie Comprehensive Cancer Center, Northwestern University Feinberg School of Medicine, Chicago, IL, USA
[3]Center for Inflammation and Epigenetics, Houston Methodist Research Institute, Houston, TX, USA
[4]Division of Hematology and Oncology, University of Florida Health Cancer Center, Gainesville, FL 2033, USA
[5]Department of Biochemistry and Molecular Genetics, Northwestern University Feinberg School of Medicine, Chicago, IL, USA
[6]These authors contributed equally
[7]Lead Contact
*Correspondence: jonathan-zhao@northwestern.edu (J.C.Z.), jindan-yu@northwestern.edu (J.Y.)
https://doi.org/10.1016/j.celrep.2018.11.035

SUMMARY

Enhancer of Zeste 2 (EZH2) is the enzymatic subunit of Polycomb Repressive Complex 2 (PRC2), which catalyzes histone H3 lysine 27 trimethylation (H3K27me3) at target promoters for gene silencing. Here, we report that EZH2 activates androgen receptor (AR) gene transcription through direct occupancy at its promoter. Importantly, this activating role of EZH2 is independent of PRC2 and its methyltransferase activities. Genome-wide assays revealed extensive EZH2 occupancy at promoters marked by either H3K27ac or H3K27me3, leading to gene activation or repression, respectively. Last, we demonstrate enhanced efficacy of enzymatic EZH2 inhibitors when used in combination with AR antagonists in blocking the dual roles of EZH2 and suppressing prostate cancer progression *in vitro* and *in vivo*. Taken together, our study reports EZH2 as a transcriptional activator, a key target of which is AR, and suggests a drug-combinatory approach to treat advanced prostate cancer.

INTRODUCTION

Prostate cancer (PCa) is the most frequently diagnosed cancer and the third most frequent cause of cancer deaths in United States males (Siegel et al., 2015). PCa patients have benefitted from androgen deprivation therapies (ADTs) and small molecular inhibitors targeting the androgen receptor (AR). However, 30% of patients have primary resistance to both forms of treatment, and the majority of patients progress from androgen-dependent PCa (ADPC) to castration-resistant PCa (CRPC). The AR remains a key driver of CRPC through aberrant activation in the milieu of low androgen.

Enhancer of Zeste 2 (EZH2) is a *bona fide* oncogene that is among the most highly upregulated genes in CRPC relative to localized PCa (Varambally et al., 2002). EZH2 is a core subunit of the Polycomb Repressive Complex 2 (PRC2), which also contains embryonic ectoderm development (EED) and suppressor of zeste 12 (SUZ12). EZH2 is the catalytic member of PRC2 and contains a C-terminal su(var)3-9, enhancer-of-zeste and trithorax (SET) domain that specifically catalyzes histone H3 lysine 27 trimethylation (H3K27me3), leading to epigenetic (defined as histone modifications) silencing of many tumor suppressor genes (Yu et al., 2010; Zhao et al., 2012).

Interestingly, evidence has emerged recently that suggests noncanonical roles of EZH2 in various cancers. For example, in addition to histone H3, EZH2 has been shown to methylate nonhistone substrates, such as Jarid2 and STAT3, to regulate their transcriptional activities (He et al., 2012; Sanulli et al., 2015). EZH2 can also methylate RORα and PLZF, in which cases the methylation leads to target protein degradation (Lee et al., 2012; Vasanthakumar et al., 2017). Moreover, several studies have reported that EZH2 can also act independently of PRC2 and/or its histone methyltransferase activities. For instance, in estrogen receptor-negative breast cancer, EZH2 forms a complex with RelA and RelB to activate nuclear factor κB (NF-κB) signaling, which does not involve methylation (Gonzalez et al., 2011). Similarly, EZH2 interacts with the SWI and SNF complex (Kim et al., 2015) in a PRC2-independent manner to activate target genes. In PCa, EZH2 has been shown to interact with the AR in CRPC, but not ADPC, to activate gene expression through a PRC2-independent but methylation-dependent mechanism (Xu et al., 2012). The precise mechanism and target genes remain unclear.

In the present study, we identify the AR as a direct target of EZH2-mediated transcriptional activation in both ADPC and CRPC. This activation is independent of PRC2 as well as its methyltransferase activity but requires EZH2 occupancy at the AR promoter. AR-driven PCa depends on dual roles of EZH2: its conventional role in epigenetic silencing of tumor suppressor genes as well as its newly discovered role in activating AR and downstream signaling. Significantly, an enzymatic EZH2 inhibitor in combination with an AR antagonist led to significant suppression of PCa growth *in vitro* and *in vivo*.

RESULTS

EZH2 Enhances Androgen Signaling in PCa

We recently reported a role of EZH2 in collaborating with the AR on transcriptional repression (Zhao et al., 2012). Importantly,

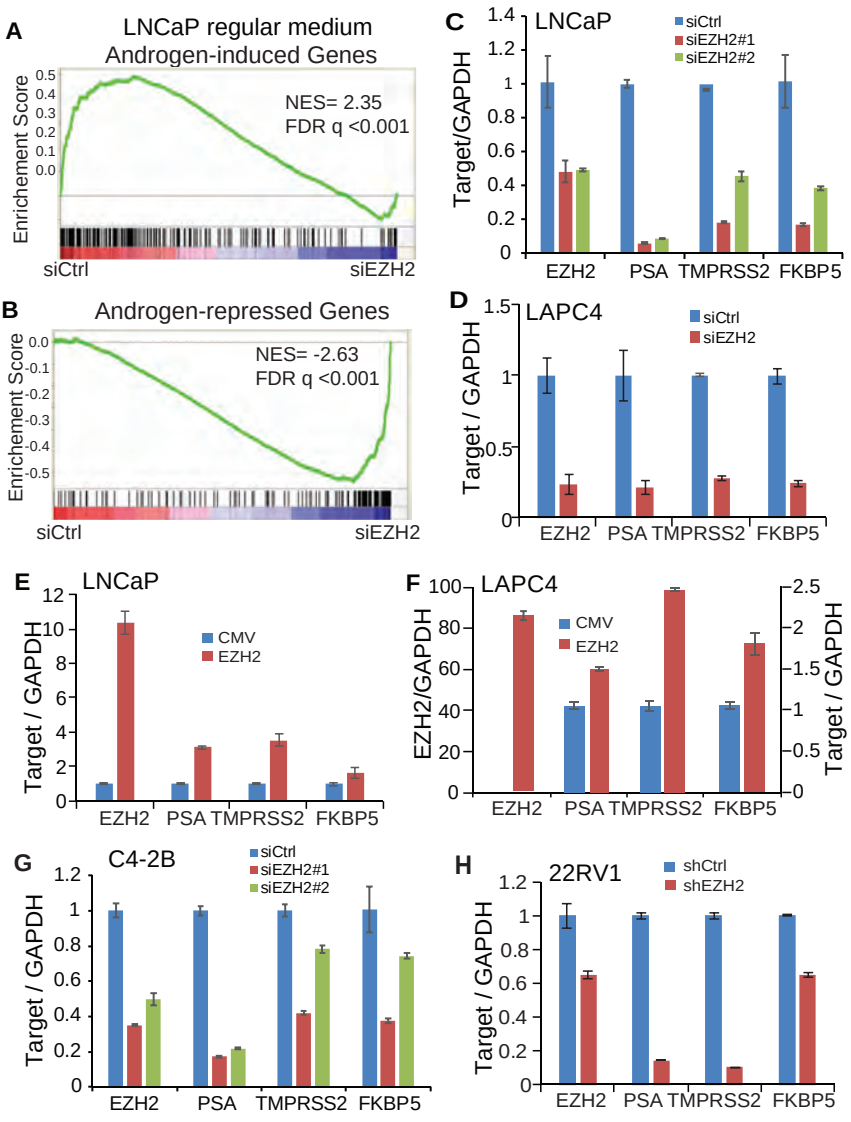

Figure 1. EZH2 Enhances Androgen Signaling in Both ADPC and CRPC Cells

(A and B) Androgen-induced genes (A) are enriched for downregulation upon EZH2 knockdown (false discovery rate [FDR] q < 0.001), whereas androgen-repressed genes (B) are enriched for upregulation upon EZH2 knockdown (FDR q < 0.001). GSEA was utilized to examine the expression of androgen (R1881)-induced and -repressed gene sets, obtained from a previous study (Zhao et al., 2012), in LNCaP cells treated with control (siCtrl) and EZH2 knockdown (siEZH2), as profiled by microarrays.

(C and D) EZH2 knockdown inhibits AR-induced genes. LNCaP cells (C) were transfected with siCtrl or two different siEZH2s, and LAPC4 (D) cells were transfected with siCtrl or a representative siEZH2. Cells were then analyzed by qRT-PCR. Data were normalized to GAPDH. Data shown are mean (±SEM) of technical replicates from one representative experiment of three.

(E and F) EZH2 overexpression increases AR-induced genes. LNCaP (E) and LAPC4 (F) cells were infected with cytomegalovirus (CMV) control or an EZH2-expressing adenovirus and analyzed by qRT-PCR. Data were normalized to GAPDH. Data shown are mean (±SEM) of technical replicates from one representative experiment of three.

(G and H) EZH2 knockdown reduces AR-induced genes in CRPC cells. (G) 22Rv1 and (H) C4-2B cells were infected with control shRNA or shEZH2 or transfected with either siCtrl or two different siEZH2s and then subjected to qRT-PCR analysis. Data were normalized to GAPDH. Data shown are mean (±SEM) of technical replicates from one representative experiment of three.

gene set enrichment analysis (GSEA) and Venn diagrams also showed inhibition of androgen-induced genes by EZH2 knockdown compared with control cells (Figures 1A, 1B, S1A, and S1B). This AR-equivalent role of EZH2 in regulating global androgen signaling was confirmed in additional PCa cell lines (Figure S1C). Moreover, qRT-PCR confirmed that AR-induced genes such as *PSA*, *TMPRSS2*, and *FKBP5* were indeed remarkably downregulated upon EZH2 knockdown using two independent small interfering RNAs (siRNAs) (Figure 1C) and confirmed in additional PCa lines (Figure 1D). Conversely, EZH2 overexpression in LNCaP and LAPC4 cells increased the expression of AR-induced genes (Figures 1E and 1F). To examine this regulatory pathway in CRPC cells, we performed EZH2 knockdown in the CRPC cell line C4-2B with both siRNAs and observed similar effects (Figure 1G), which was confirmed in an additional CRPC line, 22Rv1, also with small hairpin RNA (shRNA)-mediated knockdown of EZH2 (Figure 1H). Therefore, we demonstrate robust regulation of AR target genes by EZH2 in both ADPC and CRPC cells.

EZH2 Positively Regulates AR mRNA and Protein Levels

Next we attempted to investigate the molecular mechanisms by which EZH2 enhances androgen signaling in PCa cells. Previous studies reported that EZH2 activates gene expression through physical interaction with the AR protein (Xu et al., 2012). To examine this, we performed co-immunoprecipitation (coIP) experiments in LNCaP cells and found that, although SUZ12 interacts with EZH2 as expected, the AR failed to interact with EZH2 (Figure S2A). To preclude the potential of antibody competition and masking protein interaction during coIP experiments, we performed coIP using EZH2 and AR N- and C terminus-targeting antibodies. However, we did not observe EZH2 and AR interaction in LNCaP cells (Figure S2B), suggesting that physical interaction with AR is not required for EZH2 to induce androgen signaling.

Because EZH2 increases androgen-induced genes but decreases androgen-repressed genes, exhibiting an AR-like effect, we wondered whether EZH2 regulates AR expression. Importantly, qRT-PCR and western blot analysis of LNCaP

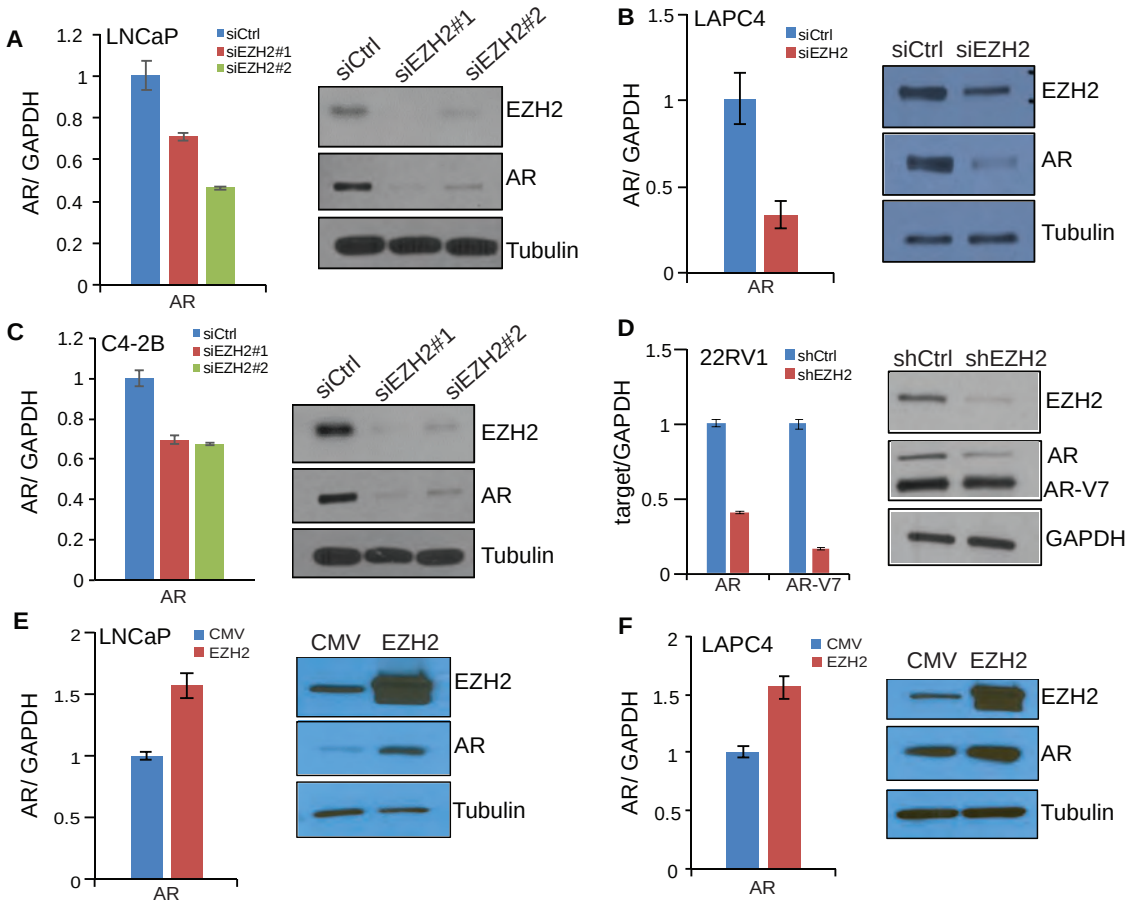

Figure 2. EZH2 Increases AR mRNA and Protein Levels

(A–D) EZH2 knockdown decreases AR mRNA and protein levels. LNCaP (A), LAPC4 (B), C4-2B (C), and 22RV1 (D) cells were transfected with control or siEZH2s or infected with control shRNA or shEZH2, followed by qRT-PCR (left) and western blot analysis (right). Data shown are mean (±SEM) of technical replicates from one representative experiment of three.

(E and F) EZH2 overexpression increases AR mRNA and protein levels. LNCaP (E) and LAPC4 (F) cells were infected with CMV or an EZH2-expressing adenovirus for 48 hr, followed by qRT-PCR (left) and western blot analysis (right). Data shown are mean (±SEM) of technical replicates from one representative experiment of three.

cells subjected to control and two independent EZH2-targeting RNA interferences revealed a drastic decrease of the AR at both the mRNA and protein levels (Figure 2A), whereas EZH2 knockdown restored the expression of its previously reported epigenetic targets such as SLIT2 and CNR1 (Figure S2C). This downregulation of the AR but upregulation of epigenetic targets by EZH2 knockdown was observed in additional ADPC and CRPC cell lines (Figures 2B–2D and S2D–S2F). To further validate this regulatory pathway, we performed EZH2 overexpression in androgen-dependent PCa cell lines, which have a relatively lower amount of endogenous EZH2. qRT-PCR and western blot analysis confirmed that EZH2 overexpression indeed increased both the AR transcript and protein levels in these already AR-high cell lines (Figures 2E and 2F) and decreased its epigenetic targets, as expected (Figures S2G and S2H). Therefore, our data strongly support that EZH2 increases AR gene expression at both the mRNA and protein levels.

EZH2 Occupies the AR Promoter to Directly Induce Its Transcription

Although EZH2, as a core subunit of the PRC2 complex, is best known as an epigenetic silencer, recent evidence has suggested that EZH2 might also function as a transcriptional activator (Gonzalez et al., 2011; Xu et al., 2012). Because our data showed concordant changes at the AR mRNA and protein levels upon EZH2 deregulation, it is likely that this regulation occurs at the step of AR transcription. Moreover, in cells treated with actinomycin D, which halts active transcription, we observed comparable AR mRNA levels over time between control and EZH2-depleted LNCaP cells (Figure S3A), precluding EZH2 regulation of AR transcript levels through altering its mRNA stability. To investigate whether EZH2 protein directly occupies the AR promoter, we performed EZH2 chromatin immunoprecipitation sequencing (ChIP-seq) in LNCaP cells and observed apparent EZH2 occupancy 1 kb downstream (around exon 1) of the AR gene transcription start site (TSS) (Figure 3A; Figure S3B). Using

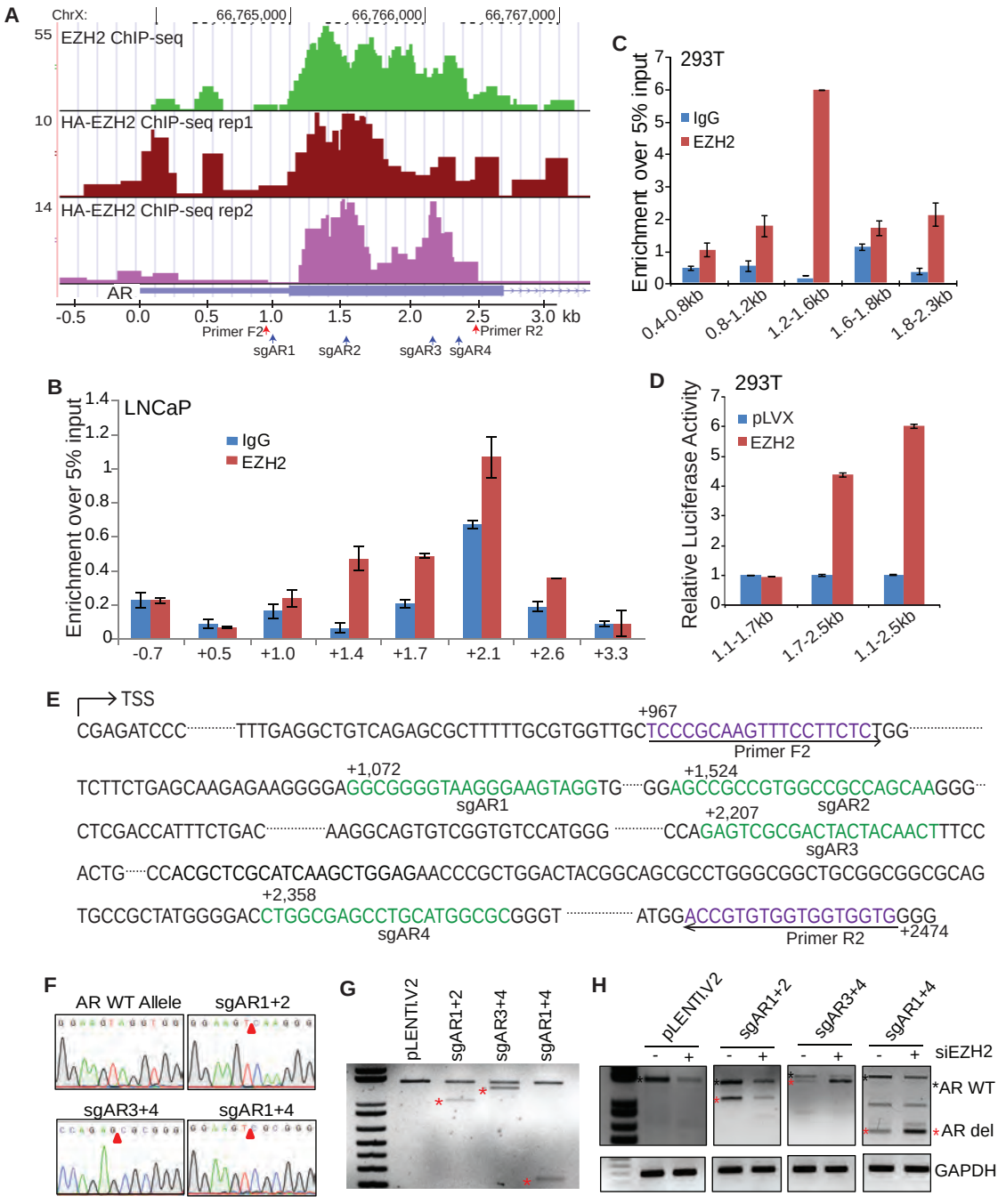

Figure 3. EZH2 Directly Activates AR Gene Transcription

(A) EZH2 protein occupies the AR gene promoter. EZH2 ChIP-seq was performed in LNCaP cells with an antibody targeting endogenous EZH2 (top). HA ChIP-seq was performed using an anti-HA antibody in LNCaP cells with ectopic HA-EZH2 overexpression. Two biological replicates are shown (center and bottom).

(B) ChIP-qPCR showing EZH2 binding along the AR gene promoter. ChIP was performed in LNCaP cells using anti-EZH2 and IgG antibodies and then subjected to qPCR using primer pairs targeting ~60-bp sliding windows within −1 kb to +3 kb of the AR gene. The x axis indicates the central location of the PCR products relative to the AR TSS. Data shown are mean (±SEM) of technical replicates from one representative experiment of three.

(C) Different regions (of 400 bp) of the AR promoter (from 0 to +3 kb) were cloned into the pRetroX-Tight-Pur-Luc vector and transfected into 293T cells, which were then subjected to ChIP by anti-EZH2 or IgG. EZH2 occupancy at the ectopically expressed AR promoter was determined by qPCR using a common forward primer targeting the vector sequence and a reverse primer specific to each fragment. Data shown are mean (±SEM) of technical replicates from one representative experiment of two.

(legend continued on next page)

an independent antibody, we conducted hemagglutinin (HA) ChIP-seq in LNCaP cells with HA-EZH2 overexpression in duplicate experiments and observed that ectopic EZH2 also binds to the same region on the AR promoter. As controls, ChIP-seq confirmed EZH2 occupancy on previously reported target genes such as *CNR1*, *NOV*, and *SLIT2* (Yu et al., 2010; Zhao et al., 2012; Figure S3C).

To validate the ChIP-seq results, qPCR analysis in primer walking experiments demonstrated strong EZH2 enrichment, compared with the immunoglobulin G (IgG) control, by primer pairs flanking the +1.4, +1.7, +2.1, and +2.6 kb regions of the AR promoter, further supporting EZH2 occupancy at this region (Figure 3B). To further examine the ability of AR promoter sequences to recruit EZH2 protein, we created an artificial system by transfecting 293T cells with various AR promoter fragments spanning 400-bp windows from 0.4 to 2.3 kb downstream of the AR TSS. To determine whether EZH2 is recruited to these exogenous DNA fragments, we performed EZH2 ChIP-qPCR using a forward primer that targets the plasmid backbone and a reverse primer that targets the inserted AR promoter fragment. Our data showed that EZH2 is strongly enriched at the ectopically expressed 1.2–1.6 kb and 1.8–2.3 kb AR promoter fragments, supporting some specificity of these DNA regions in recruiting the EZH2 protein (Figure 3C).

To determine whether the EZH2-bound AR promoter regions are indeed involved in EZH2-induced AR gene transcription, we generated three luciferase reporter constructs containing the 1.1–1.7 kb, 1.7–2.5 kb, and 1.1–2.5 kb regions of the AR promoter. Luciferase reporter assays demonstrated that EZH2 overexpression induced the transcriptional activities of distal AR promoter-containing constructs (i.e., 1.7–2.5 kb and 1.1–2.5 kb) but not the 1.1–1.7 kb construct (Figures 3D and S3D). These data suggest that, although EZH2 occupies both proximal (centered at +1.4 kb) and distal (centered at +2.0 kb) AR promoter regions, as indicated by ChIP-seq data, the regulatory function is dependent on the distal promoter. To identify potential transcription cofactors that might facilitate EZH2 in activating the AR, we performed a motif analysis of the AR promoter (from 0 to +2,500 bp to the AR TSS) using Jaspar and identified a total of 2,031 motifs (Table S1). In particular, there are 127 motifs within the AR distal promoter, among which are transcription activators such as SP1 and KLF5 that are known to bind GC-rich regions (Höller et al., 1988; Wei et al., 2018).

Next, we took one further step to characterize the significance of these EZH2-occuped AR promoter regions in the regulation of AR transcription *in vivo* by using the CRISPR-Cas9 system. Four single-guide RNAs (sgARs) were designed and paired to delete the downstream proximal AR promoter, the distal AR promoter, or both and were inserted into Cas9-containing lentiviral vectors (Figure 3E). Because the AR is crucial for LNCaP cell growth and the sgAR-targeted promoters overlap with the first exon of the AR gene, which will inadvertently knock out AR expression and lead to cell death, we opted not to select a pure population of CRISPR-mediated AR knockout cells for this experiment. LNCaP cells were infected with Cas9-sgAR lentiviruses, and genomic DNA was isolated from the pooled cells. Sanger sequencing using primers (F2 and R2 in Figures 3A and 3E) flanking the sgAR-targeted regions confirmed CRISPR-Cas9-mediated deletion at the expected sites (Figure 3F). Further, PCR analysis of genomic DNA confirmed the presence of a wild-type AR in all cells and a shorter PCR product of the expected size in CRISPR-Cas9-edited cells (Figure 3G). To examine how deletion of various AR promoter regions impairs the ability of EZH2 to activate the AR, control and CRISPR-Cas9-edited cells were subjected to control and EZH2 knockdown (Figure S3E). Because all sgARs also target the 5′ UTR and exon 1 of the AR gene, the primer set (F2 and R2) that was used to monitor genomic deletion at the AR promoter was also utilized to analyze AR mRNA expression and yielded wild-type AR and CRISPR-Cas9-deleted AR mRNA products (Figure 3H). Importantly, although EZH2 depletion reduced the levels of wild-type and CRISPR-Cas9-edited AR mRNA in cells with deletion of the AR proximal promoter (sgAR1+2), it failed to decrease the levels of CRISPR-Cas9-edited AR mRNA in cells with distal promoter deletion (sgAR3+4 or sgAR1+4), suggesting that EZH2 activates the AR through its distal promoter. Interestingly, in these cells, we found that the CRISPR-Cas9-deleted AR mRNA is surprisingly increased upon EZH2 knockdown, suggesting that EZH2 could repress AR expression through regulatory elements beyond the distal promoter. These results are consistent with our conclusion that EZH2 plays dual roles in its regulation of AR signaling and PCa.

EZH2 Activates the AR Independently of PRC2 and Its Histone Methyltransferase Activity

Our data so far suggest that EZH2 directly induces AR transcription through promoter binding. However, because the primary role of EZH2 is to catalyze H3K27me3, we wanted to test whether EZH2 activation of the AR is dependent on this catalytic function. First, we analyzed ChIP-seq data and observed EZH2, but not H3K27me3, occupancy at the AR promoter, suggesting a methylation-independent function (Figure 4A). Further, the

(D) Various AR promoter regions were cloned into the pGL4.10 vector and transfected into 293T cells with either control pLVX or HA-EZH2 overexpression. Cells were then subjected to luciferase reporter assays. Results were normalized to the *Renilla* internal control. Data shown are mean (±SEM) of technical replicates from one representative experiment of three.

(E) Schematic view of the AR promoter sequence starting from the transcription start site (TSS). The sgRNAs were labeled sgAR1 to 4, their sequences are shown in green font, and their distances to the AR TSS are marked as numbers. The primers (F2 and R2) for PCR validation are shown in purple.

(F and G) The distal AR promoter region is required for EZH2 activation of AR transcription. LNCaP cells were infected with lentiCRISPR-Cas9 containing the pLENTI.V2 control, sgAR1+2, sgAR3+4, or sgAR1+4 for 48 hr. CRISPR-Cas9-mediated genome editing was confirmed by Sanger sequencing (F) and genomic DNA PCR (G) using primers F2 and R2 (indicated in A and E).

(H) CRISPR-Cas9-edited LNCaP cells were transfected with control or EZH2-targeting siRNA for 48 hr. Total RNA was harvested and subjected to RT-PCR analysis using F2 and R2, which are expected to yield a wild-type (AR WT, top band with black asterisk) and a CRISPR-Cas9-deleted (AR del, bottom bands with red asterisk) AR mRNA.

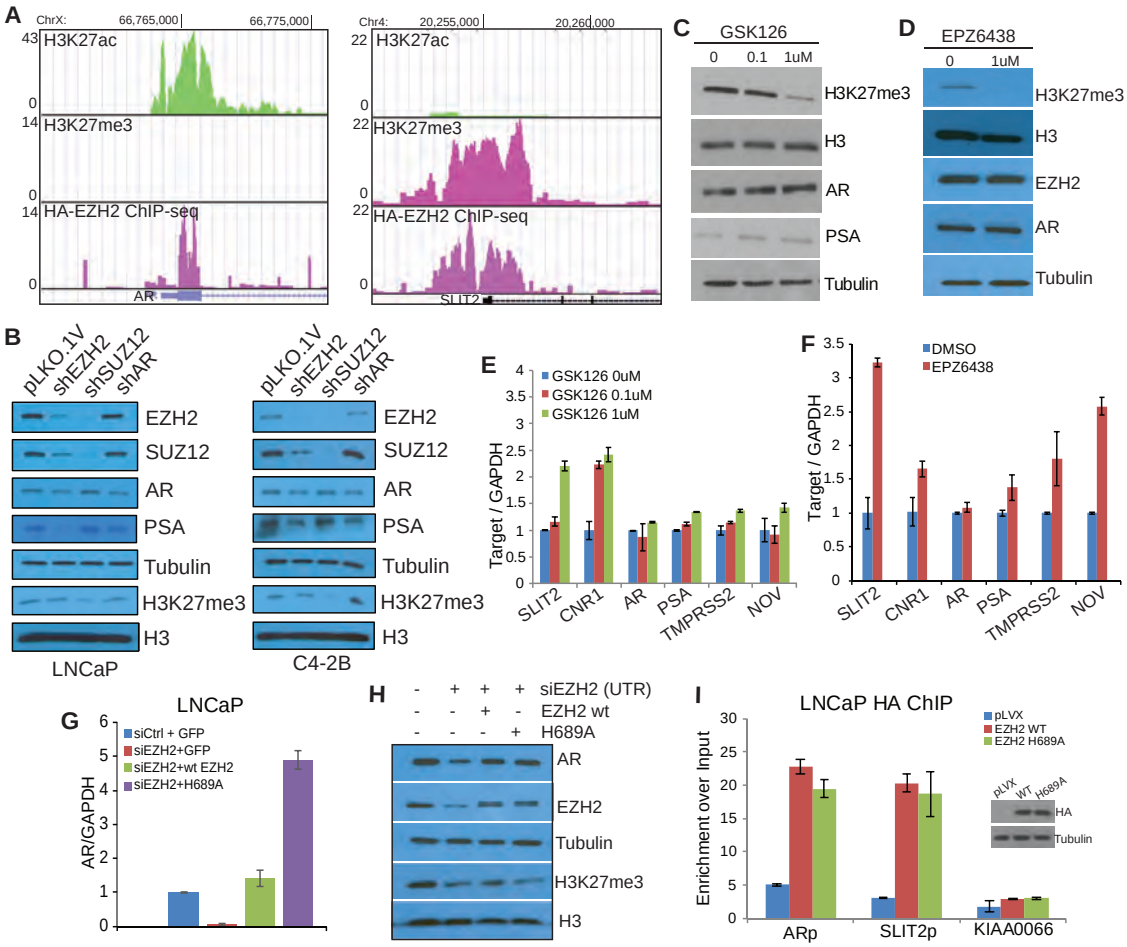

Figure 4. EZH2 Activates the AR Independently of Its Histone Methyltransferase Activity

(A) The AR promoter is occupied by EZH2 and H3K27ac but not H3K27me3, whereas the promoter of SLIT2, an epigenetic target of EZH2, is occupied with EZH2 and H3K27me3 but not H3K27ac. HA-EZH2 ChIP-seq was performed using anti-HA in LNCaP cells with HA-EZH2 overexpression. H3K27me3 and H3K27ac ChIP-seq was performed in LNCaP cells.

(B) EZH2, but not SUZ12, decreased AR expression levels. LNCaP or C4-2B cells were infected with pLKO.1V, shEZH2, shSUZ12, or shAR for 48 hr, and cell lysates were subjected to western blot analysis.

(C–F) EZH2 methyltransferase inhibitors failed to abolish AR expression. LNCaP cells were treated with EZH2 inhibitors GSK126 (C and D) or EPZ (E) for 72 hr, and the cell lysates were subjected to western blot (C and D) and qRT-PCR (E and F) analyses. The data shown in (E) and (F) are mean (±SEM) of technical replicates from one representative experiment of three.

(G and H) Both WT and the catalytically dead mutant H689A of EZH2 rescued AR expression. LNCaP cells were subjected to EZH2 knockdown (siEZH2), followed by re-introduction of WT or mutant (H689A) EZH2 for 72 hr. Cell lysates were then collected and analyzed by qRT-PCR (G) or western blotting (H).

(I) Both WT and H689A EZH2 are able to bind to the AR promoter. LNCaP cells were infected with pLVX control, HA-EZH2 WT, or HA-EZH2 H689A for 48 hr and then subjected to HA ChIP-qPCR. SLIT2 was used as a positive control and KIAA0066 as a negative control. Data shown are mean (±SEM) of technical replicates from one representative experiment of three. Overexpression of the HA-tagged WT and H689A EZH2 were validated by western blot (inset).

presence of the active histone mark H3K27 acetylation (H3K27ac) supports that this is an actively transcribed gene. By contrast, strong EZH2 and H3K27me3 occupancy and lack of the active histone mark H3K27ac were found at the promoter of the EZH2 epigenetic target SLIT2. ChIP-PCR confirmed differential H3K27me3 and H3K27ac enrichment at the AR and SLIT2 promoters in LNCaP as well as in C4-2B cells (Figures S4A and S4B). Our data thus suggest that EZH2 occupancy does not lead to H3K27me3 at the AR promoter but, rather, co-exists with H3K27ac, supporting gene activation. To demonstrate that activation of the AR by EZH2 is PRC2-independent, we performed EZH2, SUZ12, or AR knockdown side by side in LNCaP and C4-2B cells by shRNA transfection for 48 hr. Importantly, EZH2 knockdown mimicked AR knockdown in decreasing AR and prostate-specific antigen (PSA) expression in both LNCaP and C4-2B cells (Figure 4B). By contrast, SUZ2 knockdown, despite its ability to decrease total EZH2 protein levels, consistent with the previously reported regulation of PRC2 stability (Pasini et al., 2004), failed to decrease AR and PSA in both cell lines tested, whereas it successfully decreased H3K27me3 levels similar to EZH2 knockdown. Taken together, these results suggest that short-term SUZ12 knockdown did not affect EZH2

outside of the PRC2 complex and that EZH2 activates AR transcription through PRC2-independent mechanisms.

To further demonstrate that EZH2 induces AR expression independently of H3K27me3, we took advantage of catalytic EZH2 inhibitors such as GSK126 and EPZ-6438 (EPZ), which compete with S-adenosyl-methionine (SAM) to prevent H3K27me3. LNCaP cells were treated with increasing doses (0, 0.1, and 1 μM) of GSK126 for 3 days. Western blot analysis demonstrated that AR and PSA levels were not only not decreased but also slightly increased upon catalytic EZH2 inhibition, whereas H3K27me3 showed a dose-dependent reduction, as expected (Figures 4C and S4C). This increase in AR signaling by the enzymatic EZH2 inhibitor is consistent with a recent report (Ku et al., 2017), potentially because of the AR also being an epigenetic target of EZH2. Similar results were also observed in cells treated with EPZ (Figure 4D). As a control, qRT-PCR analysis confirmed restored expression of previously reported EZH2 epigenetic targets such as SLIT2 CNR1 and NOV (Figures 4E, 4F, and S4D).

Because small-molecule inhibitors might have off-target effects, we next examined the regulatory mechanism utilizing an EZH2 catalytically dead mutant, H689A. LNCaP cells were treated with control or EZH2-targeting siRNA to deplete endogenous EZH2, which was then subjected to rescue using wild-type or H689A-mutant EZH2. For this experiment, the siEZH2 that targets the 5′ UTR of the EZH2 region was utilized to prevent it from degrading ectopic EZH2. qRT-PCR analysis showed that both wild-type and H689A-mutant EZH2 restored the AR mRNA level in EZH2-depleted cells, supporting methylation-independent transcriptional activation of the AR gene by EZH2 (Figure 4G). Western blot analysis further confirmed that the AR protein level was decreased upon endogenous EZH2 knockdown, as expected, and could be rescued by re-expression of either wild-type or H689A-mutant EZH2 (Figure 4H). By contrast, H3K27me3 is decreased upon endogenous EZH2 knockdown and, as expected, can only be rescued by re-introduction of wild-type EZH2 but not the H689A catalytically dead mutant. In good agreement with this, HA ChIP-qPCR revealed that, like wild-type EZH2, the ectopically expressed H689A mutant also strongly binds to the AR gene promoter (Figure 4I). Therefore, our data provide strong evidence that EZH2 directly induces AR gene expression through PRC2- and methylation-independent mechanisms that cannot be blocked by enzymatic EZH2 inhibitors.

EZH2 Mediates Dual Transcription Programs in PCa

Our data so far suggest that EZH2 plays dual roles in PCa: as a transcriptional activator, mediated in part by the AR, and as an epigenetic silencer, mediated by H3K27me3. To further examine these dual transcriptional programs on the genome-wide scale, we performed a global expression analysis of LNCaP cells treated with control or EZH2 knockdown in parallel with LNCaP cells treated with the DMSO control or EPZ. All experiments were performed in triplicate. We identified 359 genes that were significantly increased (adjusted $p < 0.01$) upon EZH2 depletion (Figure 5A). Importantly, 224 (62%) of these EZH2-repressed genes were upregulated by treatment with EPZ, an inhibitor of EZH2 histone methyltransferase function, supporting their being targets of EZH2-mediated epigenetic silencing. On the other hand, gene expression analysis revealed 393 genes (adjusted $p < 0.0005$), including the AR and its target genes, such as TMPRSS2 and KLK2, that were downregulated upon EZH2 depletion. Interestingly, the expression of the majority of these EZH2-activated genes was not changed upon EPZ treatment, supporting a methylation-independent mechanism in EZH2-mediated gene activation (Figure 5A). These dual functions of EZH2 in epigenetic silencing and gene activation were also validated in C4-2B cells (Figure S5A).

Next we sought to gain some insights into the mechanisms underlying EZH2-mediated gene regulation. We found that EZH2-repressed and EPZ-induced genes (class I) had the strongest H3K27me3 enrichment at their promoters, whereas EZH2-activated genes (class III) were barely enriched for H3K27me3 (Figure S5B). On the contrary, class III genes were marked with strong H3K27ac, whereas class I genes were marked the weakest. Because our H3K27me3 ChIP-seq intensity was relatively low, we compared it with previously published H3K27me3 ChIP-seq data (Xu et al., 2012). We observed a significant overlap between the datasets, supporting the quality and reproducibility of our data (Figure S5C). To examine how histone modifications on these genes change upon EZH2 knockdown, we selected EZH2 target genes that contained at least one EZH2 binding site at their promoters (Figure S5D). We found that class I and II (EZH2-repressed but EPZ-independent) genes showed increased H3K27ac upon EZH2 knockdown, whereas H3K27ac was decreased on class III genes (Figure 5B), consistent with their respective expressional regulation by EZH2. As a controls H3K27me3 was decreased upon EZH2 knockdown in all three classes of genes, except that it was barely present on class III genes.

To examine whether the local chromatin environment affects the role of EZH2 as an activator or repressor, we rank-ordered all EZH2 binding sites in LNCaP cells by enrichment intensity and examined H3K27ac and H3K27me3 signals at these sites (Figures 5C and S5D). We observed that the strongest EZH2 binding sites were enriched for H3K27me3, as expected. Interestingly, there were many EZH2 binding sites that were marked by strong H3K27ac, which was nearly mutually exclusive with H3K27me3. We noticed that, although EZH2 knockdown decreased the EZH2 enrichment signal as expected, it did not alter H3K27ac and H3K27me3 globally. This is consistent with previous reports of persistent H3K27me3 on many loci upon EZH2 inactivation (Neff et al., 2012), likely because of compensation from EZH1 (Shen et al., 2008). A Venn diagram analysis revealed 8,125 (42%) and 6,449 (34%) EZH2 binding sites that, respectively, overlapped with H3K27me3 (termed EZH2-me) and H3K27ac (termed EZH2-ac), supporting association of EZH2 with both repressed and activated genes (Figure 5D). To examine whether these distinct chromatin patterns are accountable for differential regulation by EZH2, we focused on binding sites with an EZH2 ChIP-seq peak score greater than 12 and that localize within 1 kb of a TSS, leading to 1,294 and 1,415 EZH2-me and EZH2-ac genes, respectively. Analysis of RNA sequencing (RNA-seq) data (Zhang et al., 2018) revealed that genes marked with EZH2-ac were, in general, actively transcribed in LNCaP cells, whereas EZH2-me genes were often

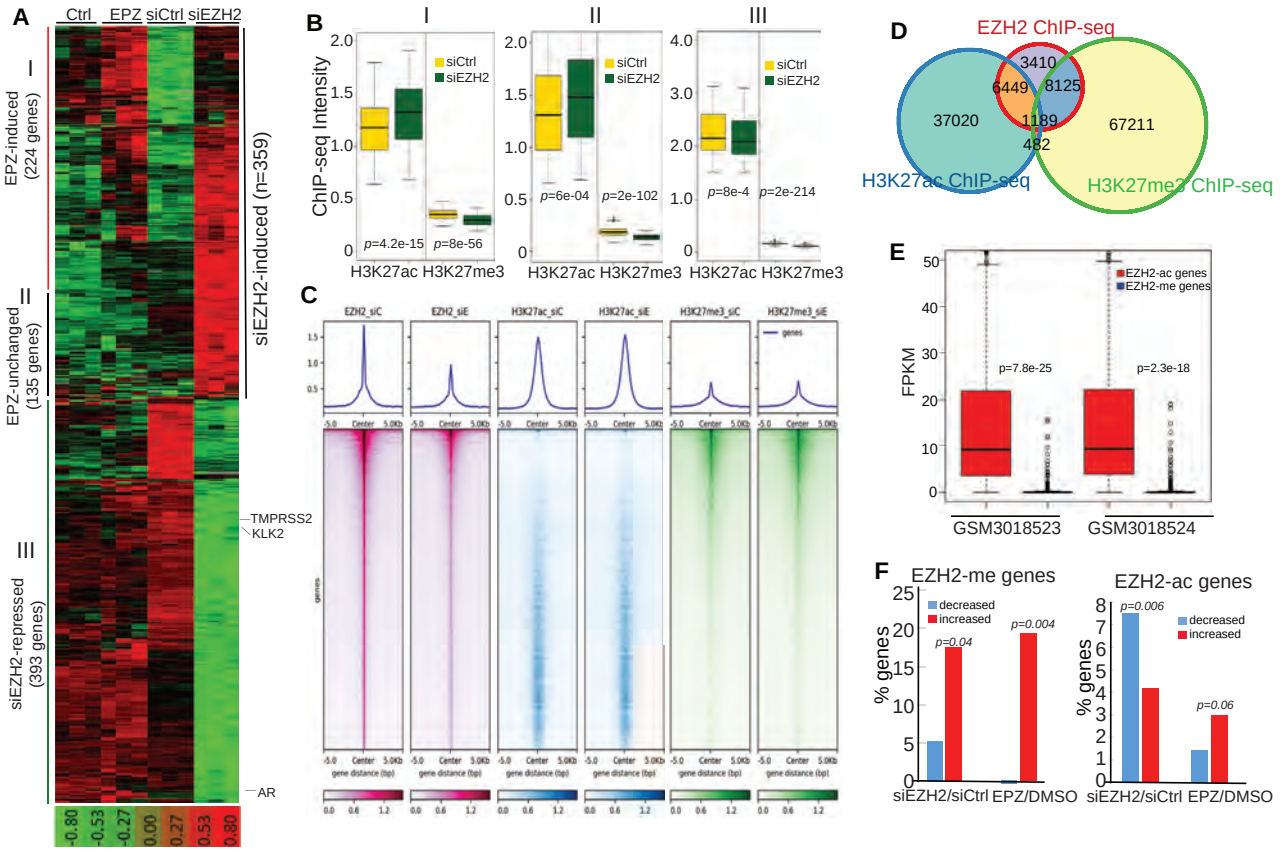

Figure 5. Methylation-Dependent and -Independent Transcriptional Programs of EZH2 in Prostate Cancer

(A) Dual EZH2 transcriptional programs in prostate cancer (PCa). LNCaP cells were treated with either EPZ versus vehicle control or siEZH2 versus siCtrl and then profiled in triplicate microarray experiments. Genes that were significantly up- or downregulated by siEZH2 compared with the control were clustered across all samples and are shown as heatmaps. Each row represents one gene and each column one sample. The siEZH2-induce genes that were also induced by EPZ were termed class I genes and those unchanged by EPZ class II genes. Genes that were activated by EZH2 were defined as class III genes.

(B) EZH2-regulated genes that contain at least one EZH2 ChIP-seq binding site at their promoter regions (±5 kb) were defined as direct targets of EZH2. H3K27ac and H3K27me3 ChIP-seq was performed in LNCaP cells with siCtrl or siEZH2, and their intensities around the three classes of direct EZH2-target genes were analyzed by boxplots. The p values evaluate the differences of ChIP-seq signals in siEZH2 versus siCtrl cells.

(C) All EZH2 binding sites identified in control LNCaP cells were rank-ordered based on EZH2 ChIP-seq intensities. Shown at the top are average intensities, and at the bottom are heatmaps of EZH2, H3K27ac, and H3K27me3 ChIP-seq around all EZH2 binding sites.

(D) Venn diagram showing overlap among EZH2, H3K27ac, and HEK27me3 binding sites. ChIP-seq was performed in control LNCaP cells.

(E) EZH2 target genes marked with H3K27ac are abundantly expressed, whereas those marked by H3K27me3 are repressed. Genes whose promoters (±1 kb to the TSS) contain at least one EZH2 binding site with a peak score greater than 12 were selected. The subset (1,415) marked by H3K27ac, but not H3K27me3, was defined as EZH2-ac genes, whereas the subset (1,294) marked by H3K27me3, but not H3K27ac, was defined as EZH2-me genes. The expression levels (FPKM) of these genes in publicly available RNA-seq data (GSM3018523 and GSM3018524) that were performed in LNCaP cells are shown as boxplots.

(F) EZH2-me genes are enriched for upregulation by EZH2 knockdown or EPZ treatment, whereas EZH2-ac genes are enriched for downregulation by EZH2 knockdown independently of EPZ. About 800 of 1,415 (57%) EZH2-ac genes, but only 60 of 1,294 (4.6%) EZH2-me genes, were detected in microarray experiments. The percentages of the genes that were significantly up- or downregulated by siEZH2 compared with siCtrl or by EPZ treatment compared with DMSO were calculated and plotted.

repressed, with FPKM (fragments per kilobase million) values of less than 1 (Figure 5E). Integration with microarray data showed that a significantly larger percentage of EZH2-me genes were upregulated than downregulated by EZH2 knockdown, and they were similarly regulated by EPZ, supporting their being epigenetic targets of EZH2 (Figure 5F). On the other hand, more EZH2-ac genes were decreased by EZH2 knockdown but not by EPZ, supporting that these genes are more likely to be activated by EZH2 through methylation-independent pathways. Further, gene ontology (GO) analysis showed that EZH2-ac genes are strongly enriched for cell cycle-related pathways, including mTORC1, MYC, p53, and E2F regulation (Table S2), whereas EZH2-me genes are involved in epithelial-mesenchymal transition (EMT), apical junction complex, and inflammatory responses (Table S3). Moreover, a motif analysis demonstrated that the promoters of EZH2-ac genes were enriched for motifs of transcription activators such as SP1 and KLF5, which were also identified in the AR promoter (Figure S5E). By contrast, the promoters of EZH2-me genes were enriched for motifs of transcriptional repressors such as RE1-silencing transcription

factor (NRSF) and non-prostate lineage transcription factors such as E2A and LHX2, supporting their repressed state in PCa cells.

Last, we attempted to examine the presence of these dual EZH2 transcription programs in PCa cells. First, we obtained an epigenetic signature composed of genes that were restored following EPZ treatment. GSEA demonstrated that this epigenetic signature was remarkably enriched for higher expression by EZH2 knockdown in both androgen-depleted and androgen-stimulated cells (Figure S5F). These data support that EZH2-mediated epigenetic silencing is a general phenomenon that is independent of AR signaling. We have shown previously that, in the presence of androgen, androgen-induced genes were markedly downregulated upon EZH2 depletion, whereas androgen-repressed genes were upregulated (Figures 1A and 1B). However, in androgen-depleted cells, we found that androgen-induced genes were only marginally reduced by EZH2 knockdown (Figure S5G), suggesting a mechanism dependent on active AR signaling. Androgen-repressed genes, on the other hand, remained significantly upregulated upon EZH2 depletion, which is likely due to many of these genes also being epigenetic targets of EZH2 (Zhao et al., 2012). Further, qRT-PCR analysis of gene expression in hormone-deprived LNCaP cells confirmed that AR-induced genes were no longer regulated by EZH2 in the absence of active androgen signaling, whereas epigenetic EZH2 targets, such as *CNR1*, *SNCA*, and AR-repressed genes, continued to be upregulated upon EZH2 knockdown (Figure S5H). In conclusion, our data support an epigenetic role of EZH2 that is present in both androgen-dependent and -independent PCas and an AR-activating role of EZH2 that may be blocked by androgen deprivation therapy.

Complete Blockade of EZH2 Dual Functions Abolishes Prostate Tumorigenesis *In Vitro*

Because EZH2 increases AR transcription, we examined co-expressed patterns of these two genes in human PCa samples and indeed observed that EZH2 and AR expression levels are significantly correlated in a number of publicly available cancer profiling datasets (Figure S6A). Cell growth assays of C4-2B cells demonstrated that EZH2 knockdown showed a much stronger growth-inhibitory effect than knockdown of SUZ12 and blockade of PRC2 epigenetic effects and of AR, blockade of AR signaling alone (Figure S6B). This suggests that full blockade of EZH2 function has stronger tumor-inhibitory effects than blocking either its catalytic function or its non-catalytic gene activation function alone. Because EZH2 degradation is not yet possible, in the present study, we attempted to combine an EZH2 enzymatic inhibitor that blocks its catalytic function with an AR antagonist that targets one key downstream pathway of the EZH2-activating role in PCa. We treated LNCaP cells with vehicle control, 0.5 μM GSK126, 0.5 μM enzalutamide (Enz), or both over a period of 60 days. When reaching 80% confluence, cells were counted, split in proportion, and cultured in media containing the corresponding drugs. Our results demonstrated that Enz-treated cells initially grew at a much slower rate, decreased in cell number at 10 days of treatment, but rapidly gained resistant growth after 15 days of treatment, whereas GSK126-treated cells continued to grow but at a slightly reduced rate. Remarkably, LNCaP cells treated with both drugs were reduced in number after 10 days of treatment and remained unable to grow, highlighting the potential of this drug combination to overcome resistance (Figure 6A). To further test the combinatorial effects of the drugs, we treated LNCaP and C4-2B cells with Enz and EPZ either alone or in combination. Because CRPC cells are much less sensitive to Enz than ADPC cells, a higher dose of Enz was utilized in C4-2B cells. Importantly, our data revealed strong combinatorial effects of EPZ and Enz treatment in suppressing the proliferation of both LNCaP and C4-2B cells (Figures 6B and 6C). Moreover, the drug combination also showed synergy in suppressing LNCaP and C4-2B cell colony formation (and in eliminating their colony formation ability) (Figures 6D and 6E). Cell cycle analysis by flow cytometry revealed that combined use of Enz and EPZ led to global cell cycle arrest at G0 and G1 and G2 and M phases, leading to a marked reduction in S phase cells (Figures 6F and 6G). Taken together, our data suggest that blockade of EZH2 dual functions through combined use of an enzymatic EZH2 inhibitor and an AR antagonist may overcome or delay the onset of drug resistance when treating PCa patients with either drug alone.

Dual EZH2 Targeting through Combinatorial Use of an Enzymatic EZH2 Inhibitor and AR Antagonist Diminished Xenograft Tumor Growth *In Vivo*

To examine the molecular effects of the drug treatment, we performed RNA-seq analysis of C4-2B cells treated with either Enz or EPZ, alone or in combination, in triplicate experiments. Significantly, we found that EZH2-induced genes were downregulated only partially by either Enz or EPZ alone but were remarkably repressed by combinatorial treatment (Figure 7A). A similar synergy of these two drugs was also observed in their ability to restore EZH2-repressed gene expression. In addition, GO pathway analyses revealed that cancer cell cycle hallmarks, such as E2F_targets, G2M_checkpoint, Mitotic Spindle, and Myc_targets, were remarkably more enriched with drug combination than either EPZ or Enz alone (Table S4). Further, the androgen response gene signature is significantly inhibited by Enz alone but is induced by EPZ as a single agent (Figure S7A), which is consistent with the findings from Ku et al. (2017) and explains at least partially the failure of the enzymatic EZH2 inhibitor in PCa. However, this "side effect" of EPZ was blocked by Enz in the drug combination because the androgen response gene signature remained inhibited. Therefore, Enz and EPZ combination is much more effective in fully blocking the transcriptional activities of EZH2 than either drug alone, justifying further investigation of this combinatorial therapeutic strategy in *in vivo* models.

To investigate the efficacy of the Enz and EPZ combination in *in vivo*, CRPC cell line C4-2B cells were inoculated subcutaneously into non-obese diabetic (NOD).severe combined immunodeficiency (SCID) mice that were surgically castrated. When the initial tumor volume reached ~200 mm^3, the tumor-bearing mice were randomized to receive vehicle control or Enz or EPZ alone or in combination daily, and the tumor volume was measured every 3 days. Importantly, we observed that combinatorial treatment significantly reduced xenograft tumor growth (ANOVA, $p < 0.001$), whereas either drug as a single agent had a minimal tumor-suppressive effect (Figures 7B and S7B). The tumor weight at

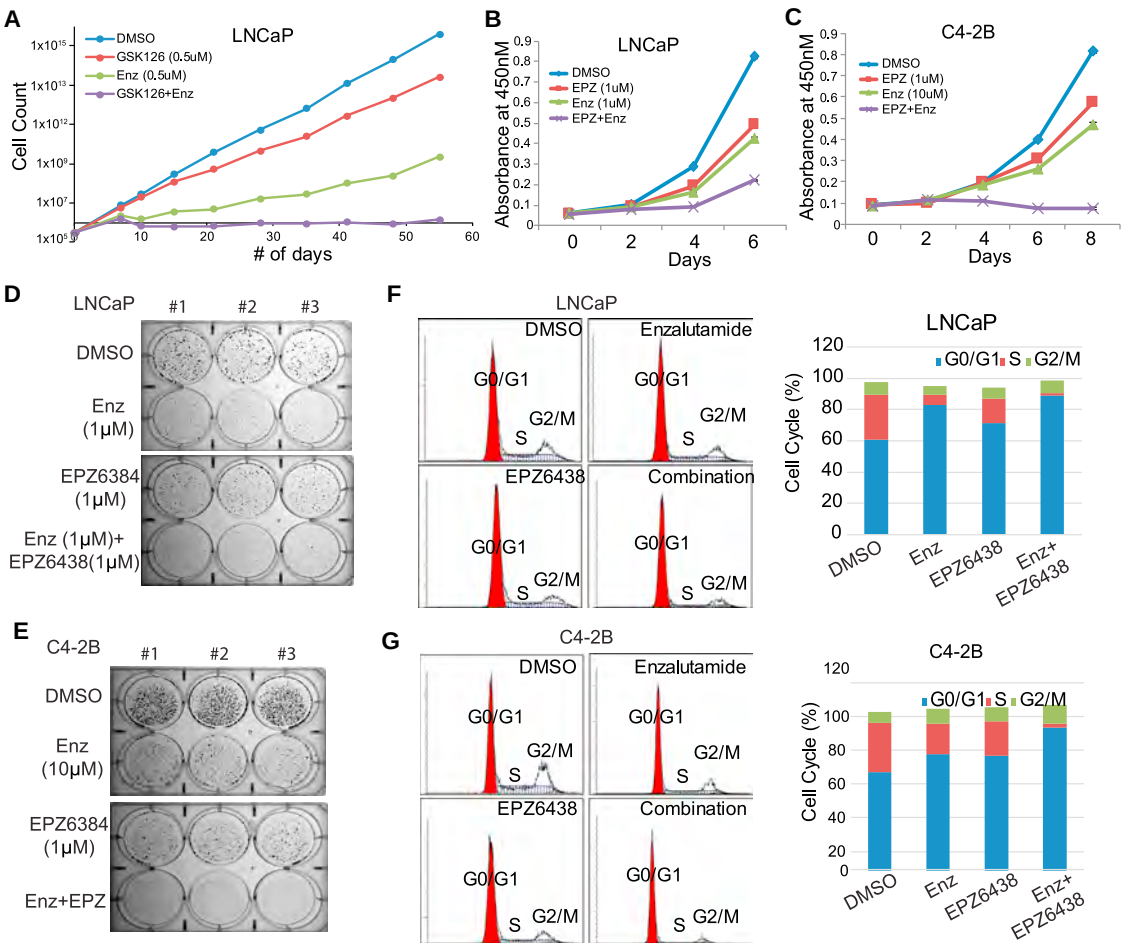

Figure 6. Simultaneous EZH2 and AR Targeting Remarkably Inhibited PCa Cell Growth

(A) Combinatorial GSK126 and enzalutamide (Enz) treatment significantly inhibited LNCaP cell growth and drug resistance. LNCaP cells were maintained in DMSO, GSK126 (0.5uM), Enz (0.5uM), or both for 55 days. Cells were counted and re-plated whenever needed, and accumulated cell numbers were determined. Data shown are for one representative experiment of two.

(B and C) LNCaP (B) or C4-2B (C) cells were treated with DMSO, Enz (1 μM for LNCaP and10 μM for C4-2B), EPZ (1 μM), or both. Cell growth was measured with WST-1 reagent every 2 days. Data shown are mean ± SEM of technical replicates from one representative experiment of three.

(D and E) LNCaP (D) or C4-2B (E) cells were treated with DMSO, Enz (1 μM for LNCaP and 10 μM for C4-2B), EPZ (1 μM), or both for 2 weeks, followed by 0.002% crystal violet staining to assay colony formation. Data shown are technical replicates from one representative experiment of three.

(F and G) Combinatorial Enz and EPZ treatment induced cell cycle arrest. LNCaP (F) or C4-2B (G) cells were treated with DMSO, Enz (1 μM for LNCaP and 10 μM for C4-2B), EPZ (1 μM), or both for 3 days, followed by cell cycle analysis via flow cytometry with propidium iodide staining.

the endpoint was significantly lower in mice treated with the drug combination (ANOVA, $p < 0.02$), whereas Enz or EPZ alone failed to inhibit CRPC tumor growth (Figures 7C and S7B).

To confirm the on-target effects of the drugs, we dissected out xenograft tumors for molecular analysis. Western blotting showed that EPZ treatment decreased H3K27me3, as expected, but also inadvertently increased AR expression (Figure 7D), which is consistent with our *in vitro* data and a recent report (Ku et al., 2017). Further, we found that PSA levels in these xenograft CRPC tumors, which were grown in castrated mice, were, in general, very low but could be detected by qRT-PCR and showed an on-target suppression by Enz (Figure S7C). Further, although PSA expression was inadvertently increased by EPZ as a single agent, it remained repressed by EPZ and Enz drug combination. In addition, we found that the EPZ and Enz combination strongly decreased the expression of the cell cycle regulator Cyclin D1, consistent with their synergetic roles in regulating global cell cycle arrest. Moreover, immunohistochemistry staining revealed a substantial decrease in Ki67 staining in cells treated with the drug combination (Figures 7E and S7D). Therefore, our data support that combinatorial Enz and EPZ treatment has synergistic effects in completely abolishing dual EZH2 pathways and in inhibiting CRPC tumor growth.

DISCUSSION

EZH2 was first found to be one of the most upregulated genes in aggressive PCa more than a decade ago (Varambally et al.,

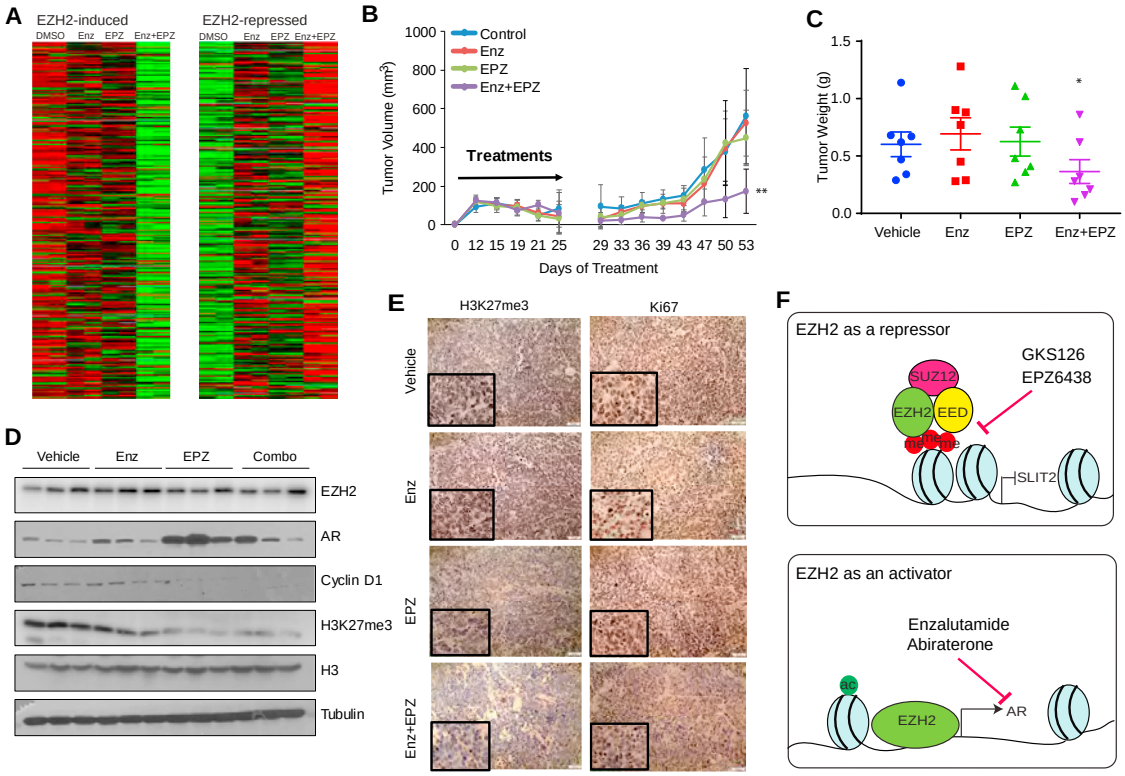

Figure 7. Combination of the Enzymatic EZH2 Inhibitor with Enz Markedly Reduced Xenograft Tumor Growth

(A) EZH2-mediated transcription activities were blocked by combinatorial EPZ and Enz treatment. C4-2B cells were treated with DMSO, EPZ (1 μM), Enz (10 μM), or both for 7 days and then subjected to RNA-seq. FPKM values of EZH2-induced and -repressed gene sets across all samples were clustered and visualized as heatmaps.

(B and C) Enz and EPZ combination greatly reduced C4-2B xenograft tumor growth *in vivo*. C4-2B cells were implanted subcutaneously in surgically castrated NOD.SCID mice. Upon palpable tumor formation, the mice (n = 7/group) were randomized to receive vehicle (1% carboxymethylcellulose sodium [CMC-Na^+] and 1% Tween 30), 10 mg/kg Enz (once a day), 250 mg/kg EPZ (twice a day), or both by oral gavage for 3 weeks. Tumor volume (B) and weight at the endpoint (C) were measured by a second person in a blinded fashion. Statistical differences in tumor volume and tumor weight among groups were determined using two-way repeated-measures ANOVA ($p < 0.001$) and one-way ANOVA ($p < 0.02$), respectively.

(D) Western blotting of target genes in C4-2B xenograft tumors at the endpoint.

(E) Representative H3K27me3 and Ki-67 immunohistochemistry images of tumor sections from each treatment group.

(F) A model depicting dual roles of EZH2 as an epigenetic silencer, a function that can be blocked by enzymatic inhibitors such as GSK126 and EPZ, and as a transcriptional activator of AR, which can be blocked by AR antagonists such as enzalutamide.

2002). Ever since, a large body of literature, including by us, has examined the function and molecular mechanisms of EZH2 in PCa, but this is largely limited to epigenetic targets of EZH2 (Yu et al., 2010). However, evidence has accumulated recently suggesting that EZH2 is capable of stimulating or repressing gene expression beyond PRC2 and H3K27me3 (Gonzalez et al., 2011). Of most relevance, Xu et al. (2012) reported that, in CRPC cells, EZH2 activates gene expression independently of PRC2 but still requires methylation activity. They postulated that this could be due to methylation of non-histone substrates that have yet to be characterized. Quite distinct from their study, here, we demonstrate a non-catalytic role of EZH2 in PCa that is independent of both PRC2 and its methyltransferase activity. Extensive analyses of the target AR gene promoter using ChIP-seq, luciferase, and CRISPR-Cas9 assays support that this regulation occurs at the transcription level and involves EZH2 protein occupancy at the AR promoter, a locus previously implicated in AR gene activation (Wang et al., 2016). We speculate that EZH2 binding at the AR promoter may recruit additional transcriptional coactivators, such as SP1 or KLF5, to induce gene expression, which will be interesting lines for future investigation. In support of this, recent studies have reported EZH2 interaction with Elongin A to increase transcription of target genes (Ardehali et al., 2017), and its paralog EZH1 has likewise been shown to associate with H3K4me3, RNA polymerase II, and transcription activation (Mousavi et al., 2012).

Through the use of diverse of PCa cell lines, we show that EZH2 activation of AR gene transcription and AR signaling occurs in both ADPC and CRPC, which is distinct from a previous report of EZH2-AR interaction only in CRPC but not ADPC (Xu et al., 2012). This disparity supports the novelty of our finding and its being a different mechanism. Further, through comparative expression profiling of cells treated with EZH2 knockdown or the enzymatic EZH2 inhibitor EPZ, we showed that a large set of genes

that were downregulated upon EZH2 knockdown is not repressed by EPZ, providing a potential list of methylation-independent EZH2-activated genes. Using ChIP-seq, we demonstrated a very interesting pattern of EZH2-occupied genomic loci: about one-third of them are co-occupied by H3K27me3 (potential EZH2-repressed targets) and another one-third are co-occupied by H3K27ac (potential EZH2-activated genes), supporting EZH2 being both a transcriptional repressor and activator. Our data suggest that the local chromatin environment may dictate the function of EZH2 at a specific genomic locus. The EZH2-bound AR promoter locus harbors the features of gene-activating elements, including high H3K27ac but no H3K27me3, and possesses motifs of many transcription activators.

Last, we demonstrate that the role of EZH2 as a transcriptional activator, with AR being a key target, coexists with its conventional catalytic role in gene repression and plays important oncogenic functions in AR-driven PCa (Figure 7F). Enzymatic EZH2 inhibitors such as EPZ and GSK126, although effective in blocking the enzymatic roles of EZH2, are unable to suppress EZH2-mediated activation of the AR. Instead, they inadvertently increase AR expression, as demonstrated in our data and in a recent report (Ku et al., 2017), which may account for their failure in suppressing AR-positive PCa, as noted previously (Dardenne et al., 2016) and also as observed in our study. In addition, these studies have found that enzymatic EZH2 inhibitors are much more effective in AR-negative NEPC cells, which is consistent with our model. Moreover, understanding the molecular mechanisms of EZH2 functions in PCa allowed us to propose a strategy for the use of these clinically available enzymatic EZH2 inhibitors, through combination with AR antagonist, in a subtype of PCa (i.e., CRPC) that is driven by AR and expresses high levels of EZH2. We understand that the AR antagonist will target all ARs, induced either by EZH2 or through other mechanisms such as AR gene amplification. Nevertheless, it is legitimate and a common practice to target a key downstream pathway when the upstream regulator itself is not yet targetable. Our results suggest that compounds capable of degrading EZH2 protein, similar to EZH2 knockdown, might greatly outperform enzymatic EZH2 inhibitors and would have higher specificity in blocking the dual roles of EZH2. It would be important to develop such small-molecule inhibitors in future studies. In summary, our study reports a non-catalytic role of EZH2 in transcriptional activation and provides compelling preclinical data to support clinical applications of combinatorial Enz and EPZ treatment in CRPC.

STAR★METHODS

Detailed methods are provided in the online version of this paper and include the following:

SUPPLEMENTAL INFORMATION

Supplemental Information includes seven figures and five tables and can be found with this article online at https://doi.org/10.1016/j.celrep.2018.11.035.

ACKNOWLEDGMENTS

We thank Dr. Ming Hu (Cleveland Clinic) for discussions regarding statistical analysis and Bin Zheng and Galina Gritsina for technical help. This work was supported in part by National Cancer Institute R01CA172384 (to J.Y.), P50CA180995 (pilot project, to J.Y.), and R50CA211271 (to J.C.Z.); American Cancer Society Research Scholar Award RSG-12-085-01 (to J.Y.); Department of Defense PC160328 (to J.Y.); and an institutional Ruth L. Kirschstein National Research Service award from the National Institute of Diabetes and Digestive and Kidney Diseases T32 DK007169 (to J.K.).

AUTHOR CONTRIBUTIONS

Conceptualization, J.Y. and J.C.Z; Investigation, J.K., Y.L., X.L., B.S., K.-W.F., Q.C., J.D.L., J.C.Z., and J.Y.; Writing, J.K., Y.L., J.C.Z., and J.Y. with input from all authors; Funding Acquisition, J.Y. and J.C.Z.

DECLARATION OF INTERESTS

The authors declare no competing interests.

Received: January 12, 2018
Revised: October 15, 2018
Accepted: November 7, 2018
Published: December 4, 2018

REFERENCES

Ardehali, M.B., Anselmo, A., Cochrane, J.C., Kundu, S., Sadreyev, R.I., and Kingston, R.E. (2017). Polycomb Repressive Complex 2 Methylates Elongin A to Regulate Transcription. Mol Cell *68*, 872–884.e6.

Dardenne, E., Beltran, H., Benelli, M., Gayvert, K., Berger, A., Puca, L., Cyrta, J., Sboner, A., Noorzad, Z., MacDonald, T., et al. (2016). N-Myc Induces an EZH2-Mediated Transcriptional Program Driving Neuroendocrine Prostate Cancer. Cancer Cell *30*, 563–577.

Gonzalez, M.E., DuPrie, M.L., Krueger, H., Merajver, S.D., Ventura, A.C., Toy, K.A., and Kleer, C.G. (2011). Histone methyltransferase EZH2 induces Akt-dependent genomic instability and BRCA1 inhibition in breast cancer. Cancer Res. *71*, 2360–2370.

He, A., Shen, X., Ma, Q., Cao, J., von Gise, A., Zhou, P., Wang, G., Marquez, V.E., Orkin, S.H., and Pu, W.T. (2012). PRC2 directly methylates GATA4 and represses its transcriptional activity. Genes Dev. *26*, 37–42.

Höller, M., Westin, G., Jiricny, J., and Schaffner, W. (1988). Sp1 transcription factor binds DNA and activates transcription even when the binding site is CpG methylated. Genes Dev. *2*, 1127–1135.

Kim, K.H., Kim, W., Howard, T.P., Vazquez, F., Tsherniak, A., Wu, J.N., Wang, W., Haswell, J.R., Walensky, L.D., Hahn, W.C., et al. (2015). SWI/SNF-mutant cancers depend on catalytic and non-catalytic activity of EZH2. Nat. Med. *21*, 1491–1496.

Ku, S.Y., Rosario, S., Wang, Y., Mu, P., Seshadri, M., Goodrich, Z.W., Goodrich, M.M., Labbé, D.P., Gomez, E.C., Wang, J., et al. (2017). Rb1 and Trp53 cooperate to suppress prostate cancer lineage plasticity, metastasis, and antiandrogen resistance. Science *355*, 78–83.

Lee, J.M., Lee, J.S., Kim, H., Kim, K., Park, H., Kim, J.Y., Lee, S.H., Kim, I.S., Kim, J., Lee, M., et al. (2012). EZH2 generates a methyl degron that is recognized by the DCAF1/DDB1/CUL4 E3 ubiquitin ligase complex. Mol. Cell *48*, 572–586.

Mousavi, K., Zare, H., Wang, A.H., and Sartorelli, V. (2012). Polycomb protein Ezh1 promotes RNA polymerase II elongation. Mol. Cell *45*, 255–262.

Neff, T., Sinha, A.U., Kluk, M.J., Zhu, N., Khattab, M.H., Stein, L., Xie, H., Orkin, S.H., and Armstrong, S.A. (2012). Polycomb repressive complex 2 is required for MLL-AF9 leukemia. Proc. Natl. Acad. Sci. USA *109*, 5028–5033.

Pasini, D., Bracken, A.P., Jensen, M.R., Lazzerini Denchi, E., and Helin, K. (2004). Suz12 is essential for mouse development and for EZH2 histone methyltransferase activity. EMBO J. *23*, 4061–4071.

Sanulli, S., Justin, N., Teissandier, A., Ancelin, K., Portoso, M., Caron, M., Michaud, A., Lombard, B., da Rocha, S.T., Offer, J., et al. (2015). Jarid2 Methylation via the PRC2 Complex Regulates H3K27me3 Deposition during Cell Differentiation. Mol. Cell *57*, 769–783.

Shen, X., Liu, Y., Hsu, Y.J., Fujiwara, Y., Kim, J., Mao, X., Yuan, G.C., and Orkin, S.H. (2008). EZH1 mediates methylation on histone H3 lysine 27 and complements EZH2 in maintaining stem cell identity and executing pluripotency. Mol. Cell *32*, 491–502.

Siegel, R.L., Miller, K.D., and Jemal, A. (2015). Cancer statistics, 2015. CA Cancer J. Clin. *65*, 5–29.

Varambally, S., Dhanasekaran, S.M., Zhou, M., Barrette, T.R., Kumar-Sinha, C., Sanda, M.G., Ghosh, D., Pienta, K.J., Sewalt, R.G., Otte, A.P., et al. (2002). The polycomb group protein EZH2 is involved in progression of prostate cancer. Nature *419*, 624–629.

Vasanthakumar, A., Xu, D., Lun, A.T., Kueh, A.J., van Gisbergen, K.P., Iannarella, N., Li, X., Yu, L., Wang, D., Williams, B.R., et al. (2017). A non-canonical function of Ezh2 preserves immune homeostasis. EMBO Rep. *18*, 619–631.

Wang, J., Zou, J.X., Xue, X., Cai, D., Zhang, Y., Duan, Z., Xiang, Q., Yang, J.C., Louie, M.C., Borowsky, A.D., et al. (2016). ROR-γ drives androgen receptor expression and represents a therapeutic target in castration-resistant prostate cancer. Nat. Med. *22*, 488–496.

Wei, B., Jolma, A., Sahu, B., Orre, L.M., Zhong, F., Zhu, F., Kivioja, T., Sur, I., Lehtiö, J., Taipale, M., and Taipale, J. (2018). A protein activity assay to measure global transcription factor activity reveals determinants of chromatin accessibility. Nat. Biotechnol. *36*, 521–529.

Xu, K., Wu, Z.J., Groner, A.C., He, H.H., Cai, C., Lis, R.T., Wu, X., Stack, E.C., Loda, M., Liu, T., et al. (2012). EZH2 oncogenic activity in castration-resistant prostate cancer cells is Polycomb-independent. Science *338*, 1465–1469.

Yu, J., Yu, J., Mani, R.S., Cao, Q., Brenner, C.J., Cao, X., Wang, X., Wu, L., Li, J., Hu, M., et al. (2010). An integrated network of androgen receptor, polycomb, and TMPRSS2-ERG gene fusions in prostate cancer progression. Cancer Cell *17*, 443–454.

Zhang, W., Bojorquez-Gomez, A., Velez, D.O., Xu, G., Sanchez, K.S., Shen, J.P., Chen, K., Licon, K., Melton, C., Olson, K.M., et al. (2018). A global transcriptional network connecting noncoding mutations to changes in tumor gene expression. Nat. Genet. *50*, 613–620.

Zhao, J.C., Yu, J., Runkle, C., Wu, L., Hu, M., Wu, D., Liu, J.S., Wang, Q., Qin, Z.S., and Yu, J. (2012). Cooperation between Polycomb and androgen receptor during oncogenic transformation. Genome Res. *22*, 322–331.

STAR★METHODS

KEY RESOURCES TABLE

REAGENT or RESOURCE	SOURCE	IDENTIFIER
Antibodies		
Rabbit monoclonal anti-Ezh2	Cell Signaling Technology	Cat# 5246S; RRID:AB_10694683
Rabbit polyclonal anti-AR	Millipore	Cat# 06-680; RRID:AB_310214
Rabbit monoclonal anti-SUZ12	Cell Signaling Technology	Cat# 3737S; RRID:AB_2196850
Rabbit monoclonal anti-H3K27me3	Cell Signaling Technology	Cat# 9733S; RRID:AB_2616029
Rabbit polyclonal anti-H3K27me3	Millipore	Cat# ABE44; RRID:AB_10563660
Rabbit monoclonal anti-Ki67	Cell Signaling Technology	Cat# 9027S; RRID:AB_2636984
Rabbit polyclonal anti-Cyclin D1	Abcam	Cat# ab24249-100; RRID:AB_447956
Rabbit polyclonal anti-H3	Abcam	Cat# ab1791-100; RRID:AB_302613
Rabbit monoclonal anti-PSA	Cell Signaling Technology	Cat# 2475S; N/A
Rabbit polyclonal anti-H3K27ac	Abcam	Cat# ab4729; RRID:AB_2118291
Rabbit polyclonal anti-HA	Abcam	Cat# ab9110; RRID:AB_307019
Rabbit polyclonal anti-HA	Santa Cruz Biotechnology	Cat# sc-805x; RRID:AB_631618
Normal Rabbit unconjugated-IgG	Santa Cruz Biotechnology	Cat# sc-2027; RRID:AB_737197
Chemicals, Peptides, and Recombinant Proteins		
Tazemetostat (EPZ-6438) Ezh2 inhibitor	Selleck Chemicals	Cat# S7128
Enz (MDV3100) AR antagonist	Selleck Chemicals	Cat# S1250
GSK 126 Ezh2 inhibitor	BioVision	Cat# 2282-5
Critical Commercial Assays		
Cell Proliferation Reagent WST-1	Clonetech	Cat# MK400
ECL prime Western Blotting Detection Reagent	Amersham	N/A
ECL Western Blotting Detection Reagent	Amersham	Cat# RPN2106
Nucleospin RNA isolation kit	Takara	Cat# 740955.25
qscript CDNA synthesis supermix	Qunatabio	Cat# 95048-25
2X bullseye EvaGreen qPCR mastermix	Midsci	Cat# BEQPCR-IC
Propidium iodide solution	ThermoFisher Scientific	Cat# P1304MP
Lipopectamine 2000	ThermoFisher Scientific	Cat# 11668019
Dual-Luciferase Reporter Assay System	Promega	Cat# E1910
NEBNext Ultra RNA Library Prep Kit	NEB	Cat# E7530S
Deposited Data		
https://data.mendeley.com/datasets/jxptxx985d/1	Unprocessed imaging data	N/A
https://www.ncbi.nlm.nih.gov/geo/query/acc.cgi?acc=GSE107782	High-throughput genomics data	N/A
Experimental Models: Cell Lines		
Human: Passage 10-20 LNCaP	ATCC	Cat# CRL-1740; RRID:CVCL_1379
Human: Passage 39-50 C4-2B	Laboratory of Dr. Arul Chinnaiyan (University of Michigan, Ann Harbor)	N/A
Human: Passage 10-20 22Rv1	ATCC	Cat# CRL-2505; RRID:CVCL_1045
Human: Passage 10-20 LAPC4	Laboratory of Dr. C Shad Thaxton (Northwestern University)	N/A
Human: Passage 5-10 293T	ATCC	Cat# CRL-3216; RRID:CVCL_0063
Experimental Models: Organisms/Strains		
Mouse: NOD.CB17—*Prkdc*^{scid}/NCrCrl 4-6 weeks old male	Charles river	Cat# 394

(*Continued on next page*)

Continued

REAGENT or RESOURCE	SOURCE	IDENTIFIER
Oligonucleotides		
See Table S5.		
Recombinant DNA		
pLKO.1V	Addgene	Cat# 10878; RRID:Addgene_10878
LentiCRISPR v2	Addgene	Cat# 52961; RRID:Addgene_52961
pGL4.10	Promega	Cat# E6651
HAF-GFP	This paper	N/A
HAF-EZH2	This paper	N/A
HAF-EZH2H689A	This paper	N/A
pAd-GFP control	This paper	N/A
pAd-EZH2	This paper	N/A
Software and Algorithms		
Incucyte softeware	Essen Bioscience	https://www.essenbioscience.com/en/products/software/incucyte-base-software/
ModFit LT	Verity Software	http://www.vsh.com/products/mflt/index.asp
Cluster		http://bonsai.hgc.jp/~mdehoon/software/cluster/software.htm
TreeView		https://sourceforge.net/projects/jtreeview/
GSEA		http://software.broadinstitute.org/gsea/index.jsp
BWA		http://bio-bwa.sourceforge.net/
STAR		https://github.com/alexdobin/STAR/releases
JASPAR^{2014}		http://jaspar2014.genereg.net/
HOMER (Hypergeometric Optimization of Motif EnRichment) suite		http://homer.ucsd.edu/homer/
deepTools		https://deeptools.readthedocs.io/en/develop/
DESeq2	R Bioconductor package	https://bioconductor.org/packages/release/bioc/html/DESeq2.html
Vennerable	R package	https://github.com/js229/Vennerable

CONTACT FOR REAGENT AND RESOURCE SHARING

Further information and requests for resources and reagents should be directed to and will be fulfilled by the Lead Contact, Jindan Yu (jindan-yu@northwestern.edu)

EXPERIMENTAL MODEL AND SUBJECT DETAILS

Cell Lines and Chemical Reagents

Human embryonic kidney cell line 293T and PCa cell lines LNCaP and 22RV1 were obtained from American Type Culture Collection (ATCC) and C4-2B cells were a provided by Dr. Arul Chinnaiyan (University of Michigan, Ann Arbor). 293T cells was cultured in DMEM with 10% fetal bovine serum (FBS) and 1x Penicillin Streptomycin and PCa cells were cultured in RPMI1640 with 10% fetal bovine serum (FBS) and 1x Penicillin Streptomycin solution. LAPC4 cells were provided by Dr. C Shad Thaxton (Northwestern University) and cultured in IMEM with 10% FBS and 1nM fresh R1881. All cell lines were authenticated (Genetica DNA Laboratories) and free of mycoplasma. GSK126 was purchased from BioVision (2282-5), Enz (S1250) and EPZ6438 (S7128) were purchased from Selleck Chemicals.

Animal Studies

Animal study were performed with approved protocol #IS00005301 by the Center for Comparative Medicine at Northwestern University. Male NOD.SCID (C.B-17/IcrHS-Prkdcscid) immune-deficient mice of 4 weeks old were purchased from Charles River. Only male, adult mice were utilized for the study as PCas only occur in adult men. Mice were housed (3-4 mice per cage) in sterilized filter-topped cages and maintained in an ABSL-2 immunodeficient animal housing facility at Northwestern University. Mice were randomly assigned to treatment groups.

METHOD DETAILS

Plasmids

AR promoter regions P1 (+1.1kb-1.7kb), P2 (1.7kb-2.5kb), P1+P2 (+1.1kb-2.5kb) and AR promoter fragments (0.4-0.8kb, 0.8-1.2kb, 1.2-1.6kb, 1.6-1.8kb, 1.8-2.3kb) were amplified by PCR from LNCaP genomic DNA. The AR promoter P1, P2 and full length were inserted into pGL4.10 vector (catalog number E6651; Promega) by using XhoI and HindIII sites and AR fragments were cloned into the pRetroX-Tight-Pur-Luc plasmid (Clontech laboratories, Inc.) by using BamHI and BglII. All plasmids were verified by sequencing.

CRISPR-Cas9-mediated editing of AR promoter

sgRNAs targeting indicated AR promoter regions (Table S5) were designed using the MIT CRISPR Design software (crispr.mit.edu). Each sgRNA oligos were synthesized and cloned into lentiCRISPR v2 vector as a gift from Dr. Feng Zhang (Addgene pladmid #52961). Lentiviral particles was produced in 293T with PEI transfecting reagent (VWR). LNCaP cells were then infected with sgRNAs lentiviral particles combination for 48 hours, then split, and transfected with either control or siEZH2 using Lipopectamine 2000 (Invitrogen) for 48 hours. Genomic DNA was prepared using the PureLink Genomic DNA kit (Life Technology). PCR of genomic DNA was performed with indicated primers flanking the sgRNA target sites on AR promoter region (Table S5). PCR products were purified from agarose gel and sequenced to assess the effects of CRISPR-Cas9-mediated editing of AR promoter. Total RNA was isolated from cells with Nucleospin RNA isolation kit (Clonetech) and 250 ug of RNA per sample was used for cDNA synthesis using qscript cDNA synthesis supermix (Quantabio). PCR of cDNA were then performed using specific AR promoter (also exon 1) primers (Primer F2 and R2) and subjected for agarose gel analysis. Protein extracts were subjected for western blot analysis to confirm EZH2 knockdown.

PCR, Quantitative PCR and Western Blot

Genomic DNA was isolated from cells with Blood & Cell culture DNA midi kit (QIAGEN). PCR was performed with indicated primers flanking the sgRNA target sites. PCR products were purified from agarose gel and sequenced. Total RNA was isolated from cells with Nucleospin RNA isolation kit (Clonetech). For cDNA synthesis, 250 ug of RNA per sample was used for cDNA synthesis using qscript cDNA synthesis supermix (Quantabio). qRT-PCRs were performed using 2xBullseye EvaGreen qPCR MasterMix (MIDSCI) and StepOne Plus (Applied Biosystems). Primers were designed using primer3 and synthesized by Integrated DNA Technologies (Table S5). Western blotting analyses were performed using standard protocols. Briefly, cell lysates were harvested with RIPA buffer and prepared in 1X-SDS sample buffer, boiled for 10 min at 95 °C, separated on a 10% SDS-polyacrylamide gel and transferred to an Amersham Hybond PVDF membrane. The membranes were blocked with either 5% w/v BSA or milk in TBST for 1h at RT, incubated in primary antibody diluted in blocking solution overnight at 4°C, washed 3 times for 5 min with TBST and incubated for 1 h in a secondary antibody (1:10,000). Membranes were washed 3 times for 10 min with TBST and chemiluminesce signal was detected by ECL solution and film (GE Healthcare).

WST-1 Cell Proliferation, Incucyte Cell Confluence Assay and Colony Formation Assay

Cell proliferation assay was measured with WST-1 (promega) reagent according to the manufacturer's instruction (Clontech). Briefly, cells were treated with WST-1 for 2hours at 37oC incubator prior to absorbance reading at 440nm using the KC4 microplate reader (BioTek). Each absorbance was normalized to the media control without any cells. For the Incucyte cell confluence assay, C4-2B cells were infected with pLKO.1V, shEZH2, shSUZ12 or shAR for 24 hours and harvested by trypsinization. 5,000 cells were counted on a Countess automated cell counter (Life Technologies, Carlsbad, CA) and plated on 24 tissue culture plates in 3 replicates. Photomicrographs were taken every two hours using an Incucyte live cell imager (Essen Biosciences, Ann Arbor, MI). Cell confluence were measured using Incucyte software (Essen Biosciences, Ann Arbor, MI) over 5 days in culture. Data were normalized to the pLKO.1 control cells and analyzed using Incucyte software (Essen Biosciences, Ann Arbor, MI).

For colony formation assay, 1,000-2,000 cells were plated in each well of a 6-well plate and treated with indicated concentration of DMSO, Enz, EPZ or both for 10-14 days, cells were fixed by 4% paraformaldehyde and stained by 0.05% crystal violet.

Cell Cycle Analysis

For cell cycle analysis, LNCaP and C4-2B cells were treated with either DMSO, Enz, EPZ or Enz+EPZ6438 for 72 hours. Cell were harvested and washed with PBS. Cells were fixed with absolute ethanol for 15 min at −20°C. Ethanol fixed cells were rehydrated with PBS at room temperature for 5 min and then stained with 3μM of propodium iodide solution (Thermo Fisher) and subjected for flow cytometry analysis using LSR Fortessa cell analyzer (BD Science). Data were analyzed by ModFit LT (Verity Software).

Luciferase reporter assay

pGL4.1 reporter constructs containing AR promoter fragment were co-transfected with pLVX-HA or pLVX-EZH2 and pRL-TK for internal control. Absorbance reading for luciferase activities were measured in 24 h post transfection at 440nm using the KC4 microplate reader (BioTek). Each absorbance was normalized to the renilla internal control values.

Chromatin Immunoprecipitation (ChIP) and ChIP-seq

ChIP and ChIP-seq was performed using previously described protocol with following modifications. $2x10^7$ LNCaP cells were cross-linked with 1% paraformaldehyde for 10 min at room temperature with gentle rotation and then quenched with 0.125 M glycine. After washing, nuclei were sonicated on a Covaris M220 Focused-ultrasonicator, and the supernatant was used for immunoprecipitation with the indicated antibody (Table S2). ChIP-qPCR primers used in the ChIP assays were listed in Table S5. For EZH2 ChIP on AR promoter fragment in 293T cells. 293T cells were transfected with pRetroX-Tight-Pur-Luc vector containing AR promoter fragments, after 7 days puromycin selection, ChIP was performed as above. ChIP-qPCR using a forward primer that targets the plasmid backbone and a reverse primer that targets the inserted AR promoter fragment.

ChIP-seq data analysis

ChIP-seq reads were aligned to the Human Reference Genome (assembly hg19) using Burrows-Wheeler Alignment (BWA) Tool Version 0.6.1. ChIP-seq peak identification, overlapping, subtraction and feature annotation of enriched regions were performed using HOMER (Hypergeometric Optimization of Motif EnRichment) suite. Weighted Venn diagrams were created by R package Vennerable. Transcription factor motif analysis on the AR promoter sequence was performed with JASPAR. Heatmap views of ChIP-seq were generated by deepTools.

RNA-seq and analysis

For RNA-seq, total RNA was isolated from cells using PureLinkTM RNA Mini Kit (Life Tech). RNA-seq libraries were prepared from 0.5 μg high-quality DNA-free total RNA by using NEBNext® Ultra RNA Library Prep Kit, according to the manufacturer's instructions. The libraries were sequenced using Illumina Hi-Seq platform. RNA-seq reads were mapped to NCBI human genome GRCh38 using STAR version 1.5.2. Raw counts of genes were calculated by STAR. FPKM values (Fragments Per Kilobase of transcript per Million mapped reads) were calculated by in house perl script. Differential gene expression was analyzed by R Bioconductor DESeq2 package, which uses shrinkage estimation for dispersions and fold changes to improve stability and interpretability of estimates.

Microarray and expression analysis

Microarray expression profiling was performed using HumanHT-12 v 4.0 Expression BeadChip (Illumina). Bead-level data were preprocessed and normalized by GenomeStudio. Differentially expressed genes were identified by Bioconductor limma package (cutoff $p < 0.005$). Clustering and heatmap view of differentially expressed genes were performed using Cluster and Java Treeview [7]. GSEA was performed as previously described.

Xenograft Experiments

For Xenograft, 2×10^6 of C4-2B cells were suspended in 200 μL PBS with 50% Matrigel (BD Science) and injected subcutaneously into the dorsal flank of the mice one week after surgical castration. Mice were randomly divided into four different groups and treated with 200 μL of vehicle control, Enz (10mg/kg), EPZ6438 (250mg/kg), or combination of Enz (10mg/kg) and EPZ6438 (250mg/kg) by oral gavage. Enz were administered once a day and EPZ6438 were given twice a day. Tumor volumes were measured with digital caliper once a week in a blinded fashion and calculated with the formula, $V = \pi/6$ (length X width2). When tumor size reached $\sim$1,000mm^3, mice were euthanized, tumors were excised and weighed. The effects of drug treatment in suppressing target pathways were examined via western blot and immunohistochemistry analysis. For western blot analysis, dissected tumor were homogenized with standard glass beads (1.0mm) using BeadBug homogenizer (Benchmark) in RIPA buffer supplemented with protease inhibitor and protein were subjected for western blot analysis. For immunohistochemistry analysis, tumor sections were fixed with formalin and embedded in paraffin. Formalin-fixed and paraffin embedded tumor section were then stained with Ki-67 and H3K27me3.

QUANTIFICATION AND STATISTICAL ANALYSIS

Statistics for qPCR, WST-1 cell Proliferation, Incucyte cell confluence assay, luciferase reporter assay ($n = 3$) and the xenograft tumor growth curves ($n = 7$) were reported as mean ± standard deviation and graphs were generated using Microsoft Excel. The results were considered significant if the p value is less than 0.05. Analysis of cell cycle upon drug treatments were performed with Modfit FT software (Verity Software, Santa Clara, CA). All the quantification and statistical analysis for the high-throughput data including microarray, RNA-seq and motif analysis were performed using R package Vennerable. R Bioconductor DESeq2 package.

DATA AND SOFTWARE AVAILABILITY

The accession number for microarray, ChIP-seq, and RNA-seq data reported in this paper is in the GEO database: GSE107782.

Raw image data of western blots were deposited to Mendeley Data with URL: https://data.mendeley.com/datasets/jxptxx985d/1

RESEARCH

Roles of the HOXA10 gene during castrate-resistant prostate cancer progression

Zhi Long[1,2,*], Yinan Li[2,*], Yu Gan[2,3], Dongyu Zhao[4,5,6], Guangyu Wang[4,5,6], Ning Xie[2], Jessica M Lovnicki[2], Ladan Fazli[2], Qi Cao[7], Kaifu Chen[4,5,6] and **Xuesen Dong[2]**

[1]Department of Urology, Third Xiangya Hospital, Institute of Prostate Disease, Central South University, Changsha, China
[2]Department of Urologic Sciences, Vancouver Prostate Centre, University of British Columbia, Vancouver, British Columbia, Canada
[3]Department of Urology, Xiangya Hospital, Central South University, Changsha, China
[4]Center for Bioinformatics and Computational Biology, Houston Methodist Research Institute, Houston, Texas, USA
[5]Department of Cardiothoracic Surgeries, Weill Cornell Medical College, Cornell University, New York, New York, USA
[6]Institute for Academic Medicine, Houston Methodist Hospital, Houston, Texas, USA
[7]Department of Urology and Robert H. Lurie Comprehensive Cancer Cancer, Northwestern University Reinberg School of Medicine, Chicago, Illinois, USA

Correspondence should be addressed to X Dong: xdong@prostatecentre.com

*(Z Long and Y Li contributed equally to this work)

Abstract

Homeobox A10 (HOXA10) is an important transcription factor that regulates the development of the prostate gland. However, it remains unknown whether it modulates prostate cancer (PCa) progression into castrate-resistant stages. In this study, we have applied RNA *in situ* hybridization assays to demonstrate that downregulation of HOXA10 expression is associated with castrate-resistant PCa. These findings are supported by public RNA-seq data showing that reduced HOXA10 expression is correlated with poor patient survival. We show that HOXA10 suppresses PCa cell proliferation, anchorage colony formation and xenograft growth independent to androgens. Using AmpliSeq transcriptome sequencing, we have found that gene groups associated with lipid metabolism and androgen receptor (AR) signaling are enriched in the HOXA10 transcriptome. Furthermore, we demonstrate that HOXA10 suppresses the transcription of the fatty acid synthase (FASN) gene by forming a protein complex with AR and prevents AR recruitment to the FASN gene promoter. These results lead us to conclude that downregulation of HOXA10 gene expression may enhance lipogenesis to promote PCa cell growth and tumor progression to castrate-resistant stage.

Key Words

- castrate-resistant prostate cancer
- HOXA10
- FASN
- lipid synthesis and androgen receptor

Endocrine-Related Cancer (2019) **26**, 279–292

Background

The homeobox A10 (*HOXA10*) gene is a member of the superfamily of homeobox genes that are master regulators of anterior-posterior (AP) axis positioning and tissue determination during development (Mark *et al*. 1997, Wellik 2009). These genes encode for transcription factors that have highly conservative ~60 aa homeodomains to recognize specific regulatory DNA elements in target promoters (Mark *et al*. 1997). Because of gene duplication and divergence, four *HOX* gene clusters (A, B, C and D) and a total of 39 *HOX* genes exist in chromosomal clusters in humans (Krumlauf 1994). Along the AP axis, *HOX* genes are expressed in a 3′ to 5′ pattern, where the 5′ genes are associated to more caudal and distal structures (Shah & Sukumar 2010). This spatial collinearity is exemplified by the fact that 5′ genes, such as *HOXA10*, *11* and *13* (there is no *HOXA12* gene), are necessary for the development

https://erc.bioscientifica.com
https://doi.org/10.1530/ERC-18-0465

of the prostate gland, a structure that develops distally (Satokata *et al.* 1995, Podlasek *et al.* 1999, Dhanasekaran *et al.* 2005). *HOX* gene expression also shows temporal collinearity. For example, the 3′ *HOX* genes are mainly expressed in the earlier structures, such as main stem bronchi during pulmonary embryogenesis, while the 5′ genes are expressed in later developed structures, such as the alveoli (Maeda *et al.* 2007). Therefore, the primary function of *HOX* genes during development is to specify the identity of body segments along the AP axis. To date, this has been demonstrated by phenotypical alterations in HOXs knockout mouse models (Podlasek *et al.* 1999, Post & Innis 1999, Villavicencio-Lorini *et al.* 2010) as well as the established association of germline mutations of *HOX* genes with inherited human diseases (Quinonez & Innis 2014).

HOXA10 is located in the most 5′ cluster of the *HOX* genes that are expressed in the posterior domains of the spinal cord, digestive tract and urogenital sinus (Warot *et al.* 1997, Podlasek *et al.* 1999). Studies using knockout mouse models have shown that *HOXA10* is necessary for the formation of reproductive organs including the prostate, epididymis and seminal vesicle in males and the oviduct and uterus in females (Satokata *et al.* 1995, Podlasek *et al.* 1999). *HOXA10* expression has been reported to be low at birth in the rat ventral prostate, but increase after day 10 to a two-fold higher-level until and throughout adulthood (Huang *et al.* 2007). In both human and mouse, persistent *HOXA10* expression in fully developed adult prostate suggests that *HOXA10* may be important to maintain terminal differentiation of prostatic cells or regulate phenotype plasticity of differentiated cells by interacting with intracellular signaling (Shah & Sukumar 2010). This is supported by the findings that while *HOXA10* is continually expressed in the endometrium, its levels fluctuate during the menstrual cycle and peak at the proliferative phase via the estrogen signaling (Taylor *et al.* 1998, Bagot *et al.* 2001). Female *HOX10*-knockout mice have serious blastocyst implantation defects due to aberrant endometrium function (Benson *et al.* 1996). However, it remains to be determined whether *HOXA10* exerts any biological functions in fully developed prostate in males, and whether *HOXA10* regulates signal pathways during prostate cancer (PCa) development or tumor progression into the castrate-resistant stage.

PCa is the most commonly diagnosed cancer in males. The primary treatment for metastatic PCa is androgen deprivation therapy that either blocks androgen synthesis or prevents androgens from activating the androgen receptor (AR) (Ferraldeschi *et al.* 2015). However, tumors will inevitably relapse and most of them restore their AR signaling and resume tumor progression to castrate-resistant prostate cancers (CRPC) (de Bono *et al.* 2011, Scher *et al.* 2012). This re-activated AR signaling modulates gene transcription to accelerate cell cycling and develop anti-apoptotic mechanisms for cell growth and tumor progression. AR also regulates genes to adapt multiple lipid metabolism signaling in order to (i) increase phospholipid synthesis for membrane production to cope with increased cell proliferation; (ii) generate and store sufficient energy required for tumor growth and (iii) modulate intracellular signaling to survive unfavorable microenvironments including hypoxia and lack of vascularity (Qi *et al.* 2013, Ackerman & Simon 2014). Androgen stimulation of lipid metabolism involves lipid synthesis and storage as well as lipid intake from dietary lipoproteins in circulation or lipid release from adjacent adipocytes in tumor tissues (Butler *et al.* 2016). It had been reported that androgen regulation of *de novo* lipogenesis involves multiple enzymes including fatty acid synthase (FASN), acetyl-coA carboxylase (ACAC), sterol regulatory element-binding proteins (SREBPs), SREBP cleavage-activating protein (SCAP), acyl-coA synthase long-chain family members (ACSLs) and ATP citrate lyase (ACLY) (Swinnen *et al.* 1997, Welsh *et al.* 2001, Singh *et al.* 2002, Vanaja *et al.* 2003, Wallace *et al.* 2008, Han *et al.* 2018).

In this study, we confirmed that *HOXA10* gene is predominantly expressed in prostate epithelial cells and its levels are reduced in tumors at the CRPC stage. HOXA10 suppresses PCa cell proliferation, colony formation and xenograft growth independent to androgens. Whole transcriptome profiling assays revealed that HOXA10 regulates lipid metabolism and AR signaling. We demonstrate that HOXA10 can form a protein complex with AR, preventing AR from being recruited to the *FASN* gene promoter and thereby inhibiting *FASN* gene transcription. These findings indicate that reduced HOXA10 expression may contribute to CRPC progression by enhancing AR-mediated lipogenesis.

Materials and methods

PCa cell lines, transfection and lentivirus transduction

LNCaP, VCaP, PC-3 and DU145 PCa cell lines were purchased from American Type Culture Collection (ATCC). C4-2, MR49F, LNAI and 293T cell lines were generously provided by Drs Rennie, Gleave and Buttyan at the Vancouver Prostate Centre, University of British

https://erc.bioscientifica.com
https://doi.org/10.1530/ERC-18-0465

Columbia. LNCaP95 and BPH1 cells were a kind gift from Dr Alan Meeker (Johns Hopkins University) and Dr Simon Haywards (Vanderbilt University). Cell culture conditions have been previously described (Liu *et al*. 2014, Palmeri *et al*. 2015, Li *et al*. 2016, Lee *et al*. 2017). STR assays confirmed cell line authentication. LNCaP cells within 40–50 passages were applied in this study. VCaP, PC-3 and DU145 lines were within 15 passages upon purchased from ATCC. C4-2, MR49F, LNAI, LNCaP95 and 293T lines were within 12 passages upon the dates when received from collaborators. Lipofectamine 3000 (Invitrogen) and SuperFect Transfection Reagents (Qiagen) were used for plasmid and siRNA transfection.

Lentivirus vectors for HOXA10, 11 and 13 were constructed as previously reported (Liu *et al*. 2014, Li *et al*. 2016, Lee *et al*. 2017). Plasmids containing the cDNA of HOXAs were kindly provided by Drs Hugh Taylor and Gunter Wagner (Yale School of Medicine). These plasmids were used as templates to clone HOXAs into the pCMV2 for transient transfection, and the pDONR201 and pFUGWBW vectors for lentivirus infections (Yu *et al*. 2013). Sanger sequencing was used to validate all expression vectors. LNCaP cells were infected with lentivirus encoding a control as well as the HOXA genes, followed by blasticidin selection to generate LNCaP(CTL), LNCaP(HOXA10), LNCaP(HOXA11) and LNCaP(HOXA13) cell lines. Vectors encoding shRNA against HOXA10 were purchased from Dharmacon (RHS4533-EG3206).

PCR and immunoblotting assays

Real-time qPCR and immunoblotting assays were performed as previously described (Liu *et al*. 2014, Li *et al*. 2016, Lee *et al*. 2017). Primer sets used include HOXA10 (F: TGGCTC A CGGCAAAGAGTG; R:GCTGCGGCTAATCTCTAGGC),FASN(F:AAGGACCTGT CTA GGTTTGATGC; R: TGGCTTCATAGGTGACTTCCA), SREBF-1 (F: CGGAACCATCTTG GCAACAGT; R: CGCTTCT CAATGGCGTTGT), SCAP (F: CTGAGGATGAGGAACTTT GGAG; R: TTGGCCAGTGTGATGTTGTAAT), GAPDH (F: GGACCGACCTGCCGTCTA GAA; R: GGTGTCGCTG TTGAAGTCAGAG). Antibodies used in immunoblotting include the anti-HOXA10 antibody (sc17158, Santa Cruz), the anti-FASN antibody (sc20140, Santa Cruz), the anti-SREBP1 antibody (ab28481, Abcam), the anti-AR antibody (ab9474, Abcam), the anti-Flag-tag antibody (F4042, Sigma-Aldrich) and the anti-Actin antibody (A5316, Sigma-Aldrich). All assays were carried out using three technical replicates and three independent biological replicates. Only one representative immunoblotting results from the three repeats is shown.

Tissue microarrays (TMAs)

Prostate tumor samples were extracted from the Vancouver Prostate Centre (VPC) tissue bank and used to build several PCa TMAs as we previously reported (Yu *et al*. 2015, Li *et al*. 2016). There are 65 cores from 40 benign prostate tissues, 157 cores from 42 primary tumors from patients with no prior hormonal therapies and 83 cores from 32 patients who had received hormonal therapy, chemotherapy or radiotherapy. The recurred tumors were removed by transurethral resection prostatectomy to relieve the lower urinary tract symptoms. Patient information is listed in the Supplementary tables (data not shown). All patients had given informed consent to a protocol that was reviewed and approved by the UBC Clinical Research Ethics Board (Certificate #: H09-01628).

RNA *in situ* hybridization (RISH) and immunohistochemistry (IHC)

The RISH probe targeting the 909–1270 bp of NM_018951.3 for HOXA10 was designed by Advanced Cell Diagnostic (Hayward, USA). A probe targeting the *dapB* gene of bacteria was used as a negative control probe. RISH assays were performed using the BaseScope assay kit following manufacture's instruction. IHC was performed by Ventana Discovery XT (Ventana) using a DAB MAP kit, as we have previously reported (Yu *et al*. 2015, Li *et al*. 2016). A Leica SCN400 scanner to form digital images scanned all stained slides. Positive RISH signals were presented as red dots under 40× magnification. RISH signals were scored as 0 if no positive signal; one if RISH signal was positive in ≤20% of all cells within a core; two if RISH signal was positive in >20% of the cells throughout the core and the dots were not merged into dot clusters; and three if RISH signal was positive in >20% of the cells and dots were merged into dot clusters. IHC signals were scored by both the percentage of stained cells (0–16, 17–33, 34–66 and 67–100%, as 0–3 scores) and the staining intensity (no staining, low, moderate and high intensity staining, as 0–3 scores). The histology index of HSCORE=Σpi(i+1), where i=the intensity of staining, and pi=the percentage of stained cells as reported (Yu *et al*. 2015, Li *et al*. 2016, 2018). Antibodies used in immunoblotting include the anti-Ki67 antibody (RM9106, Thermo Fisher Scientific)

https://erc.bioscientifica.com
https://doi.org/10.1530/ERC-18-0465

and the anti-cleaved caspase3 antibody (9661s, Cell Signaling Technology).

Cell proliferation and colony formation assays

Cell proliferation rates were measured by the CellTitre 96 AqueousOne kit (Promega) or crystal violet assays as described (Gillies *et al*. 1986). In the colony formation assays, approximately 2×10^4 cells were seeded in 0.7% soft agar in a six-well plate, with a 1% soft agar bottom base coating. Cells were allowed to grow for 14 days to form colonies. Colonies were stained with crystal violet and imaged by stitching 5× field images together to capture the entire well (Zeiss light microscope (Carl Zeiss)). Colony numbers were counted if their diameters were >100 µm. Three independent biological replicates were performed for all assays.

Human prostate cancer xenografts

LNCaP xenograft studies follow the protocols we have previously reported (Palmeri *et al*. 2015, Li *et al*. 2016). A total of 1×10^6 LNCaP(CTL) or LNCaP(HOXA10) cells in 0.1 mL Matrigel (BD Labware) were inoculated subcutaneously in the bilateral flanks of 6- to 8-week-old male athymic nude mice (n=8/group; Harlan Sprague Dawley Inc.). Tumor volume (V=L×W×D×0.5236) and body weight were measured weekly. Serum PSA levels were determined by ELISA. When tumor volumes reach 200 mm^3, mice were castrated. Mice were killed when tumor volume was >10% of bodyweight or when there was >20% loss of bodyweight. Tumors were harvested to evaluate gene expression using real-time PCR and immunoblotting assays. All animal procedures were under the guidelines of the Canadian Council on Animal Care.

Luciferase reporter assay

Cells were transfected with PSA-luciferase reporter plasmid with the Renilla reporter as a control for transfection efficiency. Luciferase activities were determined using the luciferin reagent (Promega) according to the manufacturer's protocol. Transfection efficiency was normalized by Renilla luciferase activity.

AmpliSeq transcriptome sequencing

LNCaP(CTL) and LNCaP(HOXA10) cells were cultured in medium containing 10% charcoal stripped serum for 2 days before they were treated with vehicle or 10 nM DHT for 24 h. Total RNA was extracted by using the mirVana RNA Isolation Kit (Ambion) according to the manufacturer's protocol. Two independently repeated experiments were performed for each experimental condition. The quantity and quality of the RNA samples was assessed by NanoDrop 2000 as well as Agilent 2100 Bioanalyzer (Caliper Technologies Corp., Canada) before being sent for AmpliSeq transcriptome sequencing. Library preparation, sequencing and primary analyses were performed by UBC-DMCBH Next Generation Sequencing Centre following the protocol described by Li *et al*. (Choo *et al*. 2008). In summary, cDNA was synthesized from 100 ng of total RNA using the SuperScript VILO cDNA Synthesis kit and amplified with Ion AmpliSeq technology. Barcoded cDNA libraries were diluted to 100 pM, equally pooled and amplified on Ion Torren OneTouch2 instrument using emulsion PCR. Template libraries were subjected for sequencing of >20,000 RefSeq transcripts using the Ion Torrent Proton sequencing system. Primary analysis and normalization were performed using the AmpliSeq RNA plugin available through the Ion Torrent suite Software (Choo *et al*. 2008).

Oil red O staining

Oil red O staining was performed as previously described (Ramirez-Zacarias *et al*. 1992). Briefly, formalin-fixed cells were immerged in working solution of Oil red O (Sigma). The dye was then extracted by isopropyl alcohol and quantified by spectrophotometry at a wavelength of 510 nm.

Co-immunoprecipitation (Co-IP) and chromatin immunoprecipitation (ChIP)

Co-IP and Ch-IP assays were performed as we have previously reported (Li *et al*. 2014, Palmeri *et al*. 2015, Xie *et al*. 2015). Briefly, cell lysates were extracted by NETN buffer containing 0.5% NP40, 1 mM of EDTA, 50 mM of Tris and 150 mM of NaCl plus proteinase and phosphatase inhibitor (Roche). Pre-cleared lysates were incubated with either control IgG or AR/HOXA10 antibody, and the associated proteins were immunoblotted by AR and HOXA10 antibody. In ChIP assays, chromatin was cross-linked with 1% formaldehyde for 10 min at 37°C and sonicated in the lysis buffer (1% SDS, 10 mM EDTA, and 50 mM Tris, pH 8.0, plus protease inhibitor cocktail). After centrifugation, 10 µL of the supernatants was used as input, and the remaining lysate was subjected to a ChIP assay using the AR or HOXA10 antibody. The primers

https://erc.bioscientifica.com
https://doi.org/10.1530/ERC-18-0465

used to amplify AREs on the *FASN* and *PSA* promoters include FASN (F: TATGACACCCAGGGCTTTCGTTCA; R: TAACGTTCCCTGCGCGTTTACAGA), PSA (F: ACCTGCT CAGCCTTTGTCTCTGAT; R: AGATCCAGGCTTGCTT ACTGTCCT).

Statistics

Statistical analysis was performed using R software. Public RNA-seq data were analyzed by one-way ANOVA followed by one-side Welch's *t*-test. Kaplan–Meier curves and log-rank tests were used to compare the overall survival and disease-free survival. Cox regression analyses were used to analyze the hazard ratio. The contingency table of counts of the HOXA10 RISH scores and FASN IHC scores were compared by Fisher's exact test. Spearman correlation analyses were used to test the correlation of HOXA10 RISH scores with Gleason groups. One-way ANOVA followed by Tukey tests were used in pairwise comparisons among different experimental groups. Student *t*-tests were used to compare results between the two experimental groups. Functional annotation assays with Benjamini adjustment of *P* values were performed using the DAVID 6.8 software. Pearson correlation analyses were used to test the correlation of AR and FASN expressions with HOXA10 levels. The level of significance was set at $P<0.05$ as *, $P<0.01$ as ** and $P<0.001$ as ***.

Results

Downregulation of HOXA10 expression associates with CRPC

Since *HOXA10*, *11*, and *13* are all located in the most 5′ cluster of *HOX* genes that regulate prostate development, we transduced all three *HOXA* genes into the LNCaP PCa cell line (Fig. 1A). However, only *HOXA10* significantly suppressed cell proliferation, leading our following studies to focus on this *HOXA* member. Genomic profiling of PCa patients (Chandran *et al*. 2007, Taylor *et al*. 2010, Grasso *et al*. 2012) showed that while *HOXA10* mRNA levels are similar between benign prostate and primary tumors, they are statistically lower in both the metastatic tumors from the Chandran 2007 cohort (Fig. 1B) and the CRPC from the Grasso 2012 cohort (Fig. 1C). Consistent to these public data, TCGA provisional data indicated that patients with relatively lower *HOXA10* expression have shorter total patient survival and disease-free survival rates (Fig. 1D). HOXA10 is expressed in several PCa cell lines (Fig. 1E). Except for the VCaP cell line that has gene amplifications, all PCa cell lines expressed lower levels of HOXA10 than the benign BPH1 cell line. Androgen-independent LNCaP95 and enzalutamide-resistant MR49F cells were established by treating LNCaP cells with pronged androgen depletion or enzalutamide treatments, respectively. Both LNCaP95 and MR49F cells are HOXA10 negative, in contrast to the HOXA10-positive LNCaP cells.

Currently, commercially available HOXA10 antibodies only show cytoplasmic staining in PCa tissues that do not reflect the precise localization of HOXA10 protein in PCa cells. Therefore, we utilized RISH assays on TMAs to measure *HOXA10* expression in patients. RISH signals appeared predominantly in luminal epithelial cells and were rarely present in prostate stroma. *HOXA10* was highly expressed in 26% (17/65) of the benign tissue cores that have RISH scores = 3. It is moderately expressed in 69% (45/65) of the benign tissue cores that have RISH scores = 2. No benign prostate samples were *HOXA10* negative (Fig. 2A). While similar *HOXA10* expression was observed in primary tumors comparing with benign prostate, its levels were significantly lower in CRPC (Fig. 2B). Among all 83 tissue cores, no CRPC samples had strong *HOXA10* staining. There were 65% (54/83) of cores that moderately expressed *HOXA10*, 26% (22/83) of cores that weakly expressed *HOXA10* and ~10% of CRPC samples that were *HOXA10* negative. The mean *HOXA10* RISH score was 2.22 ± 0.087 in benign prostate and 2.09 ± 0.156 in primary tumors, but 1.57 ± 0.209 in CRPC. Among primary tumors, *HOXA10* expression was negatively correlated with Gleason groups (Spearman correlation $r=-0.253$, $P=0.001$) (Fig. 2C). In summary, both public data and our RISH results indicate that reduced *HOXA10* expression associates with CRPC progression and poor patient survival.

HOXA10 suppresses PCa cell growth and xenograft progression

Cell proliferation assays showed that gain of function of *HOXA10* inhibited and *HOXA10* depletion enhanced LNCaP cell proliferation rates independent to androgen depletion (Fig. 3A). Consistently, HOXA10 also inhibited proliferation of androgen-independent LNCaP95 cells. Furthermore, HOXA10 downregulated anchorage colony formation rates in both LNCaP and LNCaP95 cells (Fig. 3B). Using the LNCaP xenograft model, we showed that HOXA10 inhibited tumor growth at not only the hormone-sensitive stage, but also the castrate-resistant stage (Fig. 3C). The CRPC stages were defined by the time of recurrence of serum PSA levels to the pre-castrate levels in mice. Immunoblotting assays confirmed HOXA10

https://erc.bioscientifica.com
https://doi.org/10.1530/ERC-18-0465

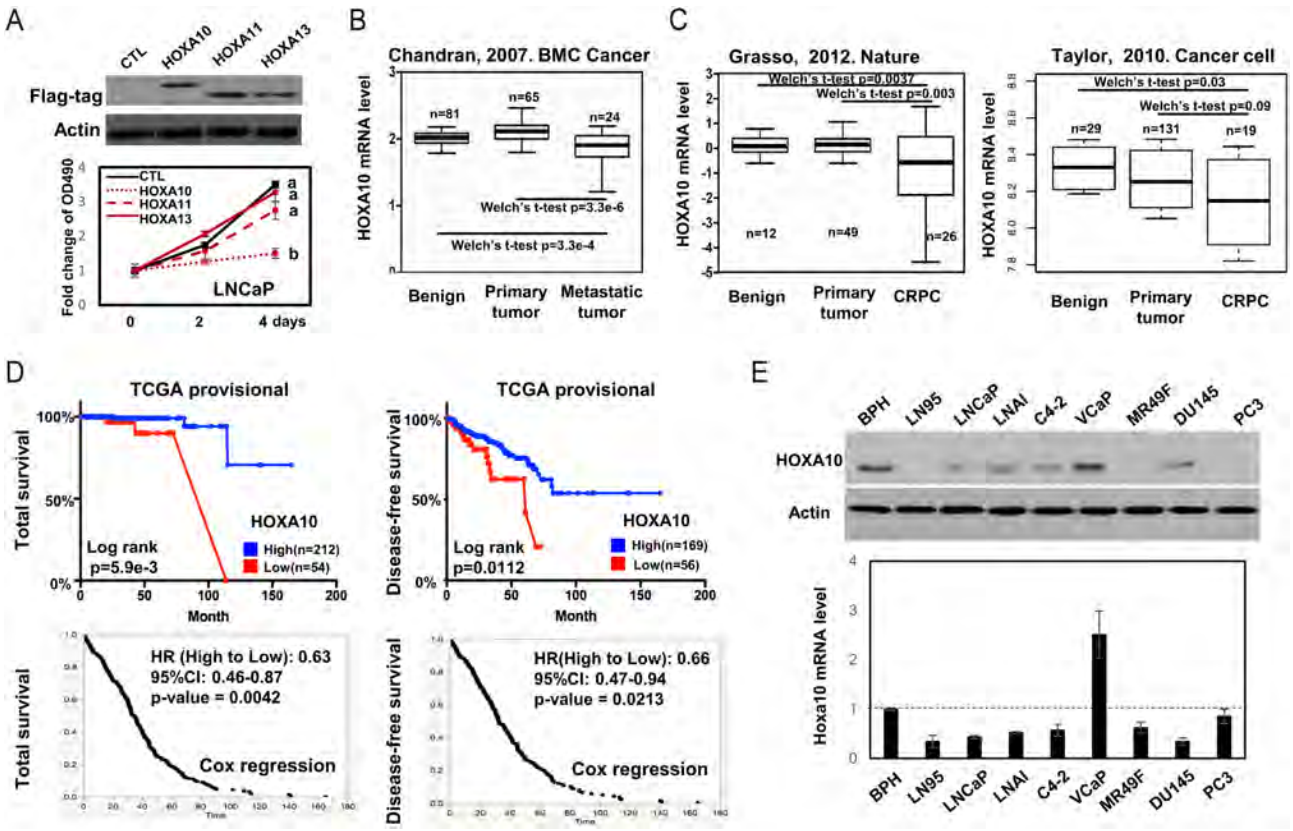

Figure 1

HOXA10 expression in PCa patients and cell models. (A) LNCaP cells were stably transduced with HOXA10, 11 and 13 by lentivirus. Cell proliferation rates were measured using MTS assay and presented as relative fold change to that at day 0. (B) Affymetrix microarray (GSE6919 – Yu, *et al*. 2004) compared *HOXA10* mRNA levels among benign prostate, primary, and metastatic prostate tumors. (C) RNA-seq analyses (GSE35988 – Grasso *et al*. 2012, GSE21032 – Taylor *et al*. 2010) compared *HOXA10* mRNA levels among benign prostate, primary prostate tumors, and CRPC. One sided Welch's t-test is use to compare results among different groups (B and C). (D) RNA-seq data from TCGA provisional database were analyzed using cbioportal software (http://www.cbioportal.org/). *Z*-scores were used to divide PCa patients into *HOXA10* low and high groups. Kaplan-Meier curves plot overall survival and disease-free survival of PCa patients by *HOXA10* expression. Cox regression was used to calculate the hazard ratio (HR) of overall survival and disease-free survival between HOXA10 low and high patient groups. (E) Multiple prostatic cell lines were used to measure HOXA10 expression in both protein and mRNA levels by immunoblotting and real-time PCR assays. Data were presented as mean ± standard error (S.E.M.). A full colour version of this figure is available at https://doi.org/10.1530/ERC-18-0465.

expression in xenograft samples (Fig. 3D). Both IHC and luciferase results confirmed the suppressive effect of HOXA10 to PSA secretion (Fig. 3D and E). Ki-67 and cleaved caspase3 IHC staining indicated that HOXA10 inhibited tumor cell proliferation, but increase cellular apoptosis. These results indicate that HOXA10 inhibits PCa cell proliferation, colony formation, and xenograft growth.

HOXA10 regulates lipid metabolism in PCa cells

We have used Ampliseq to profile the HOXA10 transcriptome in PCa cells (Fig. 4). Under androgen depletion conditions, 1040 genes were upregulated and 621 genes were downregulated by HOXA10 (fold change >1.5, $P<0.05$) (Fig. 4A). In the presence of DHT, there were 738 genes upregulated and 611 genes downregulated by HOXA10. Because HOXA10 inhibited PCa cell proliferation independent to androgens, we focused on the 267 genes that were upregulated and the 178 genes that were downregulated by HOX10 regardless of DHT treatment. DAVID 6.7 analyses showed that HOX10-induced genes that have diverse functions such as cell morphogenesis and organ formation. The genes that were induced are consistent with how HOXA10 functions in AP axis positioning during development (Supplementary Fig. 1). However, HOXA10 suppressed genes are limited to genes that regulate lipid metabolism (Fig. 4A). These findings are supported by GSEA analyses showing that lipid metabolism gene sets are highly suppressed by HOXA10 ($P<0.001$) (Fig. 4B). Additionally, androgen response genes were also inhibited (Fig. 4C). Together, these

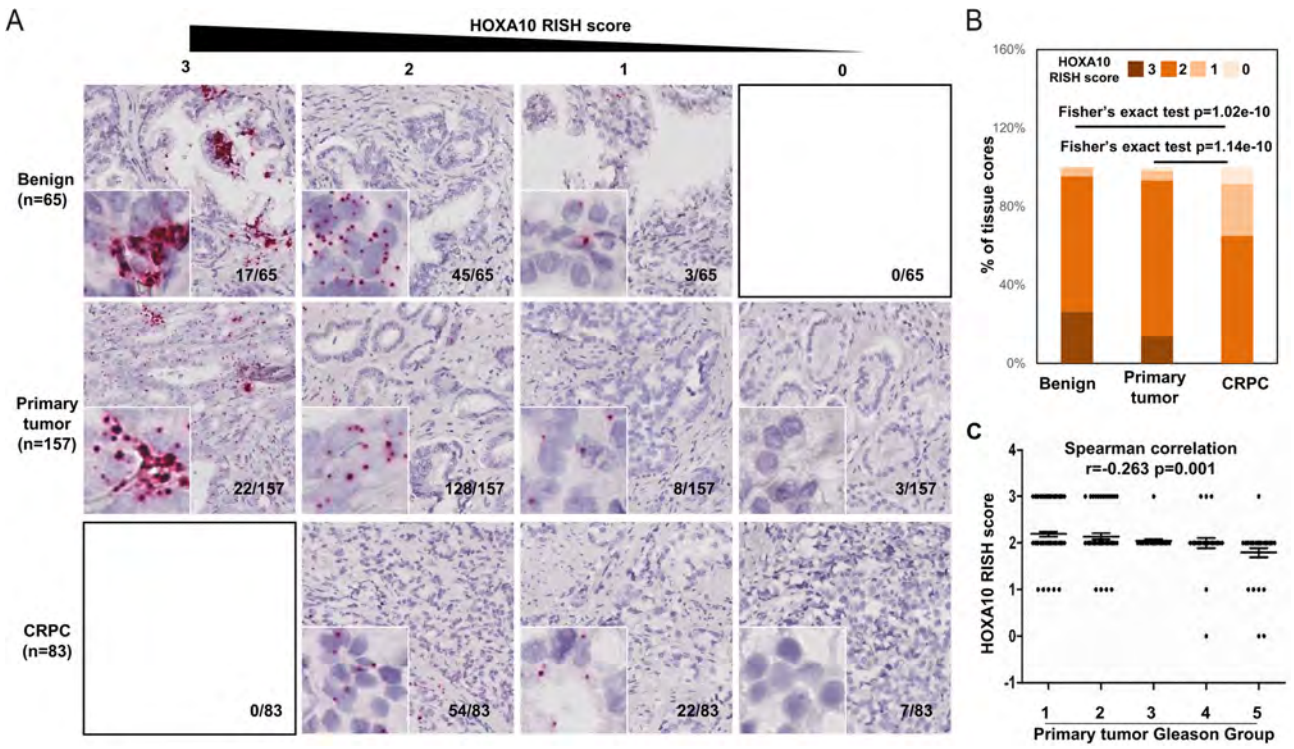

Figure 2

Application of RISH assays to measure HOXA10 expression during PCa progression. (A) RISH assays were performed on PCa TMA using a HOXA10 specific probe as described in the Materials and methods section. Representative images of RISH staining are shown. (B) Distributions of HOXA10 RISH scores in benign prostate, primary PCa tumors and CRPC were plotted. Fisher's exact tests were performed to compare HOXA10 expression among the three groups. (C) The association of *HOXA10* expression with tumor Gleason groups was calculated by Spearman's correlation test. Data were presented as mean ± S.E.M. A full colour version of this figure is available at https://doi.org/10.1530/ERC-18-0465.

results revealed an association of HOXA10 with both cell lipid metabolism and the AR signaling.

It has been reported that several lipid biosynthetic genes are regulated by the AR signaling (Han *et al.* 2018). Among these genes, the *FASN* gene is the most significantly suppressed gene by HOXA10 defined by *P* values under both CSS and DHT condition (Fig. 4D). It had been demonstrated that AR can bind directly the *FASN* gene promoter to activate *FASN* transcription (Norris *et al.* 2009). AR can also activate *SCAP* gene transcription, which in turn stimulates SREBPs to induce a wide range of enzymes including FASN for *de novo* lipogenesis (Heemers *et al.* 2004; Fig. 4E). These findings demonstrate that HOXA10 is a repressor of lipid metabolism in PCa cells, partially through the inhibition of AR-mediated *FASN* expression. Our results were further supported by clinical data showing that HOXA10 mRNA levels are negative associated with both *FASN* and *AR* in both TCGA provisional and SU2C CRPC datasets (Fig. 4F).

To further validate the prediction of Ampliseq analyses, our real-time PCR and immunoblotting assays showed that HOXA10 inhibited *FASN*, but not *SCAP* mRNA levels independent to androgens (Fig. 5A and B). Additionally, HOXA10 depletion in LNCaP cells resulted in increased *FASN* mRNA and protein levels (Fig. 5C and D). HOXA10 had no impact on SREBP1 expression, which supports the hypothesis that HOXA10 inhibition to *FASN* expression is not through the SCAP-SREBP1-FASN pathway. The inhibitory effects of HOXA10 to *FASN* have also been demonstrated by fatty acid synthesis assays using Oil red O staining (Fig. 5E). Furthermore, we found that the suppressive effects of HOXA10 to *FASN* expression were in AR positive LNCaP95 cells, but not AR negative PC3 and DU145 cells (Fig. 5F and G). This suggests that HOXA10 suppression of *FASN* transcription relies on the AR (Fig. 5F and G). Co-IP assays confirmed that both full-length AR and AR-v7 can form a protein complex with HOXA10 in LNCaP cells and 293T cell transfected with AR-v7 (Fig. 5H, I and J). ChIP assays demonstrated that HOXA10 prevents the recruitment of AR to the FASN and PSA promoters (Fig. 5K). Additionally, HOXA10 does not bind the regions next to the AREs of *FASN* and *PSA* gene promoters (Fig. 5L). These results indicate that HOXA10 suppresses *FASN* expression by forming a protein complex

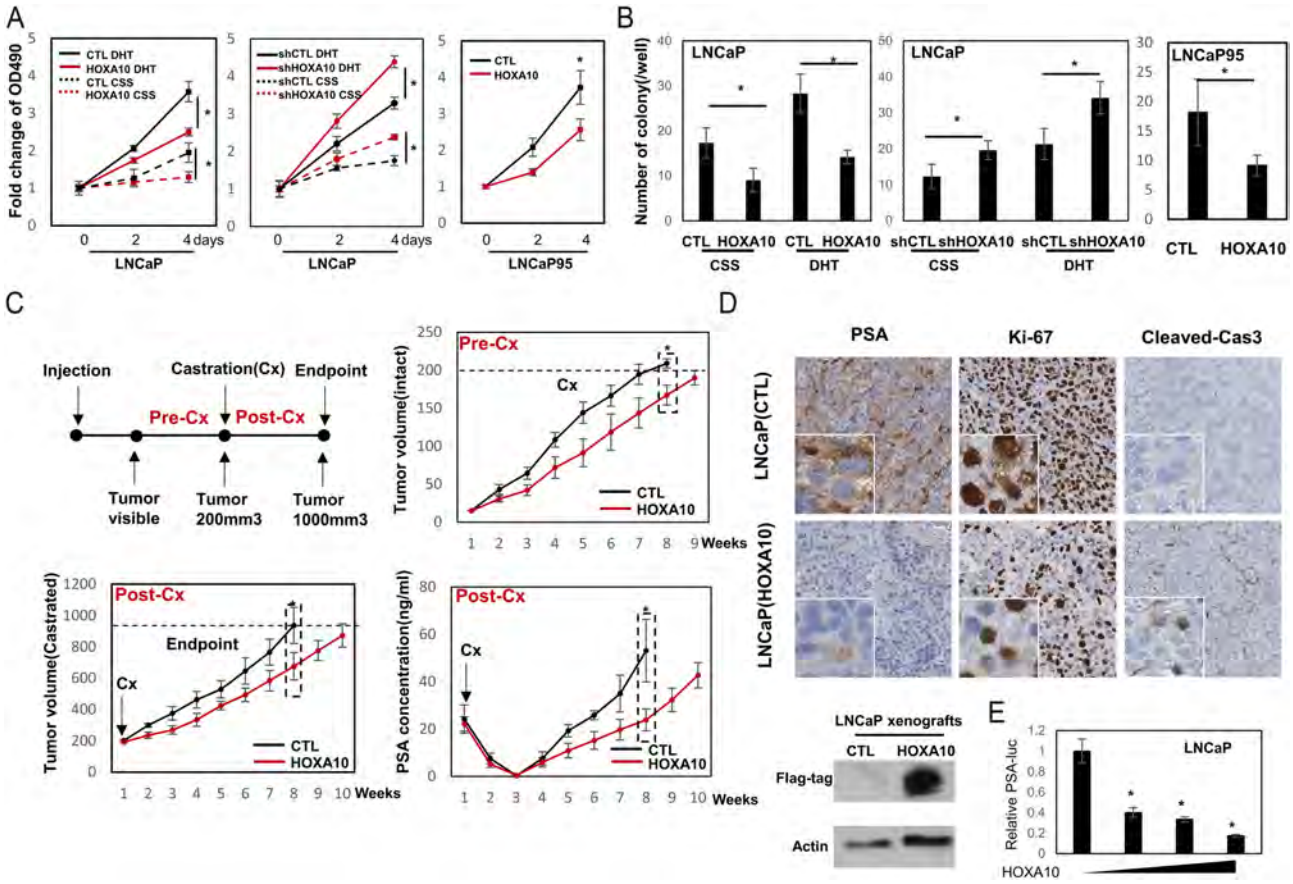

Figure 3

HOXA10 inhibits PCa cell proliferation, colony formation and xenograft growth. (A and B) Gain- and loss-of-function of *HOXA10* were applied to LNCaP and LNCaP95 cells by lentivirus. LNCaP cells were also treated with vehicle or 10 nM DHT. Cell proliferation rates were measured by crystal violet assays and presented as relative fold change to that at day 0. Student *t*-test was use to compared the results from day 4 between CTL and HOXA10 treatments under either DHT or CSS conditions. (A). LNCaP and LNCaP95 cells were used to perform colony formation assays. Colony numbers were counted if their diameters were >100 µm. Three independent biological replicates were performed (B). (C) LNCaP xenografts were established as described in the Materials and methods section. Tumor volumes and serum PSA concentrations were measured weekly and plotted. Student *t*-tests were used to compare tumor volume or PSA levels between CTL and HOXA10 groups. (D) LNCaP xenografts were collected at endpoint. IHC assays were performed to measure PSA, Ki-67 and Cleaved Caspase3 expression. Represented images were shown. Real-time PCR and immunoblotting assays confirmed HOXA10 expression in LNCaP xenografts. (E) LNCaP cells were co-transfected with PSA-luc and increased doses of HOXA10 expression plasmid for 24 h. Luciferase assays were performed as described in Materials and methods section. Data were presented as the mean ± standard deviation (s.d.) with * denotes $P < 0.05$. One-way ANOVA followed by Tukey test was used in pairwise comparisons among different groups. A full colour version of this figure is available at https://doi.org/10.1530/ERC-18-0465.

with AR and preventing AR from activating the *FASN* promoter activity.

The expression of FASN is upregulated in PCa

Reduced HOXA10 expression in CRPC (Figs 1 and 2) permits AR-mediated induction of FASN expression in PCa cells (Fig. 5). These findings are consistent to previous reports that FASN expression is upregulated in high-grade primary tumors and metastatic tumors (Rossi *et al.* 2003, Montgomery *et al.* 2008, Migita *et al.* 2009). To measure FASN protein expression in benign prostate and prostate tumors, we applied IHC assays on our CRPC TMAs. Compared to benign prostate, FASN staining was higher in primary tumors and even further upregulated in CRPC (Fig. 6). The average H-score of FASN was 1.28±0.216 in benign prostate, 1.96±0.144 in primary tumors and 2.18±0.206 in CRPC. Fisher's exact tests indicated that both primary and CRPC tumors expressed significantly higher FASN protein levels when compared to benign prostate ($P<0.0001$) and that FASN protein levels were significantly higher in CRPC when compared to primary tumors ($P=0.0294$). These results were similar to the public database (Taylor *et al.* 2010), which showed that FASN mRNA levels were upregulated in primary tumors and CRPC and that there was a trend of increased HOXA10

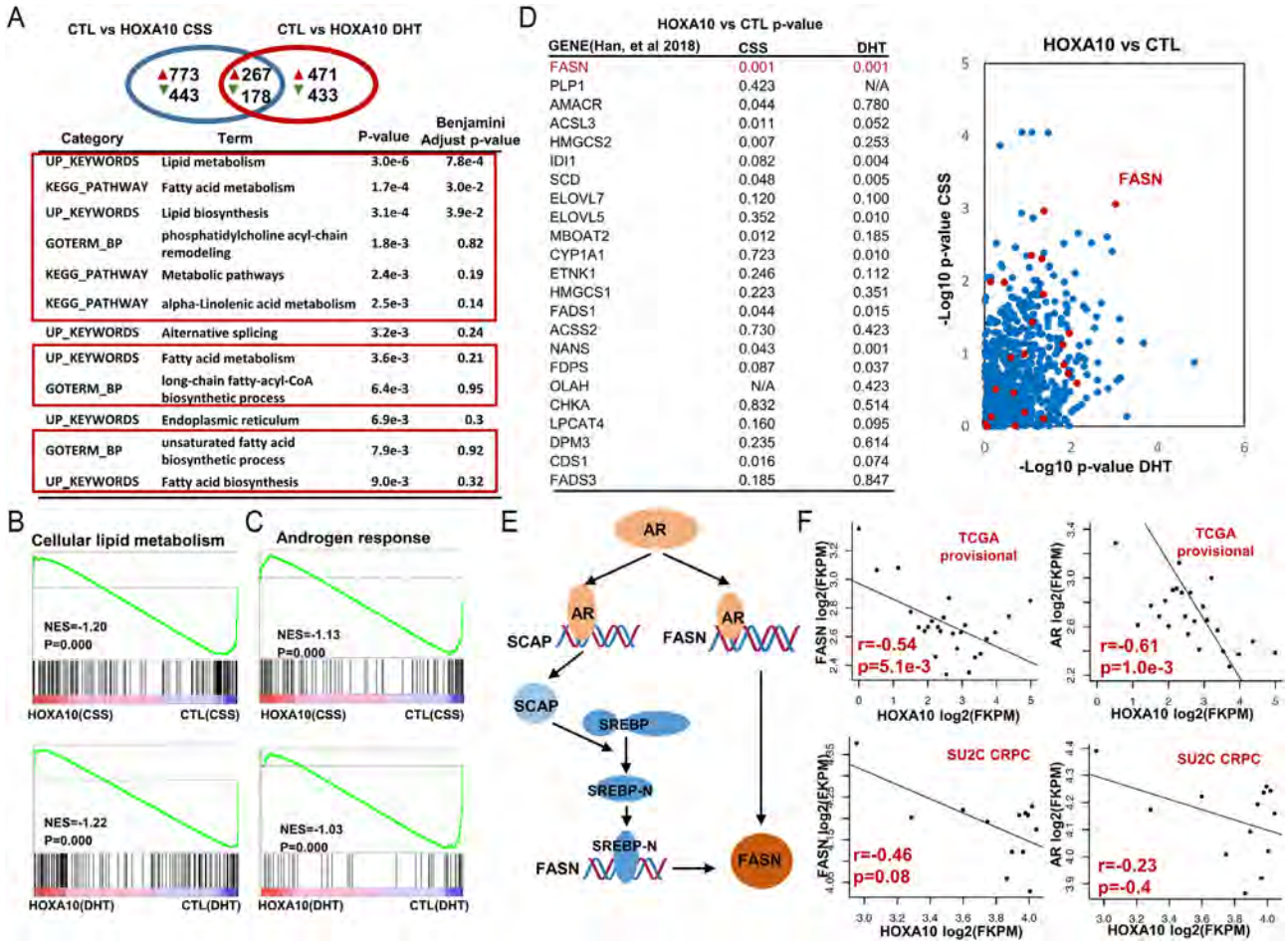

Figure 4

HOXA10 represses lipid metabolism genes and the AR signaling. (A) A Venn diagram summarized the Ampliseq results comparing transcriptomes between LNCaP(CTL) and LNCaP(HOXA10) cells in the present of –/+DHT treatment (fold change >1.5 and $P < 0.05$). Top-ranked gene functions suppressed by HOXA10 were analyzed by DAVID software (version 6.8). Benjamini adjustment of *P* values were shown. (B and C) GSEA analyses showed negative correlations of HOXA10 with cellular lipid metabolism (B) and androgen response gene sets (C). (D) A volcanic diagram showed *P* values of cellular lipid metabolism genes regulated by AR signaling describe in Han *et al*. (2018). (E) A schematic diagram summarized the mechanisms by which AR regulates FASN expression. (F) The correlation of *FASN* and *AR* expression with *HOXA10* levels in PCa patients was calculated by using TCGA provisional and SU2C database. To dilute noise for expression correlation analyses between *HOXA10* and *AR* or *FASN*, we ranked patients by expression values of *HOXA10*, divided patients into individual groups that each contain 20 and 8 neighboring patients from the TCGA and SU2C cohorts, respectively, calculate average expression value for each gene in each group, and finally determined the Pearson correlation coefficient between a pair of genes across individual patient groups. A full colour version of this figure is available at https://doi.org/10.1530/ERC-18-0465.

mRNA levels in CRPC in comparison to primary tumors (Fig. 6C). These results supported that increased FASN expression is associated with prostate cancer progression.

Discussion

This study demonstrates that downregulation of HOXA10 enhances lipogenesis through AR signaling in PCa cells to promote prostate cancer progression to the castrate-resistant stage. This HOXA10 function adds to its multiple roles in urogenital organ formation during development. We report that HOXA10 inhibits the expression of lipogenesis genes including *FASN*, which is known for its role in accelerating cell proliferation as well as and energy generation and storage during CRPC progression. Mechanically, HOXA10 abolishes AR recruitment to the *FASN* promoter, thereby preventing AR from activating *FASN* gene transcription. Importantly, we confirm that HOXA10 downregulation and FASN upregulation are both correlated with CRPC, emphasizing that HOXA10 is a key regulator linking the AR signaling and lipogenesis in promoting tumor progression to CRPC.

HOX genes are key regulators of normal organogenesis. Therefore, a balanced *HOX* gene expression and function

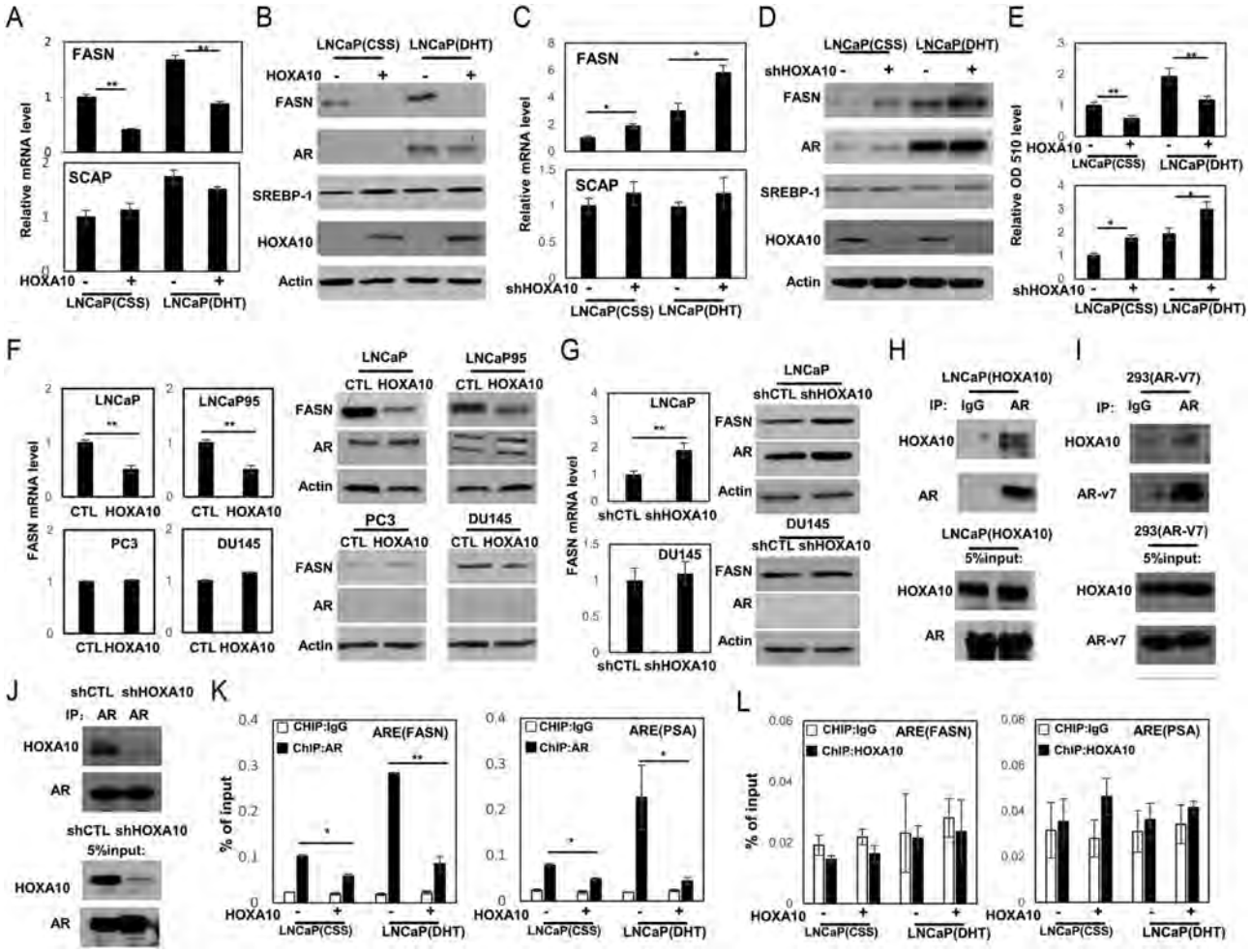

Figure 5

HOXA10 represses FASN expression through the AR. (A and B) LNCaP(CTL) and LNCaP(HOXA10) cells were treated with either vehicle or 10 nM DHT. Real-time PCR and immunoblotting measured FASN and SCAP mRNA levels in (A) and FASN, AR, SREBP1, HOXA10 protein levels by immunoblotting in (B). (C and D) LNCaP(shCTL) and LNCaP(shHOXA10) cells were treated with either vehicle or 10 nM DHT. Real-time PCR and immunoblotting measured *FASN* and *SCAP* mRNA levels in (C) and FASN, AR, SREBP1, HOXA10 protein levels by immunoblotting in (D). (E) LNCaP(CTL), LNCaP(HOXA10), LNCaP(shCTL) and LNCaP(shHOXA10) cells were used for Oil red O staining. Neural lipid levels were quantified using spectrophotometry with 510 nm wavelength. (F and G) LNCaP, LNCaP95, PC3 and DU145 cells were transfected with control or HOXA10 plasmid (F). HOXA10 expression was depleted in LNCaP and DU145 cells (G). *FASN* mRNA and protein levels were measured by Real-time PCR and immunoblotting assays, respectively. (H, I and J) Whole cell lyses were extracted from LNCaP (H), 293T cells transfected with AR-v7 plasmid (I), or LNCaP cells with HOXA10 knockdown (J) and were used to perform immunoprecipitation assays with either control IgG or an AR antibody. Precipitated proteins were immunoblotted with AR and HOXA10 antibodies. (K and L) LNCaP(CTL) and LNCaP(HOXA10) cells were treated with vehicle or DHT, and used to perform ChIP assays with the AR antibody (K) or the HOXA10 antibody (L). Eluted DNA fragments were used as templates for real-time qPCR to measure the enrichment of AR or HOXA10 to androgen response elements in *FASN* and *PSA* promoters. Signals were calculated as percentage of input. All results were derived from three independent experiments performed in triplicate. Data were presented as the mean ± s.d. Statistical analyses used one-way ANOVA test followed by Tukey test with $P < 0.05$ as * and $P < 0.01$ as **.

must be delicately controlled in both spatial and temporal manners. The 5' posterior cluster of *HOX* genes regulates prostate development by inducing mature morphogenesis and terminal differentiation of prostatic cells. Downregulation of these *HOX* genes in fully developed prostate is predicted to disrupt terminal differentiation and likely switch on cell proliferation. This hypothesis is consistent with our findings that enhanced HOXA10 expression suppresses PCa cell growth and tumor progression. Previous studies have demonstrated that the posterior *HOX* gene, *HOXB13*, is also critical for prostate development (Economides & Capecchi 2003). Enhanced HOXB13 expression inhibits AR signaling, as well as PCa cell and xenograft growth (Jung *et al.* 2004). Similarly, HOXA10 had been demonstrated to be suppressive to estrogen receptor-negative breast cancer cells by blocking *TP53* gene expression (Chu *et al.* 2004). These findings support the idea that the dysregulation of *HOX* genes can

https://erc.bioscientifica.com
https://doi.org/10.1530/ERC-18-0465

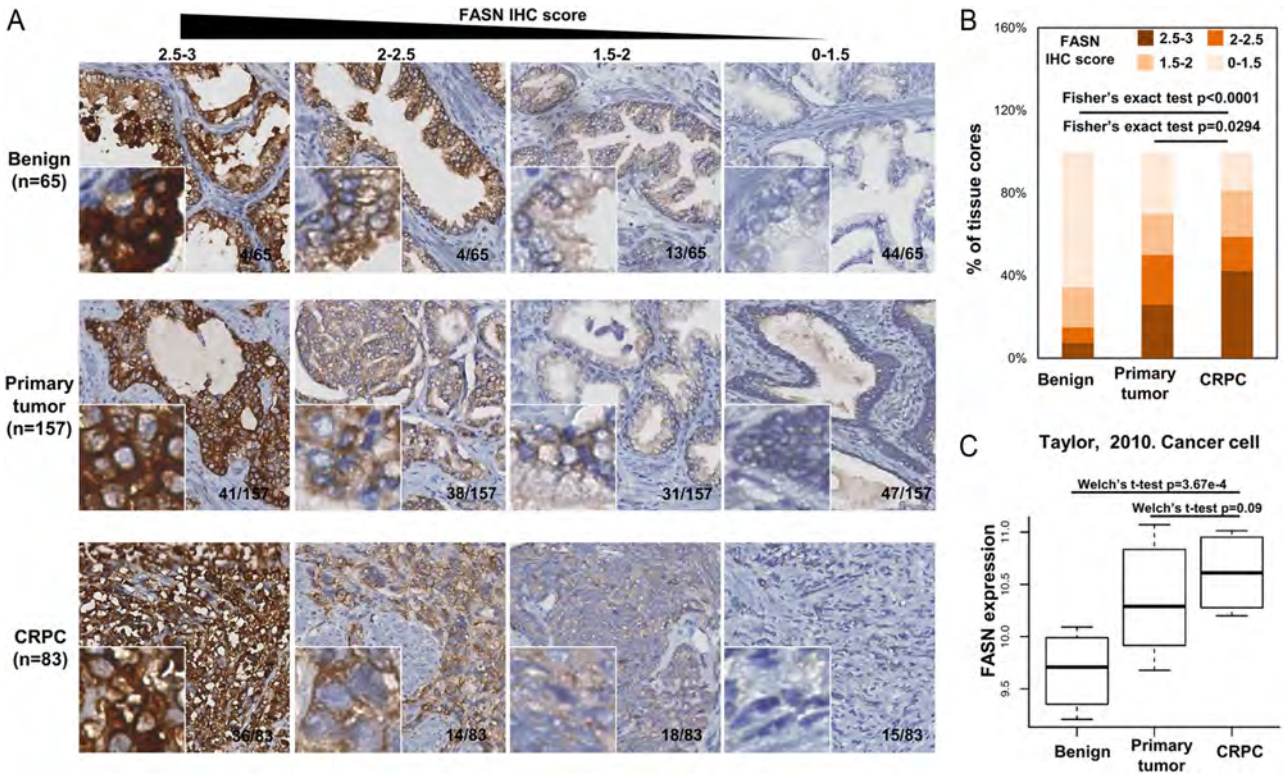

Figure 6

FASN protein expression in PCa. (A) IHC with the FASN antibody was performed on PCa TMA. IHC scores were evaluated as described in the Materials and methods section. Representative IHC images were presented. (B) Distribution of FASN IHC scores in benign, primary prostate tumor and CRPC groups were plotted. The primary tumor samples were first ranked by H-scores, then were divided into 4 groups with equal sample sizes. H-Score cutoffs were retrieved and applied to benign prostate and CRPC sample groups. Fisher's exact tests were used to compare FASN expression among the three tissue groups. (C) RNA-seq analyses (GSE21032 – Taylor *et al.* 2010) compared *FASN* mRNA levels among benign prostate, primary prostate tumors, and CRPC. One sided Welch's *t*-test is use to compare results among different groups. A full colour version of this figure is available at https://doi.org/10.1530/ERC-18-0465.

promote tumor development and disease progression by regulating intracellular signaling.

Although the AR signaling plays an important role in driving the differentiation of luminal epithelial cells during prostate development, there is a paradigm shift of AR signaling away from maintaining cell differentiation in hormone naïve PCa (Wang *et al.* 2009) to accelerating cell cycling and mitosis in CRPC (Wang *et al.* 2009, Cai *et al.* 2011). This conclusion is demonstrated by several genome-wide profiling studies showing that not only the AR cistrome, but also the AR transcriptome is re-programmed to activate mitosis in CRPC (Wang *et al.* 2009, Cai *et al.* 2011). Accompanying the re-activation of AR signaling is the alteration of lipogenesis. Our results show that FASN is upregulated in CRPC, concurrent with the downregulation of HOXA10. HOXA10 suppresses *FASN* transcription by interfering with AR functions. Therefore, HOXA10 downregulation could contribute to CRPC progression by re-activating AR signaling and enhancing AR driven lipogenesis.

HOXA10 is a transcriptional factor that recognizes the 'TAAT' motif within the target promoters to control gene transcription (Gehring *et al.* 1994). The new finding from our study indicated that HOXA10 can also form a protein complex with AR and indirectly regulate gene transcription through interfering AR transcriptional activity. Because HOXA10 also inhibits the transcriptional activities mediated by AR-v7 and HOXA10 do form a protein complex with AR-v7, it is likely that HOXA10 associates with AR are at the AR DNA-binding domain or the N-terminus. HOXA10 does not recognize the regions next to AREs in the *FASN* and *PSA* promoters, suggesting that the HOXA10-AR complex is not recruited to the AR regulated promoter.

We did not observe any negative associations between HOXA10 RISH scores and FASN IHC scores from the same TMA. This discrepancy from our *in vitro* studies using cell models could be explained by: (1) FASN protein levels are regulated by multiple mechanisms at not only transcriptional (e.g. HOXA10

and AR), but also post-transcriptional and translational levels. A copy of HOXA10 mRNA can be translated into multiple copies of HOXA10 protein, which can result in discordance between HOXA10 RISH signal and FASN IHC signal; (2) compared to *in vitro* cell models, tumor microenvironments and the heterogeneous nature of cancer cells within patient tumors also make it challenging to establish associations between HOXA10 and FASN; (3) most importantly, the principles of IHC and RISH assays, and how the scoring methods used differ from each other. In contrast to the IHC signal that was scored by not only the intensity of IHC staining but also the percentile of positive stained cells, the intensity of RISH signal is indistinguishable among tumor cells. However, regardless of these factors that prevent us from establishing a negative correlation during statistical analyses on tissues, they did not preclude us from applying IHC and RISH signals to compare FASN and HOXA10 expression between primary PCa and CRPC, nor do they impede us from drawing the conclusion that the downregulation of HOXA10 and the upregulation of FASN are both associated with CRPC.

Conclusion

Reduced HOXA10 gene expression enhances lipogenesis through AR signaling in PCa cells and may promote prostate tumor progression to the castrate-resistant stage.

Declaration of interest

The authors declare that there is no conflict of interest that could be perceived as prejudicing the impartiality of the research reported.

Funding

This work is supported by a CIHR operating grant (MOP-137007) to X D, a Hunan Natural Sciences Foundation grant (#2017JJ2370) to Z L, and visiting scholarships from China Scholar Council to Y L (#201306231021), Z L (#201606375104) and Y G (#201606370204).

Ethics approval and consent to participate

The animal protocol was approved by the Institutional Animal Care and Use Committee at the University of British Columbia. All patients had given informed consent to a protocol that was reviewed and approved by the UBC Clinical Research Ethics Board (Certificate #: H09-01628).

Availability of data and materials

The datasets used and/or analyzed during the current study are available from the corresponding author on reasonable request.

Author contribution statement

Concept and design: Dong X. Acquisition of data: Long Z, Li Y, Gan Y, Ning X, Zhao D. Analysis and interpretation of data: Long Z, Li Y. Drafting the manuscript: Li Y, Lovnicki J, Dong X. Critical revision of the manuscript: Dong X, Cao Q, Chen K. Statistically analysis: Li Y, Zhao D, Wang G. Obtain funding: Dong X. Administrative, technical or material support: Fazli L.

Acknowledgements

Authors would like to thank Drs Hugh Taylor and Gunter Wagner for sharing plasmid DNA of HOXA10, 11 and 13. They thank Estelle Li from the Pathology Core facility at the Vancouver Prostate Centre for her technical support in this study.

References

Ackerman D & Simon MC 2014 Hypoxia, lipids, and cancer: surviving the harsh tumor microenvironment. *Trends in Cell Biology* **24** 472–478. (https://doi.org/10.1016/j.tcb.2014.06.001)

Bagot CN, Kliman HJ & Taylor HS 2001 Maternal Hoxa10 is required for pinopod formation in the development of mouse uterine receptivity to embryo implantation. *Developmental Dynamics* **222** 538–544. (https://doi.org/10.1002/dvdy.1209)

Benson GV, Lim H, Paria BC, Satokata I, Dey SK & Maas RL 1996 Mechanisms of reduced fertility in Hoxa-10 mutant mice: uterine homeosis and loss of maternal Hoxa-10 expression. *Development* **122** 2687–2696.

Butler LM, Centenera MM & Swinnen JV 2016 Androgen control of lipid metabolism in prostate cancer: novel insights and future applications. *Endocrine-Related Cancer* **23** R219–R227. (https://doi.org/10.1530/ERC-15-0556)

Cai C, He HH, Chen S, Coleman I, Wang H, Fang Z, Chen S, Nelson PS, Liu XS, Brown M, *et al*. 2011 Androgen receptor gene expression in prostate cancer is directly suppressed by the androgen receptor through recruitment of lysine-specific demethylase 1. *Cancer Cell* **20** 457–471. (https://doi.org/10.1016/j.ccr.2011.09.001)

Chandran UR, Ma C, Dhir R, Bisceglia M, Lyons-Weiler M, Liang W, Michalopoulos G, Becich M & Monzon FA 2007 Gene expression profiles of prostate cancer reveal involvement of multiple molecular pathways in the metastatic process. *BMC Cancer* **7** 64. (https://doi.org/10.1186/1471-2407-7-64)

Choo AY, Yoon SO, Kim SG, Roux PP & Blenis J 2008 Rapamycin differentially inhibits S6Ks and 4E-BP1 to mediate cell-type-specific repression of mRNA translation. *PNAS* **105** 17414–17419. (https://doi.org/10.1073/pnas.0809136105)

Chu MC, Selam FB & Taylor HS 2004 HOXA10 regulates p53 expression and matrigel invasion in human breast cancer cells. *Cancer Biology and Therapy* **3** 568–572. (https://doi.org/10.4161/cbt.3.6.848)

de Bono JS, Logothetis CJ, Molina A, Fizazi K, North S, Chu L, Chi KN, Jones RJ, Goodman OB Jr, Saad F, *et al*. 2011 Abiraterone and increased survival in metastatic prostate cancer. *New England Journal of Medicine* **364** 1995–2005. (https://doi.org/10.1056/NEJMoa1014618)

Dhanasekaran SM, Dash A, Yu J, Maine IP, Laxman B, Tomlins SA, Creighton CJ, Menon A, Rubin MA & Chinnaiyan AM 2005 Molecular profiling of human prostate tissues: insights into gene expression patterns of prostate development during puberty. *FASEB Journal* **19** 243–245. (https://doi.org/10.1096/fj.04-2415fje)

Economides KD & Capecchi MR 2003 Hoxb13 is required for normal differentiation and secretory function of the ventral prostate. *Development* **130** 2061–2069. (https://doi.org/10.1242/dev.00432)

Ferraldeschi R, Welti J, Luo J, Attard G & de Bono JS 2015 Targeting the androgen receptor pathway in castration-resistant prostate cancer:

progresses and prospects. *Oncogene* **34** 1745–1757. (https://doi.org/10.1038/onc.2014.115)

Gehring WJ, Qian YQ, Billeter M, Furukubo-Tokunaga K, Schier AF, Resendez-Perez D, Affolter M, Otting G & Wuthrich K 1994 Homeodomain-DNA recognition. *Cell* **78** 211–223. (https://doi.org/10.1016/0092-8674(94)90292-5)

Gillies RJ, Didier N & Denton M 1986 Determination of cell number in monolayer cultures. *Analytical Biochemistry* **159** 109–113. (https://doi.org/10.1016/0003-2697(86)90314-3)

Grasso CS, Wu YM, Robinson DR, Cao X, Dhanasekaran SM, Khan AP, Quist MJ, Jing X, Lonigro RJ, Brenner JC, *et al*. 2012 The mutational landscape of lethal castration-resistant prostate cancer. *Nature* **487** 239–243. (https://doi.org/10.1038/nature11125)

Han W, Gao S, Barrett D, Ahmed M, Han D, Macoska JA, He HH & Cai C 2018 Reactivation of androgen receptor-regulated lipid biosynthesis drives the progression of castration-resistant prostate cancer. *Oncogene* **37** 710–721. (https://doi.org/10.1038/onc.2017.385)

Heemers H, Verrijdt G, Organe S, Claessens F, Heyns W, Verhoeven G & Swinnen JV 2004 Identification of an androgen response element in intron 8 of the sterol regulatory element-binding protein cleavage-activating protein gene allowing direct regulation by the androgen receptor. *Journal of Biological Chemistry* **279** 30880–30887. (https://doi.org/10.1074/jbc.M401615200)

Huang L, Pu Y, Hepps D, Danielpour D & Prins GS 2007 Posterior Hox gene expression and differential androgen regulation in the developing and adult rat prostate lobes. *Endocrinology* **148** 1235–1245. (https://doi.org/10.1210/en.2006-1250)

Jung C, Kim RS, Zhang HJ, Lee SJ & Jeng MH 2004 HOXB13 induces growth suppression of prostate cancer cells as a repressor of hormone-activated androgen receptor signaling. *Cancer Research* **64** 9185–9192. (https://doi.org/10.1158/0008-5472.CAN-04-1330)

Krumlauf R 1994 Hox genes in vertebrate development. *Cell* **78** 191–201. (https://doi.org/10.1016/0092-8674(94)90290-9)

Lee AR, Li Y, Xie N, Gleave ME, Cox ME, Collins CC & Dong X 2017 Alternative RNA splicing of the MEAF6 gene facilitates neuroendocrine prostate cancer progression. *Oncotarget* **8** 27966–27975. (https://doi.org/10.18632/oncotarget.23313)

Li H, Li Y, Morin D, Plymate S, Lye S & Dong X 2014 The androgen receptor mediates antiapoptotic function in myometrial cells. *Cell Death and Disease* **5** e1338. (https://doi.org/10.1038/cddis.2014.303)

Li H, Xie N, Chen R, Verreault M, Fazli L, Gleave ME, Barbier O & Dong X 2016 UGT2B17 expedites progression of castration-resistant prostate cancers by promoting ligand-independent AR signaling. *Cancer Research* **76** 6701–6711. (https://doi.org/10.1158/0008-5472.CAN-16-1518)

Li Y, Zhang Q, Lovnicki J, Chen R, Fazli L, Wang Y, Gleave M, Huang J & Dong X 2018 SRRM4 gene expression correlates with neuroendocrine prostate cancer. *Prostate* **79** 96–104. (https://doi.org/10.1002/pros.23715)

Liu LL, Xie N, Sun S, Plymate S, Mostaghel E & Dong X 2014 Mechanisms of the androgen receptor splicing in prostate cancer cells. *Oncogene* **33** 3140–3150. (https://doi.org/10.1038/onc.2013.284)

Maeda Y, Dave V & Whitsett JA 2007 Transcriptional control of lung morphogenesis. *Physiological Reviews* **87** 219–244. (https://doi.org/10.1152/physrev.00028.2006)

Mark M, Rijli FM & Chambon P 1997 Homeobox genes in embryogenesis and pathogenesis. *Pediatric Research* **42** 421–429. (https://doi.org/10.1203/00006450-199710000-00001)

Migita T, Ruiz S, Fornari A, Fiorentino M, Priolo C, Zadra G, Inazuka F, Grisanzio C, Palescandolo E, Shin E, *et al*. 2009 Fatty acid synthase: a metabolic enzyme and candidate oncogene in prostate cancer. *Journal of the National Cancer Institute* **101** 519–532. (https://doi.org/10.1093/jnci/djp030)

Montgomery RB, Mostaghel EA, Vessella R, Hess DL, Kalhorn TF, Higano CS, True LD & Nelson PS 2008 Maintenance of intratumoral androgens in metastatic prostate cancer: a mechanism for castration-resistant tumor growth. *Cancer Research* **68** 4447–4454. (https://doi.org/10.1158/0008-5472.CAN-08-0249)

Norris JD, Chang CY, Wittmann BM, Kunder RS, Cui H, Fan D, Joseph JD & McDonnell DP 2009 The homeodomain protein HOXB13 regulates the cellular response to androgens. *Molecular Cell* **36** 405–416. (https://doi.org/10.1016/j.molcel.2009.10.020)

Palmeri ML, Miller ZA, Glass TJ, Garcia-Reyes K, Gupta RT, Rosenzweig SJ, Kauffman C, Polascik TJ, Buck A, Kulbacki E, *et al*. 2015 B-mode and acoustic radiation force impulse (ARFI) imaging of prostate zonal anatomy: comparison with 3T T2-weighted MR imaging. *Ultrasonic Imaging* **37** 22–41. (https://doi.org/10.1177/0161734614542177)

Podlasek CA, Seo RM, Clemens JQ, Ma L, Maas RL & Bushman W 1999 Hoxa-10 deficient male mice exhibit abnormal development of the accessory sex organs. *Developmental Dynamics* **214** 1–12. (https://doi.org/10.1002/(SICI)1097-0177(199901)214:1<1::AID-DVDY1>3.0.CO;2-2)

Post LC & Innis JW 1999 Altered Hox expression and increased cell death distinguish Hypodactyly from Hoxa13 null mice. *International Journal of Developmental Biology* **43** 287–294.

Qi J, Tripathi M, Mishra R, Sahgal N, Fazli L, Ettinger S, Placzek WJ, Claps G, Chung LW, Bowtell D, *et al*. 2013 The E3 ubiquitin ligase Siah2 contributes to castration-resistant prostate cancer by regulation of androgen receptor transcriptional activity. *Cancer Cell* **23** 332–346. (https://doi.org/10.1016/j.ccr.2013.02.016)

Quinonez SC & Innis JW 2014 Human HOX gene disorders. *Molecular Genetics and Metabolism* **111** 4–15. (https://doi.org/10.1016/j.ymgme.2013.10.012)

Ramirez-Zacarias JL, Castro-Munozledo F & Kuri-Harcuch W 1992 Quantitation of adipose conversion and triglycerides by staining intracytoplasmic lipids with Oil red O. *Histochemistry* **97** 493–497. (https://doi.org/10.1007/BF00316069)

Rossi S, Graner E, Febbo P, Weinstein L, Bhattacharya N, Onody T, Bubley G, Balk S & Loda M 2003 Fatty acid synthase expression defines distinct molecular signatures in prostate cancer. *Molecular Cancer Research* **1** 707–715.

Satokata I, Benson G & Maas R 1995 Sexually dimorphic sterility phenotypes in Hoxa10-deficient mice. *Nature* **374** 460–463. (https://doi.org/10.1038/374460a0)

Scher HI, Fizazi K, Saad F, Taplin ME, Sternberg CN, Miller K, de Wit R, Mulders P, Chi KN, Shore ND, *et al*. 2012 Increased survival with enzalutamide in prostate cancer after chemotherapy. *New England Journal of Medicine* **367** 1187–1197. (https://doi.org/10.1056/NEJMoa1207506)

Shah N & Sukumar S 2010 The Hox genes and their roles in oncogenesis. *Nature Reviews Cancer* **10** 361–371. (https://doi.org/10.1038/nrc2826)

Singh D, Febbo PG, Ross K, Jackson DG, Manola J, Ladd C, Tamayo P, Renshaw AA, D'Amico AV, Richie JP, *et al*. 2002 Gene expression correlates of clinical prostate cancer behavior. *Cancer Cell* **1** 203–209. (https://doi.org/10.1016/S1535-6108(02)00030-2)

Swinnen JV, Ulrix W, Heyns W & Verhoeven G 1997 Coordinate regulation of lipogenic gene expression by androgens: evidence for a cascade mechanism involving sterol regulatory element binding proteins. *PNAS* **94** 12975–12980. (https://doi.org/10.1073/pnas.94.24.12975)

Taylor HS, Arici A, Olive D & Igarashi P 1998 HOXA10 is expressed in response to sex steroids at the time of implantation in the human endometrium. *Journal of Clinical Investigation* **101** 1379–1384. (https://doi.org/10.1172/JCI1597)

Taylor BS, Schultz N, Hieronymus H, Gopalan A, Xiao Y, Carver BS, Arora VK, Kaushik P, Cerami E, Reva B, *et al*. 2010 Integrative genomic profiling of human prostate cancer. *Cancer Cell* **18** 11–22. (https://doi.org/10.1016/j.ccr.2010.05.026)

Vanaja DK, Cheville JC, Iturria SJ & Young CY 2003 Transcriptional silencing of zinc finger protein 185 identified by expression profiling

is associated with prostate cancer progression. *Cancer Research* **63** 3877–3882.

Villavicencio-Lorini P, Kuss P, Friedrich J, Haupt J, Farooq M, Turkmen S, Duboule D, Hecht J & Mundlos S 2010 Homeobox genes d11-d13 and a13 control mouse autopod cortical bone and joint formation. *Journal of Clinical Investigation* **120** 1994–2004. (https://doi.org/10.1172/JCI41554)

Wallace TA, Prueitt RL, Yi M, Howe TM, Gillespie JW, Yfantis HG, Stephens RM, Caporaso NE, Loffredo CA & Ambs S 2008 Tumor immunobiological differences in prostate cancer between African-American and European-American men. *Cancer Research* **68** 927–936. (https://doi.org/10.1158/0008-5472.CAN-07-2608)

Wang Q, Li W, Zhang Y, Yuan X, Xu K, Yu J, Chen Z, Beroukhim R, Wang H, Lupien M, *et al*. 2009 Androgen receptor regulates a distinct transcription program in androgen-independent prostate cancer. *Cell* **138** 245–256. (https://doi.org/10.1016/j.cell.2009.04.056)

Warot X, Fromental-Ramain C, Fraulob V, Chambon P & Dolle P 1997 Gene dosage-dependent effects of the Hoxa-13 and Hoxd-13 mutations on morphogenesis of the terminal parts of the digestive and urogenital tracts. *Development* **124** 4781–4791.

Wellik DM 2009 Hox genes and vertebrate axial pattern. *Current Topics in Developmental Biology* **88** 257–278.

Welsh JB, Sapinoso LM, Su AI, Kern SG, Wang-Rodriguez J, Moskaluk CA, Frierson HF Jr & Hampton GM 2001 Analysis of gene expression identifies candidate markers and pharmacological targets in prostate cancer. *Cancer Research* **61** 5974–5978.

Xie N, Cheng H, Lin D, Liu L, Yang O, Jia L, Fazli L, Gleave ME, Wang Y, Rennie P, *et al*. 2015 The expression of glucocorticoid receptor is negatively regulated by active androgen receptor signaling in prostate tumors. *International Journal of Cancer* **136** E27–E38. (https://doi.org/10.1002/ijc.29147)

Yu YP, Landsittel D, Jing L, Nelson J, Ren B, Liu L, McDonald C, Thomas R, Dhir R, Finkelstein S, *et al*. 2004 Gene expression alterations in prostate cancer predicting tumor aggression and preceding development of malignancy. *Journal of Clinical Oncology* **22** 2790–2799. (https://doi.org/10.1200/JCO.2004.05.158)

Yu Y, Liu L, Xie N, Xue H, Fazli L, Buttyan R, Wang Y, Gleave M & Dong X 2013 Expression and function of the progesterone receptor in human prostate stroma provide novel insights to cell proliferation control. *Journal of Clinical Endocrinology and Metabolism* **98** 2887–2896. (https://doi.org/10.1210/jc.2012-4000)

Yu Y, Yang O, Fazli L, Rennie PS, Gleave ME & Dong X 2015 Progesterone receptor expression during prostate cancer progression suggests a role of this receptor in stromal cell differentiation. *Prostate* **75** 1043–1050. (https://doi.org/10.1002/pros.22988)

Received in final form 11 December 2018
Accepted 21 December 2018
Accepted Preprint published online 21 December 2018

IJC
International Journal of Cancer

Polycomb group proteins EZH2 and EED directly regulate androgen receptor in advanced prostate cancer

Qipeng Liu[1,2,3], Guangyu Wang[4,5], Qiaqia Li[1,2,6,7], Weihua Jiang[1], Jung-Sun Kim[1], Rui Wang[1], Sen Zhu[1], Xiaoju Wang[8,9], Lin Yan[1,2], Yang Yi[1,7,10,11], Lili Zhang[1], Qingshu Meng[1,7], Chao Li[1,6,7], Dongyu Zhao[4,5], Yuanyuan Qiao[8,9], Yong Li[8,9], Demirkan B. Gursel[12,13], Arul M. Chinnaiyan[8,9,14,15,16], Kaifu Chen[4,5,17] and Qi Cao[1,7,18]

[1]Center for Inflammation and Epigenetics, Houston Methodist Research Institute, Houston, TX
[2]Xiangya School of Medicine, Central South University, Changsha, Hunan, China
[3]Department of Urology, The Second Xiangya Hospital of Central South University, Hunan, China
[4]Center for Cardiovascular Regeneration, Houston Methodist Research Institute, Houston, TX
[5]Department of Cardiothoracic Surgery, Weill Cornell Medicine, Cornell University, New York, NY
[6]Department of Urology, Xiangya Hospital, Central South University, Changsha, Hunan, China
[7]Department of Urology, Northwestern University Feinberg School of Medicine, Chicago, IL
[8]Michigan Center for Translational Pathology, University of Michigan, Ann Arbor, MI
[9]Department of Pathology, University of Michigan, Ann Arbor, MI
[10]Key Laboratory for Stem Cells and Tissue Engineering, Ministry of Education, Sun Yat-Sen University, Guangzhou, Guangdong, China
[11]Department of Histology and Embryology, Zhongshan School of Medicine, Sun Yat-Sen University, Guangzhou, Guangdong, China
[12]Pathology Core Facility, Robert H. Lurie Comprehensive Cancer Center, Northwestern University, Chicago, IL
[13]Pathology Department, Feinberg School of Medicine, Northwestern University, Chicago, IL
[14]Howard Hughes Medical Institute, University of Michigan, Ann Arbor, MI
[15]Department of Urology, University of Michigan, Ann Arbor, MI
[16]Comprehensive Cancer Center, University of Michigan, Ann Arbor, MI
[17]Institutes for Academic Medicine, Houston Methodist Hospital, Houston, TX
[18]Robert H. Lurie Comprehensive Cancer Center, Northwestern University Feinberg School of Medicine, Chicago, IL

Polycomb group proteins are important epigenetic regulators for cell proliferation and differentiation, organ development, as well as initiation and progression of lethal diseases, including cancer. Upregulated Polycomb group proteins, including Enhancer of zeste homolog 2 (EZH2), promote proliferation, migration, invasion and metastasis of cancer cells, as well as self-renewal of cancer stem cells. In our study, we report that EZH2 and embryonic ectoderm development (EED) indicate respective direct interaction with androgen receptor (AR). In the context of AR-positive prostate cancer, EZH2 and EED regulate AR expression levels and AR downstream targets. More importantly, we demonstrate that targeting EZH2 with the small-molecule inhibitor astemizole in cancer significantly represses the EZH2 and AR expression as well as the neoplastic capacities. These results collectively suggest that pharmacologically targeting EZH2 might be a promising strategy for advanced prostate cancer.

Key words: EZH2, EED, androgen receptor, astemizole, prostate cancer

Additional Supporting Information may be found in the online version of this article.

Q.L., G.W. and Q.L. contributed equally to this work

Yong Li's current address is: Department of Anatomy and Biology, School of Medicine, Indiana University, Bloomington, IN

Grant sponsor: NIH/NHLBI; **Grant numbers:** HL099997, HL100397; **Grant sponsor:** NIH/NCI; **Grant number:** R01CA208257; **Grant sponsor:** American Cancer Society; **Grant number:** TBE-128382; **Grant sponsor:** U.S. Department of Defense; **Grant numbers:** W81XWH-15-1-0639, W81XWH-17-1-0357; **Grant sponsor:** Prostate Cancer Foundation; **Grant number:** 13YOUN007; **Grant sponsor:** Houston Methodist Research Institute; **Grant sponsor:** Northwestern University

DOI: 10.1002/ijc.32118

History: Received 12 Jun 2018; Accepted 19 Dec 2018; Online 10 Jan 2019

Correspondence to: Kaifu Chen, Ph.D. 6670 Bertner Ave, R10-217, Houston Methodist Research Institute, Houston, TX 77030, E-mail: kchen2@houstonmethodist.org; Tel.: (+1) 713-363-7205; or Qi Cao, Ph.D. 303 E. Chicago Ave, Tarry 16-707, Department of Urology, Northwestern University Feinberg School of Medicine, Chicago, IL 60611, Tel.: +1-312-503-5990, E-mail: qi.cao@northwestern.edu

What's new?

Polycomb group proteins are epigenetic regulators with important roles in cancer initiation and progression. Among them, EZH2 is a downstream target of androgen receptor (AR) in prostate cancer. How EZH2 regulates AR functions in castration-resistant prostate cancer (CRPC) however remains unclear. This study reveals that EZH2 and EED--the two core catalytic subunits of the PRC2 class of Polycomb group proteins--play a critical role related to the AR pathway in prostate cancer. Moreover, astemizole was a potent PRC2 disruptor that significantly represses EZH2 and AR expression in prostate cancer cells, thus representing a potential medication for castration-resistant prostate cancer.

Introduction

Prostate cancer (PCa) is a major health concern and the second most common cause of cancer-related mortality among men worldwide, especially in developed countries.[1] After local therapy and hormone depletion therapy, most prostate cancer patients relapse and tumors become castration-resistant. For these castration-resistant prostate cancer (CRPC) patients, anti-AR or anti-androgen synthesis therapies, including enzalutamide (MDV3100), Apalutamide (ARN-509) and Zytiga (abiraterone acetate), are most commonly used.[2] However, CRPC patients will soon develop drug-resistance to these therapies. Hence, there is a pressing need of new therapeutic targets and reagents for CRPC.

The Polycomb group proteins, which are considered paradigmatic epigenetic modulators, remodel the chromatin structure and subsequent transcriptional repression. Polycomb Repressive Complex 2 (PRC2), one of the two classes of Polycomb group proteins, catalyzes the trimethylation of lysine 27 on histone H3 (H3K27me3) on chromatin. The methylation requires physical interaction between EZH2 and EED, the two core catalytic subunits of PRC2.[3,4]

Recently, several EZH2 specific inhibitors that target the lysine methyltransferase activities of EZH2 have been developed, including the GSK126 by GSK, the EPZ5687 and EPZ6438 by Epizyme, and the EI1 by Novartis.[5–8] Even though these EZH2 inhibitors successfully decrease the methylation marks on H3K27 at relatively low concentrations, they indicated limited utility to inhibit the progression of diffuse large B-cell lymphoma (DLBCL) that harbors the gain-of-function EZH2 mutations, and fail to slow down the growth of solid tumors without EZH2 or other mutations.[9–11] Since these inhibitors do not alter EZH2 expression levels, new drugs that decrease EZH2 protein levels might be helpful to resolve this paradox.

It has been reported that EZH2 is a downstream target of AR in prostate cancer. AR directly binds to the upstream enhancer and promoter of EZH2 to activate EZH2 expression.[12] EZH2 may also bind directly to AR in CRPC to regulate AR functions.[13] However, the interaction between EZH2 and AR is not clearly understood. How EZH2/PRC2 regulates AR functions in CRPC also remains unknown. In our study, we elucidate how EZH2/PRC2 binds to AR to form a complex and alters AR functions by regulating AR expression levels. Furthermore, we newly discovered an EZH2 inhibitor, astemizole, an anti-histamine drug previously on the market as an allergy treatment. We demonstrated that degrading EZH2 with astemizole successfully decreases tumor progression, providing a new therapeutic strategy for advanced CRPC.

Materials and Methods

Cell lines

LNCaP, VCaP, 22Rv1 and HEK293T cells were purchased from ATCC. C4-2 was a gift from Dr. Leland W. Chang. All cell lines were cultured in DMEM (GenDEPOT) or RPMI-1640 (GenDEPOT) supplemented with 10% FBS (GenDEPOT) and used within 20 passages after receipt. The cells were cultured in a 37°C incubator and a humidified atmosphere with 5% CO_2. All cell lines were authenticated by the University of Arizona Genetics Core using short tandem repeat (STR) profiling. Cell lines were mycoplasma negative as reported by routine lab tests.

Reagents and antibodies

GSK126 (406,228, MedKoo), EPZ5687 (S7004, Selleckchem), EPZ6438 (S7128, Selleckchem), EED226 (S8496, Selleckchem) and astemizole (3,489, Tocris) were dissolved in 100% ethanol or DMSO for cell treatment. Lipofectamine 3,000 (Thermo Fisher Scientific) was used to perform the transfection of EZH2 shRNA and EED shRNA (Sigma). The following antibodies were used: AR (06–680, Millipore), EZH2 (5,246, Cell Signaling), rabbit polyclonal anti-EED (09–774, Millipore), mouse monoclonal anti-EED (05–1,320, Millipore), normal rabbit IgG (12–370, Millipore), normal mouse IgG (12–371, Millipore), GST (sc-138, Santa Cruz), FLAG (14,793, Cell Signaling), PSA (A0562, Dako), GAPDH (sc-32,233, Santa Cruz), H3K27me3 (9,733, Cell Signaling), H3 (9,715, Cell signaling), β-Actin (A2228, Sigma), LC3-A/B (12,741, Cell Signaling).

Immunoprecipitation

Whole-cell lysate IP was performed by lysing cells in 1× NP-40 lysis buffer (2×) (GenDEPOT) or Pierce RIPA Buffer (Thermo Fisher Scientific) with protease and phosphatase inhibitor (Thermo Fisher Scientific). The lysate was kept on ice for 15 min and sonicated for 2 s on and 2 s off for 30 s and the insoluble pellet was removed after centrifugation. Lysates were pre-cleared using Dynabeads protein A (10002D, Invitrogen) or protein G (10004D, Invitrogen). Antibodies were added to lysates and incubated at 4°C for 2 hr. The immune complexes were then mixed with Dynabeads protein A (10002D, Invitrogen) or protein G (10004D, Invitrogen) at 4°C overnight, and beads were washed three times extensively with the corresponding lysis buffer.

For *in vitro* immunoprecipitation, AR-FL (346101-5,000 U, EMD Millipore), EZH2 (50,279, BPS Bioscience), EED (50,280, BPS Bioscience) and AR-NTD (ab82124, Abcam) were purchased from the vendor listed. RING1B was produced and fused with a GST tag. The proteins were mixed and added into chilled PBS (1 mL) with a protease and phosphatase inhibitor. 50 μL of the solution was aspirated as input. The remaining protein mixture was incubated with anti-AR antibody at 4°C for 2 hr. The immune complexes were then mixed with Dynabeads protein A (10002D, Invitrogen) at 4°C overnight, and beads were washed three times extensively with NP-40 lysis buffer.

The beads were eluted by 2× reducing SDS-sample buffer prepared by an equal volume of lysis buffer and 4× reducing SDS-sample buffer (BP-110R, Boston BioProducts) and heated to 95°C for 15 min.

Western blotting

To denature proteins, lysates were added to 1× reducing SDS-sample buffer prepared by lysis buffer and 4× reducing SDS-sample buffer (BP-110R, Boston BioProducts) and heated to 95°C for 10 min. Protein levels were assessed by standard SDS–polyacrylamide gel electrophoresis and transferred to PVDF membranes (162–0177, BIO-RAD). Images were captured using the ChemiDoc XRS+ Molecular Imager system (BIO-RAD). Primary antibodies used in western blot analyses are listed above. Blots were incubated overnight with primary antibodies at 4°C, followed by detection with Clean-Blot IP Detection Reagent (HRP) (21,230, Thermo Fisher Scientific), goat anti-mouse IgG (H+L)-HRP (SA001-500, GenDEPOT), or goat anti-rabbit IgG (H+L)-HRP (SA002-500, GenDEPOT) secondary antibody.

Mass spectrum analysis

The mass spectrum analysis was performed as previously described.[14]

Lentiviral constructs

Lentivirus was packaged by cotransfection of constructs with third-generation packaging plasmids pMD2.G, pRRE and pRSV/REV with Fugene HD (Roche) into 10-cm plates with HEK293T cells. The transfection mixture was replaced with growth medium 24 hr after transfection (2 μg of MDLG, 1 μg of VSVG, 1 μg of Rev, and 4 μg of target plasmid). The supernatant was collected at 72 and 96 hr after transfection and centrifuged to remove the cells. Lentiviral titers were determined by p24 assay, in addition to functional titration to determine the multiplicity of infection (MOI) of 1 for each initial batch of virus. Expression was verified by western blotting.

Fusion protein induction and purification

RING1B was cloned into pFN2K vector (Promega) in accordance to the manufacturer's instructions. BL21 competent *E. coli* was used as bacterial host strain for the transformation. The transformed bacteria were added into 200 mL of LB medium containing 50 μg/mL of kanamycin. After shaking at 37°C for 2 hr, 100 ul of 0.1 M Isopropyl β-D-1-thiogalactopyranoside (IPTG) was added to induce the expression of fusion protein. The culture was collected by centrifugation after further incubation by shaking overnight at 16°C. The bacterial pellets were lysed using PBS supplemented with 1%Triton X-100 (GenDEPOT) and protease and phosphatase inhibitor (1,861,280, Thermo Fisher Scientific). For protein purification, the cell lysates were sonicated. The cleared supernatants were collected and incubated with Glutathione-Sepharose beads (17–0756-01, GE healthcare). The system was rotated at 4°C for 12 hr. The beads were washed for three times and the proteins were eluted from the beads with PBS supplemented with 0.1% NP-40 and 50 mM Glutathione (Sigma). The purified protein was collected and added with glycerol for preservation.

Reporter luciferase assays

The enhancer and promoter luciferase constructs were gifts from Dr. J. Chad Brenner and sequenced to confirm its precision. The promoters were cotransfected together with pRL-TK at a ratio of 10:1 into stable cell lines LNCaP and VCaP. Lentivirus packaged with EZH2 or EED shRNA was added 24 hr after cotransfection. Cells were lysed 24 hr later and conducted using the Dual-Luciferase Reporter Assay System (E1910, Promega). The bioluminescence was read on Synergy 2 Multi-Mode Reader (BioTek). PSA and TMPRSS2 promoter luciferase activity was normalized with Renilla luciferase activity. Each experiment was performed in quadruplicate.

RNA isolation and RT-qPCR

Total RNA was isolated from cells to generate cDNA using the RNA MiniPrep kit (Direct-zol, R2052, ZYMO Research) and amfiRivert cDNA Synthesis Platinum Master Mix (R5600-100, GenDEPOT). Each cDNA sample was amplified using iTaq Universal SYBR Green Supermix (172-5,124, BioRad) on the QuantStudio 6 Flex Real-time PCR System (403115082, GE Healthcare). Briefly, the reaction conditions consisted of 2 μL of cDNA and 0.2 μM primers in a 10 μL total volume of super mix. The whole system was hold at 95°C for 10 min to denature. Then each cycle consisted of denaturation at 95°C for 30 s and annealing/extension at 60°C for 30 s. GAPDH was used as an endogenous control to normalize each sample. The primers are listed in Supporting Information Table 1.

RNA-sequencing analysis

The RNA-seq reads were mapped to the human reference genome version hg19 using TopHat (version 2.0.12) default parameters.[15] The human reference gene set (RefSeq gene) was downloaded from https://www.ncbi.nlm.nih.gov/refseq/rsg/. Cuffdiff (v2.0.12) was used to calculate gene expression level and the significance of differential expression based on the classic-FPKM using default parameters.[16] We used p value<0.05 as a threshold to select differentially expressed genes. For clustering analysis, we used hierarchical clustering method with Spearman correlation distance to cluster samples based on the

log scaled FPKM, and used MORPHEUS (https://software.broadinstitute.org/morpheus/) to plot the heat map. We used Fisher's exact test to calculate *p* values for significance of overlapping between two groups of genes. Gene set enrichment analysis (GSEA) was applied to assess the significance of associations between AR target genes and genes affected by astemizole treatment or EZH2 knockdown.[17] To compare the expression level of EZH1 and EZH2, gene expression data for metastatic prostate tumor was collected from the Gene Expression Omnibus (GEO) database (accession no. GSE35988). Raw expression data was downloaded as a SOFT formatted family file. The expression value is the log2 ratio of prostate tissue (test) / pooled benign prostate tissue (reference). To analyze differential expression in different prostate tumor stage, gene expression data for EZH1 and EZH2 and clinical data were obtained from The Cancer Genome Atlas (TCGA) database *via* cBioPortal (http://www.cbioportal.org). For gene expression data, the relative expression (z score) of an individual gene comparing to the gene expression distribution in a reference population was analyzed. The reference population was all tumors that are diploid for the gene in question. Two-tailed Wilcox test was used to access the significance for differential expression when two groups were compared.

Data accessibility

The GEO accession number for the RNA-seq data sets reported in this paper is GSE124268.

Cell growth assay

Cells were seeded in 96-well plates and treated at concentration gradients for 72 hr. Bioluminescence was measured to quantify cell viability using CellTiter-Glo® Luminescent Cell Viability Assay Kit (Promega) and was read on Synergy 2 Multi-Mode Reader (BioTek). The cell proliferation curve was drawn and fit by the bioluminescence to drug concentration. Half-maximum inhibitory concentration (IC50) was calculated with nonlinear fitting.

Wound healing assay

Cell migration capacities were detected using wound healing assay. C4-2 cells were plated with 80–90% confluence in 6-well plates. Wounds were created across the monolayer of cell culture using a bio-clean pipette tip. The cells were incubated in serum-free medium supplemented with 5 or 10 μM of astemizole after rinsed with PBS. Wound closure were captured at 0, 24 and 72 hr.

Boyden chamber invasion assay

Polycarbonate membrane cell culture inserts (CLS3422, Corning) were applied with Basement Membrane Matrix (Cultrex). After the matrix condensed at 37°C in cell incubator, the inserts were added with 1×10^5 of C4-2 cells in RPMI-1640 without FBS. The outside wells were added with RPMI-1640 with FBS. Astemizole or ethanol was added to keep the same concentration inside and outside of the inserts. The inserts were fixed with methanol and cells that permeated through the membrane were stained with 0.5% crystal violet. Images were captured and cell count was calculated.

Autophagy assay

C4-2 cells were seeded in 6-well plates and treated with astemizole at dose gradients for 72 hr. Cells were lysed for western blotting to detect LC3-A/B. Densitometry measurements of bands were quantitated and calculated in ImageJ. In another set of plates, autophagosome activity was detected with specific dye using an autophagy assay kit (MAK138, Sigma). The pictures were captured under fluorescence microscopy, and bioluminescence was read on Synergy 2 Multi-Mode Reader (BioTek).

Apoptosis assay

C4-2 cells were plated and treated with astemizole at dose gradients in 6 well plates for 72 hr. Apoptosis was detected using FITC annexin V apoptosis detection kit (556,547, BD Biosciences). The staining was analyzed by flow cytometry (LX200 Luminex Multiplexing Assay system).

Murine prostate tumor xenograft model

CB17SCID mice were purchased from Charles River. Animal care and conditions were followed in accordance with institutional and National Institutes of Health protocols and guidelines, and all studies were approved by Houston Methodist Institution Animal Care and Use Committee. Tumor xenograft model was induced as previously described.[18] Mice were anesthetized using 2% isoflurane (inhalation), and 2×10^6 of VCaP prostate cancer cells suspended in 100 μL of PBS with 50% Basement Membrane Matrix (Cultrex) were implanted subcutaneously into the dorsal flank on the right side of each mouse. Tumor volumes were measured by length (a), width (b) and calculated as tumor volume = $\mathrm{MIN}(a)^2 \times \mathrm{MAX}(b)/2$. For VCaP castration-resistant prostate tumor model, VCaP tumor-bearing mice were castrated when tumors grew to approximately 200–300 mm^3 in size (approximately 5 weeks after implantation of tumor cells) and once tumors started to relapse, mice were randomized and treated with vehicle or astemizole (50 $mg \cdot kg^{-1}$) daily (5 days per week), and terminated 28 days later. A total of 20 mice were utilized, with 12 mice in vehicle-treated group and 8 mice in astemizole-treated group. Body weight of mice was also monitored during the course of the study. Kaplan–Meier analysis of tumor volume doubling time was performed as previously described.[19,20]

Immunohistochemistry

Mice were sacrificed for tumor tissues. Part of tumor tissues were fixed in 10% neutral-buffered formalin, processed and embedded in paraffin. EZH2(1:1000, AR(1:600) and PSA (1:2000) staining were developed using DAB (Vector Laboratories, Burlingame, CA) followed by Hematoxylin counterstaining (Sigma, St. Louis, MO). Detection was developed by Alexa

594 nm conjugated secondary antibodies (Molecular Probes, Eugene, OR) and visualized with microscopes (Daco). The slides were scanned and then quantitated using ImageJ to determine the proportion of stained cells. The results were normalized with the vehicle control group.

Statistical analysis

No statistical method was used to predetermine sample size. Mice were assigned at random to treatment groups and, where possible, mixed among cages. There were no inclusion or exclusion criteria. Whenever possible, the investigators were blinded to group allocation during the experiments and when assessing outcomes. Experiments were repeated two to three times. Data were analyzed using Prism 6.0 software (GraphPad) and presented as mean ± SEM. The p values were assessed using a two-tailed unpaired Student's t-test or a two-way analysis of variance (ANOVA), with significance considered as follows: $*p < 0.05$; $**p < 0.01$; and $***p < 0.001$. For tumor-free mice frequency, statistics were done with log-rank (Mantel–Cox) test.

Results

EZH2 and EED directly interact with AR in prostate cancer

Our previous mass spectrometry analysis[14] indicated that Polycomb Group protein EED interacts with AR (Supporting Information Fig. 1). To confirm this finding, we performed immunoprecipitation with the anti-EED antibody, followed by immunoblot analysis using lysates from prostate cancer cell line VCaP. Two distinct anti-EED antibodies pulled down AR successfully (Fig. 1*a*). In addition, we used anti-EZH2 and anti-AR antibodies to perform immunoprecipitation in 22Rv1, C4-2, LNCaP and VCaP, and discovered that EZH2 and AR were able to pull down each other in all four AR-positive prostate cancer cell lines (Fig. 1*b*).

AR has three functional domains: N-Terminal Domain (NTD), DNA Binding Domain (DBD) and Ligand Binding Domain (LBD) (Supporting Information Fig. 2). To determine which AR domain is involved in AR-EED interaction, we first overexpressed halo-tagged full-length AR (AR-FL), AR-NTD, AR-DBD and AR-LBD in HEK293T cells. Pulldown assays demonstrated that EED interacted with AR-NTD as well as AR-FL, whereas EZH2 interacted with AR-DBD and AR-FL (Fig. 1*c*).

Next, we performed *in vitro* interaction assay using the purified proteins. As expected, EED was detected to directly interact with AR and AR-NTD, and EZH2 was also detected to interact with AR-FL (Figs. 1*d* and 1*e*). Our discoveries collectively reveal the intense interaction between PRC2 and AR, which implies the significant function of PRC2 in the progression of prostate cancer.

PRC2 regulates AR and AR pathway

When we knocked down EED by EED specific shRNA packaged in lentivirus, AR and PSA were significantly decreased along with EED (Fig. 2*a*). Similarly, knocking down EZH2 by shRNA also decreased AR and PSA levels (Fig. 2*b*). To confirm that EED and EZH2 regulate AR signaling, we transfected firefly luciferase reporters, which have PSA and TMPRSS2 upstream region promoter and enhancer regions, containing AR binding sites, into EED and EZH2 stable knockdown cells. As shown in Figure 2*c*, in both LNCaP and VCaP cells, PSA and TMPRSS2 promoter activities were significantly decreased by knocking down EED or EZH2. These results collectively confirmed that PRC2 regulates the AR pathway in prostate cancer.

Astemizole, a newly identified PRC2 inhibitor, represses both EZH2 and AR

Since EZH2 and EED are found to be profoundly involved in the epigenetic aberrations of prostate cancer progression, tremendous efforts have been made to develop PRC2 inhibitors. GSK126, EPZ5687 and EPZ6438, which suppress EZH2 methyltransferase activities, were successfully developed. EED226 is a newly discovered PRC2 inhibitor, which targets the H3K27me3 binding site of EED.[21] Intriguingly, these inhibitors failed to alter AR and AR downstream targets (Fig. 3*a*). However, astemizole[22], a newly identified PRC2 inhibitor which can disrupt the EZH2-EED interaction and then induce the degradation of EED and EZH2 proteins, successfully decreased EZH2, AR and PSA levels (Fig. 3*a*). The expression levels of EZH1, a paralog of EZH2 in mammals and the other known H3K27 methyltransferase, are very weak or not detectable in prostate cancer tissues, and much lower than the levels of EZH2 in prostate cancer (Supporting Information Fig. 3a and b). Because EZH1 expression levels are not altered in prostate cancer, while EZH2 is significantly upregulated in high-grade prostate cancer tissues (Supporting Information Fig. 3c–f), we focused on investigating the effect of astemizole on EZH2 in our study. We tested astemizole in different AR-positive prostate cell lines, and similar results were observed (Figs. 3*b*–3*d*). The data suggest that EZH2 regulates AR independently of its methyltransferase activity. Moreover, astemizole is a PRC2 inhibitor with promising inhibitory effects targeting both EZH2 and AR.

Astemizole has EZH2 and AR inhibitory effects similar to EZH2 shRNA

To investigate EZH2 inhibitory effects, we performed RNA-seq for C4-2 cells treated with astemizole, GSK126 and EZH2 shRNA. We retrieved 1,571 (top 10%) genes that display the largest expression variation across these samples, and clustered the samples based on the expression values for these genes. This unbiased comparison revealed that astemizole-treated samples were the closest to the shRNA-treated samples, whereas the GSK126-treated samples had a larger distance to the shRNA-treated sample (Fig. 4*a*). We further defined genes that were up or down regulated after shRNA treatment, and found that the expression profile of these genes was closer between astemizole-treated and shRNA-treated samples than between GSK126-treated and shRNA-treated

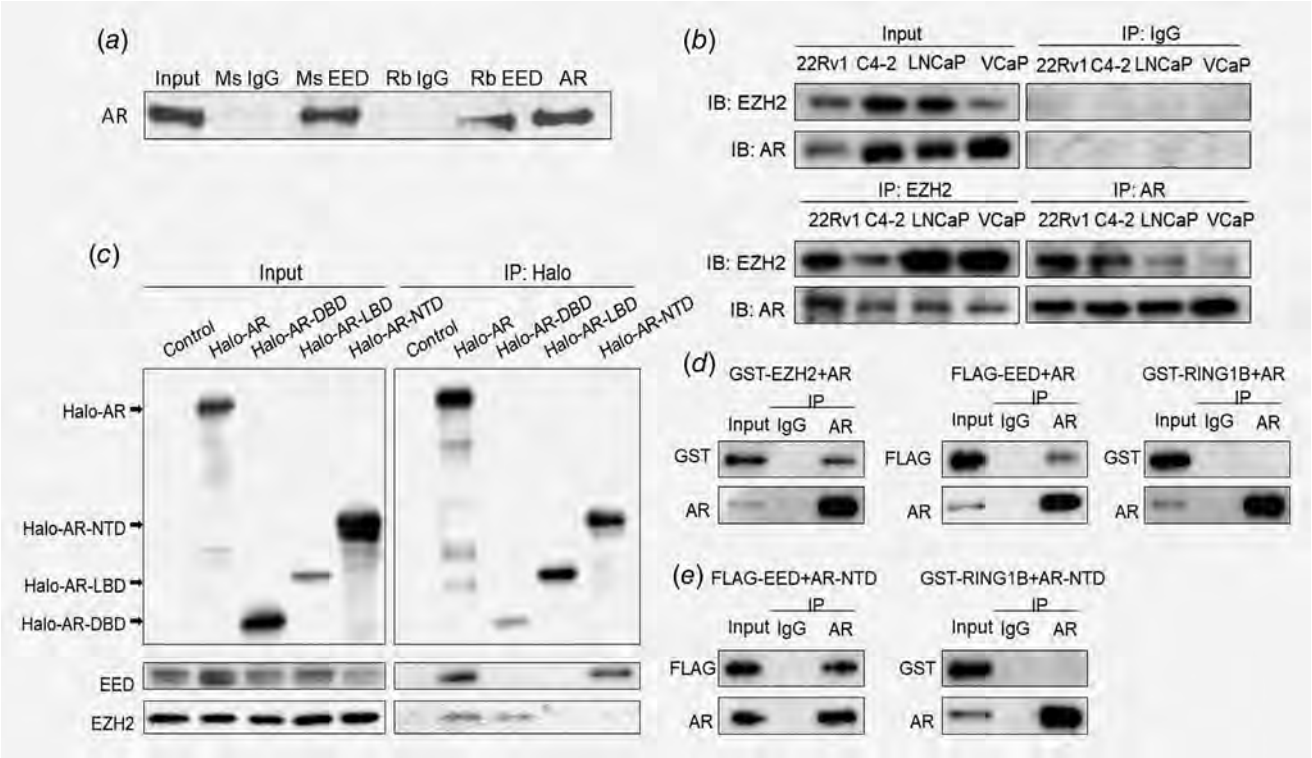

Figure 1. PRC2 protein EED and EZH2 interact with AR. (*a*) Immunoprecipitation of VCaP cell lysates with the indicated mouse monoclonal anti-EED antibody (05–1,320, Millipore), rabbit polyclonal anti-EED antibody (09–774, Millipore), control IgG and anti-AR antibody was followed by immunoblot analysis. Representative graph from at least three independent experiments is shown. (*b*) Immunoprecipitation of 22Rv1, C4-2, LNCaP and VCaP cell lysates with anti-EZH2, anti-AR antibody and control IgG was followed by immunoblot analysis. (*c*) HEK293T cells transfected with Halo-AR (full length), Halo-DBD, Halo-LBD, Halo-NTD plasmids and empty vector were lysed and subjected to pull-down assay using HaloLink resin (Promega), followed by immunoblot analysis. (*d*) Purified EZH2 and EED were respectively mixed with AR (full length) and pulled down with anti-AR antibody and protein A beads. RING1B served as a negative control. (*e*) Purified EED was mixed with AR N-terminal fragment and pulled down with anti-AR antibody and protein A beads. RING1B served as a negative control.

samples (Fig. 4*b*). We observed a 67.89% overlap of downregulated genes from the astemizole-treated and shRNA-treated C4-2 cells. Notably, the number of overlapped differential genes was significantly larger than the number of genes overlapped by chance (Fig. 4*c*), and the overlap was even more significant between astemizole-treated and shRNA-treated samples (Fisher's exact test $p < 1e\text{-}300$) than between GSK126-treated and shRNA-treated samples ($p = 1.16e\text{-}166$).

Expression changes of AR target genes in response to astemizole treatment also had a pattern analogous to that in response to EZH2 knockdown. Upon analyzing 426 AR-induced genes,[23] we found that the expression patterns of both AR upregulated and downregulated genes were similar between astemizole-treatment and EZH2-knockdown samples (Fig. 4*d*). Further, 113 AR target genes defined by another independent data resource[19] also showed similar patterns (Supporting Information Fig. 4). Manual inspection on PSA and TMPRSS2, two known downstream targets of AR, revealed that astemizole and EZH2 shRNA induced the same pattern of RNA expression change (Figs. 4*e* and 4*f*). Gene set enrichment analysis (GSEA) also confirmed that AR target genes were significantly enriched in genes downregulated by EZH2 knockdown as well as astemizole treatment. In conclusion, astemizole is a promising inhibitor of EZH2 and AR pathway (Figs. 4*g* and 4*h*).

Astemizole inhibits prostate cancer tumor growth

To further investigate if inhibiting EZH2 and AR by astemizole has any effect on the phenotypes of prostate cancer cells, we first performed cell growth assay for AR-positive prostate cancer cell lines LNCaP, VCaP, C4-2 and 22Rv1 (Fig. 5*a*, Supporting Information Fig. 5), and analyzed the antiproliferative effect of astemizole treatment at different doses. As expected, astemizole was effective on inhibiting the proliferation of each cell line at low dose (Fig. 5*a*). Next, we performed the wound healing assay for C4-2 cells and demonstrated that astemizole impaired migration capacities (Fig. 5*b*). Furthermore, we detected thwarted invasive abilities after astemizole treatment in C4-2 cells by performing Boyden Chamber invasion assay (Fig. 5*c*).

Recently, a study reported that EZH2 regulates autophagy *via* the mTOR signaling pathway and EZH2 knockdown would significantly induce autophagy.[24] We observed that the ratio of LC3-A/B-II to LC3-A/B-I was significantly elevated due to astemizole treatment (Fig. 5*d*). We also detected induced

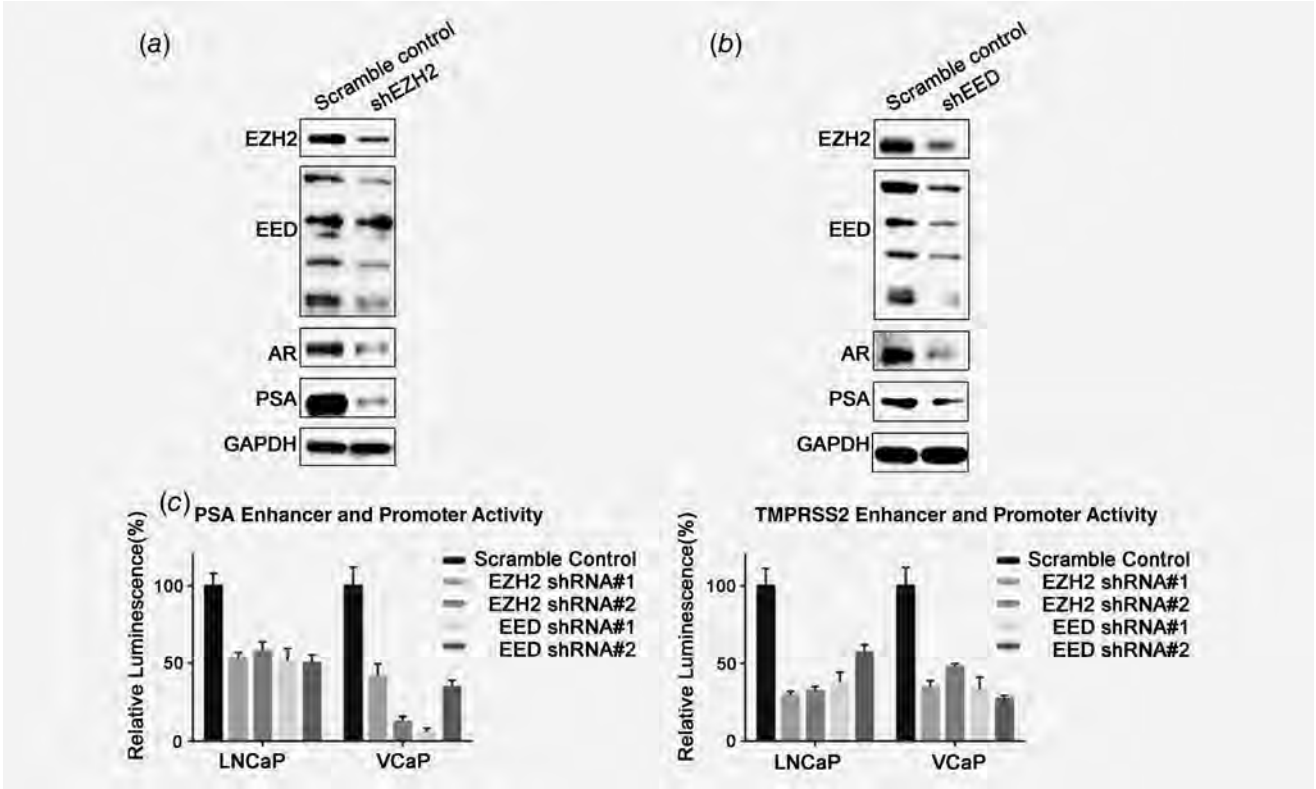

Figure 2. EZH2 and EED knockdown decreases AR and downstream targets. (*a*) EZH2 was depleted by shRNA in C4-2 cells. After 48 hr, cells were lysed and blotted by EZH2, EED (rabbit polyclonal anti-EED antibody, 09–774, Millipore), AR, PSA and GAPDH. (*b*) EED was depleted by shRNA in C4-2 cells. After 48 hr, cells were lysed and blotted by EZH2, EED (rabbit polyclonal anti-EED antibody, 09–774, Millipore), AR, PSA and GAPDH. (*c*) LNCaP and VCaP cells were subjected to cotransfection of PSA or TMPRSS2 firefly luciferase reporter constructs and pRL-TK (Renilla luciferase). Lentivirus packaged with two distinct shRNAs of EZH2 or EED were added 24 hr after the cotransfection to knockdown EZH2 or EED. The luciferase activity was normalized using Renilla bioluminescence.

autophagy by staining a proprietary fluorescent autophagosome marker and observed that astemizole treatment significantly promoted the formation of autophagosome (Supporting Information Fig. 6). These results suggest that astemizole functions as a potent EZH2 inhibitor and induces autophagy in prostate cancer cells. However, astemizole treatment did not alter induced apoptosis (Supporting Information Fig. 7), which implies autophagy might be a major phenotypic alteration as a result of astemizole treatment.

To evaluate the therapeutic efficacy of astemizole in CRPC, we utilized castration-resistant mouse xenograft models with implanted VCaP cells. We observed that astemizole significantly inhibited tumor growth when compared to vehicle treatment (Fig. 5*e* and Supporting Information Fig. 8a). The survival analysis also revealed the anti-tumor effects of astemizole (Fig. 5*f*) without effect on body weight in the mice xenograft models (Supporting Information Fig. 8b). Furthermore, we extracted protein and RNA from the harvested tumor tissue from mice xenograft models. By immunoblot analysis with anti-EZH2 and anti-AR, we found that EZH2 and AR were decreased in astemizole-treated tumors compared to vehicle-treated tumors (Fig. 5*g*). We also utilized the formalin-fixed tumor tissues assayed for immunochemistry. We observed that astemizole inhibited the expression of EZH2 and AR, which further validated that astemizole had therapeutic effects by targeting EZH2 and AR in tumor (Fig. 5*h*). Furthermore, real-time qPCR analysis showed that the well-known AR targets were also decreased by astemizole treatment in xenograft tumors (Supporting Information Fig. 9).

Collectively, our results suggest that astemizole may be repurposed as a feasible treatment for castration-resistant prostate cancer with less adverse effects.

Discussion

EZH2 and other PRC2 components are well-known transcriptional repressors that methylate H3K27 and condense chromatin conformation. We previously reported that EZH2 directly represses multiple downstream targets, including ADRB2, CDH1, rap1GAP, SLIT2 and miRNAs (miR-203, miR-200 family and miR-181 family) by binding to their promoter regions.[12,25–28] Other groups also reported that tumor suppressors, such as DAB2IP and miRNAs let-7 family, are EZH2 and PRC2 downstream targets.[29,30] The majority of previous reports suggest that EZH2 and PRC2 perform their oncogenic function by repressing these tumor suppressors. However, several groups have recently reported that EZH2

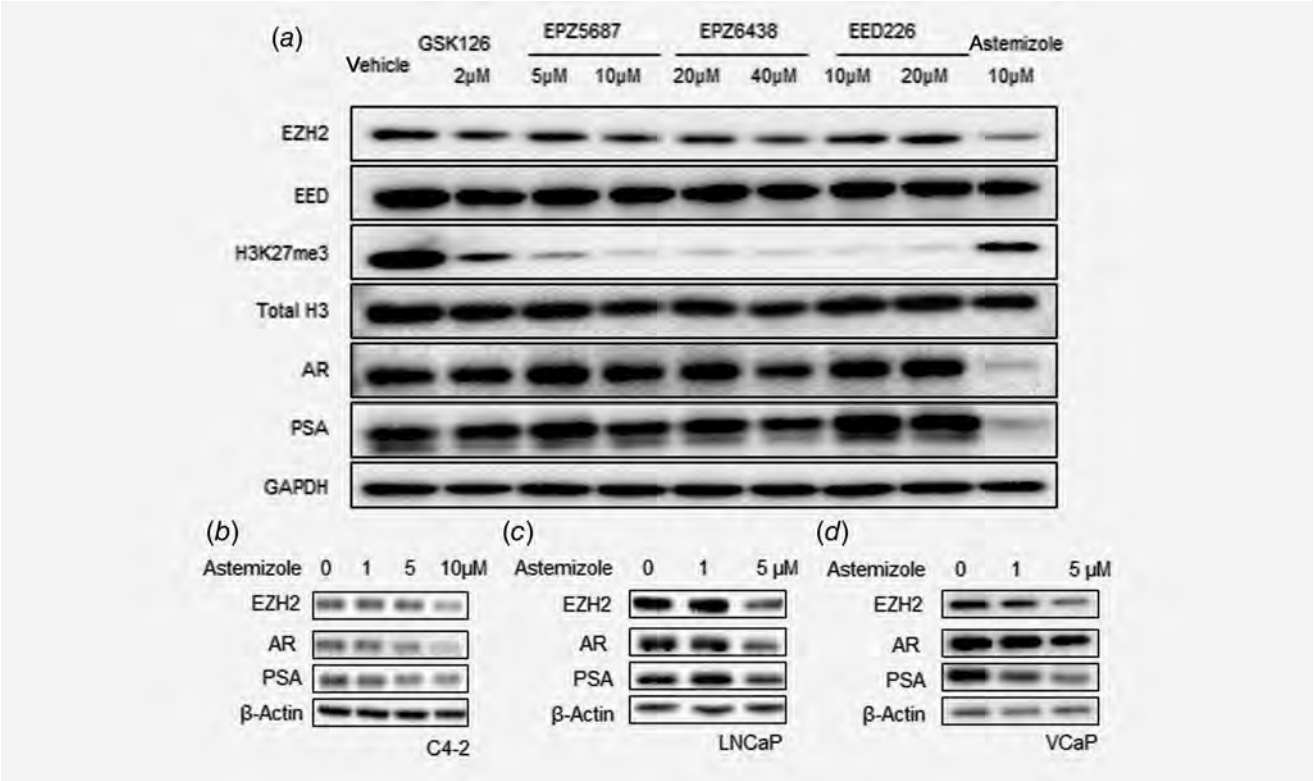

Figure 3. Astemizole functions as a better PRC2 inhibitor by degrading PRC2 and AR. (*a*) C4-2 cells were treated with GSK126 (2 μM), EPZ5687 (5 and 10 μM), EPZ6438 (20 and 40 μM), EED226 (10 and 20 μM), astemizole (10 μM) as well as vehicle and lysed for immunoblot analysis 72 hr after drug treatment. (*b-d*) C4-2, LNCaP and VCaP cells treated with astemizole at dose gradients and lysed for immunoblot analysis 72 hr after treatment.

might perform its oncogenic functions by interacting with novel binding partners, such as RELA and RELB, and regulating the NF-κB pathway, and these functions are independent of its lysine methyltransferase activities.[31] Besides histone H3, EZH2 can methylate several nonhistone proteins, including GATA4, STAT3, RORα and JARID2, and also regulates the transcriptional activities of these transcriptional factors.[32–35] In our study, we discovered that, in prostate cancer, EZH2 and EED directly interact with AR. Intriguingly, knocking down EZH2 remarkably decreased AR at both transcript and protein levels, and then reduced the expression levels of AR activated genes, such as PSA and TMPRSS2. RNA-Seq also supported the activation of AR targets *via* EZH2. Our data support the idea that in addition to functioning as a transcriptional repressor, EZH2 is also an AR coactivator and activates many downstream targets in prostate cancer.

Targeting EZH2 for advanced cancer patients has been proposed for many years. DZNep was the first discovered EZH2 inhibitor that decreases protein levels but not transcript levels.[36] However, it was demonstrated that DZNep is a pan-inhibitor for several histone lysine methyltransferases.[37] In addition, many reports showed that DZNep lacks therapeutic specificity. Since 2012, several other EZH2 inhibitors targeting its enzymatic activities have been developed by pharmaceutical companies. These EZH2 specific inhibitors successfully remove the methyl-groups from histone H3K27 at low concentrations. However, many studies revealed that targeting enzymatic activities of EZH2 failed to inhibit tumor progression of most solid tumors, except in those harboring EGFR or ARID1A mutants.[10,11] Recently, a study reported a new EZH2 inhibitor, astemizole, which could disrupt the interaction between EZH2 and EED, to degrade EZH2 proteins.[22] In our study, we compared the effects of astemizole and GSK126 in treating prostate cancer. We demonstrated that astemizole treatment could mimic the effect of knocking down EZH2 by siRNAs. Our RNA-Seq analyses revealed that most dysregulated genes by EZH2 siRNAs were also altered by astemizole treatment, but not altered by GSK126. In comparison to the enzymatic inhibitors of EZH2, only astemizole decreased EZH2 protein levels, AR and AR signaling (Fig. 4*a*). More importantly, we demonstrated that astemizole significantly inhibits the cell growth and tumor growth of CRPC, even though these tumors do not harbor previously known mutations. The EZH2 protein itself is more important than its enzymatic activity for cancer initiation and progression. Therefore, EZH2 degraders, rather than EZH2 enzyme inhibitors, are more potent for advanced cancers. Furthermore, our murine xenografts provide a rationale for repurposing the previously approved anti-histamine drug for treating CRPC patients, for which there is a pressing need to develop more

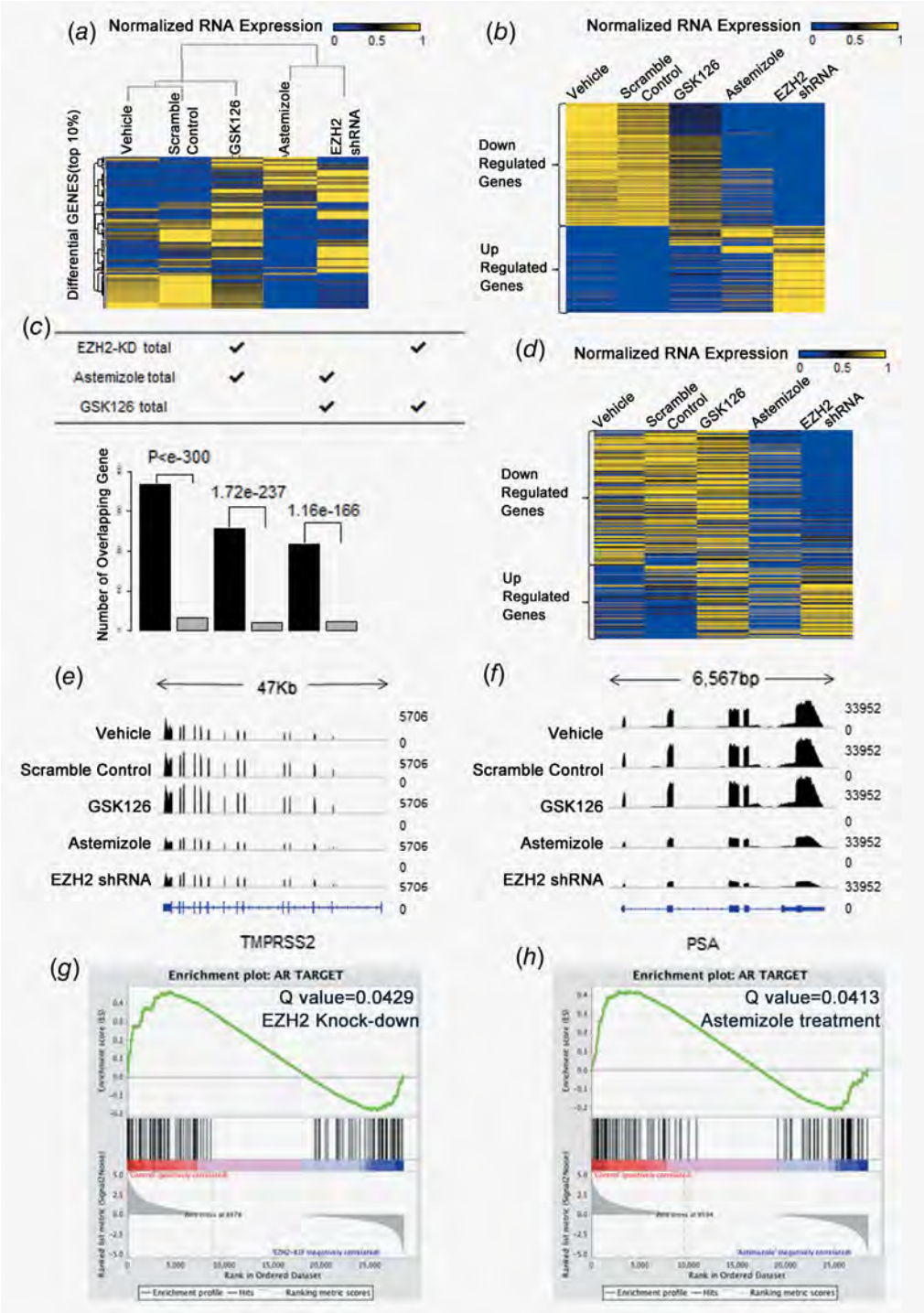

Figure 4. EZH2 knockdown and astemizole treatment demonstrate similar inhibition patterns of AR signaling blockage.(*a*) EZH2 knockdown and astemizole-treated samples cluster together based on log expression of 1,571 (top 10%) high variation genes. (*b*) Heat maps for the expression level of genes down- or up-regulated by EZH2 knockdown, GSK126 and astemizole treatment. (*c*) The number of overlapped differential genes in each paired group is significantly larger than the number of genes overlapped by chance. (*d*) 426 AR-induced genes were compared and the expression is similar between EZH2 knockdown and astemizole-treated samples. (*e*) Comparison of PSA gene track between groups. (*f*) Comparison of PSA gene track between groups. (*g*) GSEA shows that AR target genes are significantly enriched (Q value = 0.0429) in downregulated genes due to EZH2 knockdown. (*h*) GSEA shows that AR target genes are significantly enriched (Q value = 0.0413) in downregulated genes due to astemizole treatment. [Color figure can be viewed at wileyonlinelibrary.com]

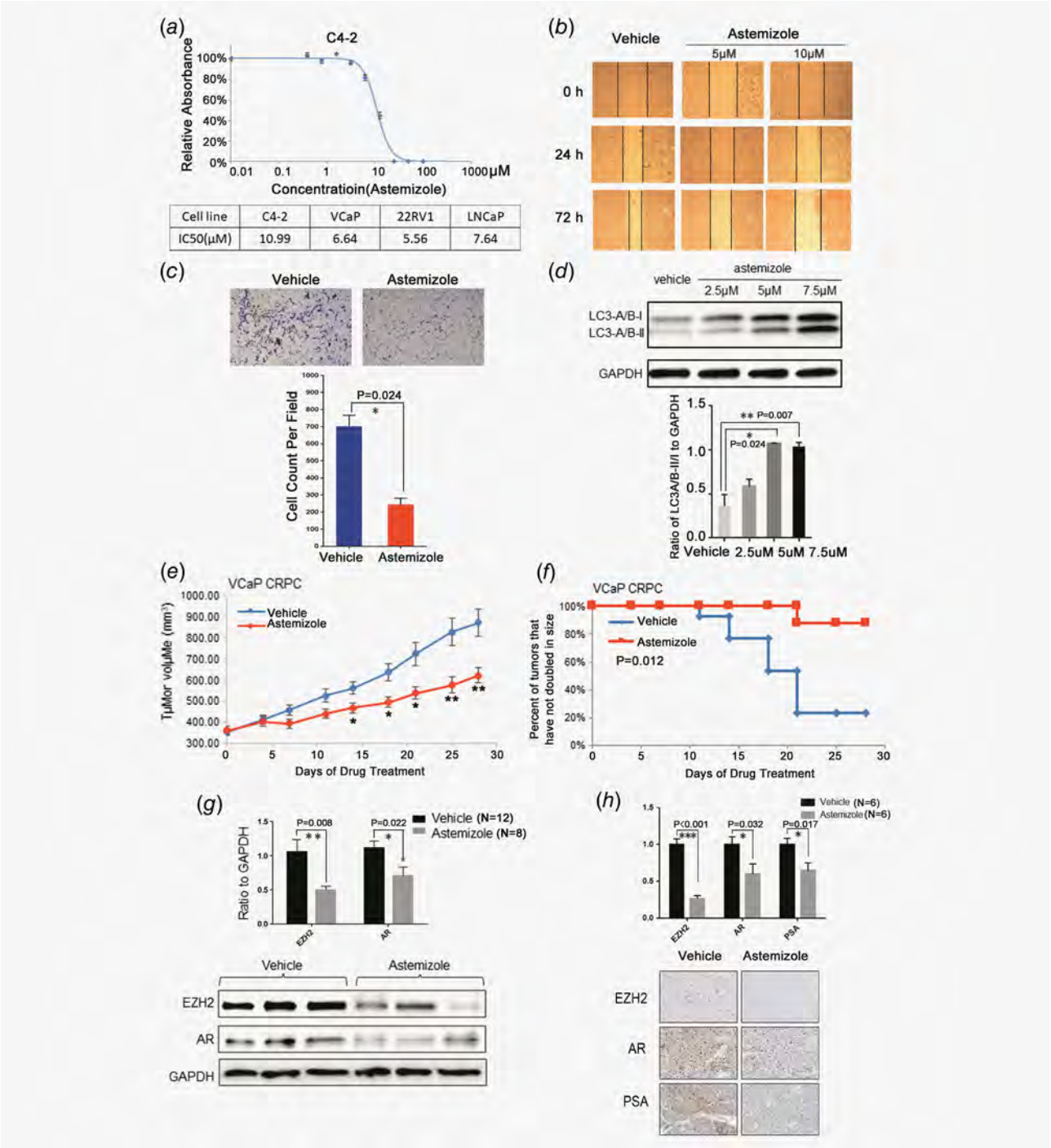

Figure 5. Astemizole has potent therapeutic effects on prostate cancer. (*a*) Astemizole critically thwarts cell proliferation in C4-2 and other AR-positive prostate cancer cell lines. (*b*) The wound healing assay indicates that astemizole compromises the migration of C4-2 cells. (*c*) Astemizole decreases the invasive abilities of C4-2 cells compared to vehicle treatment. Cell count was analyzed and the difference was statistically significant. (*d*) C4-2 cells were treated with 2.5 , 5 and 7.5 μM of astemizole. Cells were lysed 48 hr after treatment and blotted with anti-LC3-A/B antibody. The ratio of LC3-A/B-II/I to GAPDH was elevated as dose increased, which indicates that astemizole induces autophagy in prostate cancer cells. (*e*) Castration-resistant VCaP xenograft mouse models were generated. Castrated mice bearing CPRC xenografts received vehicle or astemizole treatment (50 $mg \cdot kg^{-1}$) daily (5 days per week). Caliper measurements were taken every 4 days to determine tumor volume. Mean tumor volume ± SEM, $*p < 0.05$, $**p < 0.01$ *vs.* vehicle was marked. (*f*) Kaplan–Meier survival plot compares progression-free survival. (*g*) Upper panel: Proteins were blotted and quantitated to compare the protein levels of EZH2 and AR in astemizole-treated group (n = 8) compared to vehicle-treated group (n = 12). Lower panel: The expression of EZH2 and AR was decreased in response to astemizole treatment. (*h*) The proportion of the cells stained with EZH2/AR/PSA in astemizole-treated group (n = 6) were significantly lower than that in vehicle-treated group (n = 6). [Color figure can be viewed at wileyonlinelibrary.com]

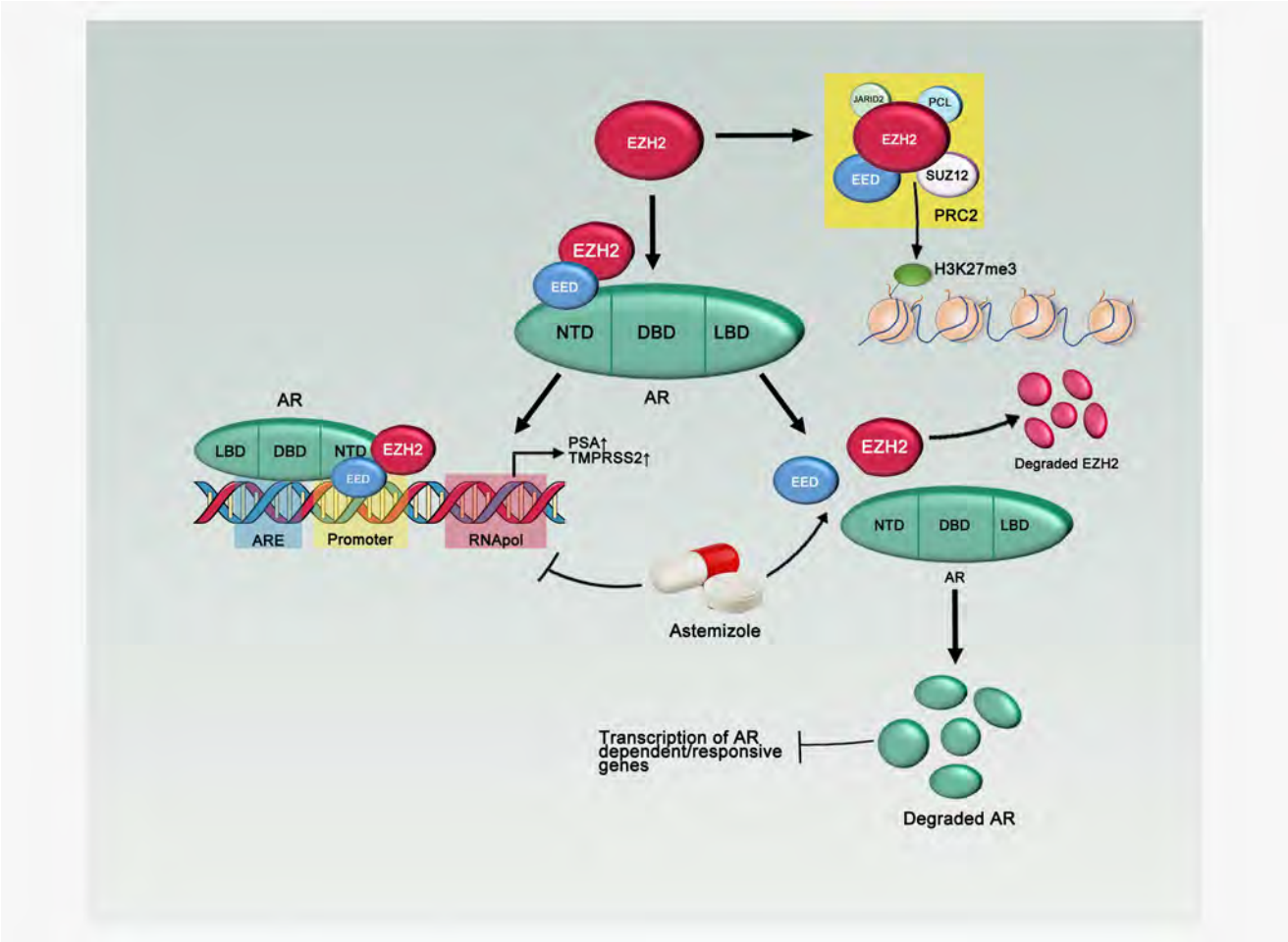

Figure 6. Model for the regulation of EZH2/EED on androgen receptor. EZH2 and EED directly bind to AR and regulate its downstream targets. Astemizole is a newly identified PRC2 disruptor, which degrades EZH2 and AR. [Color figure can be viewed at wileyonlinelibrary.com]

treatment options. For CRPC patients resistant to available anti-AR and/or anti-androgen drugs, astemizole could be one of the available last options.

Acknowledgements

We appreciate the strong support from Dr. Anastasia K. Yocum, Dr. Leland W. Chang and Dr. J. Chad Brenner. We thank Johnique T. Atkins for comments and editing our study. We appreciate the support from Dr. Bella Shmaltsuyeva and Dr. Shanshan Zhang from Pathology Core Facility of Northwestern University.

Houston Methodist Research Institute, Prostate Cancer Foundation (13YOUN007 to Q.C.), U.S. Department of Defense (W81XWH-15-1-0639 and W81XWH-17-1-0357 to Q.C.), American Cancer Society (TBE-128382 to Q.C.), and NIH/NCI (R01CA208257 to Q.C.); K.C. is supported in part by grants from NIH/NHLBI (R01CA208257, HL100397 and HL099997) and Department of Defense (W81XWH-17-1-0357);

Authors' contributions

Q.Liu and Q.C. conceived and designed the research. Q.Liu performed a majority of experiments with assistance from W.J., Q.Li, J-S.K., R.W., S.Z., X.W., L.Y., Y.Y, L.Z., Q.M., C.L., Y.Q., Y.L., D.B.G and A.M.C; W.J., R.W., S.Z., L.Y. and Q.Liu performed mouse xenograft studies. G.W. and K.C. performed bioinformatics analysis with input from Q. Liu and Q.C.; Q. Liu, Q. Li and Q.C. contributed to the writing of the study with information from G.W. and K.C.. All authors discussed the results and commented on the study.

References

1. Siegel RL, Miller KD, Jemal A. Cancer statistics, 2018. *CA Cancer J Clin* 2018;68:7–30.
2. Rathkopf D, Scher HI. Androgen receptor antagonists in castration-resistant prostate cancer. *Cancer J* 2013; 19:43–9.
3. Czermin B, Melfi R, McCabe D, et al. Drosophila enhancer of Zeste/ESC complexes have a histone H3 methyltransferase activity that marks chromosomal Polycomb sites. *Cell* 2002; 111:185–96.
4. Montgomery ND, Yee D, Chen A, et al. The murine polycomb group protein Eed is required for global histone H3 lysine-27 methylation. *Curr Biol* 2005;15:942–7.
5. McCabe MT, Ott HM, Ganji G, et al. EZH2 inhibition as a therapeutic strategy for lymphoma with EZH2-activating mutations. *Nature* 2012;492:108–12.
6. Knutson SK, Wigle TJ, Warholic NM, et al. A selective inhibitor of EZH2 blocks H3K27 methylation and kills mutant lymphoma cells. *Nat Chem Biol* 2012;8:890–6.

7. Knutson SK, Warholic NM, Wigle TJ, et al. Durable tumor regression in genetically altered malignant rhabdoid tumors by inhibition of methyltransferase EZH2. *Proc Natl Acad Sci USA* 2013;110:7922–7.
8. Qi W, Chan H, Teng L, et al. Selective inhibition of Ezh2 by a small molecule inhibitor blocks tumor cells proliferation. *Proc Natl Acad Sci USA* 2012;109:21360–5.
9. Yap DB, Chu J, Berg T, et al. Somatic mutations at EZH2 Y641 act dominantly through a mechanism of selectively altered PRC2 catalytic activity, to increase H3K27 trimethylation. *Blood* 2011;117:2451–9.
10. Fillmore CM, Xu C, Desai PT, et al. EZH2 inhibition sensitizes BRG1 and EGFR mutant lung tumours to TopoII inhibitors. *Nature* 2015;520:239–42.
11. Bitler BG, Aird KM, Garipov A, et al. Synthetic lethality by targeting EZH2 methyltransferase activity in ARID1A-mutated cancers. *Nat Med* 2015;21:231–8.
12. Yu J, Yu J, Mani RS, et al. An integrated network of androgen receptor, polycomb, and TMPRSS2-ERG gene fusions in prostate cancer progression. *Cancer Cell* 2010;17:443–54.
13. Xu K, Wu ZJ, Groner AC, et al. EZH2 oncogenic activity in castration-resistant prostate cancer cells is Polycomb-independent. *Science* 2012;338: 1465–9.
14. Cao Q, Wang X, Zhao M, et al. The central role of EED in the orchestration of polycomb group complexes. *Nat Commun* 2014;5:3127.
15. Trapnell C, Pachter L, Salzberg SL. TopHat: discovering splice junctions with RNA-Seq. *Bioinformatics* 2009;25:1105–11.
16. Trapnell C, Hendrickson DG, Sauvageau M, et al. Differential analysis of gene regulation at transcript resolution with RNA-seq. *Nat Biotechnol* 2013;31:46–53.
17. Liu YC, Morley M, Brandimarto J, et al. RNA-Seq identifies novel myocardial gene expression signatures of heart failure. *Genomics* 2015;105:83–9.
18. Asangani IA, Dommeti VL, Wang X, et al. Therapeutic targeting of BET bromodomain proteins in castration-resistant prostate cancer. *Nature* 2014; 510:278–82.
19. Zhu S, Zhao D, Yan L, et al. BMI1 regulates androgen receptor in prostate cancer independently of the polycomb repressive complex 1. *Nat Commun* 2018;9:500.
20. Speers C, Zhao SG, Kothari V, et al. Maternal embryonic Leucine zipper kinase (MELK) as a novel mediator and biomarker of Radioresistance in human breast cancer. *Clin Cancer Res* 2016;22: 5864–75.
21. Qi W, Zhao K, Gu J, et al. An allosteric PRC2 inhibitor targeting the H3K27me3 binding pocket of EED. *Nat Chem Biol* 2017;13:381–8.
22. Kong X, Chen L, Jiao L, et al. Astemizole arrests the proliferation of cancer cells by disrupting the EZH2-EED interaction of polycomb repressive complex 2. *J Med Chem* 2014;57:9512–21.
23. Zhao JC, Yu J, Runkle C, et al. Cooperation between Polycomb and androgen receptor during oncogenic transformation. *Genome Res* 2012;22: 322–31.
24. Wei FZ, Cao Z, Wang X, et al. Epigenetic regulation of autophagy by the methyltransferase EZH2 through an MTOR-dependent pathway. *Autophagy* 2015;11:2309–22.
25. Cao Q, Yu J, Dhanasekaran SM, et al. Repression of E-cadherin by the polycomb group protein EZH2 in cancer. *Oncogene* 2008;27:7274–84.
26. Yu J, Cao Q, Yu J, et al. The neuronal repellent SLIT2 is a target for repression by EZH2 in prostate cancer. *Oncogene* 2010;29:5370–80.
27. Cao Q, Mani RS, Ateeq B, et al. Coordinated regulation of polycomb group complexes through microRNAs in cancer. *Cancer Cell* 2011;20: 187–99.
28. Banerjee R, Mani RS, Russo N, et al. The tumor suppressor gene rap1GAP is silenced by miR-101-mediated EZH2 overexpression in invasive squamous cell carcinoma. *Oncogene* 2011;30: 4339–49.
29. Chen H, Tu SW, Hsieh JT. Down-regulation of human DAB2IP gene expression mediated by polycomb Ezh2 complex and histone deacetylase in prostate cancer. *J Biol Chem* 2005;280: 22437–44.
30. Kong D, Heath E, Chen W, et al. Loss of let-7 upregulates EZH2 in prostate cancer consistent with the acquisition of cancer stem cell signatures that are attenuated by BR-DIM. *PLoS One* 2012;7: e33729.
31. Lee ST, Li Z, Wu Z, et al. Context-specific regulation of NF-kappaB target gene expression by EZH2 in breast cancers. *Mol Cell* 2011;43: 798–810.
32. He A, Shen X, Ma Q, et al. PRC2 directly methylates GATA4 and represses its transcriptional activity. *Genes Dev* 2012;26:37–42.
33. Kim E, Kim M, Woo DH, et al. Phosphorylation of EZH2 activates STAT3 signaling via STAT3 methylation and promotes tumorigenicity of glioblastoma stem-like cells. *Cancer Cell* 2013;23: 839–52.
34. Lee JM, Lee JS, Kim H, et al. EZH2 generates a methyl degron that is recognized by the DCAF1/DDB1/CUL4 E3 ubiquitin ligase complex. *Mol Cell* 2012;48:572–86.
35. Sanulli S, Justin N, Teissandier A, et al. Jarid2 methylation via the PRC2 complex regulates H3K27me3 deposition during cell differentiation. *Mol Cell* 2015;57:769–83.
36. Tan J, Yang X, Zhuang L, et al. Pharmacologic disruption of Polycomb-repressive complex 2-mediated gene repression selectively induces apoptosis in cancer cells. *Genes Dev* 2007;21: 1050–63.
37. Miranda TB, Cortez CC, Yoo CB, et al. DZNep is a global histone methylation inhibitor that reactivates developmental genes not silenced by DNA methylation. *Mol Cancer Ther* 2009;8:1579–88.

Oncogene
https://doi.org/10.1038/s41388-019-0902-7

ARTICLE

Epigenetic loss of AOX1 expression via EZH2 leads to metabolic deregulations and promotes bladder cancer progression

Venkatrao Vantaku[1] · Vasanta Putluri[2] · David A. Bader[1] · Suman Maity[3] · Jing Ma[4] · James M. Arnold[5] · Kimal Rajapakshe[1] · Sri Ramya Donepudi[2] · Friedrich-Carl von Rundstedt[6,7] · Vaishnavi Devarakonda[8] · Julien Dubrulle[1,2] · Balasubramanyam Karanam[9] · Sean E. McGuire[1] · Fabio Stossi[1,2] · Abhinav K. Jain[10] · Cristian Coarfa[1,2] · Qi Cao[11] · Andrew G. Sikora[2,12] · Hugo Villanueva[2,12] · Shyam M. Kavuri[8] · Yair Lotan[13] · Arun Sreekumar[1,2,5] · Nagireddy Putluri[1,2]

Received: 4 March 2019 / Revised: 4 April 2019 / Accepted: 5 April 2019

Abstract

Advanced Bladder Cancer (BLCA) remains a clinical challenge that lacks effective therapeutic measures. Here, we show that distinct, stage-wise metabolic alterations in BLCA are associated with the loss of function of aldehyde oxidase (AOX1). AOX1 associated metabolites have a high predictive value for advanced BLCA and our findings demonstrate that AOX1 is epigenetically silenced during BLCA progression by the methyltransferase activity of EZH2. Knockdown (KD) of AOX1 in normal bladder epithelial cells re-wires the tryptophan-kynurenine pathway resulting in elevated NADP levels which may increase metabolic flux through the pentose phosphate (PPP) pathway, enabling increased nucleotide synthesis, and promoting cell invasion. Inhibition of NADP synthesis rescues the metabolic effects of AOX1 KD. Ectopic AOX1 expression decreases NADP production, PPP flux and nucleotide synthesis, while decreasing invasion in cell line models and suppressing growth in tumor xenografts. Further gain and loss of AOX1 confirm the EZH2-dependent activation, metabolic deregulation, and tumor growth in BLCA. Our findings highlight the therapeutic potential of AOX1 and provide a basis for the development of prognostic markers for advanced BLCA.

These authors contributed equally: Venkatrao Vantaku, Vasanta Putluri

Supplementary information The online version of this article (https://doi.org/10.1038/s41388-019-0902-7) contains supplementary material, which is available to authorized users.

✉ Nagireddy Putluri
putluri@bcm.edu

[1] Department of Molecular and Cellular Biology, Baylor College of Medicine, Houston, TX, USA

[2] Dan L. Duncan Cancer Center, Advanced Technology Core, Alkek Center for Molecular Discovery, Baylor College of Medicine, Houston, TX, USA

[3] Department of Biostatistics, School of Public Health, University of Texas, Houston, TX, USA

[4] Fred Hutchinson Cancer Research Center, Division of Public Health Sciences, Seattle, WA, USA

[5] Verna and Marrs McLean Department of Biochemistry and Molecular Biology, Baylor College of Medicine, Houston, TX, USA

[6] Scott Department of Urology, Baylor College of Medicine, Houston, TX, USA

[7] Department of Urology, Jena University Hospital, Friedrich-Schiller-University, Jena, Germany

[8] Lester and Sue Smith Breast Center, Baylor College of Medicine, Houston, TX, USA

[9] Department of Biology and Center for Cancer Research, Tuskegee University, Tuskegee, AL, USA

[10] Center for Cancer Epigenetics, Department of Epigenetics and Molecular Carcinogenesis, The University of Texas M. D. Anderson Cancer Center, Houston, TX, USA

[11] Center for Inflammation and Epigenetics, Institute for Academic Medicine Houston Methodist Research Institute, Houston, TX, USA

[12] Department of Otolaryngology-Head & Neck Surgery, Baylor College of Medicine, Houston, TX, USA

[13] Department of Urology, University of Texas Southwestern, Dallas, TX, USA

Introduction

Urinary bladder cancer (BLCA) is the ninth most common cancer worldwide and is more prevalent in men [1]. The

Published online: 05 August 2019

American Cancer Society estimated about 81,190 new cases of bladder cancer and about 17,240 deaths from bladder cancer occurred in the United States in 2018 [2]. Low-grade tumors are generally noninvasive and carry a low risk of progression though disease recurrence is frequent. However, high-grade papillary tumors and carcinoma in situ are associated with a high risk of recurrence and disease progression, warranting close surveillance and intravesical therapy. Monitoring and repeated treatment, accounts for the relatively high cost of BLCA management compared to other cancers [3]. Molecular studies of non-muscle-invasive urothelial carcinoma of the bladder (NMIBC) have clearly shown the effects of genomic instability, chromosomal alterations, and allelic loss on the development and progression of BLCA [4, 5]. However, the metabolic changes associated with these genetic aberrations remain unknown. Here, we aimed to understand the potential metabolic dysregulations resulting from chromatin alterations that trigger the advanced bladder carcinogenesis.

Aldehyde oxidase 1 (AOX1) is a phase I xenobiotic enzyme that belongs to the xanthine oxidase family of cytosolic molybdoenzymes [6, 7]. AOX1 plays an important role in xenobiotic and drug metabolism by catalyzing the oxidation of endogenous and exogenous aldehydes and aromatic N-heterocycles [8]. Previous metabolomic analyses have shown altered patterns in phase I/II metabolism and the adverse effects of methylation-driven gene silencing on xenobiotic metabolism in BLCA tissues [9]. Promoter hypermethylation is a common mechanism for transcriptional silencing of tumor suppressor genes, such as *RB1* and *p16INK4A* [10–12]. Enhancer of Zeste homolog 2 (EZH2), an enzymatic subunit of the polycomb repressive complex 2 (PRC2), catalyzes methylation to induce chromatin compaction and transcriptional silencing [13]. Consistent with its previously known function as an epigenetic silencer in tumorigenesis and tumor progression [14], we sought to examine the role of EZH2 in *AOX1* silencing during BLCA progression.

In this study, we show that *AOX1* is epigenetically silenced by EZH2-mediated chromatin alterations in its promoter. Loss of AOX1 resulted in distinct metabolic alterations that are highly predictive of the different stages of BLCA progression. In normal bladder epithelial cells, knockdown of AOX1 led to the activation of the tryptophan-kynurenine pathway. This resulted in elevated nicotinamide-adenine dinucleotide phosphate (NADP) levels, which enhanced carbon flux via the pentose phosphate pathway (PPP), nucleotide synthesis and cell invasion. Ectopic expression of AOX1 in cancer cells resulted in decreased PPP metabolic flux, cell invasion, and nucleotide synthesis. Also, ectopic AOX1 expression reduced tumor xenograft growth in mice, possibly via a reduction in nucleotide synthesis. Together, our findings suggest a novel oncogenic role for AOX1 in BLCA progression, suggest a metabolic basis for early tumor detection, and targeted therapies for BLCA.

Results

Detection of stage-specific metabolic alterations and risk prediction of BLCA tissues

To identify key altered metabolic pathways at different stages of BLCA, we analyzed metabolomic data collected from BLCA tissue samples obtained from the University of Texas Southwestern Medical Center, Dallas (clinical information in Supplementary Table 1). A total of 94 metabolites showed significantly altered levels in stages T1 to T4 compared with the Ta stage (Fig. 1a). Interestingly, a subset of the altered metabolites was associated with reactions catalyzed by AOX1 (Fig. 1a). A network-based pathway enrichment method NetGSA was [15] used to identify several enriched biochemical pathways such as nicotinamide, glycolysis, fatty acid, purine, and pyrimidine metabolism (Fig. 1b). These identified pathways were associated with several metabolic reactions catalyzed by AOX1 (Fig. 1c). Integration of metabolomics mapped genes from our study and transcriptomics from TCGA data revealed that AOX1 ranked second in the list of genes downregulated in cancer (Supplementary Fig. 2a). We analyzed the predictive power of the identified stage-specific BLCA-associated metabolites in an independent tissue cohort for validation. We used 119 tissue specimens collected at three institutions (clinical information in Supplementary Table 2). We selected a subset of seven metabolites (nicotinamide, methyl adenosine, asparagine, methyl histidine, indolacetaldehyde, tyrosine, and gentisatealdehyde) associated with AOX1 metabolic pathways and calculated the activity scores for each pathway based on Z-score transformed data. The activity score represents the likelihood that a metabolic pathway is active inside the cell and provides a basis for comparing metabolic pathway activities. A logistic regression model was used to build a classifier using activity scores derived from a training dataset comprised of two-thirds of the tissue samples ($n = 80$, randomly selected). We validated the predictive performance of the classifier by applying it to the remaining one-third of the samples ($n = 39$). The resultant receiver operating characteristic (ROC) curve was statistically significant ($p = 0.023$) with an area under curve (AUC) value of 0.689 (Fig. 1d). These results suggest AOX1-associated, stage-specific metabolites can be used as reliable prognostic markers for BLCA.

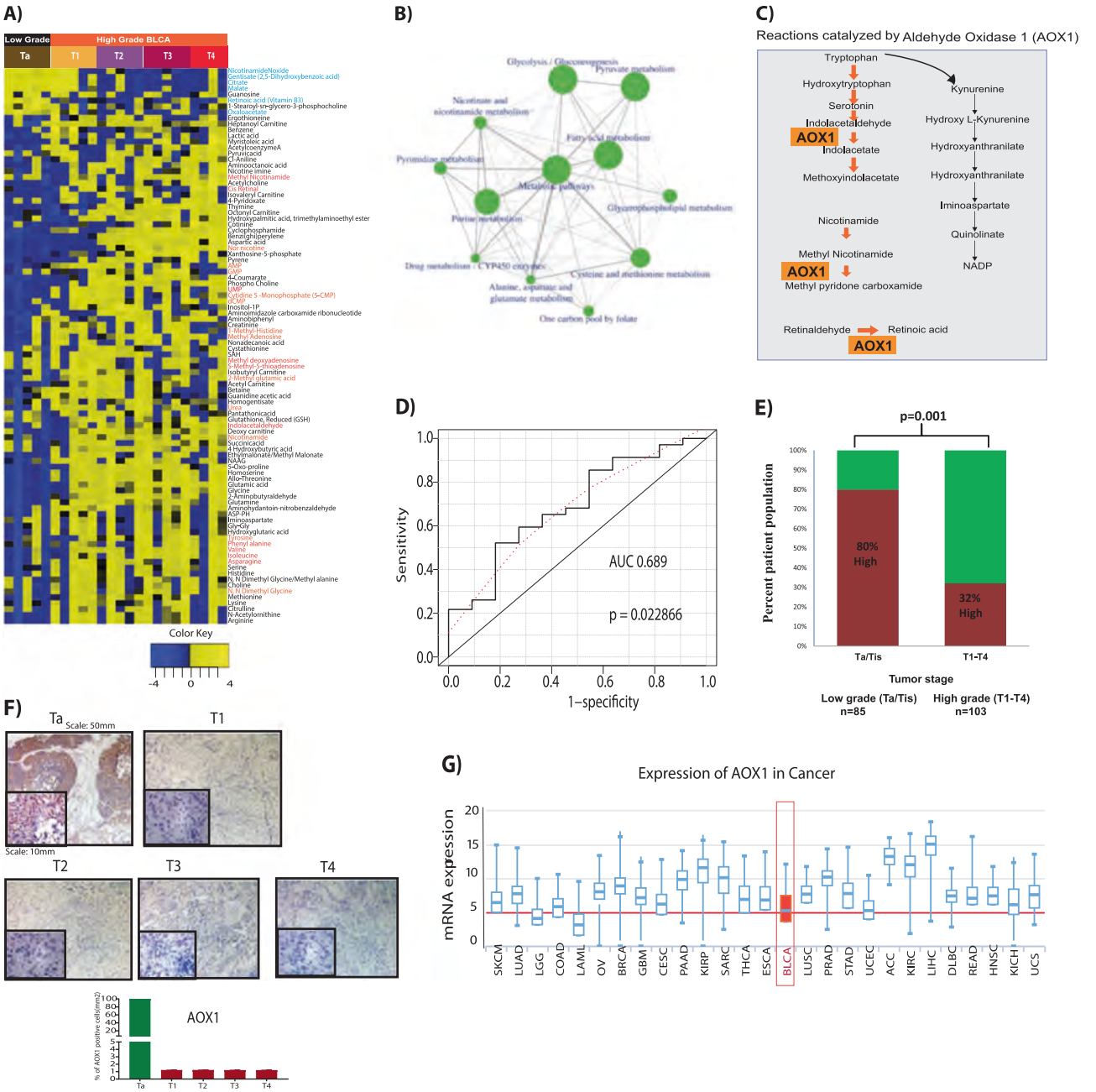

Fig. 1 Metabolic analysis of different-staged tissues, alterations in the AOX1-associated pathways and AOX1 expression in BLCA. **a** Heat map of hierarchical clustering of 95 differential metabolites from 25 BLCA tissue samples at different stages of BLCA. Columns represent individual tissue samples arranged according to BLCA stage, and rows represent distinct metabolites. Shades of yellow and blue represent higher and lower levels of metabolites, respectively, relative to the median metabolite levels (false discovery rate, FDR < 0.25). **b** Network representation of pathways (solid green colored circles: enriched pathways after integrative analysis using combined gene/metabolite-derived enrichment scores) altered in aggressive BLCA (stage Ta vs stages T1–T4). Arrow thickness correlates with the number of interacting components between two pathways. **c** Overview of metabolic pathway reactions associated with AOX1 (indicator represents exact reaction catalyzed by AOX1 in the pathway). **d** The plot describes the ROC based on the overall activity score for a select group of AOX1 associated metabolites ($n = 7$) in the logistic regression which yields a significant p-value ($p = 0.03$) with an AUC of 0.689. **e** Tissue microarray analysis of AOX1 expression comparing low-grade (Ta-Tis) and high-grade (T1-T4) BLCA. The scores of 0–3 were considered low and scores from 4 to 8 were considered high. The score represents a combination of staining intensity and percentage of tumor cells showing protein expression. **f** Representative photomicrograph of AOX1 immunostaining in stages Ta, T1, T2, T3, and T4 of BLCA. The bar graphs show relative AOX1 expression levels for the same slides. For normalization, AOX1 staining of Ta was used as 100% and AOX1 expression in other stages are shown as relative percentages. **g** Photographic representation of AOX1 mRNA expression in all cancers in TCGA dataset

AOX1 is significantly downregulated during BLCA progression

Our computational analysis suggested AOX1 may be a useful biomarker for BLCA progression. To examine this idea further, we used a tissue microarray to evaluate AOX1 expression in 188 human BLCA tissue samples at varying cancer stages. Low-grade (stages Ta and Tis) BLCA tissue specimens had higher AOX1 protein expression than high-grade (stages T1–T4) BLCA tissues (Fig. 1e). Immunohistochemical analysis also showed AOX1 downregulation in high-grade BLCA tissues (Fig. 1f). A comparison of AOX1 mRNA expression in the TCGA dataset revealed that BLCA had the lowest AOX1 mRNA expression levels across all cataloged tumors (Fig. 1g). AOX1 expression was lower in high-grade BLCA cell lines (UMUC3, J82, and T24) than low-grade RT4 BLCA cells, suggesting AOX1 expression may be lost during BLCA progression (Supplementary Fig. 1a). Analysis of data from public BLCA cohorts (Kim [16], TCGA [17], Sanchez [18]) showed significantly lower expression of AOX1 in cancerous tissue compared with normal bladder tissue (Supplementary Fig. 2b, c). Moreover, analysis of AOX1-associated substrate metabolites (Supplementary Fig. 3a) and product metabolites (Supplementary Fig. 3b) coupled with the AOX1 expression pattern suggest AOX1 levels decrease during BLCA progression.

AOX1 is silenced by EZH2

To determine if AOX1 loss during BLCA progression is controlled by epigenetic regulation, we treated UMUC3 cells with methyltransferase inhibitors, 5-aza-2′-deoxycytidine (AZA) and Adenosine dialdehyde (Adox). Both AZA and Adox treatments resulted in increased mRNA and protein expression of AOX1. Treatment of UMUC3 cells with Trichostatin A, a histone deacetylase inhibitor, had no effect (Fig. 2a and Supplementary Fig. 4a), suggesting AOX1 expression in these cells was suppressed by methylation. To identify the methyltransferase(s) responsible for silencing the AOX1 locus, we performed a correlation analysis of AOX1 with EZH2, DNMT1, DNMT3A, or DNMT3B, using data from public cohorts (TCGA [17], Choi [19], Kim [16], and Sanchez [18]). We observed a strong negative correlation between AOX1 and EZH2 in all cohorts (Fig. 2b, c). In addition, we found the potential methylated CpG islands at the AOX1 promotor region (Supplementary Fig. 5a) and have moderate negative correlation of DNMT3B with AOX1where as DNMT1 and DNMT3A showed no correlation with AOX1 (Supplementary Fig. 5b).

To examine the regulatory relationship between EZH2 and AOX1, we treated, UMUC3 BLCA cells, with a highly selective pharmacological EZH2 inhibitor GSK126 [20], and found the increase in AOX1 expression. (Fig. 2d). Next, we examined AOX1 and EZH2 protein expression in BLCA specimens and found that EZH2 expression increased while AOX1 expression decreased in a stage-dependent manner (Fig. 2e). Moreover, EZH2 knockdown resulted in a significant increase of AOX1 expression in UMUC3 and T24 cells (Fig. 2f, g).

EZH2 alters chromatin structure at the AOX1 promoter locus

EZH2 regulates epigenetic silencing by methylation of histone H3 on lysine 27 (H3K27) at the gene promoter locus [20] or controls DNA methylation [21]. To determine the mechanism by which EZH2 silenced AOX1 expression, we performed bisulfite sequencing and chromatin immunoprecipitation (ChIP) experiments. Stage-specific DNA from BLCA tissues were used for bisulfite conversion and pyrosequencing. We observed high levels of methylation at the AOX1 promoter locus in stage T1–T4 BLCA tissues. Methylation was absent at the AOX1 promoter locus in benign, normal, and Ta tissues (Fig. 3a). We performed ChIP assays to assess enrichment of EZH2 and H3K27me3 at the AOX1 promoter in EZH2 knockdown and GSK126-treated BLCA cells. Quantitative real-time PCR (ChIP-qPCR) was used to measure the H3K27 trimethylation and EZH2 occupancy at the AOX1 promoter locus. EZH2 levels were significantly reduced at the AOX1 promoter locus in EZH2 knockdown cells, but remained unchanged in GSK126-treated cells. However, both EZH2 knockdown and GSK126-treated BLCA cells showed a significant reduction in H3K27 trimethylation at the AOX1 promoter, which correlated with increased AOX1 expression in these cells (Fig. 3b).

Next, we examined the role of EZH2 methyltransferase activity in *AOX1* silencing. We transfected normal immortalized bladder epithelial cells (SV-HUC-1) with adenovirus constructs expressing wild type EZH2 and a mutant version of EZH2 (ΔSET) that had a truncated C-terminal SET domain and lacked methyltransferase activity [22]. SV-HUC-1 cells that expressed wild type EZH2 showed decreased AOX1 mRNA and protein levels compared with control cells. In contrast, cells expressing the ΔSET construct showed no significant decrease in AOX1 mRNA and protein levels (Fig. 3c). These results indicate EZH2 binds and methylate the *AOX1* promoter, silencing AOX1 expression (Fig. 3d).

Knockdown of AOX1 altered cell morphology and increased cell proliferation, NADP levels, glucose metabolism, and nucleotide synthesis

To examine phenotypic responses to AOX1 modulation, we introduced AOX1shRNA or control shRNA constructs into SV-HUC-1 cells. Cells with AOX1 shRNA showed significant reduction in both AOX1 mRNA and protein (Fig.

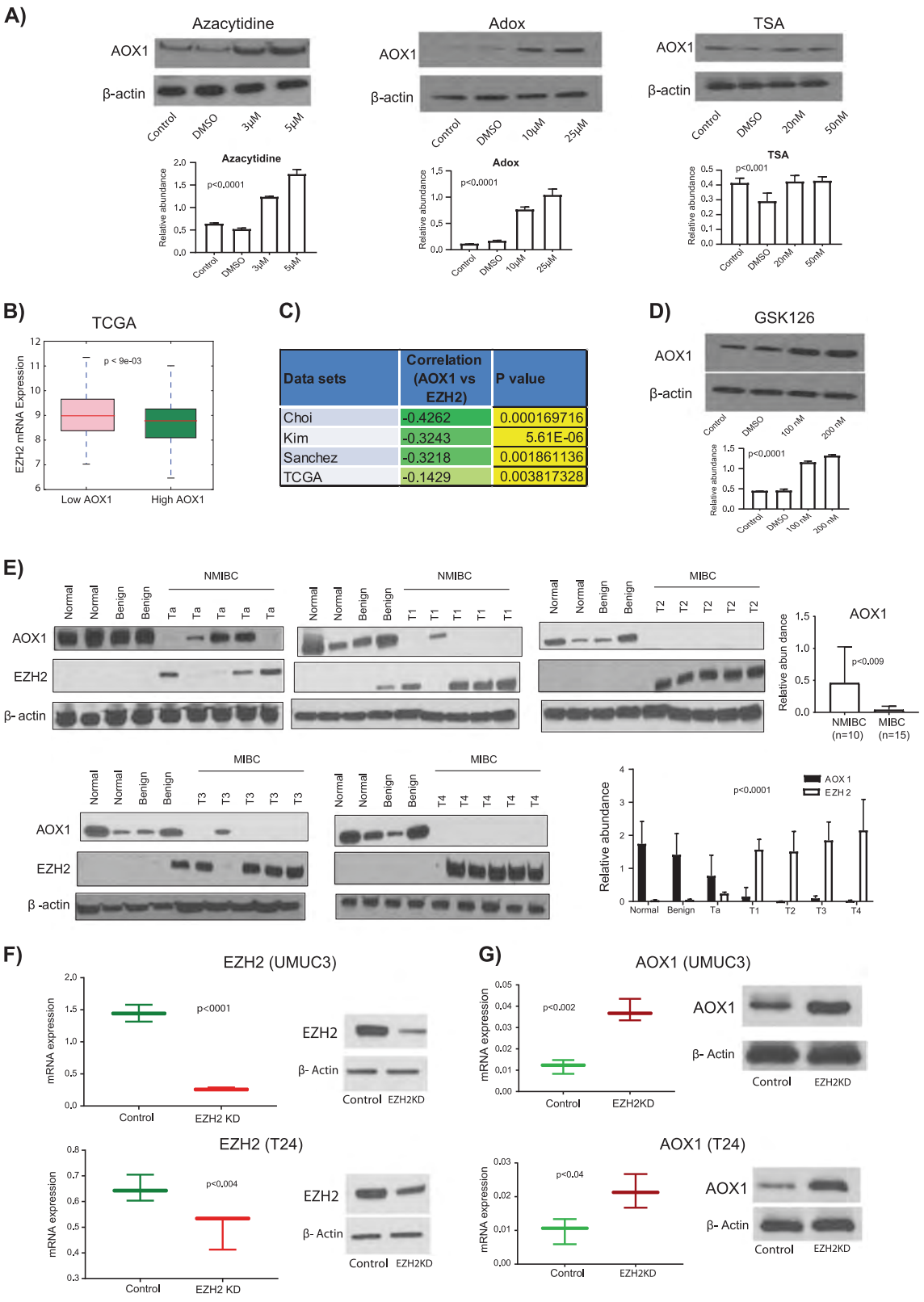

4a). AOX1 knockdown (KD) cells grew faster (Fig. 4b) and were significantly smaller (Fig. 4c) than control cells, showed altered cell growth and morphology. They also had a significantly elevated growth rate compared with control cells (Fig. 4b). Cells were labeled with Alexa 594-conjugated phalloidin and the major and minor axis

◀ **Fig. 2** EZH2-mediated suppression of AOX1 in BLCA. **a** Immunoblot analysis of AOX1 in UMUC3 cells treated with methylation and histone deacetylation inhibitors. Cells were treated with Azacitidine, Adox, and trichostatin A, respectively, for 24 h and the bar graphs show relative protein expression levels for the same blots. Protein levels were normalized using β-actin expression levels. **b** Negative correlation between AOX1 and EZH2 mRNA expression in TCGA. **c** Significant negative correlation ($p < 0.05$) between AOX1 and EZH2 mRNA expression in Choi, Kim, Sanchez, and TCGA cohorts. **d** Immunoblot analysis of AOX1 in UMUC3 cells treated with GSK126 for 24 h and the bar graphs show relative protein expression levels for the same blots. Protein levels were normalized using β-actin expression levels. **e** Immunoblot analysis of AOX1 and EZH2 at different stages of matched BLCA tissues and bar graphs show relative protein expression levels for the same blots. AOX1 quantification in NMIBC ($n = 10$) and MIBC ($n = 15$). Protein levels were normalized using β-actin expression levels. **f** qPCR and western blot of EZH2 shRNA knockdown in UMUC3 and T24. **g** qPCR and western blot of AOX1 in UMUC3 and T24 EZH2 knockdown cells. mRNA levels were normalized using GAPDH expression levels

lengths were calculated for each cell area. A significant decrease in cell size and major to minor axis length ratio was observed in AOX1 KD cells compared with control cells (Fig. 4c). A wound-healing assay to assess cell migration potential showed that the rate of wound closure was accelerated in AOX1 KD cells compared with control (Fig. 4d).

AOX1 is one of the key enzymes of tryptophan catabolism and loss of AOX1 may lead to the accumulation of kynurenine and NADP (Fig. 4e). To address this, we performed metabolomic analyses of AOX1 KD and control cells using liquid chromatography-mass spectrometry (LC-MS). AOX1 KD cells showed elevated levels of kynurenine, NADP, and a higher NADP/NADPH ratio compared with control cells (Fig. 4f). Isotropic tracing experiments with ^{15}N-labeled tryptophan demonstrated elevated levels of ^{15}N kynurenine in AOX1 KD cells (Fig. 4g) suggesting tryptophan may be shunted to the kynurenine pathway in the absence of AOX1.

We analyzed changes in the transcriptome in AOX1 KD cells by RNA sequencing and observed significant differences in levels of metabolic enzymes and epithelial-mesenchymal transition [23] markers (Fig. 4h). Metabolic flux analysis, using (U)^{13}C glucose demonstrated, enrichment of glucose derived carbon in glucose-6-phosphate (M + 6), fructose 1,6-bisphosphate (M + 6), glyceraldehyde-3-phosphate (M + 3), and lactate (M + 3) in AOX1 KD compared with control (Fig. 4i). This suggested that the glycolytic pathway was activated in the absence of AOX1. PPP metabolites such as 6-phosphogluconate (M + 6), ribulose/xylose 5-phosphate (M + 5), and sedoheptulose 7-phosphate (M + 7) were also significantly increased in AOX1 KD compared with control (Fig. 4i). However, tricarboxylic acid (TCA) metabolites such as citrate (M + 2), succinate (M + 2), and malate (M + 2) showed lower incorporation of ^{13}C (Fig. 4i), which indicated reduced flow of glucose into the TCA cycle in AOX1 KD. Nucleotide flux analysis showed a significant increase in the synthesis of adenosine monophosphate (M + 5), guanosine monophosphate (M + 5) cytidine monophosphate (M + 5), and inosine monophosphate (M + 5) in AOX1 KD (Fig. 4i). Immunoblotting assays showed elevated levels of the regulatory enzymes involved in glycolysis and PPP in AOX1 KD cells (Fig. 4j), which is consistent with the activation of glycolysis and PPP in cells without AOX1. Together, our results suggested that AOX1 played a critical role in regulating central metabolic pathways to divert glucose towards the PPP, which is a major source of intermediates for nucleotide synthesis in rapidly dividing cells.

Pharmacological inhibition of NAD synthesis rescued the metabolic effects caused by loss of AOX1

Because levels of kynurenine and NAD were elevated in the absence of AOX1, we tested whether pharmacological inhibition of NAD synthesis altered the metabolic effects caused by the loss of AOX1. NAD is predominantly synthesized via the kynurenine pathway and tryptophan 2,3-dioxygenase (TDO2) is the rate-limiting enzyme for this pathway [24]. AOX1 KD cells were treated with the TDO2 inhibitor, 680C91 [25], for 24 h. Levels of kynurenine, NAD, and PPP intermediates were measured by LC-MS (Fig. 4k). Inhibition of TDO2 resulted in decreased NAD synthesis leading to a reduction in 6-phosphogluconate and ribose/ribulose 5-phosphate in AOX1 KD cells compared with untreated AOX1 KD (Fig. 4k). These findings suggest loss of AOX1 in BLCA cells may enable increased NADP production.

Ectopic expression of AOX1 in BLCA cells affects NADP production, PPP metabolite levels, and nucleotide synthesis

To further assess the impact of AOX1 on central carbon metabolism, we ectopically expressed AOX1 in BLCA cells. UMUC3, and T24 cells were infected with adenovirus constructs expressing AOX1 (Ad-AOX1) and mRNA and protein levels were detected by western blotting and qPCR (Fig. 5a). Ectopic expression of AOX1 in BLCA cells significantly reduced the levels of kynurenine and NADP, suggesting activation of the regular tryptophan pathway (Fig. 5b). ^{15}N-labeled tryptophan flux also demonstrated decreased levels of ^{15}N kynurenine in Ad-AOX1 cells, confirmed the rewiring of the tryptophan-kynurenine pathway (Fig. 5c).

Next, we studied the effect of ectopic AOX1 expression on central carbon metabolism using U^{13}C-labeled glucose in Ad-AOX1 UMUC3 BLCA cells. Ectopic AOX1 expression resulted in a decrease in levels of the glycolytic

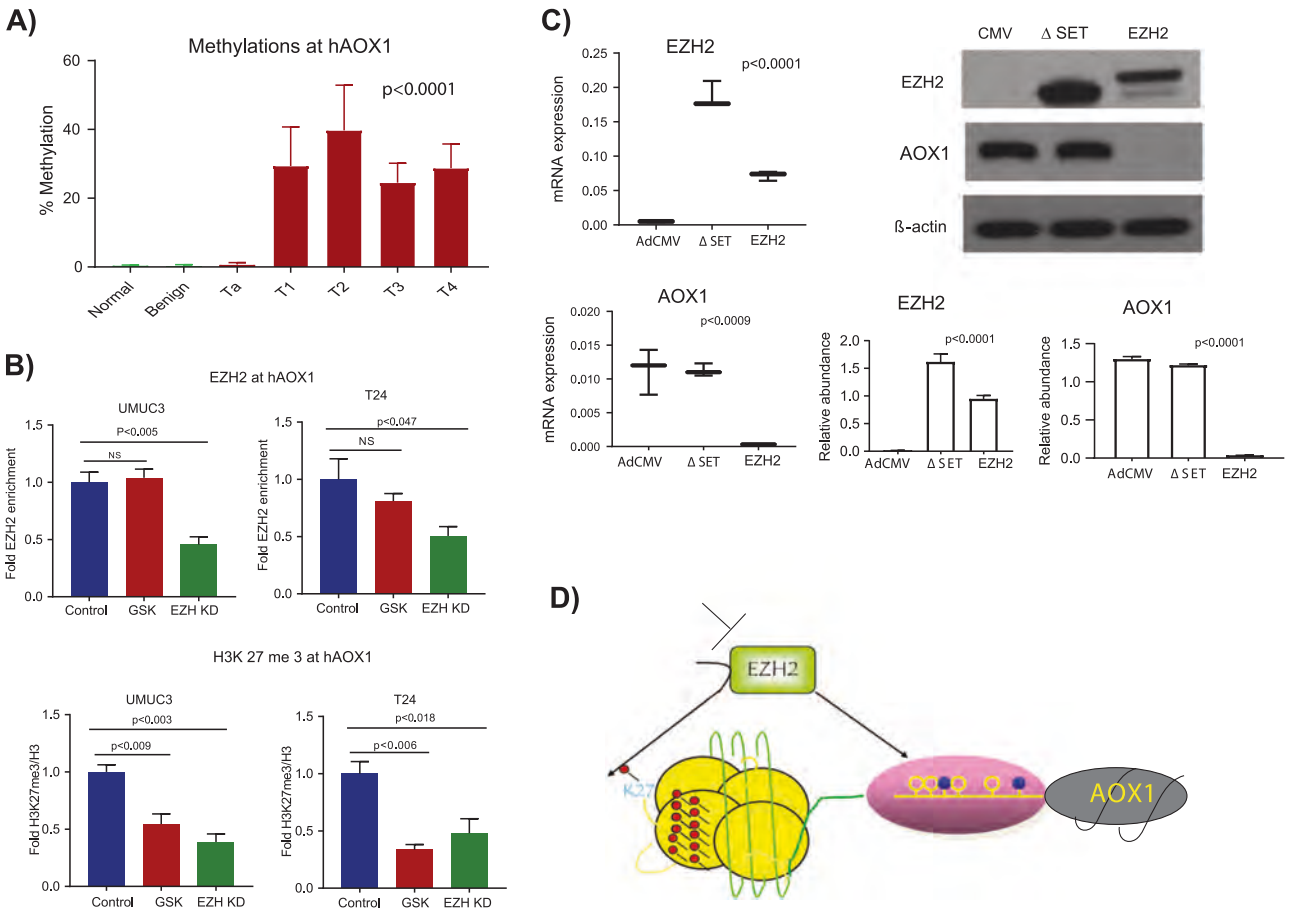

Fig. 3 EZH2-mediated hypermethylation at AOX1 promoter locus. **a** Quantification of DNA methylation using bisulfite repetitive PCR and pyrosequencing and percentage of DNA CpG methylation of the AOX1 promoter region at different stages of BLCA ($n = 4$, Normal, Benign Ta, T1, T2, T3, and T4). **b** qPCR analysis from ChIP shows significant reduction of the H3K27tri methylation at the AOX1 promoter in UMUC3 and T24 BLCA cell lines. 100 nM GSK126 reduces the H3K27 trimethylation at AOX1 promoter without affecting EZH2 levels. On the other hand, EZH2 knockdown significantly affected EZH2 occupancy and H3K27 trimethylation at the AOX1 promoter locus. EZH2 enrichment is normalized to IgG and H3K4me3/K27me3 markers are normalized to IgG and H3. **c** mRNA analysis and immunoblots of SV-HUC-1 cells infected with adenovirus encoding EZH2 or Δ SET mutant and vector adenoviruse for 48 h. Ectopic overexpression of EZH2 significantly reduces AOX1 expression but ΔSET mutant does not have effect on AOX1 expression, the bar graphs show relative protein expression levels for the same blots. Protein levels were normalized using β-actin expression levels. **d** Graphical representation of AOX1 suppression by EZH2-mediated promoter methylation

intermediates, glucose-6-phosphate (M + 6) and fructose 1,6-bisphosphate (M + 6) (Fig. 5d). However, levels of the TCA cycle intermediates, citrate (M + 2), succinate (M + 2), and malate (M + 2), were elevated (Fig. 5d), suggesting a shift in carbon metabolism toward the TCA cycle. Accordingly, levels of PPP intermediates, 6-phosphogluconate (M + 6), ribulose/xylose 5- phosphate (M + 5), and sedoheptulose 7-phosphate (M + 7) were decreased in Ad-AOX1 BLCA cells (Fig. 5d). Analysis of nucleotide flux in Ad-AOX1 BLCA cells showed decreased levels of adenosine monophosphate (M + 5), guanosine monophosphate (M + 5), cytidine monophosphate (M + 5), and inosine monophosphate (M + 5) (Fig. 5d).

To further examine the role of AOX1 in metabolic regulation of tryptophan and PPP pathways in BLCA, we compared the effect of gain and loss-of-function of AOX1 in the UMUC3 cells. UMUC3 does not natively express meaningful amounts of AOX1. Therefore, UMUC3 cells were maintain in a sub-lethal dose of GSK126 until AOX1 expression was achieved (Fig. 5e). The enzymatic activity of AOX1 was active in GSK126-treated cells as evidenced by low levels of kyneurenine, NADP and PPP pathway metabolites (Fig. 5f). In contrast, the knockdown of AOX1 under these conditions significantly increases the abundance of kynuerenine, NADP and PPP pathway metabolites (Fig. 5f), further corroborating the role of AOX1 in metabolic rewiring of tryptophan towards increased NADP synthesis. Together, these experiments suggest AOX1 plays a pivotal role in central carbon metabolism by rewiring the tryptophan metabolic pathway, which further regulates PPP pathway through NADP.

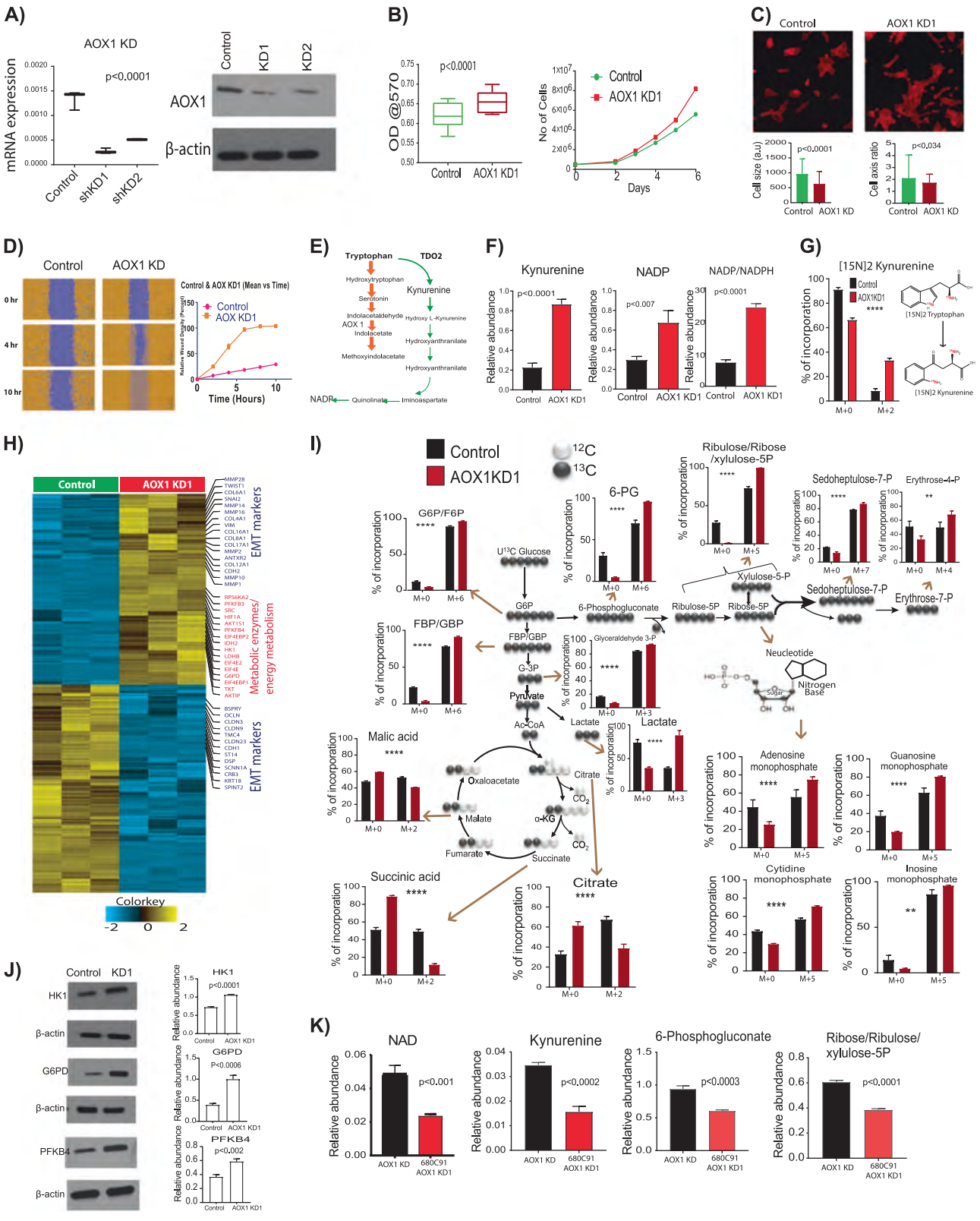
A)
AOX1 KD
mRNA expression
p<0.0001
Control
shKD1
shKD2
AOX1
β-actin
KD1
KD2
B)
OD @570
p<0.0001
Control
AOX1 KD1
No of Cells
Days
C)
Control
AOX1 KD1
Cell size (a.u)
p<0.0001
Cell axis ratio
p<0.034
D)
Control
AOX1 KD
0 hr
4 hr
10 hr
Control & AOX KD1 (Mean vs Time)
Time (Hours)
E)
Tryptophan
TDO2
Hydroxytryptophan
Kynurenine
Serotonin
Indolacetaldehyde
AOX 1
Hydroxy L-Kynurenine
Indolacetate
Hydroxyanthranilate
Methoxyindolacetate
Hydroxyanthranilate
NADP
Quinolinate
Iminoaspartate
F)
Kynurenine
NADP
NADP/NADPH
p<0.0001
p<0.007
Relative abundance
G)
[15N]2 Kynurenine
% of incorporation
[15N]2 Tryptophan
H)
Control
AOX1 KD1
EMT markers
Metabolic enzymes/
energy metabolism
Colorkey
I)
Control
AOX1KD1
12C
13C
G6P/F6P
6-PG
Ribulose/Ribose
/xylulose-5P
Sedoheptulose-7-P
Erythrose-4-P
U13C Glucose
G6P
6-Phosphogluconate
Xylulose-5-P
Ribulose-5P
Ribose-5P
Sedoheptulose-7-P
Erythrose-7-P
FBP/GBP
Glyceraldehyde 3-P
G-3P
Pyruvate
Ac-CoA
Lactate
Neucleotide
Nitrogen Base
Malic acid
Oxaloacetate
Citrate
Malate
α-KG
Fumarate
Succinate
Adenosine monophosphate
Guanosine monophosphate
Cytidine monophosphate
Inosine monophosphate
Succinic acid
Citrate
J)
Control
KD1
HK1
β-actin
G6PD
PFKB4
K)
NAD
Kynurenine
6-Phosphogluconate
Ribose/Ribulose/
xylulose-5P
AOX1 KD
680C91
AOX1 KD1

◀ **Fig. 4** Knockdown of AOX1 altered cell morphology and increased cell proliferation, glucose metabolism, and nucleotide synthesis. **a** shRNA knockdown (KD) of AOX1 in SV-HUC-1 leads to significant reduction in mRNA and protein levels. **b** Cell viability and proliferation of AOX1 KD cells. The cytotoxicity was determined by MTT assay. For proliferation assay 0.5×10^6 vector control and AOX1 KD cells were cultured in 100-mm culture dishes in triplicate. Total cells were counted on days 2, 3, 4, 5, and 6 using a Countess automated cell counter. **c** AOX1 KD causes the reduced cell size. Cell size and the ratio between the major axis length and the minor axis length were compared between control ($n = 76$) and AOX1 KD ($n = 159$) cells. **d** Wound-healing assay shows high migration rate of AOX1 KD cells compared to control. AOX1 KD and vector control cells were plated in 96-well image lock plate and grown to full confluency. Scratch was made using IncuCyte wound maker. The images were captured every 2 hours using Incucyte ZOOM. The images were analyzed for relative wound density (%) on Integrated cell migration analysis module. **e** Tryptophan-kynurenine pathway for the synthesis of NADP. **f** Kynurenine, NADP, and NADP/NADPH ratio levels in control and AOX1 KD measured by LC-MS. Metabolite levels were normalized using ^{13}C labeled internal standards to represent relative abundance level. **g** ^{15}N tryptophan flux shows elevated levels of ^{15}N kynurenine (M + 2) in AOX1 KD1 compared to control. **h** Heat map showing differential ($P < 0.05$) genes in AOX1 KD compared with vector control. **i** ^{13}C-labeled metabolic flux results in elevated levels of glycolytic intermediates, glucose-6-phosphate (M + 6) and fructose 1, 6-bisphosphate (FBP) (M + 6); increased levels of PPP intermediates, ribulose 5-phosphate (M + 5), sedoheptulose 7-phosphate (M + 7), and erythrose 4-phosphate (M + 4); increased levels of nucleotides, AMP, GMP, CMP, and IMP; decreased levels of TCA intermediates, citrate (M + 2), succinate (M + 2), and malate (M + 2) in AOX1 KD. **j** Western blot analyses for HK1, G6PD, and PFKB4 expression in AOX1 KD cells and the bar graphs show relative protein expression levels for the same blots. Protein levels were normalized using β-actin expression levels. **k** NADP, kynurenine, 6PG, and ribose/ribulose 5-P relative measurements by LC-MS analysis. M + 2, M + 5, M + 6, and M + 7 indicate two, five six, and seven Dalton shift respectively compare to unlabeled metabolites

Loss of AOX1 induces EMT phenotype and invasion in BLCA

EMT is a crucial mechanism by which cancer cells gain migratory and invasive properties [26, 27]. Our results demonstrate SV-HUC-1 AOX1 KD cells display altered cell growth, morphology, and metabolic phenotype. To further examine the link between AOX1 and EMT, we measured mRNA and protein expression levels of EMT markers such as E-cadherin, vimentin, and N-cadherin in AOX1 KD and Ad-AOX1 cells. AOX1KD cells showed lower levels of E-cadherin and higher levels of vimentin and N-cadherin (Fig. 6a). In contrast, Ad-AOX1 BLCA cells showed increased expression of E-cadherin and decreased expression of vimentin (Fig. 6b). Therefore, loss of AOX1 during BLCA progression may contribute to the EMT phenotype of cancer cells. Cell invasion assays showed loss of AOX1 resulted in increased invasiveness of SV-HUC-1 cells (Fig. 6c) and Ad-AOX1 decreased invasiveness of high-grade UMUC3 and T24 BLCA cells (Fig. 6d). These results suggest loss of AOX1 contributes the transition from low-grade to high-grade during BLCA progression.

AOX1 suppresses the tumor potential of BLCA cells in vivo

To examine the tumor-suppressive potential of AOX1 in vivo, we introduced Ad-AOX1 into UMUC3 BLCA cells, which were then injected into the flank region of immunocompromised mice. UMUC3 BLCA cells with empty adenoviral vectors were used as control. Tumors were collected for analysis after 4 weeks of growth. We found that tumors of Ad-AOX1 showed significantly reduced growth rate and size compared with control tumors (Fig. 7a, b). To determine whether AOX1 regulated the same biochemical pathways in vitro and in vivo, we analyzed AOX1-associated metabolites and nucleotides by LC-MS. We found that the Ad-AOX1 tumors were enriched in energy metabolites and AOX1-product metabolites, and showed lower levels of nucleotides and AOX1-substrate metabolites (Fig. 7c). To further examine the role of AOX1 in tumor growth, we performed chicken embryo chorioallantoic membrane [5] xenografts [28] to assess the effects of gain and loss-of-function of AOX1. GSK126 treated cells were used for AOX1 gain, followed by shAOX1 knockdown for loss of AOX1 in the same setting. One million cells from each experimental group (control, GSK, GSK + luc, and GSK + shAOX1) were grafted on the embryo's CAM and allowed to expand for 5 days. We found AOX1 expression resulted in a significant reduction in tumor growth while AOX1 knockdown enhanced growth (Fig. 7d). Immunohistochemistry (IHC) analysis of the CAM tumors demonstrated the expected experimental loss and gain of AOX1 (Fig. 7d). In addition, we have performed EZH2 overexpression followed by AOX1 overexpression in cell line model (Supplementary Fig. 6a). The results demonstrated reduced tryptophan pathway metabolites, NADP, and PPP intermediates (Supplementary Fig. 6b) and increase in ovivo tumor growth (Supplementary Fig. 6c). Overall these results indicate expression of AOX1 reduces nucleotide synthesis and suppresses tumor growth in vivo.

Discussion

Previous metabolomic studies have investigated disease-specific metabolite signatures in BLCA [9, 29, 30]. Our study is the first to identify stage-specific metabolic markers associated with AOX1 that are predictive of BLCA progression. We found the metabolic state of bladder tumors at the Ta stage was markedly different from that of tumors at the T1–T4 stages. The accumulation of AOX1-substrate

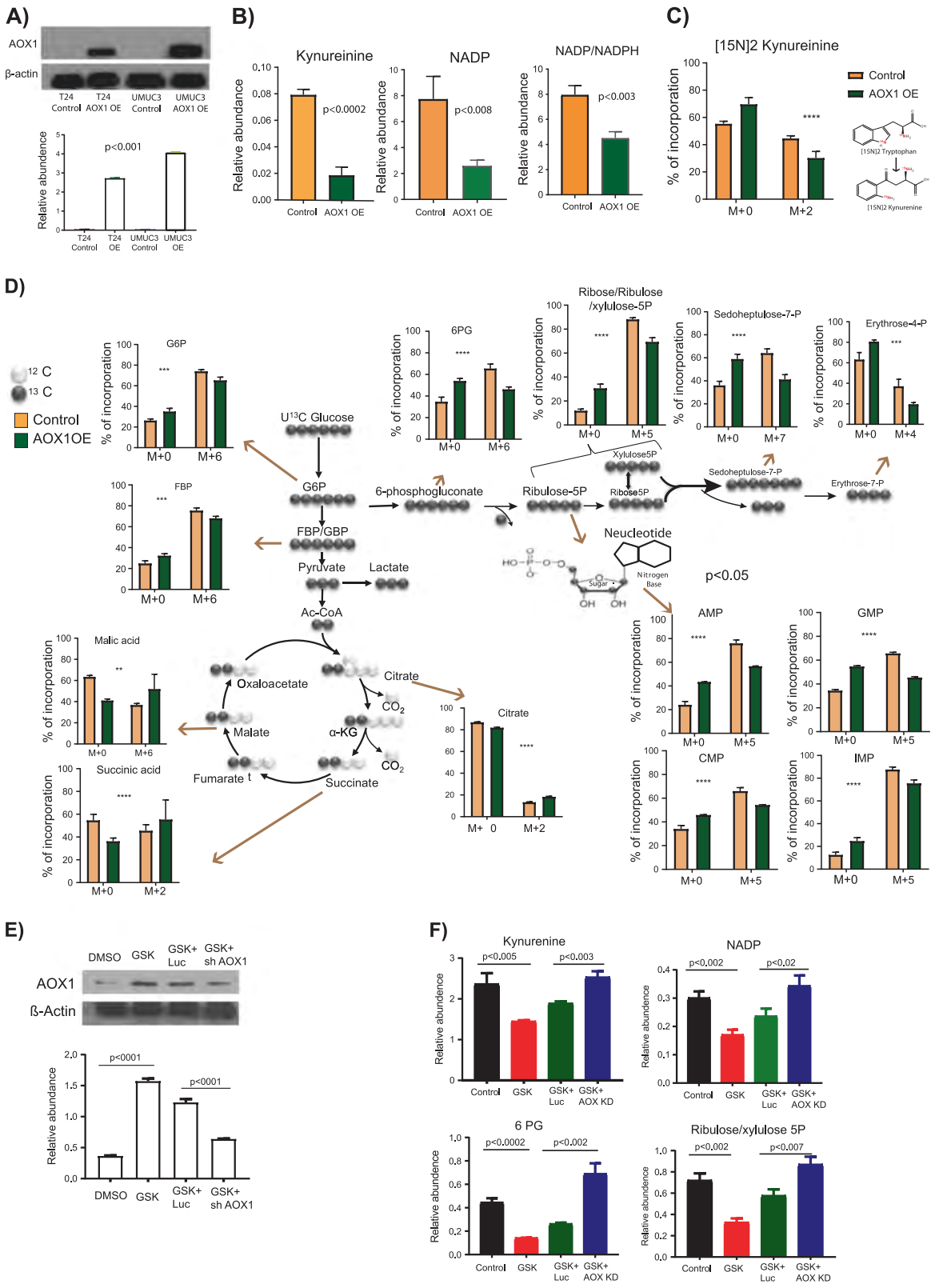

metabolites, such as tryptophan, tyrosine, retinol, nicotinamide, and indole acetaldehyde and the reduction of AOX1-product metabolites, such as gentisate, retinoic acid, indole acetate, and TCA metabolites in advanced BLCA tissues suggests AOX1 loss is an indicator of high-grade BLCA. Previous studies have shown that some of these metabolites

◀ **Fig. 5** Ectopic expression of AOX1 in BLCA affects NAD/NADP, pentose phosphate pathway, and nucleotide synthesis. **a** Adenoviral ectopic expression (Ad-AOX1) of AOX1 in UMUC3 and T24 cells causes upregulation of AOX1 protein levels. **b** Levels of kynurenine, NADP, and NADP/NADPH ratio in control and Ad-AOX1 UMUC3 cells. Metabolite levels were normalized using internal standards to represent relative abundance level. **c** ^{15}N tryptophan flux shows decreased levels of ^{15}N kynurenine (M + 2) in Ad-AOX1 UMUC3 cells compared with control. **d** ^{13}C-labeled metabolic flux results of Ad-AOX1 UMUC3 cells shows decreased levels of glycolytic intermediates, glucose-6-phosphate (M + 6), fructose 1, 6-bisphosphate (M + 6); decreased levels of PPP intermediates, ribulose 5-phosphate (M + 5), sedoheptulose 7-phosphate (M + 7), and erythrose 4-phosphate (M + 4); decreased nucleotides, AMP, GMP, CMP, and IMP; and elevated levels of TCA intermediates, citrate (M + 2), succinate(M + 2), and malate (M + 2). M + 2, M + 5, M + 6, and M + 7 indicate two, five six, and seven Dalton shift respectively compare to unlabeled metabolites. **e** Western blot analysis AOX1 gain and loss upon 100 nM GSK treatment followed by shAOX1. Protein levels were normalized using β-actin expression levels for the quantification. **f** Levels of kynurenine, NADP, 6-phosphogluconate and ribulose/xylulose-5-phosphate during AOX1 gain and loss conditions. Metabolite levels were normalized using internal standards to represent relative abundance level

play a significant role in the development of various cancers [31–35]. It is possible that some of these metabolites play a crucial role in the clinical outcome of the BLCA and thus may be useful prognostic markers for BLCA. Our study also found high-grade BLCA tumors showed low levels of AOX1 expression, thus, highlighting the possible prognostic potential of AOX1 in BLCA. Recent studies have shown that AOX1 expression is low in breast, prostate, colorectal, and ovarian cancers [23, 36–38], but the metabolic significance of AOX1 levels in these cancers remains unknown. Our study has identified the predictive power of AOX1 associated metabolites for BLCA prognosis. However, the practical clinical implications of these prognostic markers for BLCA need to be further elucidated.

EZH2 is an epigenetic modulator that is commonly expressed at high levels in many types of cancers, such as melanoma, glioblastoma, breast, prostate, endometrial, liver, and lung [39–43]. We found that EZH2 expression was up-regulated in aggressive BLCA compared with benign and Ta stage tumors. This result supports a recent study demonstrating loss of tumor suppressor KDM6A (a H3K27 demethylase) amplifies PRC2-regulated transcriptional repression by EZH2 in BLCA [42]. GSK126 [44], treatment leads to reactivation of AOX1 by inhibiting EZH2, which suggests that small molecule drugs that target epigenetic enzymes provide a promising target to develop effective therapeutic agents against advanced BLCA. The EZH2 small molecule inhibitors Tazemetostat, EPZ005687, GSK343, UNC1999, and EPZ-6438 are in clinical trials to treat various advanced cancers [45, 46] ChIP experiments, and SET domain studies also demonstrated that the methyltransferase activity of EZH2 was essential for H3K27 methylation at AOX1 promoter. Our results add merit to the emerging mechanisms of epigenetic gene silencing of xenobiotic enzymes during BLCA development. Hypermethylated genes have been shown to be promising cancer markers for early detection of BLCA [47, 48]. DNA hypermethylation is a common mechanism to silence many tumor suppressor genes [48, 49]. Muscle invasive bladder cancer (MIBC) shows distinct patterns of CpG island hypermethylation at the AOX1 promoter when compared with NMIBC [49]. Hyper DNA methylation of AOX1 promoter in advanced stage BLCA patients and AOX1 negative correlation of AOX1 with DNMT3b in public cohorts also suggests the occupied EZH2 at AOX1 promoter may be interacts with DNMT3b and associated with it DNA methyltransferase activity in vivo [21].

NAD and NADP are required for various biological processes, including energy metabolism, oxidative stress, immunological functions, aging, and cell death [50, 51]. NAD/NADP is produced through the tryptophan- kynurenine pathway by the rate-limiting enzyme Tryptophan 2,3-dioxygenase (TDO2). Loss of AOX1 may disrupt the tryptophan- kynurenine pathway resulting in production of NADP and fueling nucleotide synthesis. We also demonstrated a significant effect on invasion in AOX1 KD and Ad-AOX1 BLCA cells. It is possible that the effects could be mediated through either the tryptophan-kynurenine pathway intermediates or via NAD/NADP. Kynurenine is an important intermediate of this pathway and can act as an important signaling molecule. Kynurenine may mitigate immune suppressive effects by binding to the aryl hydrocarbon (AhR) receptor there by promoting invasion and metastasis [52]. NAD also acts as a cofactor for many enzymes particularly sirtuins, which regulate many cellular pathways involved in cell invasion and metastasis [53, 54].

Loss of AOX1 leads to upregulation of metabolic enzymes such as hexokinase 1, phosphofructokinase 1, and glucose-6-phosphate dehydrogenase, which suggest a possible role for increased glucose metabolism in activating the PPP. Ribose 5-phosphate, a major product of the PPP is the precursor for nucleotide and nucleic acid synthesis [55]. Signaling events that promote flux through PPP could enhance tumor growth by fueling nucleotide synthesis. Our results suggest, TDO2 is an important contributor to NADP synthesis through kynurenine production in AOX1 BLCA. TDO2 expression is increased in metastatic uterine leiomyosarcoma and glioma [56, 57]. Moreover, increased levels of kynurenine is associated with breast cancer metastasis to lung and brain [58, 59]. The effects of gain and loss-of-function of AOX1 demonstrated that AOX1 plays an essential role in regulating tryptophan pathway by modulating NADP production and there by the PPP pathway. Thus, multiple metabolic pathways may be altered to provide the necessary precursors for rapidly proliferating

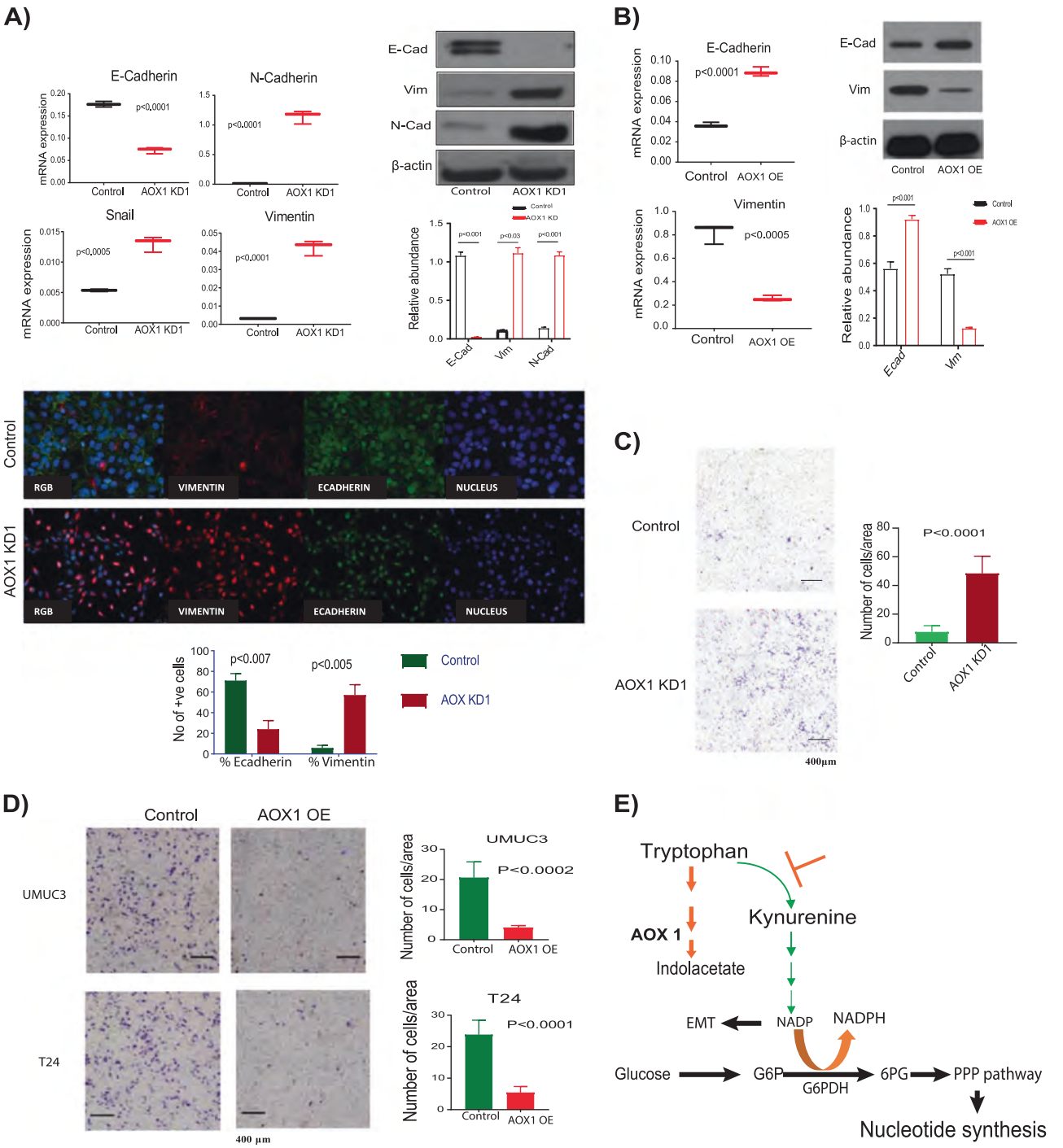

Fig. 6 Loss of AOX1 triggers EMT phenotype and invasion in BLCA. **a** mRNA and protein expression of EMT markers (E-cadherin, N-cadherin, and Vimentin) in AOX1 KD cells and their quantification. β-actin was used as internal control. Immunoflurescence microscopy of E-cadherin and vimentin expression in AOX1 KD and control cells. **b** Ad-AOX1 in UMUC3 shows increased levels of E- cadherin and decreased vimentin. **c** Boyden chamber cell invasion assay of AOX1 KD shows the increased invasion. **d** Boyden chamber cell invasion assay of Ad-AOX1 in UMUC3 and T24 cells, shows reduced cell invasion after 48 hours incubation. Cells were stained with crystal violet, counted in five individual fields, and the mean values were determined. **e** Graphical representation of rewired tryptophan-kynurenine pathway in AOX1 KD that leads to metabolic activation of PPP and nucleotide synthesis

cells during tumor progression. Pharmacologic inhibition of TDO2 in AOX1KD decreases flux through PPP suggesting a novel therapeutic opportunity to suppress nucleotide biosynthesis at the level of the kynurenine pathway.

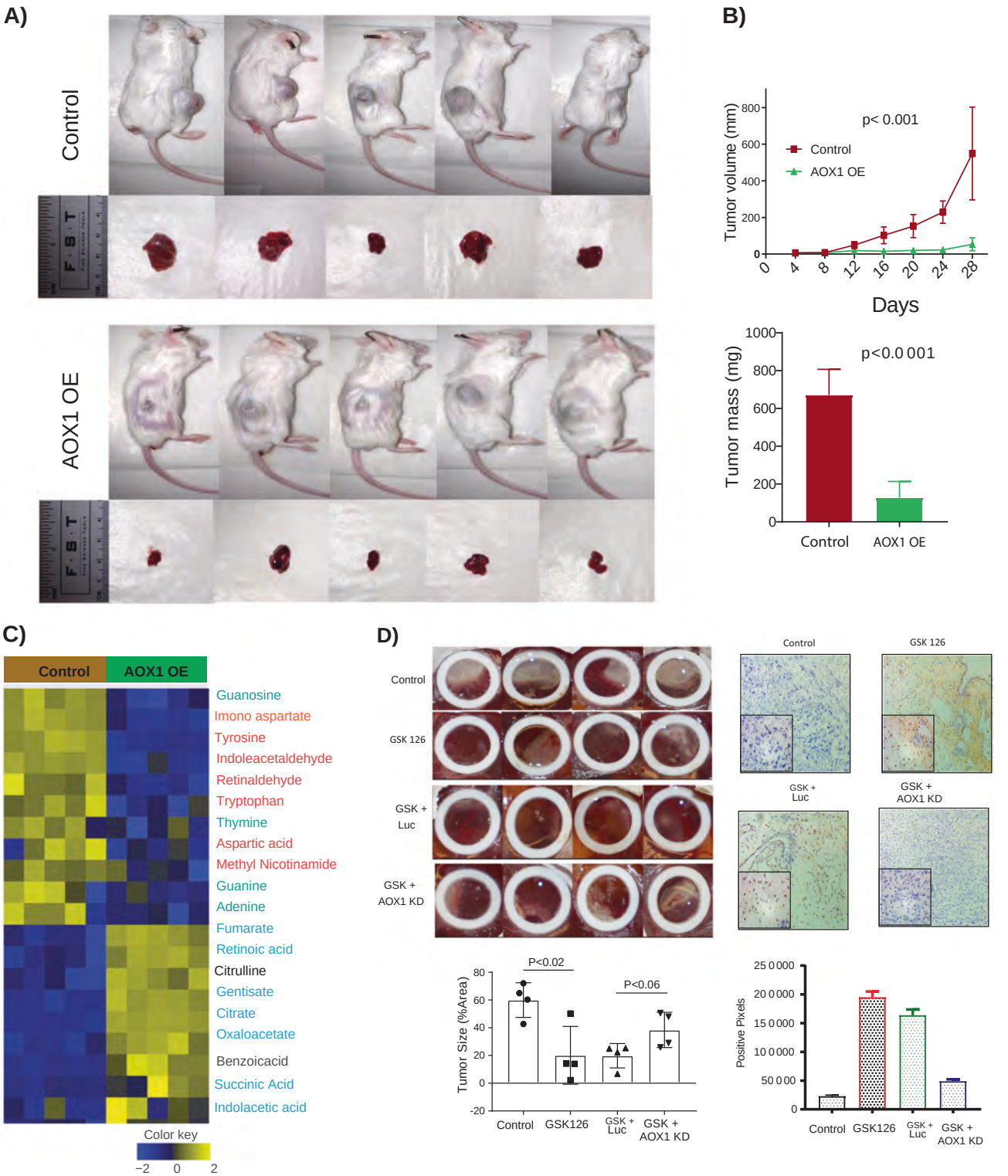

In conclusion, we show that loss of AOX1 expression in BLCA is mediated by the methyltransferase activity of EZH2. This leads to rewiring of the tryptophan-kynurenine pathway resulting in elevated NADP levels that potentially drive carbon flux through the PPP and promote EMT and cell invasion during BLCA progression. This is the first study to demonstrate the generation of NAD/NADP via a previously unrecognized pathway in response to loss of

◀ **Fig. 7** AOX1 Suppresses in vivo tumor potential of BLCA cells. **a** Mice xenograft shows reduced tumor size upon ectopic expression of Ad-AOX1 in UMUC3 BLCA cells. **b** UMUC3 xenograft tumors containing Ad-AOX1 show a significantly lower growth rate compared with controls ($n = 5$, Ad-h-AOX1 and $n = 5$ vector control). *Y*-axis represents median tumor volumes in mm^3 and associated median absolute deviation (MAD) for each group and Tumor mass after 28 days. **c** Heat map of hierarchical clustering of differential metabolites in tumor xenograft after 28 days. Shades of yellow and blue represent higher and lower levels of metabolites, relative to the median metabolite levels, respectively (false discovery rate, FDR < 0.25). **d** The CAM assay for the AOX1 gain and loss conditions after 5 days. To gain the AOX1 UMUC3 cells continuously treated with 100 nM GSK in CAM. Tumor size on the CAM was calculated as a percentage of the total area within the inner, 9 mm portion of the silicon ring. ImageJ was used to manually segment the area occupied by each of the tumors in all groups. IHC of CAM tissues confirm the gain and loss of AOX1 and stained slides were scanned using Aperio CS2 and analyzed with Aperio positive pixel count algorithm for quantification

AOX1, thus connecting metabolism and carcinogenesis. Furthermore, our stage-specific metabolomic data provide a basis for prognostic and therapeutic measures for advanced BLCA. Future studies should focus on in-depth analyses of AOX1 regulation and function to help identify effective prognostic and therapeutic targets for BLCA.

Materials and methods

Reagents

Acetonitrile, methanol, and water for high-performance liquid chromatography were purchased from Burdick and Jackson. Formic acid and internal standards, Gibberellic acid, Jasmonic acid, [^{15}N]2-Tryptophan, Thymine-d4, [^{13}C]-Creatinine, [^{15}N] Arginine, [^{15}N]-Anthranilic acid, and Testosterone-d3 (Supplementary Table 3), were purchased from Sigma Aldrich. U^{13}6 glucose was used purchased from Cambridge isotope laboratories, 5-Azacytidine, Adox, 680C91 were purchased from Sigma and GSK126 was procured from Cayman chemicals.

Tissue microarray

Tissue Microarray [3] slide with all the BLCA stages was procured from US Biomax. Immunostaining was performed using AOX1 antibody (Proteintech, 1:100 dilution) and AOX1 expression was analyzed and scored by a genito-urinary pathologist. The scores of 0–3 were considered low and scores from 4–8 were considered high. The score represents a combination of staining intensity and percentage of tumor cells showing protein expression

Cell culture, generation of stable AOX1, EZH2 knockdown, and Ad-h-AOX1 in BLCA cells

SV-HUC-1, RT4, T24, UMUC3 J82, and TCCSUP were procured from American Type Culture Collection (ATCC) and maintained as per ATCC instructions. All cell lines were verified using Short-Tandem Repeat DNA fingerprinting at the MD Anderson Cancer Center and were tested negative for mycoplasma contamination using MycoAlert Detection Kit (Lonza). To generate stable AOX1 and EZH2 KD in SV-HUC-1, UMUC3, and T24 cells, lentiviral transduction using shRNA (Sigma Aldrich) was carried out at a viral titer of 5 MOI. Cells with stable KD of the gene were cultured in respective media with 1 µg/ml of puromycin. Knockdown was assessed by qRT-PCR and western blotting. Customized Ad-h-AOX1 was procured from vector bio labs and transfections carried out according to manufacturer's instructions.

Targeted metabolomics using mass spectrometry

Human tissue samples were stored at −140 °C until the analysis. All the BLCA specimens were procured from UTSW (The University of Texas Southwestern Medical Center), UWH (Witten-Herdecke University), and BCM (Baylor College of Medicine) according to a prior written informed consent under institute review board (IRB) approved protocols Mice experiments were conducted according to the guidelines for humane treatment of animals approved by Baylor College of Medicine. For validation studies, we used an aliquot of extracted samples from earlier studies [60, 61].

Sample preparation for mass spectrometric analysis

Metabolites were extracted from tissues, cell lines, following the extraction procedure described previously [9, 62–65] and and mouse liver pool was used as quality controls. For metabolomics, 25 mg of tissue homogenized in ice cold water: methanol (1:4) containing an internal standards (Supplementary Table 3). For cell lines, 3×10^6 cells were subjected to three freeze-thaw cycles in liquid nitrogen and ice alternatively for three times to rupture the cell membrane. Following this, cells were sonicated in ice cold water: methanol (1:4) containing an internal standards (Supplementary Table 3). This was followed by metabolic extraction using sequential application of ice cold organic and aqueous solvents methanol: chloroform: water 4:3:2), deproteinization and drying of the extract. The latter was resuspended in injection solvent, and 5 µl used for LC-MS. LC-MS performed on Agilent 1290 series HPLC system

equipped with a degasser, binary pump, thermostatted autosampler and column oven. The multiple reaction monitoring (MRM)-based measurement of relative metabolite levels (Supplementary Table 5), used either reverse phase or normal phase chromatographic separation.

Separation of metabolites

Electrospray ionization (ESI) Positive mode was used to separate the metabolites. The LC column was Waters XBridge Amide 3.5 µm, 4.6 × 100 mm. Mobile phase A and B were 0.1% formic acid in water and acetonitrile respectively. Gradient: 0 min-85% B; 3–12 min- 85% to 10% B, 12–15 min-10% B, 16 min- 85% -B, followed by re-equilibration end of the gradient- the 23 min to the initial starting condition 85% B. Flow rate: 0.3 ml/min. ESI negative mode was also used to separate the metabolites. The HPLC column was Waters XBridge Amide 3.5 µm, 4.6 × 100 mm. Mobile phase A and B were 20 mM ammonium acetate in water with pH 9.0 and 100% acetonitrile respectively. Gradient: 0 min-85% B; 0–3 min- 85% to 30% B, 3–12 min-30%-2% B, 12–15 min- 2% -B, 15–16 min- 85% B followed by re-equilibration end of the gradient- the 23rd min to the initial starting condition 85% B. Flow rate: 0.3 ml/min.

Statistical analysis

The data was log2 transformed and normalized with internal standards on a per-sample, per-method basis. For every metabolite in the normalized dataset, two sample *t*-tests were conducted to compare expression levels between Ta and other stages (T1–T4). Differential metabolites were identified by adjusting the p-values for multiple testing at an FDR threshold of <0.25. A hierarchical cluster of the differentially expressed metabolites was generated using the R statistical software system (https://www.r-project.org/).

Generation of the ROC plots

We used 119 tissue specimens collected at three institutions (clinical information in Supplementary Table 2) and selected a subset of seven metabolites such as Nicotinamide, Methyl adenosine, Asparagine, Methyl histidine, Indolacetaldehyde, Tyrosine, Gentisatealdehyde which are associated with AOX1 metabolic pathways to derive an activity score. The metabolic data was normalized following median IQR and log2 transformed prior to running the predictive analyses. The dataset was z-score transformed. These subset of seven metabolites was used to estimate an overall activity score for each sample. For each individual sample, out of those seven metabolites, the total sum of negative z-scores was calculated and subtracted from total sum of positive z-scores (measured in a similar manner from remaining metabolites out of seven) to yield the final activity score for that sample. Next, using the activity scores as an input, we implemented a logistic regression model to build a predictive classifier on the disease status.

Following the method described above, we build a training model using the activity scores derived from two-thirds of the samples (selected randomly, $n = 80$). Next, we validated the predictive performance of the classifier by employing it on a test dataset comprised of remaining one-third of the samples ($n = 39$). Again the activity scores of the test samples were the input for the previously built model and the goal was to test if using those activity scores, it can predict the actual status (disease vs. control) in the test dataset. The classifier performance was characterized by measuring the area under Receiver Operating Characteristic (ROC) curve. The AUC value was 0.689 with a significance level of $p = 0.023$.

Pathway analysis

Networks of all pathways were visualized using the Fruchterman-Reingold layout algorithm implemented in the R package 'igraph'. Each node represents a metabolic pathway, with node sizes indicating statistical significance (−log10(adjusted *p*-value) - larger nodes correspond to lower *p*-values). An edge is drawn between two pathways if they have one or more metabolites in common. The width of an edge indicates the number of common metabolites between two pathways.

Promoter methylation analysis by bisulfite sequencing

The promoter methylation by bisulfite sequencing protocol used in this study was described earlier [66]. In brief, genomic DNA isolated from tissues by DNeasy blood and tissue kit (Qiagen). In all, 600 ng of genomic DNA from was treated with sodium bisulfite using the EZ DNA Methylation-Gold Kit (Zymo Research) according to the manufacturer's protocol. The samples were eluted in 40 µl of M-Elution Buffer, and 2 µl (equivalent to 25 ng of bisulfite-modified DNA) were used for each PCR reaction. Both bisulfite conversion and subsequent pyrosequencing analysis were done at the DNA Methylation Analysis Core, The University of Texas MD Anderson Cancer Center. PCR primers for the genomic area proximal to the transcription start site (TSS) of AOX1 (interrogating six CpG sites between 1-bp and 27-bp from TSS) were designed using the Pyromark® Assay Design SW 2.0 software (Qiagen). A sequencing primer is identified within 1–5 base pairs near the CpG sites of interest, with an annealing temperature of 40 ± 5 °C. After that, forward and reverse primers are identified upstream and downstream to the sequencing

primer, with a target annealing temperature ranging from 50 °C to 60 °C and amplicon product size ranging from 100 to 200 bp. Controls for high methylation (SssI-treated DNA), low methylation (WGA amplified DNA), and no-DNA template were included in the PCR reaction. PCR product purification was done with streptavidin-sepharose high-performance beads (GE Healthcare Life Sciences), and co-denaturation of the biotinylated PCR products and sequencing was conducted following the PSQ96 sample preparation guide. Sequencing was performed on a PyroMark Q96 ID instrument with the PyroMark Gold Q96 Reagents according to the manufacturer's instructions. The degree of methylation for each individual CpG site was calculated using the PyroMark Q96 software (Biotage AB). The average methylation of all sites and duplicates was reported for each sample.

Chromatin immunoprecipitation

ChIP assays were performed using a high throughput protocol as described [67]. In brief, cells were crosslinked in 1% formaldehyde for 10 min at room temperature, followed by incubation with glycine for 5 min to stop crosslinking. Cells were collected and washed with ice cold PBS and lysed for 30 min on ice using lysis buffer (12 mM Tris-HCl pH 7.5, 6 mM EDTA pH 8.0, 0.5% SDS) supplemented with a protease inhibitor. Lysates were fragmented with a Bioruptor (Diagenode) to obtain DNA fragments ranging 200–600 bp. After centrifugation, the supernatant was collected and incubated with respective antibodies conjugated with Dynabeads Protein G (Invitrogen) overnight at 4 °C. The immunocomplexes were collected using Dynamag, washed as described in the protocol, treated with RNase and Proteinase K, and reverse crosslinked overnight followed by DNA extraction. The DNA region of interest was detected by SYBR green real-time quantitative PCR using primer encompassing EZH2 binding and H3K4me3/H3M27me3 enrichment locus on human *AOX1* promoter determined using ENCODE database. The sequences of the forward and reverse primers used for ChIP-qPCR at *AOX* promoter are described in Supplementary Table 4.

Boyden Chamber invasion assay

Cell migration and invasion were measured using trans well chambers (Corning, USA) according to the manufacturer's protocol. AOX1 KD and Ad-AOX1 UMUC3 and T24 cells were incubated for 48 hours. Then, the cells in the upper chamber were removed with sterile cotton buds, and the remaining cells were fixed in 4% paraformaldehyde and stained with crystal violet solution. Cells were quantified in five randomly selected fields for each membrane, and the average cell number was used for calculations.

Wound healing

AOX1 KD and vector control cells were plated at 5×10^4 cells/ml in each well of 96-well image lock plate (Essen Bioscience) grown to full confluency and growth-arrested by adding mitomycin 1 ug/mL for 2 h. Following growth-arresting period, the media was replaced and a scratch was made using IncuCyte wound maker. The plates were then incubated in the 37° incubator, 5% CO_2 connected to IncuCyte and images were captured every 2 h using Incucyte ZOOM. The images were later analyzed for relative wound density (%) on Integrated cell migration analysis module (Essen Bioscience)

Cell size and morphology analysis

AOX1 KD and vector control cells were fixed, labeled with Alexa 594-conjugated phalloidin for 30 min and imaged with an IC200 (Vala Sciences) high throughput microscope using a Nikon 20 × /0.75 Plan Apo VC objective. Image analysis was performed in Matlab (R2016b). In brief, images were binarized using the Otsu's method, and single cells were filtered by size. For each single cell, area, major axis length and minor axis length values were extracted. Cell size and the ratio between the major axis length and the minor axis length were then compared between control ($n = 76$) and knocked down ($n = 159$) cells.

Metabolic flux analysis using $U^{13}C$-glucose

AOX1 KD (SVH) and Ad-AOX1 (UMCU3) BLCA equal cells (3×10^6) were seeded into 10-cm plates. After 24 h of incubation at 37 °C, the cells were washed twice with glucose-free RPMI containing 10% FBS, 2 mM glutamine, and penicillin-streptomycin. After overnight starvation, 12 mM $U^{13}C$-glucose (Cambridge isotope laboratories) was added, and cells were incubated for 3 h for glycolysis and 6 h for TCA, PPP metabolites. The plates were then washed with PBS, and snap-frozen in liquid nitrogen. The frozen plates were then used for extraction and LC-MS analysis.

Isotope labeling by targeted MS

Plates were scraped into a 500-µL water:methanol (1:1), sonicated for 1 min (two 30-s pulses) and then mixed with 450 µL ice cold chloroform. The resulting homogenate was then mixed with 150 µL ice cold water and vortex for 2 min. The homogenate was incubated at –20 °C for 30 min and centrifuged at 4 °C for 10 min to partition the aqueous and organic layers. The aqueous and organic layers were combined and dried at 37 °C for 45 min in an automatic environmental speed vac system (GeneVac). The extract was reconstituted in a 500-µL solution of ice cold methanol:

water (1:1) and filtered through a 3-kDa molecular filter (Amicon Ultracel) at 4 °C for 90 min to remove proteins. The filtrate was dried at 37 °C for 45 min in a speed vacuum. For MS analysis, the dried extract was resuspended in a 50-µL solution of methanol:water (1:1) containing 0.1% formic acid and then analyzed using MRM. Solution (10 µL) was injected and analyzed using a 6495 QQQ triple quadrupole mass spectrometer (Agilent Technologies) coupled to a 1290 series HPLC system. Metabolites were targeted in negative ion modes: the electrospray source ionization (ESI) voltage was −3500 V. Approximately 9–12 data points were acquired per detected metabolite. To target the glycolysis, TCA, PPP flux, the samples were delivered to the mass spectrometer via normal phase chromatography using a Luna amino column (3 µm, 100A 2 × 150 mm). The mobile phase containing water (solvent A), with solvent A modified by the addition of 5 mM ammonium acetate (pH 9.9), and 100% acetonitrile (ACN) solvent B). The binary pump flow rate was 0.2 ml/min with a gradient spanning 80% B to 2% A over a 20-min period followed by 2% solvent B to 80% solvent A for a 5-min period and followed by 80% B for 13-min time period. The flow rate was gradually increased during the separation from 0.2 mL/min (0–20 mins), 0.3 mL/min (20.1–25 min), 0.35 mL/min (25–30 min), 0.4 mL/min (30–37.99 min), and finally set at 0.2 mL/min (5 min).

Metabolic flux to measure the nucleosides, nucleotides, and kynurenine

AOX1 KD (SV-HUC-1) and Ad-AOX1 UMCU3 cells were seeded into 10-cm plates. After 24 h at 37 °C, the cells were washed twice with glucose-free RPMI. After overnight starvation, 12 mM U^{13}C-glucose was added and incubated for 72 h. For tryptophan flux 25 µM 15N2 tryptophan was added for 6 h. Cell pellets were stored at −80 °C until the metabolite extraction.

DNA extraction and digestion

Genomic DNA was isolated using Qiagen DNeasy blood and tissue kit, the quantity and quality of the DNA was determined by absorbance using a Biotek microplate reader and digestion procedure was followed from earlier publications [60]. In brief, 1 µg of DNA was denatured by heating at 100 °C for 3 min and subsequently chilled in ice. One-tenth volume of 0.1 M ammonium acetate (pH 5.3) and 2 units of nuclease P1 (Roche Molecular Biochemicals) were added. The mixture was incubated at 45 °C for 2 h. To the solution were subsequently added 1/10 volume of 1 M ammonium bicarbonate and 0.002 units of venom phosphodiesterase I. The incubation was continued for an additional 2 h at 37 °C. Thereafter, the mixture was incubated for 1 h at 37 °C with 0.5 units of alkaline phosphatase. Samples were dried and stored at –80 °C until MS analysis. Prior to MS analysis, the dried extract was resuspended in a 50 µL of methanol:water (1:1) containing 0.1% formic acid and then analyzed using MRM. Targeting the nucleosides and nucleotides, the samples were delivered to the MS via reverse phase chromatography using RRHD SB-CN column (1.8 µm, 3.0 × 100 mm, Agilent Technologies) at 300 µl/min. The initial flow rate was 0.2 ml/min with 2% mobile phase B and 98% mobile phase A. The gradient was set at 2% B at time 0, increased to 5% at 5 min, then increased to 80% at 5.1 min. After that, the gradient was kept at 80% B for 2 min and then decreased to 2% for 3 min. The flow rate was gradually increased during the separation from 0.2 mL/min (0–5 mins), 0.4 mL/min (5.1 to 7 min), 0.2 mL/min (7–10 min), and finally set at 0.2 mL/min (5 min). Buffers A and B were comprised of 0.1% formic acid in water and acetonitrile, respectively.

For ^{13}C labeling experiments, glycolysis, TCA, PPP and nucleosides, and nucleotides expected SRM transitions were calculated for ^{13}C incorporation into various molecules for targeted LC-MS. To assess the validity of our method for calculating isotopomers, we determined the complete isotopomer distribution for each metabolite. Data analysis was performed using Mass Hunter quantitative B.07 software version (Agilent Technologies) and the estimated percent of isotopomer incorporation was calculated using the formula: percent fractional incorporation = $^{13}C/^{13}C + ^{12}C \times 100$ and corrected for isotopomeric distribution and natural abundance.

680C91 Treatment

AOX1 KD and normal bladder epithelium cells were treated with 10 µM TDO2 inhibitor 680C91 (Sigma) for 24 h. After the 24 h, an equal number of cells were collected, processed for the metabolite extraction, and LC-MS analysis.

Kynurenine and NADP measurements

Metabolites extraction procedure adopted from earlier publications [9, 62–65]. The extract was resuspended in an injection solvent, and analyzed by LC-MS. ESI Positive mode was used to separate the metabolites. The LC column was Waters XBridge Amide 3.5 µm, 4.6 × 100 mm. Mobile phase A and B were 0.1% formic acid in water and ACN respectively. Gradient: 0 min-85% B; 0–10 min-85% to 2% B, 10–12 min-2% B, 12–12.1 min-85%-B, followed by re-equilibration end of the gradient–the 4 min to the initial starting condition 85% B. Flow rate: 0.3 ml/min.

Immunofluorescence (IF) microscopy

In all, 2×10^4 AOX1 KD and 1×10^4 Ad-AOX1 UMUC3 cells were seeded in 12-well plates for 48 and 24 h respectively, later cells were fixed in 4% paraformaldehyde for 20 min at room temperature, quenched in 100 mM ammonium chloride and permeabilized with 0.1% TritonX-100 in PBS. After blocking for 1 h in 5% milk/TBST, cells were incubated overnight at 4 °C with rabbit anti-vimentin (1:250, Cell Signaling) or mouse anti-E-cadherin (1:250, Cell Signaling) in TBST/5% milk. After extensive washes, cells were incubated with secondary Alexa647 anti-rabbit (1:1000) or Alexa488 anti-mouse (1:2000) for 1 hour at RT, respectively. Coverslips were mounted with Slow Fade Gold anti-fade reagent (Life Technologies). Images were then acquired on a Biotek Cytation5 image reader using 10X objective, or on a GE Healthcare DeltaVision LIVE high-resolution deconvolution microscope using a 60X plan Apo/1.4 N.A., oil objective.

Western blot

Antibodies to AOX1 (Proteintech, 1:500), EZH2 (BD Biosciences, 1:1000), E-cadherin, vimentin, N-cadherin (Cell Signaling, 1:1,000) and Actin (Sigma, 1:3000), were used. Protein lysates were prepared using RIPA buffer (Sigma) as per the manufacturer's instructions. Secondary anti-rabbit/mouse HRP antibodies (Sigma) were used. Super signal westpico chemiluminescent substrate (Thermo Scientific) used for western blot development.

RNA and qPCR analysis

Standard RNA extraction was carried out by RNeasy Mini Kit (Qiagen), reverse transcription (Quanta Biosciences) and SYBR green (Life Technologies) qPCR were performed. Primers used in this study are listed in Supplementary Table 4.

RNA-seq analysis

Total RNA quality assessment using BioRad Experion Automated Electrophoresis Station and Quantification using Qubit 3.0 fluorometer (Qubit RNA BR Assay Kit). Sample libraries were prepared using the Illumina TruSeq Stranded mRNA Sample Preparation Kit and IDT-TruSeq RNA UD Index, 24 Idx-96 samples. This process purifies the poly A containing mRNA molecules using poly-T oligo attached magnetic beads using two rounds of purification. During the second elution of the poly A RNA, the RNA was also fragmented and primed for cDNA synthesis. DNA was subjected to end repair, A-tailing and adapter ligation. Post ligation cleanup was performed using AMpure XP beads (Agencourt). DNA fragments were amplified using PCR and purified using AMpure XP beads (Agencourt). The quality of the amplified libraries was checked on an Agilent 4200 Tape Station System using the D1000 Screen Tape Assay. The libraries were normalized to 2 nM and pooled (16 samples/flow cell) in equal volumes and sequenced on Illumina NextSeq 550 using Next Seq 500/550 High Output reagent kit V2 (150 cycles). The bcl files were converted to fastq files using Illumina BaseSpace.

In vivo xenograft studies

Animal experiments were performed in accordance with the Baylor College of Medicine (BCM) Institutional Animal Care and Use Committee. Male SCID-Beige fox chase mice (6–8 weeks of age) were obtained from Michael Lewis laboratory at BCM. The mice were used to generate xenografts using SV-HUC-1 cells that were stably transduced with either control shRNA or shRNA targeting AOX1 and Ad-AOX1 UMUC3 and vector control. To generate the xenografts, subcutaneous injection of 100 µL of a mixture containing cells (50 µl of 1×10^6 Ad-AOX1 UMUC3 in 1xDPBS) and 50 µl matrigel (BD Biosciences) was carried out in the hind-flank area of the mice under isoflurane anesthesia. Tumors were measured using calipers thrice per week for a minimum of 4 weeks. Tumor volume was calculated using the formula $TV = (\text{length} \times \text{width}^2) \times 0.52$ [68]. At the end of the study, the tumors were harvested and flash frozen and later used for metabolomic analysis.

Chorioallantoic membrane assay (CAM)

Fertilized chicken eggs were purchased from Charles River (Norwich, Connecticut, US). The chick chorioallantoic membrane was accessed as previously described [69] on embryonic day 7, and the eggs were inoculated with 5×10^5 UMUC3 control, 100 nM GSK, GSK + Luc and GSK + shAOX1 cells per egg. Photographs of the CAM were taken on 3rd and 5th days of post engraftment. Imaging was conducted on embryonic days 10 and 13, (3 and 5 days after seeding the tumor cells). On the 5th day after inoculation, the eggs were euthanized as per the AVMA guidelines. Tumor size on the CAM was calculated as a percentage of the total area within the inner, 9 mm portion of the silicon ring. In brief, ImageJ was used to manually segment the area occupied by each of the tumors in all groups. The percent tumor area was calculated by dividing the segmented tumor area by the total area within the inner portion of the ring and multiplied by 100. Prism was used to plot the average tumor size per group on a bar graph and to run statistical tests on the data. The CAM tumors were harvested followed by fixed in 10% formalin and embedded in paraffin. To achieve this, the eggshell opening was widened

to allow excision of the CAM and tumor. The paraffin-embedded for used immunohistochemistry (IHC). IHC was performed with AOX1, EZH2, E CAD, N CAD, and Vimentin to check the EMT.

Immuno histochemstry

Tissues were de-paraffinized in xylene and rehydrated in graded alcohols. For antigen retrieval the slide was pressure-cooked for 10 min. Endogenous peroxidase activity was quenched with 3% hydrogen peroxide for 5 min. Slides were blocked by 3% goat serum then incubated with AOX1 antibody (Proteintech, IL), at room temperature for 1 h in humidity chambers. The HRP conjugated goat anti- anti-rabbit secondary antibody (Jackson Immunoresearch Laboratories Inc, West Grove, PA) was applied for 40 min. The antigen–antibody reaction was visualized after diaminobenzidine (Sigma-Aldrich, MO) was applied for 7 min. The slides were counterstained with hematoxylin (Sigma-Aldrich, MO) for 1 min. Positive controls were included in each staining run; negative controls were obtained by omitting the primary antibody. Slides were then dehydrated in alcohols and cleared in three xylene baths before being mounted with Permount (Sigma-Aldrich, MO) media. Stained slides were scanned using Aperio CS2 and analyzed with Aperio positive pixel count algorithm (Leica Biosystems, IL).

Acknowledgements This research was fully supported by American Cancer Society (ACS) Award 127430-RSG-15-105-01-CNE (N.P.), NIH/NCI R01CA220297 (N.P), and NIH/NCI R01CA216426 (N.P.), partially supported by the following grants: NIH 1RO1CA133458-01 (A.S.K.), and NIH U01 CA167234, Komen CCR award to S.M.K. (CCR16380599) as well as funds from Alkek Center for Molecular Discovery (A.S.K.). This project was also supported by the Agilent Technologies Center of Excellence in Mass Spectrometry at Baylor College of Medicine, Metabolomics Core, Human Tissue Acquisition and Pathology at Baylor College of Medicine with funding from the NIH (P30 CA125123), CPRIT Proteomics and Metabolomics Core Facility (D.P.E.), (RP170005), and Dan L. Duncan Cancer Center. Imaging for this project was supported by the Integrated Microscopy Core at Baylor College of Medicine with funding from NIH (DK56338, CA125123, and 1S10OD020151-01), CPRIT (RP150578), the Dan L. Duncan Comprehensive Cancer Center, and the John S. Dunn Gulf Coast Consortium for Chemical Genomics. CAM assay was supported by the Patient-Derived Xenograft and Advanced in vivo Models Core Facility at Baylor College of Medicine with funding from the Cancer Prevention and Research Institute of Texas (CPRIT) grant #170691. Imaging for this project was supported by the Integrated Microscopy Core at Baylor College of Medicine with funding from NIH (DK56338, and CA125123), CPRIT (RP150578, RP170719), the Dan L. Duncan Comprehensive Cancer Center, and the John S. Dunn Gulf Coast Consortium for Chemical Genomics. Research reported in this study was supported by the National Cancer Institute of the National Institutes of Health under award number 5 P30 CA142543 09.

Author contributions V.V., V.P., A.S. and N.P., conceived the project and wrote the manuscript with editorial input from all of the authors. V.V., V.P., D.A.B., S.M.K., Q.C. and N.P. designed the experiments. V.V., V.P., D.A.B., V.D., S.M.K., S.R.D., J.D., A.K.J., F.S. and B.K. performed the experiments. S.M., J.M., J.A., K.R. and C.C. assisted with the dataset analysis. A.S. and N.P. assisted with mass spectroscopy measurements and functional study. F.V.R. and Y.L. provided clinical specimens. F.V.R. and Y.L. provided clinical input on data interpretation. A.G.S. and H.V. performed the OVIVO experiments.

Compliance with ethical standards

Conflict of interest S.M.K. is stake holder of NeoZenome Therapeutics Inc.

Publisher's note: Springer Nature remains neutral with regard to jurisdictional claims in published maps and institutional affiliations.

References

1. Ferlay J, Soerjomataram I, Dikshit R, Eser S, Mathers C, Rebelo M, et al. Cancer incidence and mortality worldwide: sources, methods and major patterns in GLOBOCAN 2012. Int J Cancer. 2015;136:E359–86.
2. Siegel RL, Miller KD, Jemal A. Cancer statistics, 2018. CA Cancer J Clin. 2018;68:7–30.
3. Sievert KD, Amend B, Nagele U, Schilling D, Bedke J, Horstmann M, et al. Economic aspects of bladder cancer: what are the benefits and costs? World J Urol. 2009;27:295–300.
4. Thoma C. Bladder cancer: genomics of noninvasive disease. Nat Rev Urol. 2018;15:1.
5. Hurst CD, Alder O, Platt FM, Droop A, Stead LF, Burns JE, et al. Genomic subtypes of non-invasive bladder cancer with distinct metabolic profile and female gender bias in KDM6A mutation frequency. Cancer Cell. 2017;32:701–15 e7.
6. Garattini E, Fratelli M, Terao M. The mammalian aldehyde oxidase gene family. Hum Genom. 2009;4:119–30.
7. Garattini E, Fratelli M, Terao M. Mammalian aldehyde oxidases: genetics, evolution and biochemistry. Cell Mol Life Sci. 2008;65:1019–48.
8. Kitamura S, Sugihara K, Ohta S. Drug-metabolizing ability of molybdenum hydroxylases. Drug Metab Pharm. 2006;21:83–98.
9. Putluri N, Shojaie A, Vasu VT, Vareed SK, Nalluri S, Putluri V, et al. Metabolomic profiling reveals potential markers and bioprocesses altered in bladder cancer progression. Cancer Res. 2011;71:7376–86.
10. Baylin SB, Herman JG, Graff JR, Vertino PM, Issa JP. Alterations in DNA methylation: a fundamental aspect of neoplasia. Adv Cancer Res. 1998;72:141–96.
11. Merlo A, Herman JG, Mao L, Lee DJ, Gabrielson E, Burger PC, et al. 5' CpG island methylation is associated with transcriptional silencing of the tumour suppressor p16/CDKN2/MTS1 in human cancers. Nat Med. 1995;1:686–92.
12. Esteller M, Tortola S, Toyota M, Capella G, Peinado MA, Baylin SB, et al. Hypermethylation-associated inactivation ofp14(ARF) is independent of p16(INK4a) methylation and p53 mutational status. Cancer Res. 2000;60:129–33.
13. Di Croce L, Helin K. Transcriptional regulation by Polycomb group proteins. Nat Struct Mol Biol. 2013;20:1147–55.
14. Sun S, Yu F, Zhang L, Zhou X. EZH2, an on-off valve in signal network of tumor cells. Cell Signal. 2016;28:481–7.
15. Ma J, Shojaie A, Michailidis G. Network-based pathway enrichment analysis with incomplete network information. Bioinformatics. 2016;32:3165–74.
16. Kim WJ, Kim EJ, Kim SK, Kim YJ, Ha YS, Jeong P, et al. Predictive value of progression-related gene classifier in primary non-muscle invasive bladder cancer. Mol Cancer. 2010;9:3.

17. Cancer Genome Atlas Research Network Comprehensive molecular characterization of urothelial bladder carcinoma. Nature. 2014;507:315–22.
18. Sanchez-Carbayo M, Socci ND, Lozano J, Saint F, Cordon-Cardo C. Defining molecular profiles of poor outcome in patients with invasive bladder cancer using oligonucleotide microarrays. J Clin Oncol. 2006;24:778–89.
19. Choi W, Porten S, Kim S, Willis D, Plimack ER, Hoffman-Censits J, et al. Identification of distinct basal and luminal subtypes of muscle-invasive bladder cancer with different sensitivities to frontline chemotherapy. Cancer Cell. 2014;25:152–65.
20. McCabe MT, Ott HM, Ganji G, Korenchuk S, Thompson C, Van Aller GS, et al. EZH2 inhibition as a therapeutic strategy for lymphoma with EZH2-activating mutations. Nature. 2012;492:108–12.
21. Vire E, Brenner C, Deplus R, Blanchon L, Fraga M, Didelot C, et al. The Polycomb group protein EZH2 directly controls DNA methylation. Nature. 2006;439:871–4.
22. Kleer CG, Cao Q, Varambally S, Shen R, Ota I, Tomlins SA, et al. EZH2 is a marker of aggressive breast cancer and promotes neoplastic transformation of breast epithelial cells. Proc Natl Acad Sci USA. 2003;100:11606–11.
23. Oster B, Thorsen K, Lamy P, Wojdacz TK, Hansen LL, Birkenkamp-Demtroder K, et al. Identification and validation of highly frequent CpG island hypermethylation in colorectal adenomas and carcinomas. Int J Cancer. 2011;129:2855–66.
24. Salter M, Pogson CI. The role of tryptophan 2,3-dioxygenase in the hormonal control of tryptophan metabolism in isolated rat liver cells. Effects of glucocorticoids and experimental diabetes. Biochem J. 1985;229:499–504.
25. D'Amato NC, Rogers TJ, Gordon MA, Greene LI, Cochrane DR, Spoelstra NS, et al. A TDO2-AhR signaling axis facilitates anoikis resistance and metastasis in triple-negative breast cancer. Cancer Res. 2015;75:4651–64.
26. Yang J, Weinberg RA. Epithelial-mesenchymal transition: at the crossroads of development and tumor metastasis. Dev Cell. 2008;14:818–29.
27. De Craene B, Berx G. Regulatory networks defining EMT during cancer initiation and progression. Nat Rev Cancer. 2013;13:97–110.
28. Deryugina EI, Quigley JP. Chick embryo chorioallantoic membrane model systems to study and visualize human tumor cell metastasis. Histochem Cell Biol. 2008;130:1119–30.
29. Kompier LC, Lurkin I, van der Aa MN, van Rhijn BW, van der Kwast TH, Zwarthoff EC. FGFR3, HRAS, KRAS, NRAS and PIK3CA mutations in bladder cancer and their potential as biomarkers for surveillance and therapy. PLoS ONE. 2010;5:e13821.
30. Vantaku V, Dong J, Ambati CR, Perera D, Donepudi SR, Amara CS, et al. Multi-omics integration analysis robustly predicts high-grade patient survival and identifies CPT1B effect on fatty acid metabolism in Bladder Cancer. Clin Cancer Res. 2019;15:3689–701.
31. Platten M, Wick W, Van den Eynde BJ. Tryptophan catabolism in cancer: beyond IDO and tryptophan depletion. Cancer Res. 2012;72:5435–40.
32. Ablain J, de The H. Retinoic acid signaling in cancer: the parable of acute promyelocytic leukemia. Int J Cancer. 2014;135:2262–72.
33. Yang M, Pollard PJ. Succinate: a new epigenetic hacker. Cancer Cell. 2013;23:709–11.
34. Zhai L, Spranger S, Binder DC, Gritsina G, Lauing KL, Giles FJ, et al. Molecular pathways: targeting IDO1 and other tryptophan dioxygenases for cancer immunotherapy. Clin Cancer Res. 2015;21:5427–33.
35. Icard P, Poulain L, Lincet H. Understanding the central role of citrate in the metabolism of cancer cells. Biochim Biophys Acta. 2012;1825:111–6.
36. Ozturk S, Papageorgis P, Wong CK, Lambert AW, Abdolmaleky HM, Thiagalingam A, et al. SDPR functions as a metastasis suppressor in breast cancer by promoting apoptosis. Proc Natl Acad Sci USA. 2016;113:638–43.
37. Haldrup C, Mundbjerg K, Vestergaard EM, Lamy P, Wild P, Schulz WA, et al. DNA methylation signatures for prediction of biochemical recurrence after radical prostatectomy of clinically localized prostate cancer. J Clin Oncol. 2013;31:3250–8.
38. Park JS, Choi SB, Chung JW, Kim SW, Kim DW. Classification of serous ovarian tumors based on microarray data using multi-category support vector machines. Conf Proc IEEE Eng Med Biol Soc. 2014;2014:3430–3.
39. Varambally S, Dhanasekaran SM, Zhou M, Barrette TR, Kumar-Sinha C, Sanda MG, et al. The polycomb group protein EZH2 is involved in progression of prostate cancer. Nature. 2002;419:624–9.
40. Bachmann IM, Halvorsen OJ, Collett K, Stefansson IM, Straume O, Haukaas SA, et al. EZH2 expression is associated with high proliferation rate and aggressive tumor subgroups in cutaneous melanoma and cancers of the endometrium, prostate, and breast. J Clin Oncol. 2006;24:268–73.
41. Sudo T, Utsunomiya T, Mimori K, Nagahara H, Ogawa K, Inoue H, et al. Clinicopathological significance of EZH2 mRNA expression in patients with hepatocellular carcinoma. Br J Cancer. 2005;92:1754–8.
42. Hussain M, Rao M, Humphries AE, Hong JA, Liu F, Yang M, et al. Tobacco smoke induces polycomb-mediated repression of Dickkopf-1 in lung cancer cells. Cancer Res. 2009;69:3570–8.
43. Yan J, Ng SB, Tay JL, Lin B, Koh TL, Tan J, et al. EZH2 overexpression in natural killer/T-cell lymphoma confers growth advantage independently of histone methyltransferase activity. Blood. 2013;121:4512–20.
44. Tan JZ, Yan Y, Wang XX, Jiang Y, Xu HE. EZH2: biology, disease, and structure-based drug discovery. Acta Pharmacol Sin. 2014;35:161–74.
45. The EZH2 Inhibitor Tazemetostat Is Well Tolerated in a Phase I Trial. Cancer Discov. 2018;8:OF15. http://cancerdiscovery.aacrjournals.org/content/early/2018/04/20/2159-8290.CD-RW2018-067, https://doi.org/10.1158/2159-8290.CD-RW2018-067. Accessed 9 Apr 2018.
46. Kim KH, Roberts CW. Targeting EZH2 in cancer. Nat Med. 2016;22:128–34.
47. Dudziec E, Goepel JR, Catto JW. Global epigenetic profiling in bladder cancer. Epigenomics. 2011;3:35–45.
48. Reinert T, Modin C, Castano FM, Lamy P, Wojdacz TK, Hansen LL, et al. Comprehensive genome methylation analysis in bladder cancer: identification and validation of novel methylated genes and application of these as urinary tumor markers. Clin Cancer Res. 2011;17:5582–92.
49. Wolff EM, Chihara Y, Pan F, Weisenberger DJ, Siegmund KD, Sugano K, et al. Unique DNA methylation patterns distinguish non-invasive and invasive urothelial cancers and establish an epigenetic field defect in premalignant tissue. Cancer Res. 2010;70:8169–78.
50. Agledal L, Niere M, Ziegler M. The phosphate makes a difference: cellular functions of NADP. Redox Rep. 2010;15:2–10.
51. Ying W. NAD+/NADH and NADP+/NADPH in cellular functions and cell death: regulation and biological consequences. Antioxid Redox Signal. 2008;10:179–206.
52. Prendergast GC. Cancer: why tumours eat tryptophan. Nature. 2011;478:192–4.
53. Chen Y, Guillemin GJ. Kynurenine pathway metabolites in humans: disease and healthy States. Int J Tryptophan Res. 2009;2:1–19.
54. Chalkiadaki A, Guarente L. The multifaceted functions of sirtuins in cancer. Nat Rev Cancer. 2015;15:608–24.
55. Beaconsfield P, Ginsburg J, Jeacock MK. Glucose metabolism via the pentose phosphate pathway relative to nucleic acid and protein synthesis in the human placenta. Dev Med Child Neurol. 1964;6:469–74.
56. Davidson B, Abeler VM, Forsund M, Holth A, Yang Y, Kobayashi Y, et al. Gene expression signatures of primary and metastatic uterine leiomyosarcoma. Hum Pathol. 2014;45:691–700.

57. Opitz CA, Litzenburger UM, Sahm F, Ott M, Tritschler I, Trump S, et al. An endogenous tumour-promoting ligand of the human aryl hydrocarbon receptor. Nature. 2011;478:197–203.
58. Minn AJ, Gupta GP, Siegel PM, Bos PD, Shu W, Giri DD, et al. Genes that mediate breast cancer metastasis to lung. Nature. 2005;436:518–24.
59. Bos PD, Zhang XH, Nadal C, Shu W, Gomis RR, Nguyen DX, et al. Genes that mediate breast cancer metastasis to the brain. Nature. 2009;459:1005–9.
60. Jin F, Thaiparambil J, Donepudi SR, Vantaku V, Piyarathna DWB, Maity S, et al. Tobacco-specific carcinogens induce hypermethylation, DNA adducts, and DNA damage in bladder cancer. Cancer Prev Res. 2017;10:588–97.
61. Piyarathna DWB, Rajendiran TM, Putluri V, Vantaku V, Soni T, von Rundstedt FC, et al. Distinct lipidomic landscapes associated with clinical stages of urothelial cancer of the bladder. Eur Urol Focus. 2018;4:907–915.
62. Terunuma A, Putluri N, Mishra P, Mathe EA, Dorsey TH, Yi M, et al. MYC-driven accumulation of 2-hydroxyglutarate is associated with breast cancer prognosis. J Clin Invest. 2014;124:398–412.
63. Putluri N, Maity S, Kommagani R, Creighton CJ, Putluri V, Chen F, et al. Pathway-centric integrative analysis identifies RRM2 as a prognostic marker in breast cancer associated with poor survival and tamoxifen resistance. Neoplasia. 2014;16:390–402.
64. Putluri N, Shojaie A, Vasu VT, Nalluri S, Vareed SK, Putluri V, et al. Metabolomic profiling reveals a role for androgen in activating amino acid metabolism and methylation in prostate cancer cells. PLoS ONE. 2011;6:e21417.
65. Bhowmik SK, Ramirez-Pena E, Arnold JM, Putluri V, Sphyris N, Michailidis G, et al. EMT-induced metabolite signature identifies poor clinical outcome. Oncotarget. 2015;6:42651–60.
66. Estecio MR, Yan PS, Ibrahim AE, Tellez CS, Shen L, Huang TH, et al. High-throughput methylation profiling by MCA coupled to CpG island microarray. Genome Res. 2007;17:1529–36.
67. Blecher-Gonen R, Barnett-Itzhaki Z, Jaitin D, Amann-Zalcenstein D, Lara-Astiaso D, Amit I. High-throughput chromatin immunoprecipitation for genome-wide mapping of in vivo protein-DNA interactions and epigenomic states. Nat Protoc. 2013;8:539–54.
68. O'Reilly MS, Boehm T, Shing Y, Fukai N, Vasios G, Lane WS, et al. Endostatin: an endogenous inhibitor of angiogenesis and tumor growth. Cell. 1997;88:277–85.
69. Li M, Pathak RR, Lopez-Rivera E, Friedman SL, Aguirre-Ghiso JA, Sikora AG. The in ovo chick chorioallantoic membrane (CAM) assay as an efficient xenograft model of hepatocellular carcinoma. J Vis Exp. 2015.

Oncogene
https://doi.org/10.1038/s41388-019-0966-4

ARTICLE

BMI1 is directly regulated by androgen receptor to promote castration-resistance in prostate cancer

Sen Zhu[1] · Dongyu Zhao[2,3] · Chao Li[1,4,5] · Qiaqia Li[1,4,6] · Weihua Jiang[1] · Qipeng Liu[1,6] · Rui Wang[1] · Ladan Fazli[7,8] · Yinan Li[7,8] · Lili Zhang[1] · Yang Yi[1,4] · Qingshu Meng[1,4] · Wanyi Wang[9] · Guangyu Wang[2,3] · Min Zhang[3,10] · Xiongbing Zu[5] · Wei Zhao[11] · Tuo Deng[12] · Jindan Yu[13,14] · Xuesen Dong[7,8] · Kaifu Chen[2,3] · Qi Cao[1,4,14,15]

Received: 16 December 2018 / Revised: 29 April 2019 / Accepted: 28 May 2019

Abstract

B lymphoma Mo-MLV insertion region 1 (BMI1) has been reported to be an oncoprotein. BMI1 represses tumor suppressors to promote cell proliferation, epithelial-mesenchymal transition (EMT), and cancer progression. Although it is known that the expression of BMI1 is increased in many cancer types, the mechanism of BMI1 upregulation is not yet clear. We performed integrative analysis for 3 sets of prostate cancer (PCa) genomic data, and found that BMI1 and androgen receptor (AR) were positively correlated, suggesting that AR might regulate BMI1. Next, we showed that dihydrotestosterone (DHT) upregulated both mRNA and protein levels of BMI1 and that BMI1 was increased in castration-resistant prostate cancer (CRPC) from both human patients and a mouse xenograph model. We further identified an AR binding site in the promoter/enhancer region of BMI1, and confirmed BMI1 as the direct target of AR using gene-editing technology. We also demonstrated that high expression of BMI1 is critical for the development of castration-resistance. Our data also suggest that BMI1-specific inhibitors could be an effective treatment of CRPC.

These authors contributed equally: Sen Zhu, Dongyu Zhao, Chao Li

Supplementary information The online version of this article (https://doi.org/10.1038/s41388-019-0966-4) contains supplementary material, which is available to authorized users.

✉ Kaifu Chen
kchen2@houstonmethodist.org

✉ Qi Cao
qi.cao@northwestern.edu

[1] Center for Inflammation and Epigenetics, Houston Methodist Research Institute, Houston, TX 77030, USA

[2] Center for Bioinformatics and Computational Biology, Houston Methodist Research Institute, Houston, TX 77030, USA

[3] Department of Cardiothoracic Surgery, Weill Cornell Medicine, Cornell University, New York, NY 10065, USA

[4] Department of Urology, Northwestern University Feinberg School of Medicine, Chicago, IL 60611, USA

[5] Department of Urology, Xiangya Hospital, Central South University, Changsha 410008, China

[6] Xiangya School of Medicine, Central South University, Changsha 410008, China

[7] Vancouver Prostate Centre, Vancouver General Hospital, Vancouver, BC V6H 3Z6, Canada

[8] Department of Urologic Sciences, University of British Columbia, Vancouver, BC V6H 3Z6, Canada

[9] Center for Research Design & Analysis, Office of Research and Sponsored Programs, Texas Woman's University, Houston, TX 77030, USA

[10] Center for Cardiovascular Regeneration, Department of Cardiovascular Sciences, Houston Methodist Research Institute, Houston, TX, USA

[11] Zhongshan School of Medicine, Sun Yat-sen University, Guangzhou 510080, China

[12] Department of Metabolism and Endocrinology, The Second Xiangya Hospital and Key Laboratory of Diabetes Immunology, Central South University, Ministry of Education, Changsha 410011, China

[13] Division of Hematology/Oncology, Department of Medicine, Northwestern University Feinberg School of Medicine, Chicago, IL 60611, USA

[14] Robert H. Lurie Comprehensive Cancer Center, Northwestern University Feinberg School of Medicine, Chicago, IL 60611, USA

[15] Houston Methodist Cancer Center, Houston Methodist Research Institute, Houston, TX 77030, USA

Published online: 28 August 2019

Introduction

BMI1 is a core member of polycomb repressive complex 1 (PRC1). BMI1 plays important roles in many pathological progresses, such as cancer stem cell maintenance, differentiation, and EMT [1, 2]. BMI1 interacts with RING1B (also known as RNF2), another PRC1 core protein, to enhance its histone H2A ubiquitin E3 ligase activities and repress downstream targets.

BMI1 is expressed in normal prostate luminal epithelial cells, with an unveiled role in PCa development [3]. BMI1 is enriched in a population of PCa cells that have higher tumor-initiating capacities, and high expression of BMI1 is strongly correlated with PCa, with adverse pathologic and clinical outcomes [4]. Further, the presence of BMI1 in lower-grade PCa specimens is intensely predictive of detectable serum levels of prostate-specific antigen (PSA) (i.e., PSA recurrence) [4]. Also, BMI1 expression was highly correlated with therapy failure and poor survival in five types of epithelial tumors, including PCa [5]. However, the mechanism for dysregulation of BMI1 in PCa is not yet clear.

AR is a critical regulator for PCa development and progression. Blocking AR signaling is the mainstay in PCa therapy. When activated by androgen, AR complexes with DNA at androgen response elements (AREs) in the promoter or enhancer regions of target genes. Although AR and BMI1 are both abundantly expressed in PCa, whether there is a regulatory network between AR and BMI1 has not been determined. Very recently, we have reported that BMI1 directly binds to AR and regulates AR protein stability and signaling [6]. In this study, we investigated if and how AR regulates BMI1 expression and function. We also examined if BMI1 has any functions involved in castration-resistance.

Results

Expression of BMI1 and AR is positively correlated in PCa

We initially analyzed the TCGA prostate adenocarcinoma RNA-Seq dataset and observed that the expression levels of BMI1 and AR were positively correlated, $R = 0.615$ (Fig. 1a, left panel). However, other PRC1 components, including RING1A, RING1B, SCML4, PCGF6, PHC, and CBX genes, were weakly or negatively correlated with AR (Fig. 1b, left panel; Supplementary Fig. 1A–H, left panel). To further confirm this observation, we analyzed two additional datasets (MSKCC and Michigan) for PCa gene expression profiling [7, 8]. Consistently, BMI1 expression levels were positively correlated with AR levels ($R \geq 0.613$), while other PRC1 components were not (Fig. 1a, b, middle and right panels; Supplementary Fig. 1A–H, middle and right panels). In addition, the positive correlation of BMI1 levels with AR activities was statistically significant, which was supported by higher levels of well-known target genes of AR in the BMI1-high expression group compared (all p-values < 0.05) with the BMI1-low expression group (Fig. 1c–e). This result suggests a regulatory link between BMI1 and AR in PCa.

BMI1 is regulated by AR signaling in PCa cells

Very recently, we reported that AR is regulated by BMI1 at the protein level, but not at the transcript level [6]. To test whether BMI1 is regulated by AR signaling, we first examined the expression levels of BMI1 in castration-resistant prostate cancer (CRPC) cell lines C4-2 and LNCaP-abl, along with its parental androgen-dependent, non-CRPC LNCaP cell line. As shown in Fig. 2a and Supplementary Fig. 2A, the AR protein levels were much higher in CRPC cell lines C4-2 and LNCaP-abl compared with the non-CRPC cell line LNCaP. Consistent with increased AR expression, both transcript and protein levels of BMI1 were elevated in the CRPC cell lines. To investigate whether AR directly regulates BMI1, we cultured LNCaP, C4-2, and LNCaP-abl cells in androgen-depleted medium (5% charcoal-stripped fetal bovine serum [FBS] in phenol red-free medium) for 2 days, and then stimulated with 5 nM dihydrotestosterone (DHT). As expected, BMI1, along with AR and the well-known androgen-induced gene KLK3 (i.e., PSA), were markedly increased by DHT treatment (Fig. 2b). To further confirm this finding, we performed time-course analysis. First, LNCaP and C4-2 cells were treated with DHT for different time periods after culturing for 2 days in androgen-depleted medium. As demonstrated in Fig. 2c, d and Supplementary Fig. 2B, C, PSA and BMI1 decreased substantially in the absence of androgen. Further, DHT treatment, which activated AR signaling (significantly increased PSA levels), restored the expression of BMI1. Furthermore, we examined BMI1 mRNA levels post-DHT treatment at 2, 4, 8, and 16 h, and observed that DHT started to stimulate the BMI1 gene expression by 0.636-fold ($p = 0.0018$) after 2 h of treatment. However, the proliferation of cells did not increase before 8 h post treatment (Fig. 2e and Supplementary Fig. 2D). These results suggest that AR signaling regulates BMI1 at the transcriptional level, and this regulation is independent of cell proliferation rate.

BMI1 expression corresponds with the activity of AR signaling in VCaP xenografts post castration and after enzalutamide treatment

Next, we investigated whether androgen/AR signaling in vivo regulates BMI1. Androgen-dependent PCa VCaP

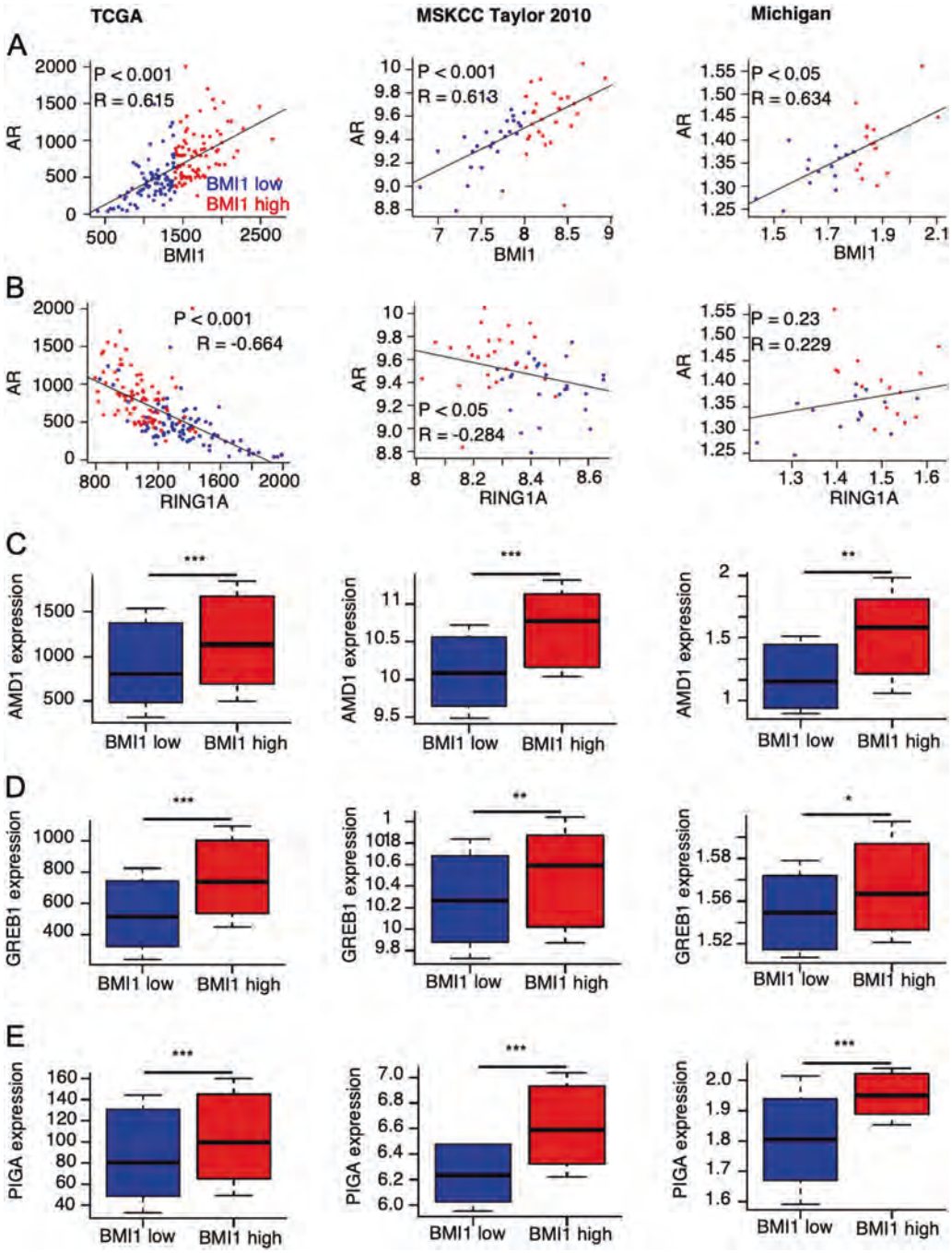

Fig. 1 AR and BMI1 are significantly and positively correlated in PCa patients. Scatter plots for expression values of AR against BMI1 (**a**) and RING1A (**b**) in patient samples from the TCGA (left panels), MSKCC (middle panels), and Michigan projects (right panels), respectively. Boxplots for expression values of AR target genes AMD1 (**c**), GREB1 (**d**), and PIGA (**e**) in patients that display low or high BMI1 expression levels based on data from the TCGA (left panels), MSKCC (middle panels), and Michigan (right panels) projects, respectively. *P*-values were determined by significance tests of the correlation coefficient (**a**, **b**) and Wilcoxon tests (**c**–**e**). Correlation coefficient values were determined by the Pearson method (**a**, **b**). $*p < 0.05$, $**p < 0.01$, $***p < 0.001$ vs. BMI1 low

cells were subcutaneously injected into 5-week-old male SCID mice. Three weeks post injection, xenograft tumors formed, and mice were randomly grouped for castration or non-castration. A proportion of mice were sacrificed 1–3 weeks after castration, and tumors were collected. The remaining mice were retained until tumors started to regrow, and then mice were randomly grouped to receive either enzalutamide or vehicle. Tumors were collected at 4 weeks post-enzalutamide treatment (Supplementary Fig. 3). The protein levels of AR, PSA, and BMI1 were

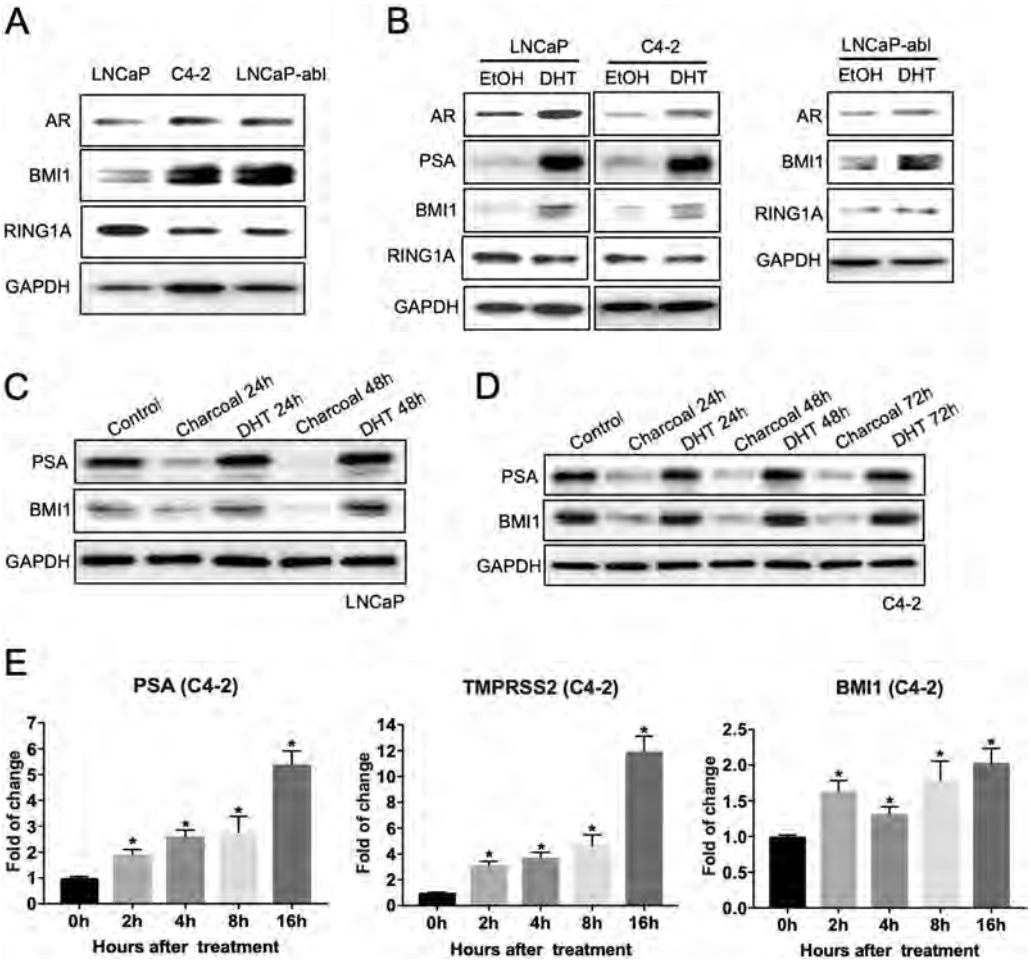

Fig. 2 Androgen/AR signaling regulates BMI1 in PCa cells. **a** 2×10^5 LNCaP, C4-2, or LNCaP-abl cells were plated, and after 2 days of culture, total cell lysates were blotted for AR, BMI1, and RING1A, while GAPDH served as a loading control. **b** LNCaP, C4-2, or LNCaP-abl cells were cultured in androgen-depleted culture medium (5% charcoal-stripped FBS in phenol red-free medium) for 48 h, and then stimulated with 5 nM DHT for another 48 h. Ethanol (EtOH) was used as a control. Total cell lysates were immunoblotted for AR, PSA, BMI1, RING1A, and GAPDH (**b**). After growing in androgen-depleted culture medium for 48 h, LNCaP (**c**) and C4-2 (**d**) cells were treated with DHT for the times indicated. The protein levels of PSA, BMI1, and GAPDH were tested. All experiments were biologically repeated at least three times. Representative images are shown. **e** C4-2 cells were allowed to grow in androgen-depleted culture medium for 48 h, then treated with DHT for the time indicated, and mRNA levels of PSA, TMPRSS2, and BMI1 were tested by QPCR. $^*p < 0.05$ vs. 0 h (normalized to 18 S mRNA, mean ± SD)

measured by immunoblot analysis. The PSA levels markedly decreased at 1-week post castration, demonstrating the effectiveness of castration. BMI1 levels were significantly decreased by 0.406-fold ($p = 0.0238$) in the tumors from mice 1-week post castration compared to non-castrated mice (Fig. 3a). However, resistance developed after castration, as indicated by increasing AR and PSA levels. Notably, BMI1 levels were also increasing by 1.408-fold ($p = 0.0026$) in this process (Fig. 3a) 1-week earlier than the rebound of PSA (i.e., PSA recurrence). This indicated that BMI1 plays an important role in castration-resistant tumor growth. Additionally, changes in mRNA levels of AR, PSA, and BMI1 positively correlated with each other, suggesting that AR signaling regulates BMI1 at the transcription level (Fig. 3b). Further, enzalutamide treatment in vivo significantly suppressed AR signaling and remarkably downregulated BMI1 expression by 0.645-fold, ($p = 0.0345$) (Fig. 3c). Taken together, these findings indicate that BMI1 is regulated by hormone-depletion and enzalutamide treatment, and is involved in the progression of castration-resistance.

BMI1 protein levels are increased in human tissues from CRPC patients

To further investigate whether BMI1 protein levels are changed during PCa progression in human patients, we retrieved prostate tumor biopsies from Vancouver Prostate Centre tissue bank (see more details in "Methods" section) and performed tissue microarray analysis using a cohort of

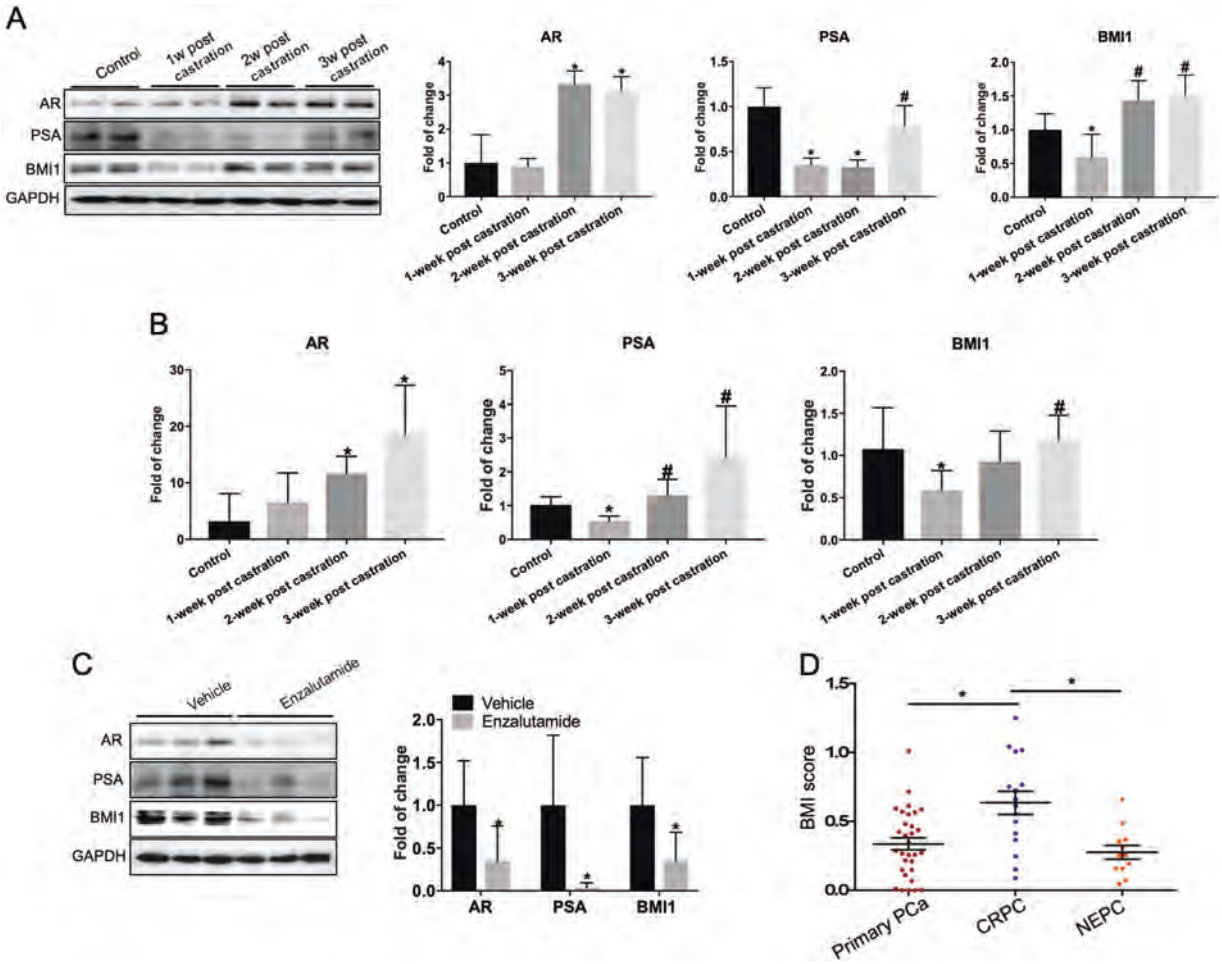

Fig. 3 BMI1 protein levels are increased in CRPC and altered during neoadjuvant hormone-depletion treatment. Mice possessing 200–300 mm^3 VCaP tumors were sacrificed as control or castrated, and tumors were collected at three time-points as indicated. **a** Protein levels of AR, PSA, and BMI1 were tested by western blotting, GAPDH served as loading control; $^{*}p < 0.05$ vs. control, $^{\#}p < 0.05$ vs. 1-week post castration (normalized to GAPDH, mean ± SD, $n = 6$). **b** Transcript levels of AR, PSA, and BMI1 were quantified by QPCR; $^{*}p < 0.05$ vs. control, $^{\#}p < 0.05$ vs. 1-week post castration (normalized to 18S mRNA, mean ± SD, $n = 6$). **c** Castrated mice possessing CRPC xenograft received vehicle or enzalutamide (10 mg/kg per day) for 5 days per week. Tumors were collected 4 weeks later, and AR, PSA, BMI1, and GAPDH were analyzed by western blot; $^{*}p < 0.05$ vs. vehicle (normalized to GAPDH, mean ± SD, $n = 6$). **d** IHC of BMI1 was performed in primary PCa, CRPC, and NEPC. BMI1 scores are expressed as mean ± SD; $^{*}p < 0.05$

prostate tissues (Supplementary Table 1) that included 31 primary PCa tissues (17 patients), 16 CRPC tissues (8 patients), and 12 Neuroendocrine Prostate Cancer (NEPC) tissues (6 patients). In accordance with BMI1 being a nuclear protein, BMI1 protein staining was mainly found in the nuclei of cells (Supplementary Fig. 4) As shown in Fig. 3d, CRPC tissues had dramatically higher BMI1 expression levels than primary PCa and NEPC, strongly suggesting that BMI1 is involved in castration-resistance. Since AR expression levels and AR signaling are decreased in NEPC [9], a positive correlation may exist between BMI1 and AR during the transition from CRPC to NEPC. Additionally, we confirmed the increase of BMI1 in CRPC utilizing another batch of human samples (Supplementary Table 2 and Supplementary Fig. 5).

BMI1 is the direct target gene of AR

Analysis of PCa cell lines (Fig. 2c–e), mouse xenografts (Fig. 3a–c), and tissues from human patients (Fig. 3d) strongly suggest that AR signaling directly regulates BMI1. Next, we questioned how AR regulates BMI1 in vitro and in vivo. We hypothesized that AR may directly bind to the promoter or enhancer region of BMI1 to regulate the transcription of BMI1. To test this hypothesis, we first performed a de novo-motif search using the MEME tool [10] and found 6 potential AR binding motifs in BMI1 promoter or enhancer regions (Fig. 4a and Supplementary Fig. 6). We further performed chromatin immunoprecipitation (ChIP) followed by sequencing (Seq) [6]. ChIP-Seq revealed that AR was recruited to 5 distinct genomic loci around BMI1

A

Motif ID	Sequence Name	Start	End	p-value	Matched Sequence
1	hg19-dna	159	173	7.77e-05	AGGAACTCTATGTAT
2	hg19-dna	1208	1222	4.15e-05	AAGAACAAAGAGACT
3	hg19-dna	4482	4496	4.99e-05	AAGGACATCCAGCTC
4	hg19-dna	16501	16515	5.72e-05	TAGAACACAAAGTAT
5	hg19-dna	24661	24675	7.95e-05	CAGAACATACAGTCC
6	hg19-dna	27153	27167	2.85e-05	AGGCACATTCTGTTA

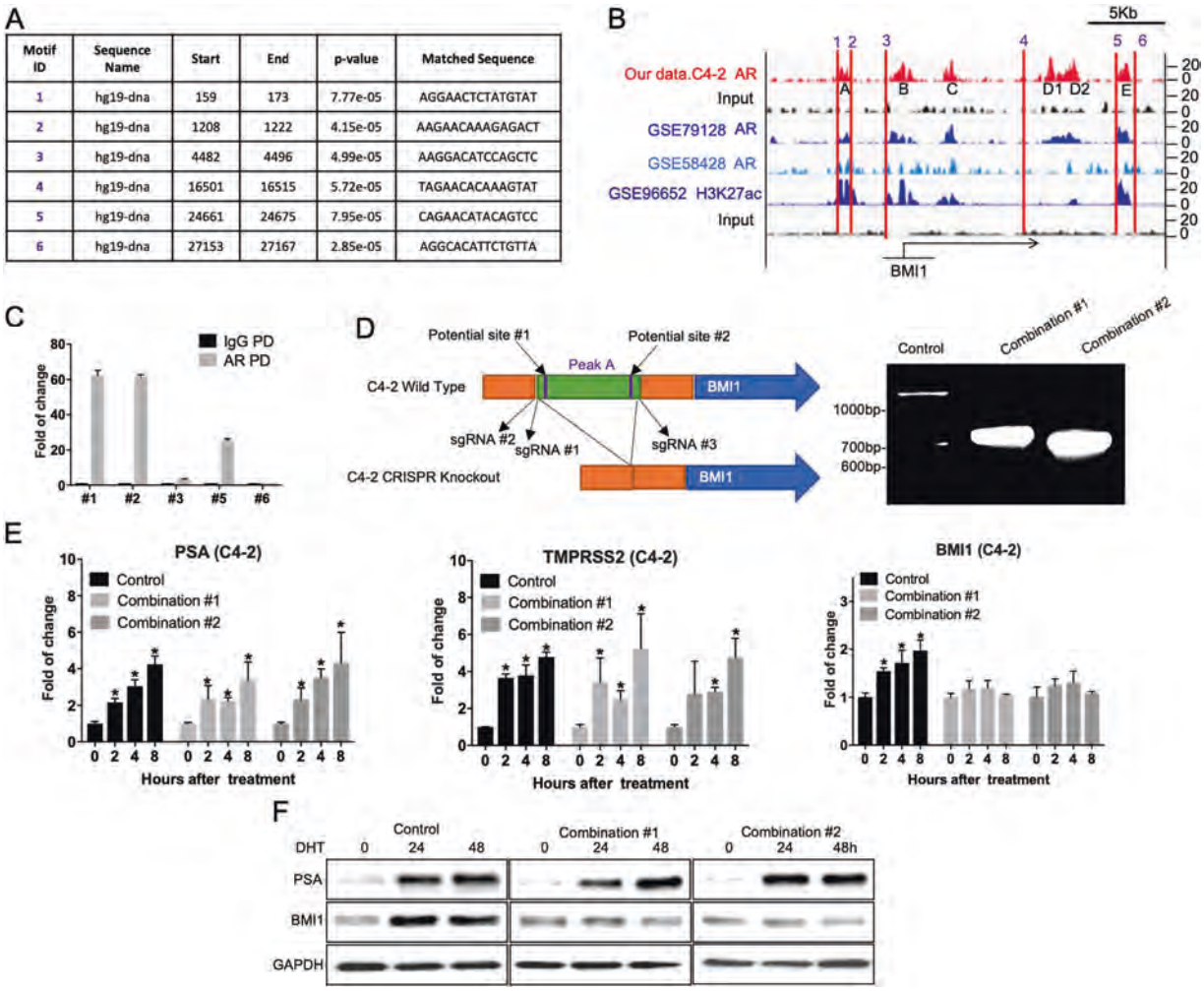

Fig. 4 BMI1 is the direct target gene of AR. **a** MEME analysis of highly represented motifs. **b** ChIP-Seq peaks depicting AR and H3K27ac-binding profiles in BMI1 promoter (enhancer) regions. **c** ChIP-qPCR was conducted using specific primers to validate AR enrichment on BMI1 promoter (enhancer) regions. **d** Left panel: Schematic of CRISPR strategy used to cleave the targeted part of genomic DNA. Right panel: C4-2 cells were infected by lentiviral sgRNA #1 + #3 (Combination #1) or lentiviral sgRNA #2 + #3 (Combination #2) followed by puromycin selection, empty lentivirus as control. Genomic DNA were extracted, and the fragments of expected size were amplified by PCR: Control: 1992bp, Combination #1: 710 bp, Combination #2: 665 bp. Control and knockout cells were cultured in androgen-depleted medium and then treated with DHT. Cells were collected at indicated time points. **e** mRNA levels of PSA, TMPRSS2, and BMI1 at 0, 2, 4, or 8 h after DHT treatment were tested by QPCR. *$p < 0.05$ vs. 0 h (normalized to 18S mRNA, mean ± SD). **f** Protein levels of PSA and BMI1 at 0, 24, or 48 h after DHT treatment were analyzed by western blot. All experiments were biologically repeated at least three times. Representative images are shown

(Fig. 4b). In addition, we analyzed publicly available AR ChIP-Seq using the VCaP cell line [11, 12]. As expected, AR was recruited to the same genomic regions around BMI1 (Fig. 4b). Interestingly, H3K27ac, which is known as the enhancer marker [13], is also enriched in loci A, B, and E. Notably, locus A & motif #1 & 2, and locus E & motif #5 are closely located, suggesting that motif #1, 2, and 5 might be AREs. To validate this finding, we designed primer pairs surrounding motif #1, 2, and 5 and primer pairs surrounding motif #3 and 6 as negative controls. As shown in Fig. 4c, AR was significantly and remarkably enriched in motif #1 and #2. As expected, AR was not enriched in motif #3 and #6.

To further confirm BMI1 is the direct target gene of AR, we utilized Clustered Regularly Interspaced Short Palindromic Repeats (CRISPR) gene-editing technology to knockout locus A, including motif #1 & 2. We designed several single-guide RNAs (sgRNAs), and found two combinations that could successfully knockout the targeted site, as shown in Fig. 4d. The expected sizes of the PCR-amplified products were obtained: 710 bp for combination #1 (sgRNA #1 + #3), and 665 bp for combination #2 (sgRNA #2 + #3). The sequencing results of these two products further confirmed the success of the knockout (Supplementary Table 3). We treated these knockout cells with DHT for different time periods, and found that BMI1

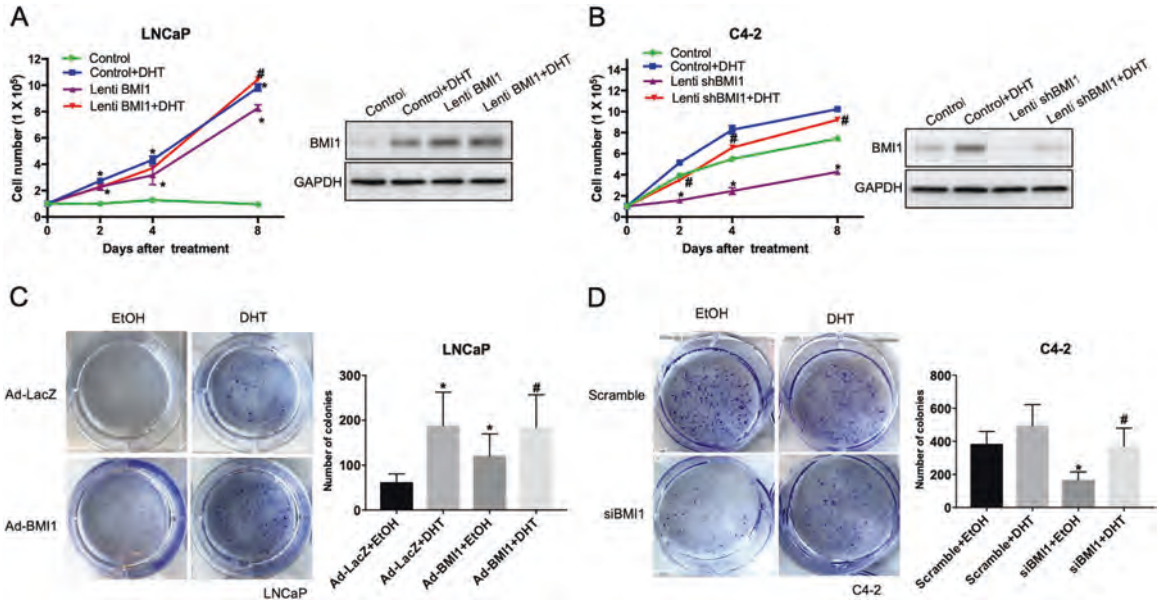

Fig. 5 BMI1 plays an important role in regulation of the proliferation and colony formation of PCa cells. **a** Left panel: 1×10^5 LNCaP cells per well (6-well plate) were infected with lentivirus to overexpress mBMI1, and GFP lentivirus was used as control. Cells were cultured in medium without androgen for 24 h, treated with DHT (5 nM) or EtOH, and cell number was counted at indicated time points; $*p < 0.05$ vs. Control, $\#p < 0.05$ vs. Lenti BMI1 (mean ± SD). Right panel: cells treated for 8 days were collected, the protein levels of BMI1 and GAPDH were analyzed. BMI1 antibody, purchased from Millipore (05-637-K), was used to detect overexpressed mouse BMI1 and endogenous human BMI1. **b** Left panel: 1×10^5 C4-2 cells per well (6-well plate) were infected with lentiviral shBMI1 or scrambled shRNA as control. Cells were cultured without androgen for 24 h and then treated with DHT (5 nM) or EtOH. Cell number was counted at indicated time-points; $*p < 0.05$ vs. Control, $\#p < 0.05$ vs. shBMI1 (mean ± SD). Right panel: cells treated for 8 days were collected, the protein levels of BMI1 and GAPDH were analyzed. **c** LNCaP cells were infected with adenovirus (Ad) to overexpress BMI1. LacZ Ad was used as a control. After 24 h, cells were seeded in 6-well plates (200 cells/well, in triplicates), and after another 24 h, the cells were treated with DHT (5 nM) or EtOH. After 12–14 days, the plates were gently washed with PBS and stained with 0.1% crystal violet. Left panel shows representative pictures of the colonies. Right panel shows colonies with over 50 cells were counted; $*p < 0.05$ vs. LacZ Ad (mean ± SD). **d** C4-2 cells were transfected with siBMI1 or scramble control and 24 h later the cells were seeded in 6-well plates (200 cells/well, in triplicates). After another 24 h, the cells were treated with DHT (5 nM) or EtOH. After 12–14 days, the plates were gently washed with PBS and stained with 0.1% crystal violet. Left panel shows representative pictures of the colonies. Right panel shows colonies with over 50 cells were counted; $*p < 0.05$ vs. scramble, $\#p < 0.05$ vs. siBMI1 (mean ± SD)

expression levels were not altered by DHT at either mRNA or protein levels, although AR signaling was significantly activated, as indicated by increased PSA and TMPRSS2 levels. The mRNA levels of PSA at 8 h post-DHT treatment changed accordingly: Combination #1 increased by 2.4-fold ($p = 0.0129$) and Combination #2 increased by 3.313-fold ($p = 0.0273$). The mRNA levels of TMPRSS2 at 8 h post-DHT treatment changed accordingly: Combination #1 increased by 4.246-fold ($p = 0.0175$) and Combination #2 increased by 3.759-fold ($p = 0.0034$) (Fig. 4e, f). These results strongly support the concept that BMI1 is a direct target gene of AR.

BMI1 plays a critical role in the development of castration-resistance

Since we showed that BMI1 expression levels were higher in CRPC than those in non-CRPC (Figs. 2 and 3), we hypothesized that BMI1 may promote CRPC progression and induce androgen-independent growth. To test our hypothesis, we overexpressed BMI1 by lentivirus transfection in androgen-dependent LNCaP cells and cultured the cells in androgen-depleted growth medium. As expected, we observed that androgen depletion arrested cell growth, and DHT treatment significantly stimulated cell growth, confirming that the growth of LNCaP cells is dependent on androgen (Fig. 5a). However, BMI1 overexpression markedly increased LNCaP cell growth by 7.26-fold (8 days post treatment, $p < 0.0001$) in the absence of DHT (Fig. 5a), suggesting that BMI1 alone was sufficient to convert LNCaP cells from androgen-dependent to androgen-independent (castration-resistant). We also utilized an adenovirus system to overexpress BMI1 in LNCaP cells and obtained similar results (Supplementary Fig. 7A). Further, as shown in Fig. 5b, CRPC cell line C4-2 grew normally in androgen-depleted growth medium, but its growth was significantly inhibited by 0.425-fold after BMI1 knockdown (8 days post treatment, $p < 0.0001$). Notably, this inhibition could be abolished by DHT treatment. We further confirmed this result after siRNA induced

knockdown in C4-2 cells (Supplementary Fig. 7B). These results suggest that BMI1 depletion could reverse C4-2 cells from a castration-resistant to an androgen-dependent state. Additionally, we observed that BMI1 overexpression in LNCaP cells significantly increased by 0.941-fold the number of colonies formed in the absence of DHT ($p = 0.0194$) compared to control cells (Fig. 5c), and BMI1 depletion in C4-2 cells decreased by 0.56-fold the number of colonies formed ($p = 0.0001$), which could be rescued by DHT (Fig. 5d). These results further indicate that BMI1 plays a critical role in the development of castration resistance.

BMI1 inhibitor PTC596 delays CRPC progression in vivo

PTC209, a BMI1-specific inhibitor, has been shown to effectively decrease tumor growth mediated by colon, lung, PCa stem cells, and leukemia [14–17]. Recently, we reported that PTC209 significantly inhibited CRPC tumor growth [6]. However, the poor oral bioavailability of PTC209 limits its therapeutic usefulness. PTC596, a recently developed BMI1 inhibitor [18], is an orally active small molecule in contrast to PTC209. Additionally, PTC596 has entered a Phase 1 clinical trial in patients with advanced solid tumors (NCT02404480). PTC596 has been reported to effectively increase apoptosis of acute myeloid leukemia (AML) cells [18]. Combination treatment with PTC596 and the Enhancer Of Zeste 2 polycomb repressive complex 2 subunit (EZH2) inhibitor EPZ6438 achieved remarkable efficacy in high-BMI1 and high-EZH2 Glioblastoma PDX tumors compared to control Glioblastoma tumors [19]. To test the effects of PTC596 in PCa, we first examined the effects of PTC596 on cell proliferation of VCaP and C4-2 cells, and observed a low IC50 (less than 0.05 μM) (Supplementary Fig. 8A and B). We further observed that both PTC209 and PTC596 substantially decreased BMI1 levels as well as androgen/AR signaling (Fig. 6a, b), consistent with our recent discovery that depleting BMI1 decreases AR protein levels signaling [6]. To assess the therapeutic efficacy of PTC596 in CRPC in vivo, we used a castration-resistant VCaP xenograft mouse model. PTC596 treatment significantly reduced tumor growth compared to vehicle control treatment (tumor volumes decreased by 0.466-fold 28 days after treatment, $p = 0.0001$), and its inhibitory effect is superior to that of PTC209 (Fig. 6c). Furthermore, Kaplan–Meier survival analysis revealed that PTC596 markedly and significantly prolonged the survival rate of tumor-bearing mice compared to vehicle control treatment ($p = 0.006$) (Fig. 6d) and had no effect on body weight (Supplementary Fig. 9). As expected, BMI1 and AR were dramatically decreased in PTC596-treated CRPC tumors compared with control tumors (BMI1 decreased by 0.606-fold, $p = 0.0457$) (Fig. 6e), suggesting PTC596 attained its target in vivo.

Discussion

BMI1 plays an important role in the initiation and development of castration-resistance as well as metastasis of PCa [20, 21]. Recently, a study reported that the presence of BMI1 is a distinguishing attribute between castration-resistant prostate epithelial cells (BMI1-high CRPC) and other castration-resistant prostate epithelial cells (i.e. Nkx3.1-high CRPC) [22]. However, it was not determined how BMI1 was upregulated in CRPC and how BMI1 played its role in castration-resistance.

In this study, we demonstrated that BMI1 expression is positively correlated with AR signaling. Our Tissue Microarrays (TMAs) indicated similar patterns of expression levels of BMI1 and AR at different stages of PCa progression. Further, our investigation revealed that BMI1 and AR protein levels are positively correlated with each other during disease progression. We further demonstrated that AR signaling both in vitro and in vivo regulates BMI1. We also used CRISPR gene editing technology to confirm that BMI1 is an AR direct target gene.

The majority of patients with neoadjuvant hormonal therapy (NHT)-treated PCa will develop CRPC, and treatment options for CRPC remain limited. We demonstrated that CRPC cells express more BMI1 than non-CRPC cells, suggesting that BMI1 contributes to CRPC development. Our mouse xenograft model revealed that the restored expression of BMI1 was associated with the establishment of castration-resistance. More interestingly, enzalutamide treatment, which successfully inhibited AR signaling in CRPC tumors, could significantly decrease BMI1 expression. Furthermore, we demonstrated that overexpression of BMI1 could convert PCa cells from the androgen-sensitive state to the castration-resistant (i.e., androgen-independent) state. In contrast, depleting BMI1 could reverse CRPC cells from their castration-resistant state to an androgen-sensitive state. These results strongly suggest that BMI1 is a major contributor to the development of castration-resistance.

Targeting BMI1 for advanced cancer patients has been proposed for many years. However, targeting BMI1 was not successful until the recent development of PTC209 and PTC596 [14, 18, 23]. PTC596 has entered a Phase-I clinical trial in patients with advanced solid tumors (NCT02404480). Here, we demonstrated that both PTC596 and PTC209 treatment decreased BMI1 and AR in CRPC cell lines and tumors, and significantly inhibited CRPC tumor growth in murine xenograft models. These results strongly support the notion that targeting BMI1 is a potential therapy for CRPC treatment.

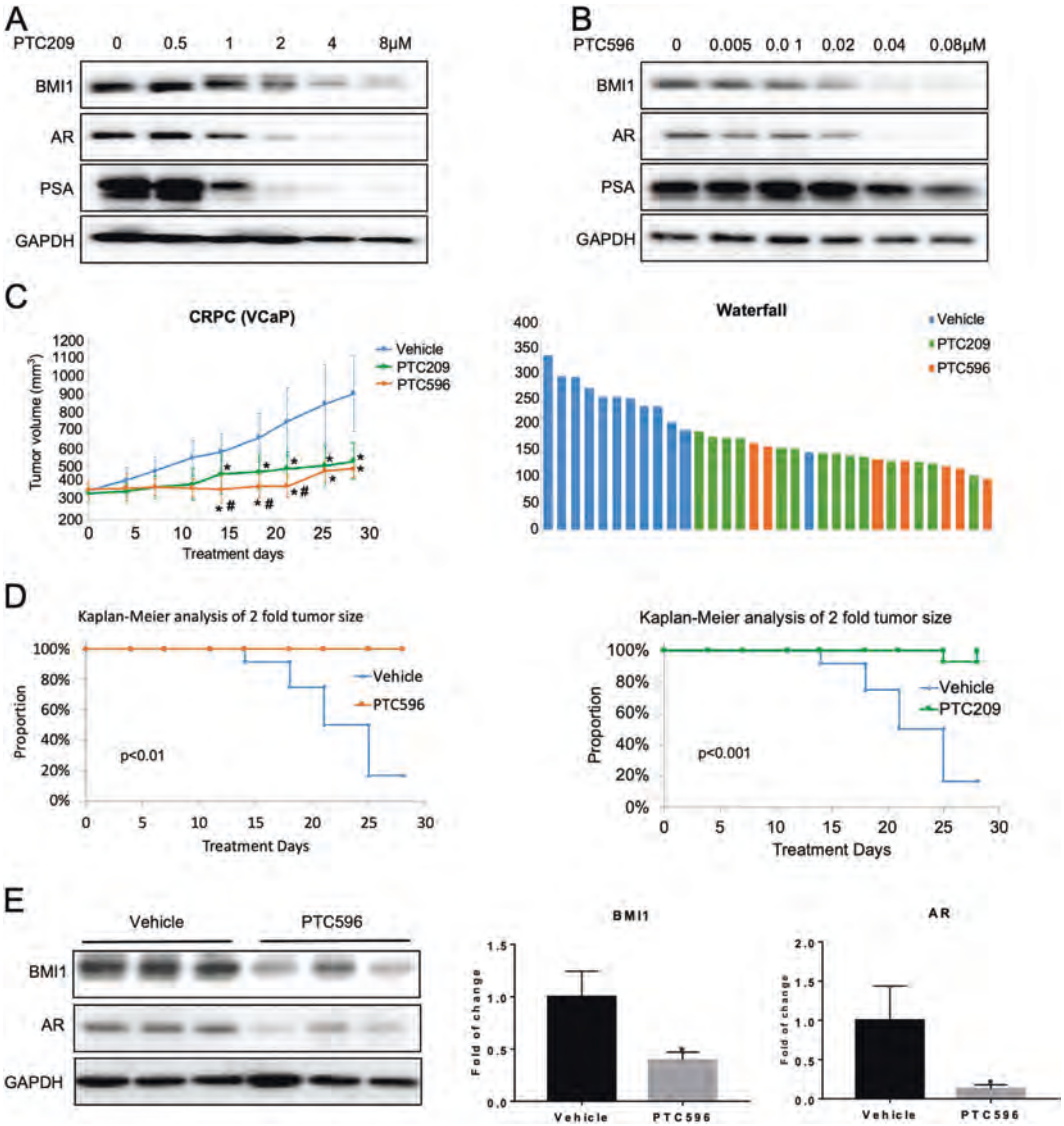

Fig. 6 BMI1 inhibitor delays CRPC progression in vivo. C4-2 cells were treated with PTC209 (**a**) or PTC596 (**b**) at indicated concentrations for 48 h. BMI1, AR, and PSA were analyzed by western blot, and GAPDH served as loading control. All experiments were biologically repeated at least three times. Representative images are shown. **c** Castrated mice possessing CRPC xenografts received vehicle ($n = 12$), PTC596 (12 mg/kg per day, 2 days per week, $n = 7$) or PTC209 (60 mg/kg per day, 5 days per week, $n = 13$). Caliper measurements were taken every 4 days to obtain tumor volume: Mean tumor volume ± SD, $*p < 0.05$ vs. vehicle, $\#p < 0.05$ vs. PTC209; right panel shows waterfall plot of tumor volume response. **d** Kaplan–Meier survival plot comparing progression-free survival. **e** Tumor tissues were lysed and analyzed by Western blot for BMI1, AR, and GAPDH. The left panel shows the representative western blot. Protein levels were quantified and normalized to GAPDH (right panel); $*p < 0.05$ vs. Vehicle (mean ± SD, $n = 6$)

In conclusion, BMI1 is directly regulated by androgen/AR signaling in PCa and is upregulated in CRPC along with AR signaling. Increased BMI1 could bind and stabilize AR protein, forming a positive feedback loop. BMI1 and AR together promote PCa cells proliferation independently of androgen and further facilitate CRPC progression (Fig. 7). Since elevated BMI1 plays a key role in the castration-resistance, targeting BMI1 may be a potential therapy for CRPC patients. This study sheds new light on the regulation mechanism of BMI1 in PCa and advances our understanding of CRPC development.

Methods

Drug treatments and antibodies

All drugs were commercially obtained and used at the designated concentrations (unless otherwise indicated): enzalutamide (IN034, Dieckmann), PTC209 (0, 0.5, 1, 2, and 4 μM, HY-15888, MedChem Express), PTC596 (0, 0.005, 0.01, 0.02, 0.04 and 0.08 μM, PTC Therapeutics), and DHT (A8380, Sigma). Enzalutamide were diluted in a vehicle of 0.5% CMC (C9481, Sigma) and 0.25% Tween-

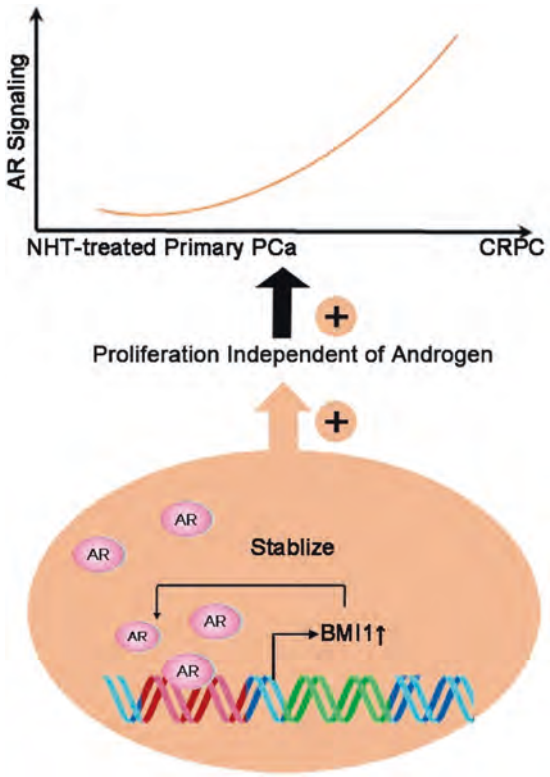

Fig. 7 Model for the regulatory mechanism of BMI1 and its role in the development of prostate cancer

80 (P8074, Sigma). PTC209 and PTC596 were diluted in a vehicle of 14% DMSO, 36% polyethylene glycol 400, and 50% polypropylene glycol 400. DHT was dissolved in ethanol and diluted using charcoal-stripped serum medium to 5 nM. Protein lysates were prepared in SDS-sample buffer (4 × reducing, BP-110R, Boston BioProducts). The secondary antibodies were Clean-Blot IP Detection Reagent (HRP, 21230, Thermo Scientific), goat anti-mouse IgG (H + L)-HRP (SA001-500, GenDEPOT), or goat anti-rabbit IgG (H+L)-HRP (SA002-500, GenDEPOT). Antibodies used for immunoblot assays are listed in Supplementary Table 4.

Cell culture

Human prostate cancer LNCaP cells were purchased from ATCC. C4-2 cells were provided by Dr. Arul M. Chinnaiyan. LNCaP-abl were provided by Dr. Zoran Culig. All cells used in this study were within 20 passages after receipt. LNCaP, C4-2, and LNCaP-abl were cultured in 5% CO_2 and maintained in vitro in RPMI 1640 medium supplemented with 10% FBS, 2 mmol/L glutamine, 100 units/ml penicillin, and 100 mg/ml streptomycin. These cell lines were recently authenticated by the University of Arizona Genetics Core using short tandem repeat (STR) profiling. Cell lines were mycoplasma negative during routine tests.

Gene expression data analysis

Normalized expression values of individual genes for 497, 160, and 87 patients from the TCGA, MSKCC, and Michigan cohorts, respectively (Fig. 1 and Supplementary Fig. 1), were downloaded from the Cbioportal website [24, 25].

Murine prostate tumor xenograft model

CB17 SCID mice were purchased from Charles River. Animal care and use conditions were followed in accordance with institutional and National Institutes of Health protocols and guidelines, and all studies were approved by Houston Methodist Institution Animal Care and Use Committee. Xenograft experiments in mice were performed as previously described [6]. Briefly, mice were anesthetized using 2% isoflurane (inhalation), and 2×10^6 VCaP prostate cancer cells suspended in 100 µl of PBS with 50% Matrigel were implanted subcutaneously into the dorsal flank on both sides of the mice. Tumor volumes were measured by length (a), width (b), and calculated as tumor volume = $\mathrm{MIN}(a)^2 \times \mathrm{MAX}(b)/2$. For the VCaP castration-resistant prostate tumor model, VCaP tumor- bearing mice were castrated when the tumors were approximately 200–300 mm^3 in size and once tumors started to grow back, mice were randomized and treated with vehicle, enzalutamide (10 mg/kg), PTC209 (60 mg/kg), or PTC596 (12 mg/kg) daily (5 days per week) and terminated approximately 28 days later. Loss of body weight during the course of the study was also monitored.

Western blotting

To denature proteins, lysates were added to 4 × reducing buffer and heated to 95 °C for 10 min. Protein levels were assessed by standard SDS–polyacrylamide gel electrophoresis and transferred to PVDF membranes (162-0177, BIO-RAD). Images were captured using the ChemiDoc XRS + Molecular Imager system (BIO-RAD). Blots were incubated overnight with primary antibodies at 4 °C, followed by detection with secondary antibody.

RNA isolation and QPCR

Total RNA was isolated from cells to generate cDNA using the RNA MiniPrep kit (Direct-zol, R2052, ZYMO Research) and amfiRivert cDNA Synthesis Platinum Master Mix (R5600-100, GenDEPOT). Each cDNA sample was amplified using Power SYBR Green PCR Master Mix (4367659, Applied Biosystem) on the QuantStudio 6 Flex Real-time PCR System (403115082, GE Healthcare). Briefly, the reaction conditions consisted of 2 µl of cDNA and 0.2 µM primers in a 10 µl final volume of super mix.

Each cycle consisted of denaturation at 95 °C for 15 s, annealing at 58.5 °C for 5 s, and extension at 72 °C for 10 s, respectively. 18S was used as an endogenous control to normalize each sample. The primers are listed in Supplementary Table 5. The experiment was performed in triplicate with three independent experiments.

Tissue microarrays (TMAs)

Prostate tumor biopsies were retrieved from Vancouver Prostate Centre tissue bank and used to construct several TMAs that had been reported previously [26, 27]. The first batch of a neoadjuvant hormonal therapy (NHT) TMA contained 31 tissue cores from patients who had not received hormonal therapies before radical prostatectomy and 28 tissue cores from patients who had tumor recurrence after receiving hormonal therapies and who had been diagnosed with CRPC. The tumors that had recurred were removed by transurethral resection prostatectomy to relieve obstructive symptoms. This CRPC TMA was also stained with Chromogranin A (CHGA) and N-CAM antibodies to identify any NEPC tissue cores. The second batch of NHT TMAs contained 125 tissue cores from patients who had not received hormonal therapies before radical prostatectomy and 44 tissue cores from patients who had tumor recurrence after receiving hormonal therapies and who had been diagnosed with CRPC.

Immunohistochemistry (IHC) analyses

IHC was performed by Ventana Discovery XT (Ventana) using a DAB MAP kit, as previously reported [26, 27]. All stained slides were scanned by a Leica SCN400 scanner. Digital images were evaluated by a pathologist, Dr. Ladan Fazli. BMI-1 histology score (H-score) was calculated by the Aperio ImageScope software based on both intensity and percentage of the IHC signals, according to the manufacturer's instructions (Leica Biosystems). The H-scores of Chromogranin A and N-CAM were also evaluated based on intensity and percentage of the IHC signals. A NEPC tissue core was defined if either CHGA or N-CAM H-score reached 0.3.

Lentiviral constructs

Lentivirus was packaged by co-transfection of constructs with second-generation packaging plasmids pMD2.G and psPAX2 into HEK293T cells on 6-well plates. After the first 24 h of transfection (250 ng of pMD2.G, 750 ng of psPAX2, 1 µg of target plasmid), the medium was changed to DMEM, and 48 and 72 h after transfection, the supernatants were pooled, filtered through a 0.45-µm filter, and used for infection.

Transfection

BMI1 siRNA (#1 s2015, #2 s2016) sequences were purchased from Thermo Scientific. Lipofectamine 2000 reagent (1815561, Invitrogen) and Opti-Mem (1774114, Gibco) were used in the transfection process. Cells (3×10^5) were plated in 6-well plates, grown without antibiotics to 80% confluence, and then transfected with siRNA sequences or their corresponding mock sequences using a Lipofectamine 2000 kit with the procedure provided by the manufacturer.

Chromatin immunoprecipitation (ChIP)

Chromatin immunoprecipitation (ChIP) was performed using the ChIP Assay kit (Millipore, Cat. 17-295) with the procedure provided by the manufacturer. For PCR analysis of enrichment of target gene promoters, 2 µl each of input DNA, AR-enriched, or IgG-enriched DNA were subjected to PCR using Platinum PCR Super mix (Invitrogen). Primers specific for target gene promoters or enhancers are listed in Supplementary Table 6.

ChIP-Seq data analysis

All ChIP-Seq reads were mapped to the version hg19 of the human genome using Bowtie (version 1.1.2) [28]. The Dregion function in DANPOS (version 2.2.3) [29] was used to calculate read density and define enrichment peaks. Briefly, we extended each read at the 3′ end to be 200 bp long and then calculated read density as the number of reads covering each base pair in the genome. For each sample, the total number of mapped reads was normalized to 25 million. DANPOS subtracted input background signal from the ChIP signal. Wigtobigwig [30] software was employed to convert signal file to bigwig format. The Chip-Seq peaks were visualized from UCSC genome browser [31].

Colony formation assay

Clonogenic growth assay methods are performed as previously described [32]. More details are described in the legend of Fig. 5.

CRISPR Single-guide RNA (sgRNA) preparation

Two open-access software programs, Cas-Designer (http://www.rgenome.net/cas-designer/) and CCTop (https://crispr.cos.uni-heidelberg.de) were used to design guide RNAs (gRNA). The sequences of the sgRNAs are: #1 GCAGTTGGCTTTATTTGCAG, #2 TAAAACGGGACC CATAGATG, #3 TTCCAGGGCTAGGCTAGCAA. Target DNA oligos were purchased from IDT (Integrated DNA Technologies) and cloned into the lentiCRISPR v2 plasmid

(Addgene plasmid# 52961) via BsmBI restriction enzyme sites upstream of the scaffold sequence of the U6-driven gRNA cassette. All plasmids were sequenced to confirm successful ligation.

Statistical analysis

Data were analyzed using Prism 6.0 software (GraphPad) and SPSS V.17, and presented as mean ± SD. Pearson's correlations were conducted to examine the relationships between AR and BMI1/RING1A et al. Two-tailed unpaired Student's *t*-tests were used to test for statistical significance in in vivo and in vitro experiments when two groups were compared. When the PCa genomic data were not normally distributed, Wilcoxon analysis was used. Statistical analyses comparing different tissue core groups (3 groups) were performed by one-way analysis of variance (ANOVA). Two-way ANOVA (4 groups × 4 time points) was conducted in in vitro experiments, while repeated measures of ANOVA (2 groups × 7 time points) were used in *in vivo* experiments. Kaplan–Meier analyses were performed to evaluate mouse survival rate of murine xenograft models. A $p < 0.05$ was considered to be significant. No statistical method was used to predetermine sample size. Mice were assigned at random to treatment groups and, where possible, mixed among cages. There were no inclusion or exclusion criteria. Whenever possible, the investigators were blinded to group allocation during the experiments and when assessing outcomes. Experiments were repeated two to three times.

Data availability

The next-generation sequencing data haves been deposited into Gene Expression Omnibus (GEO) under accession GSE97831.

Acknowledgements We thank Marla Weetall, John Baird, Art Branstrom and PTC Therapeutics for providing PTC596 and valuable inputs. We thank The University of Texas MD Anderson Cancer Center Science Park Next-Generation Sequencing (NGS) Facility for assistance with next-generation sequencing, and the Houston Methodist Comparative Medicine core facility, Jenny Chang, Anthony Kozielski, and Wei Qian for assistance with in vivo work. We thank Johnique Atkins for comments and editing this manuscript.

Funding This work is supported, in part, by grants from Houston Methodist Research Institute, Prostate Cancer Foundation (13YOUN007 to QC), U.S. Department of Defense (W81XWH-15-1-0639 and W81XWH-17-1-0357 to QC), American Cancer Society (Research Scholar Grant RSG-15-192-01-TBE to QC), and NIH/NCI (R01CA208257 to QC); KC is supported in part by grants from NIH/NIGMS (R01GM125632 to KC) and NIH/NHLBI (R01HL133254 to KC); JY is supported by NIH/NCI (R01CA172384), US Department of Defense (W81XWH-17-1-0405, W81XWH-17-1-0362, and W81XWH-17-1-0578). XD is supported by the Canadian Institute of Health Research (#MOP-137007) and TFRI New Frontier Grant #1062. WZ is supported by the National Natural Science Foundation of China (81572766,81972651 and 31771630), Guangdong Innovative and Entrepreneurial Research Team Program (2016ZT06S029), and Natural Science Foundation of Guangdong Province (2017A030312009); CL is supported by the China Scholarship Council (201706370147). TD is supported by National Natural Science Foundation of China (81770868 and 91742103), and Innovation-driven Project of Central South University (2017CX011). The University of Texas MD Anderson Cancer Center Science Park Next-Generation Sequencing (NGS) Facility is supported by CPRIT grants RP120348 and RP170002.

Compliance with ethical standards

Conflict of interest The authors declare that they have no conflict of interest.

References

1. Song LB, Li J, Liao WT, Feng Y, Yu CP, Hu LJ, et al. The polycomb group protein Bmi-1 represses the tumor suppressor PTEN and induces epithelial-mesenchymal transition in human nasopharyngeal epithelial cells. J Clin Invest. 2009;119:3626–36.
2. Ren H, Du P, Ge Z, Jin Y, Ding D, Liu X, et al. TWIST1 and BMI1 in cancer metastasis and chemoresistance. J Cancer. 2016;7:1074–80.
3. Glinsky GV, Berezovska O, Glinskii AB. Microarray analysis identifies a death-from-cancer signature predicting therapy failure in patients with multiple types of cancer. J Clin Invest. 2005;115:1503–21.
4. van Leenders GJ, Dukers D, Hessels D, van den Kieboom SW, Hulsbergen CA, Witjes JA, et al. Polycomb-group oncogenes EZH2, BMI1, and RING1 are overexpressed in prostate cancer with adverse pathologic and clinical features. Eur Urol. 2007;52:455–63.
5. Siddique HR, Saleem M. Role of BMI1, a stem cell factor, in cancer recurrence and chemoresistance: preclinical and clinical evidences. Stem Cells. 2012;30:372–8.
6. Zhu S, Zhao D, Yan L, Jiang W, Kim JS, Gu B, et al. BMI1 regulates androgen receptor in prostate cancer independently of the polycomb repressive complex 1. Nat Commun. 2018;9:500.
7. Taylor BS, Schultz N, Hieronymus H, Gopalan A, Xiao Y, Carver BS, et al. Integrative genomic profiling of human prostate cancer. Cancer Cell. 2010;18:11–22.
8. Grasso CS, Wu YM, Robinson DR, Cao X, Dhanasekaran SM, Khan AP, et al. The mutational landscape of lethal castration-resistant prostate cancer. Nature. 2012;487:239–43.
9. Wang W, Epstein JI. Small cell carcinoma of the prostate. A morphologic and immunohistochemical study of 95 cases. Am J Surg Pathol. 2008;32:65–71.
10. Grant CE, Bailey TL, Noble WS. FIMO: scanning for occurrences of a given motif. Bioinformatics. 2011;27:1017–8.
11. Mounir Z, Korn JM, Westerling T, Lin F, Kirby CA, Schirle M et al. ERG signaling in prostate cancer is driven through PRMT5-dependent methylation of the androgen receptor. *Elife* 2016; 5:pii: e13964.
12. Takayama K, Suzuki T, Fujimura T, Urano T, Takahashi S, Homma Y, et al. CtBP2 modulates the androgen receptor to promote prostate cancer progression. Cancer Res. 2014;74:6542–53.
13. Kron KJ, Murison A, Zhou S, Huang V, Yamaguchi TN, Shiah YJ, et al. TMPRSS2-ERG fusion co-opts master transcription factors and activates NOTCH signaling in primary prostate cancer. Nat Genet. 2017;49:1336–45.

14. Bansal N, Bartucci M, Yusuff S, Davis S, Flaherty K, Huselid E, et al. BMI-1 targeting interferes with patient-derived tumor-initiating cell survival and tumor growth in prostate cancer. Clin Cancer Res. 2016;22:6176–91.
15. Yong KJ, Basseres DS, Welner RS, Zhang WC, Yang H, Yan B, et al. Targeted BMI1 inhibition impairs tumor growth in lung adenocarcinomas with low CEBPα expression. Sci Transl Med. 2016;8:350ra104.
16. Kreso A, van Galen P, Pedley NM, Lima-Fernandes E, Frelin C, Davis T, et al. Self-renewal as a therapeutic target in human colorectal cancer. Nat Med. 2014;20:29–36.
17. Mourgues L, Imbert V, Nebout M, Colosetti P, Neffati Z, Lagadec P, et al. The BMI1 polycomb protein represses cyclin G2-induced autophagy to support proliferation in chronic myeloid leukemia cells. Leukemia. 2015;29:1993–2002.
18. Nishida Y, Maeda A, Kim MJ, Cao L, Kubota Y, Ishizawa J, et al. The novel BMI-1 inhibitor PTC596 downregulates MCL-1 and induces p53-independent mitochondrial apoptosis in acute myeloid leukemia progenitor cells. Blood Cancer J. 2017;7:e527.
19. Jin X, Kim LJY, Wu Q, Wallace LC, Prager BC, Sanvoranart T, et al. Targeting glioma stem cells through combined BMI1 and EZH2 inhibition. Nat Med. 2017;23:1352–61.
20. Kassi E, Moutsatsou P. Glucocorticoid receptor signaling and prostate cancer. Cancer Lett. 2011;302:1–10.
21. Clyne M. Prostate cancer: androgen deprivation causes EMT in the prostate. Nat Rev Urol. 2011;9:4.
22. Yoo YA, Roh M, Naseem AF, Lysy B, Desouki MM, Unno K, et al. Bmi1 marks distinct castration-resistant luminal progenitor cells competent for prostate regeneration and tumour initiation. Nat Commun. 2016;7:12943.
23. Yong KJ, Basseres DS, Welner RS, Zhang WC, Yang H, Yan B, et al. Targeted BMI1 inhibition impairs tumor growth in lung adenocarcinomas with low CEBPalpha expression. Sci Transl Med. 2016;8:350ra104.
24. Gao J, Aksoy BA, Dogrusoz U, Dresdner G, Gross B, Sumer SO, et al. Integrative analysis of complex cancer genomics and clinical profiles using the cBioPortal. Sci Signal. 2013;6:pl1.
25. Cerami E, Gao J, Dogrusoz U, Gross BE, Sumer SO, Aksoy BA, et al. The cBio cancer genomics portal: an open platform for exploring multidimensional cancer genomics data. Cancer Disco. 2012;2:401–4.
26. Yu Y, Yang O, Fazli L, Rennie PS, Gleave ME, Dong X. Progesterone receptor expression during prostate cancer progression suggests a role of this receptor in stromal cell differentiation. Prostate. 2015;75:1043–50.
27. Li H, Xie N, Chen R, Verreault M, Fazli L, Gleave ME, et al. UGT2B17 expedites progression of castration-resistant prostate cancers by promoting ligand-independent AR signaling. Cancer Res. 2016;76:6701–11.
28. Langmead B, Trapnell C, Pop M, Salzberg SL. Ultrafast and memory-efficient alignment of short DNA sequences to the human genome. Genome Biol. 2009;10:R25.
29. Chen K, Xi Y, Pan X, Li Z, Kaestner K, Tyler J, et al. DANPOS: dynamic analysis of nucleosome position and occupancy by sequencing. Genome Res. 2013;23:341–51.
30. Kent WJ, Zweig AS, Barber G, Hinrichs AS, Karolchik D. BigWig and BigBed: enabling browsing of large distributed datasets. Bioinformatics. 2010;26:2204–7.
31. Kent WJ, Sugnet CW, Furey TS, Roskin KM, Pringle TH, Zahler AM, et al. The human genome browser at UCSC. Genome Res. 2002;12:996–1006.
32. Ji Q, Hao X, Zhang M, Tang W, Yang M, Li L, et al. MicroRNA miR-34 inhibits human pancreatic cancer tumor-initiating cells. PLoS ONE. 2009;4:e6816.

Title: N6-methyladenosine Modulates Nonsense-mediated mRNA Decay in Human Glioblastoma

Authors and affiliations

Fuxi Li[#1, 2], Yang Yi[#3], Yanyan Miao[#4], Wenyong Long[5], Teng Long[1, 2], Siyun Chen[1, 2], Weisheng Cheng[2], Changye Zou[6], Yueyuan Zheng[4], Xingui Wu[2], Junjun Ding[2], Kaiyu Zhu[4], Delin Chen[1, 2], Qiongcong Xu[1,2], Jinkai Wang[2], Qing Liu[5], Feng Zhi[7], Jian Ren[4], Qi Cao[3,8]*, Wei Zhao[1, 2]*

[1]RNA Biomedical Institute, Sun Yat-Sen Memorial Hospital, Sun Yat-Sen University, Guangzhou 510120, China

[2]Key Laboratory of Stem Cells and Tissue Engineering (Sun Yat-Sen University), Ministry of Education, Guangzhou 510080, China

[3]Department of Urology, Northwestern University Feinberg School of Medicine, Chicago, IL, USA

[4]State Key Laboratory of Oncology in South China, Cancer Center, Collaborative Innovation Center for Cancer Medicine, School of Life Sciences, Sun Yat-sen University, Guangzhou 510060, China

[5]Neurosurgery Department, Xiangya Hospital, Central South University, Changsha, Hunan 410008, China

[6]Musculoskeletal Oncology Center, the First Affiliated Hospital of Sun Yat-Sen University, Guangzhou 510080, China

[7]Department of Neurosurgery, the First People's Hospital of Changzhou, Changzhou, Jiangsu, China

[8]Robert H. Lurie Comprehensive Cancer Center, Northwestern University Feinberg

School of Medicine, Chicago, IL, USA

#Contributed equally

Running title: m^6A modification Modulates NMD in GBM

Keywords: N6-methyladenosine (m^6A), METTL3, nonsense-mediated mRNA decay, glioblastoma, mRNA alternative splicing

Additional information

This work was supported by National Natural Science Foundation of China (81572766, 81702784, 81972651, 31771630, 81802974, 31771462, 81772614, 31471252, and 31500813), Guangdong Innovative and Entrepreneurial Research Team Program (2016ZT06S029), the Natural Science Foundation of Guangdong Province (2017A030312009, 2017A030310228, 2014TQ01R387, 2017A030313134 and 2016A030313238), the Special funds for Dapeng New District Industry Development (KY20160309). Q.C. is supported by U.S. Department of Defense (W81XWH-15-1-0639 and W81XWH-17-1-0357), American Cancer Society (TBE-128382) and NIH/NCI (R01CA208257).

*Correspondence:

Wei Zhao

Email: zhaowei23@mail.sysu.edu.cn

Phone: +86-13928976506

Mail address: Zhongshan School of Medicine, Sun Yat-Sen University, Guangzhou 510080, China

Qi Cao

Email: qi.cao@northwestern.edu

Phone: 1-312-503-5990

Mail address: NORTHWESTERN UNIVERSITY, 303 E CHICAGO AVE, TARRY 16-759, CHICAGO, IL 60611, USA

Disclosure of Potential Conflicts of Interest

No potential conflict of interest to disclose

Abstract

The N6-methyladenosine (m^6A) modification influences various mRNA metabolic events and tumorigenesis, however, its functions in nonsense-mediated mRNA decay (NMD) and whether NMD detects induced carcinogenesis pathways remain undefined. Here, we showed that the m^6A methyltransferase METTL3 sustained its oncogenic role by modulating NMD of splicing factors and alternative splicing isoform switches in glioblastoma (GBM). MeRIP-seq analyses showed that m^6A modification peaks were enriched at metabolic pathway-related transcripts in glioma stem cells (GSCs) compared with neural progenitor cells (NPCs). In addition, the clinical aggressiveness of malignant gliomas was associated with elevated expression of METTL3. Furthermore, silencing *METTL3* or overexpressing dominant-negative mutant METTL3 suppressed the growth and self-renewal of GSCs. Integrated transcriptome and MeRIP-seq analyses revealed that downregulating the expression of METTL3 decreased m^6A modification levels of serine- and arginine-rich splicing factors (*SRSFs*), which led to YTHDC1-dependent NMD of *SRSFs* transcripts and decreased SRSFs protein expression. Reduced expression of SRSFs led to larger changes in alternative splicing isoform switches. Importantly, the phenotypes mediated by METTL3 deficiency could be rescued by downregulating *BCL-X* or *NCOR2* isoforms. Overall, these results establish a novel function of m^6A in modulating NMD and uncover the mechanism by which METTL3 promotes GBM tumor growth and progression.

75 **Statement of significance:** Findings establish the oncogenic role of m^6A writer
76 METTL3 in glioblastoma stem cells.
77
78
79

Introduction

Nonsense-mediated mRNA decay (NMD) contributes to mRNA surveillance pathways that affect a broad spectrum of cellular functions and maintain homeostasis. Although the primary function of NMD in reducing errors in gene expression by eliminating mRNA transcripts that contain premature termination codons (PTCs) is well known, the mechanisms of target mRNA selection for NMD are still not well understood.

RNA methylation is a reversible modification of mRNA and has been linked to many types of cancer. N6-Methyladenosine (m^6A) represents the most abundant methylation modification of mRNAs in eukaryotes(1-3), and it regulates almost every aspect of mRNA metabolism, including RNA processing(4, 5), transport from the nucleus to cytoplasm(6, 7), translation(8, 9), and decay(10, 11). The m^6A methylation marks on mRNA are dynamically regulated in mammals through the methyltransferase complex, composed of the catalytic subunit METTL3, and demethylases (e.g., FTO and ALKBH5)(7, 11-13), and are detected by "m^6A readers". YTH domain-containing proteins, including YTHDF1-3, YTHDC1, and YTHDC2 act directly as "m^6A readers" and can interact with distinct subsets of m^6A sites to produce different effects on RNA processing(9, 10, 14-16). The function of m^6A RNA methylation is highly variable and context-dependent, and its underlying mechanisms in the recognition of NMD targets are not well understood.

Recent studies have revealed that m^6A methylation of mRNA results in diverse regulatory functions in cancer initiation and progression. In addition, dysregulated

m^{6}A methylation is closely related to various types of cancers. It has been reported that the m^{6}A methyltransferase METTL3 is required for the growth, survival, and invasion of cancer cells(17-19). The m^{6}A demethylase FTO was found to play a critical oncogenic role in promoting acute myeloid leukaemia (AML)(20). Although evidence is emerging, linking m^{6}A modulators and tumorigenesis, it remains to be determined whether m^{6}A modifications on different regions of mRNA, recognized by distinct readers, will lead to different cell fates. METTL3 elevates m^{6}A methylation modification to promote GSC stemness by enhancing SOX2 stability in GBM(21). Controversially, another research group found knockdown (KD) of *METTL3* dramatically promoted GSC self-renewal and tumorigenesis(22). Moreover, ALKBH5, which decreases m^{6}A modification in GSCs, exerts an important tumorigenic role in the progression of GBM through regulation of FOXM1 expression(23). These findings have raised questions about whether m^{6}A methylation modifications that affect GBM progression are dependent on the RNA sequence and are dynamically regulated.

Here, we observed preferential distribution of m^{6}A peaks in GBM cells. Elevated METTL3 in clinical specimens correlated with higher grades of gliomas, increased tumor recurrence, and worse clinical outcomes. Moreover, we found that silencing of *METTL3* led to reduced aggressive and tumorigenic capabilities, as well as diminished GSC phenotypes in GBM cells. MeRIP-seq and RNA-seq analyses revealed KD of *METTL3* led to downregulation of NMD-targeted splicing factor mRNA transcripts that was dependent on the m^{6}A reader YTHDC1. Importantly,

124 splice alterations of targeted mRNAs were critical for tumor growth inhibition and
125 suppression of stemness due to *METTL3* KD. Together, our study identifies m^6A
126 methyltransferase METTL3 as a modulator of NMD to sustain malignancy in GBM.
127

Materials and Methods

Glioma specimens and brain tissue collection

Both GBM and normal brain tissue surgical specimens were collected in The First People's Hospital of Changzhou and Xiangya Hospital of Central South University, in accordance with institution-approved protocols. Written informed consent was obtained from each study participant after a thorough explanation of the procedure and its risk, in compliance with the Declaration of Helsinki. Collected specimens were further split into two parts for RNA extraction and protein isolation. If only a limited amount of specimens was obtained, only a RNA extraction assay was performed. Three freshly obtained specimens were specifically used for primary cell establishment (see section below). All specimens were examined by neuropathologists to verify tumor types and grades.

Cell culture and reagents

The human GBM cell lines of U251 and U87MG were provided as a gift from Dr. Jun Cui's laboratory at Sun Yat-sen University and were grown in Gibco® Dulbecco's Modified Eagle's medium (DMEM) containing 10% fetal bovine serum (FBS, Gibco, USA) at 37°C in a humidified atmosphere containing 5% CO_2.

For the culture of primary GBM cells, surgically removed GBM specimens were washed with and minced in sterile phosphate-buffered saline (PBS). Next, a single-cell suspension was obtained by pressing the minced tissues through 40 μm cell strainers (Falcon, USA). Dissociated cells were cultured in DMEM supplemented with 15% FBS (Gibco, USA), 1× B27 (Invitrogen, USA), 20 ng/mL epidermal growth

factor (EGF) (CantonBIO, China), and 20 ng/mL fibroblast growth factor (FGF) (CantonBIO, China) at 37°C in a humidified atmosphere containing 5% CO_2. All primary cells were passaged every 7 days.

Subcutaneous tumor model and intracranial GBM Xenograft Model.

Five-week-old female Balb/c athymic nude mice were purchased from Model Animal Research Center of Nanjing University and housed in individually ventilated micro-isolator cages. Nude mice were divided into three groups of 6 mice each.

For subcutaneous tumor model, each mouse was injected subcutaneously in the right flank with 2×10^6 U87MG cells (*METTL3*-KD or control) in 100 μL PBS. Tumor sizes were determined with callipers every five days by measuring the length and width. Tumor volumes were calculated according to the following formula: volume (mm^3) = (length × width × width)/2. Fifty-eight days after the tumor cell injection, the mice were sacrificed and tumor xenografts were removed, weighted, fixed in formalin, and stored at 4°C.

For intracranial GBM Xenograft Model, each mouse was intracranially injected with 5×10^5 luciferase-transduced U87MG cells (*METTL3*-KD or control) in 10 μL PBS solution as described previously(24). Tumor growth was monitored by using a Xenogen IVIS Spectrum system (Caliper Life Sciences) weekly.

Animal experiments were approved by the Animal Care and Use Committee of Sun Yat-sen University.

Measurements of total m^6A mRNA levels

Total m^6A content was measured in 200 ng aliquots of total RNA extracted from

METTL3-KD or scrambled, control U87MG or U251 GBM cells using an m^{6}A RNA methylation quantification kit (Epigentek, USA), according to the manufacturer's instructions.

Methylated RNA immunoprecipitation-seq (MeRIP-seq)

Total RNA was isolated from *METTL3*-KD or scrambled control U87MG GBM cells, as mentioned above, and the mRNA was further separated using Dynabeads mRNA Purification Kit (Invitrogen, 61006). After fragmentation, using RNA fragmentation reagent (Invitrogen, AM8740), the obtained mRNA was immunoprecipitated with anti-m^{6}A antibody (Synaptic Systems, 202003), and then washed and eluted by competition with m^{6}A sodium salt (Sigma-Aldrich, M2780). Both input samples and immunoprecipitation (IP) eluates were used for preparing the sequencing libraries using NEBNext Ultra RNA Library Prep Kit for Illumina and submitted for sequencing using Illumina HiSeq 2500. Reads, mapping and m^{6}A peak calling, were performed as previously described(25). The m^{6}A peaks of sh*METTL3* U87MG cells were from the overlapped peaks of sh*METTL3*-1 and sh*METTL3*-2.

RNA immunoprecipitation (RIP)-qPCR analysis

In YTHDC1 RIP-qPCR experiments, U87MG cells were harvested and lysed in IP lysis buffer (150 mM KCL, 0.5 mM DTT, 5 mM EDTA, 0.5% NP-40, 25 Mm Tris, pH 7.4). Each lysate was further divided into three groups for anti-YTHDC1, anti-IgG (negative control), and Input (positive control). Either YTHDC1 antibody (Abcam, USA) or IgG was added to each sample to enrich RNA binding protein (RBP). Subsequently, the RBP of interest, together with the bound RNA, were collected using

194 dynabeads (Thermo fisher, USA). After washing off unbound material, the RBP was
195 digested by Proteinase K, and the RNA bound to immunoprecipitated RBP was
196 purified and reverse transcribed into cDNA. Then, qPCR assay was performed to
197 measure the %Input of *SRSFs* mRNAs in each group. The primer sequences used for
198 RIP-qPCR analysis were provided in **Supplementary Table 2**.

199 **Statistical analysis**

200 All analyses were performed using GraphPad Prism version 5.0 (GraphPad
201 Software, USA). The survival curves for combined expression of *METTL3* and
202 splicing factors were plotted according to the Kaplan-Meier method, using
203 PROGgene V2 software online (http://watson.compbio.iupui.edu/chirayu/proggene/).
204 The association among the expression levels of *METTL3* and splicing factors was
205 analyzed using Spearman's rank correlation. Data were presented as the mean ± SD,
206 and the significance levels of all tests were two-sided. The P value of less than 0.05
207 was considered statistically significant and marked as ' * '; a P value less than 0.01 or
208 0.001 was marked as ' ** ' and ' *** ', respectively.

Results

The m^{6}A methylome in glioma stem cells is distinct from that of normal neural progenitor cells

Previous studies have suggested that glioma stem cells (GSCs) are derived from mutated neural progenitor cells (NPCs), which are critical for GBM tumorigenesis(26). Using MeRIP-seq data from GSE87515(27) and GSE54365(28), we first compared the m^{6}A peaks at each locus between GSCs and NPCs, respectively, (**Fig. 1A**), and then, divided the peaks into three categories comprising gene loci with m^{6}A peak enrichment in: 1) both GSCs and NPCs; 2) GSCs, or 3) NPCs (denoted as "shared," "GSC," and "NPC," respectively) (**Fig. 1B; Supp. Fig. 1A**). We found that 9,627 loci in GSCs had elevated levels of m^{6}A modifications that were initially unmodified in NPCs (**Fig. 1B**). We further analyzed the signaling pathways of the three categories and found that loci with elevated levels of m^{6}A modifications were associated with metabolic pathways (**Fig. 1C and Supp. Fig. 1B**). Specifically, the cancer metabolism-associated loci TGFB2, TGFB3, and TEAD2 were highly enriched with m^{6}A modifications in GSCs (**Fig. 1D**).

The m^{6}A methyltransferase METTL3 is elevated in GBM clinical specimens.

To determine the expression of m^{6}A modulators in GBM, we first queried the Repository for Molecular Brain Neoplasia Data (REMBRANDT) datasets. Compared with normal brain controls, GBM specimens displayed increased levels of *METTL3*, *METTL14*, *YTHDF1*, and *YTHDF2* (**Supp. Fig. 2A**). To confirm these findings, we

examined the mRNA expression of m^6A modulators in 36 GBM specimens from the First People's Hospital of Changzhou. *METTL3* and *YTHDF2* were markedly elevated in GBM patient samples as compared with normal brain tissues (**Fig. 2A**). Western blot analysis also showed higher METTL3 protein levels in GBMs compared to that in normal brain tissues (**Supp. Fig. 2B**). Next, we examined METTL3 expression in a paraffin-embedded human glioma tissue array by immunohistochemistry. As expected, there were remarkably more METTL3-positive cells in GBMs (grade 4) compared to that in normal brain tissues or to that in lower grade gliomas (**Fig. 2B**). Intriguingly, significantly higher levels of METTL3 were found in recurrent tumors compared with paired, original tumors (**Fig. 2C**).

Next, we designed a screen based on a CRISPR/Cas9 library of sgRNAs to identify potential m^6A modulators regulating GBM cell proliferation and GSC sphere formation (**Supp. Table 1 and Supp. Fig. 2C**). We transduced U87MG cells with 16 sgRNA lentiviral supernatants (one sgRNA per well), containing a puromycin selection cassette to eliminate uninfected cells. Infected cells were grown in a 2D-monolayer and 3D-Matrigel for 7 days. After three rounds of screening, we found that METTL3 and YTHDF2 were involved in the maintenance of GBM cell proliferation (**Supp. Fig. 2D**) and sphere-forming capacity (**Fig. 2D**). Notably, high *METTL3* levels in GBMs predicted poorer patient survival (GBM patient data from REMBRANDT, GSE7696(29), and GSE43378(30)) (**Fig. 2E**). However, the expression of other modulators, except *YTHDF2*, did not significantly correlate with the time of GBM patient survival (**Supp. Fig. 2E**). Collectively, METTL3 was upregulated in GBMs

and may be critical for tumor growth.

The m^{6}A methylation catalytic domain of METTL3 is essential for its function in GBM.

To test whether METTL3 was essential for GBM cell growth, we suppressed the expression of METTL3 in GBM cells through shRNA-expressing lentiviruses. Both sh*METTL3*-1 and sh*METTL3*-2 could downregulate METTL3 expression in GBM cells (**Supp. Fig. 3A, B**). As expected, depletion of METTL3 also led to significantly reduced m^{6}A modification levels of mRNAs in both GBM cell lines (**Supp. Fig. 3C**). Compared with cells expressing control shRNAs, both *METTL3*-KD GBM cell lines (U87MG and U251) showed significantly reduced cell proliferation (**Fig. 3A**). Similar results were also obtained in *METTL3*-KD primary GBM cells derived from three patients with GBM at Xiangya Hospital (**Fig. 3A**). Moreover, overexpression of the m^{6}A catalytic inactive mutant METTL3 acted in a dominant-negative manner to suppress cell growth and m^{6}A modification levels of mRNAs in U87MG and U251 cells (**Fig. 3B; Supp. Fig. S3D, E**). Consistent with previous reports, *METTL3* KD increased the proportion of apoptotic cells in GBMs (**Fig. 3C; Supp. Fig. 3F**). Furthermore, *METTL3* KD resulted in significantly decreased migration and invasiveness of GBM cells (**Supp. Fig. 3G, H**). Conversely, overexpression of the METTL3 dominant-negative mutant in GBMs inhibited cell migration and invasion (**Supp. Fig. 3I**). These data support an important role of the m^{6}A catalytic domain of METTL3 in controlling GBM cell growth, survival, and invasion *in vitro*.

We further investigated whether METTL3 inhibits the tumorigenic capacity of GBM cells *in vivo*. When U87MG cells, transduced with sh*METTL3* lentiviruses, were inoculated into nude mice, the cells produced much smaller xenograft tumors compared to cells expressing scrambled, control shRNAs (**Supp. Fig. 3J, K**). Subsequently, the excised xenograft tumors were processed for immunohistochemistry (IHC) and terminal deoxynucleotidyl transferase dUTP nick end labelling (TUNEL) assay (**Supp. Fig. 3L**). Significantly reduced ratios of KI67-positive cells to apoptotic cells were observed in *METTL3* KD cell-derived tumors (**Supp. Fig. 3L**).

Compared with the control shRNA, both sh*METTL3* sequences significantly decreased stem cell size (**Supp. Fig. 4A**), number (**Fig. 3D**), and frequency (**Fig. 3E**) in GSC-derived tumor neurospheres. Whereas overexpression of WT METTL3 promoted U87MG and U251 neurosphere formation and stem cell frequency, the METTL3 mutant inhibited these phenotypes (**Fig. 3F; Supp. Fig. 4B, C**). Moreover, sh*METTL3* decreased the CD133-positive populations in U251- and U87MG-derived neurospheres (**Supp. Fig. 4D**). Compared with the mice injected with control U87MG spheroid-derived GSCs, those injected with shMETTL3-spheroid-derived GSCs displayed impaired tumor growth and a lower rate of tumor formation (**Fig. 3G**).

The m^{6}A modifications of splicing factor mRNAs are regulated by METTL3

To map m^{6}A modification sites and unveil potential METTL3 functions in GBM, we performed MeRIP-seq on U87MG cells with silenced *METTL3* (**Supp. Fig. 5A,**

297 **B**). Consistent with previous studies, we demonstrated that m^{6}A peaks in GBMs were
298 enriched in the RGACH motif (R = G/A; H = A/C/U) (**Fig. 4A**), and abundant in
299 coding sequences (CDSs) and untranslated regions (UTRs) of mRNAs (**Fig. 4B**).
300 Compared to the control GBMs, the m^{6}A peaks across entire gene bodies and 3'UTRs
301 were markedly decreased in sh*METTL3* GBMs (**Supp. Fig. 5C**). Furthermore, 6,444
302 genes with significantly decreased m^{6}A levels in sh*METTL3* GBMs were identified as
303 potential m^{6}A-regulated genes (**Fig. 4C**). Moreover, carcinogenesis pathways were
304 significantly enriched in these m^{6}A-regulated genes (**Fig. 4D**), suggesting a role for
305 METTL3-mediated m^{6}A modifications in GBM tumorigenesis.

306 We further characterized the molecular signaling pathways regulated by
307 METTL3 using RNA-seq (**Fig. 4E; Supp. Fig. 5D, E**). Transcripts encoding
308 apoptotic signaling pathways and glial cell differentiation genes were enriched in both
309 *METTL3*-KD GBM cells (**Fig. 4F, G**). The upregulated expression of apoptotic and
310 differentiation genes was confirmed by RT-qPCR (**Fig. 4H**). Interestingly, a large
311 number of genes was also significantly downregulated in *METTL3*-KD cells. Gene
312 ontology (GO) and GSEA analyses revealed that these downregulated genes were
313 mainly involved in RNA processing and mRNA splicing (**Fig. 4F, G**). The
314 downregulated expression of these splicing factors was also confirmed by RT-qPCR
315 (**Fig. 4H; Supp. Fig. 5F**). Next, we randomly selected several splicing factors
316 regulated by METTL3 and found that KD of these genes impaired the proliferation of
317 GBM cells (**Fig. 4I; Supp. Fig. 5G**). Consistently, we found that *METTL3* expression
318 positively correlated with splicing factors, especially *SRSF3*, *SRSF6*, and *SRSF11*

(**Fig. 4J; Supp.Fig.5H**). GBM specimens displayed increased levels of *SRSF3/6/11* compared with normal brain controls (**Supp. Fig. 5I**). Kaplan-Meier survival analysis revealed that patients with elevated expression of *METTL3* and *SRSF3/6/11* had shorter overall survival time (**Supp. Fig. 5J**). Together, these results identify SRSFs as downstream targets regulated by METTL3, which are dysregulated in GBM.

The m^{6}A modification of splicing factor transcripts mediates mRNA selection for NMD

Expression of splicing factors is regulated via alternative splicing of the conserved regions to yield mRNAs, which are degraded by NMD. However, whether a significant proportion of splicing factor mRNA transcripts occur via reduced levels of m^{6}A modifications and are ultimately degraded by NMD is not known. NMD analyses using the *METTL3*-KD RNA-seq data revealed that the mRNA transcripts that undergo NMD were significantly enriched in genes associated with RNA splicing **(Supp. Fig. 6A**). By comparing the m^{6}A modification of *SRSFs* in NPCs and GSCs, we found that m^{6}A modifications around start codon of splicing factor transcripts (e.g., *SRSFs*) were elevated (**Fig. 5A; Supp. Fig. 6B**). The specific m^{6}A modification sites of the mRNAs of *SRSFs* were identified by miCLIP-seq analyses(31) (**Supp. Fig. 6C**). Importantly, on the basis of the markedly decreased m^{6}A modification peaks, premature termination (i.e., stop) codons (PTCs) in the mRNAs of *SRSFs* were generated via exon inclusion or skipping upon METTL3 depletion (**Fig. 5B; Supp. Fig. 6D, E**). Therefore, these mRNAs with PTCs were predicted to be subject to

NMD, and the predicted protein products were not physiologically relevant. A similar phenotype was also found in other splicing factors (**Supp. Fig. 6E**). Silencing *METTL3* significantly reduced protein-coding mRNAs (mRNAs without PTCs) of *SRSFs* (**Fig. 5C**). In contrast, an inhibitory effect on mRNAs with PTCs was also observed upon overexpression of WT METTL3 (**Fig. 5D**). Moreover, protein-coding mRNAs of *SRSFs* were significantly decreased, upon overexpression of mutant METTL3 (**Fig. 5E**).

In order to investigate whether the mRNAs of *SRSFs* with PTCs were substrates for NMD, we analyzed steady-state levels of these mRNAs via inhibition of NMD. We used shRNA targeted at *UPF1* **(Supp. Fig. 6F**), which is the central component of the NMD pathway. Treatment with shRNA against *UPF1* greatly increased the steady-state levels of the mRNAs with PTCs and total mRNAs of *SRSFs* (**Fig. 5F)**. Similar increases in the levels of the mRNAs with PTCs were also observed after inhibition of NMD by treatment of cycloheximide (CHX) (**Fig. 5G**). In addition, we found that the expression levels of *SRSFs* NMD variants were decreased in clinical GBM samples **(Supp. Fig. 6G)**

The removal of m^{6}A modification around start codon of splicing factors are required for NMD in a YTHDC1 dependent manner

In order to analyze m^{6}A modification levels around start codon that modulate NMD signaling, we used a previously described (32) in vitro luciferase reporter systems (**Fig. 6A**). The reporter systems were derived from *SRSF6*, including the

pre-mRNA sequence from transcription start site (TSS) up to exon 3. The PTC in the intron 2 of *SRSF6* is maintained. In addition, we mutated the A with G to inactivate the m^6A modification-mediated exon inclusion. We observed that the *SRSF6*-Renilla fused mRNA is m^6A modified (**Supp. Fig. 7A**). Consistent with previous results, KD *METTL3* efficiently promoted the formation of the mRNA with PTC in the WT reporter, as indicated by reduced luciferase activity (**Fig. 6B**). However, no significant change of luciferase activity occurred in the reporter with the mutation in m^6A modification (**Fig. 6B**). Similarly, a lack of luciferase activity increase has also been observed with addition of the METTL3 mutant in GBM cells, compared with addition of the WT METTL3 (**Fig. 6C**). RT-qPCR analyses showed higher NMD RNA (RNA with PTC) levels and lower protein-coding mRNA (mRNA without PTC) levels in mutated *SRSF6* reporter compared to WT reporter, further suggesting that the m^6A modification is critical for inhibition of NMD (**Supp. Fig. 7B**). Inhibition of NMD with sh*UPF1* greatly increased the Renilla-*SRSF6* NMD RNA and total mRNA of mutated reporter (**Supp. Fig. 7C**). To further analyze the effects of m^6A modifications on NMD, a reporter was constructed consisting of exon 2, exon 3, and flanking intron sequences of *SRSF3* without m^6A modification site (**Supp. Fig. 7D**). In contrast to the m^6A modification around start codon reporter system data, this reporter was greatly resistant to KD of *METTL3* induced NMD (**Supp. Fig. 7E**). Consistently, WT METTL3 cannot increase the luciferase activity of *SRSF3* minigene reporter contracts without m^6A modification site (**Supp. Fig. 7F**).

Adenine base editing is a novel genome editing approach to convert a target T•A

385 to C•G without requiring homology directed repair or introducing double-stranded
386 DNA breaks(33). To generate m^{6}A site mutation in the *SRSFs* gene of interest in
387 U87MG cells, we transduced the base editor construct and guide RNA targeting the
388 *SRSF3* m^{6}A modification site around start codon (**Fig. 6D**). A total of 14 cell clones
389 were obtained by limited dilution and Sanger sequencing indicated that 9 carried the
390 expected mutation (**Fig. 6E**). We next found the NMD RNA of *SRSF3* significantly
391 increased in m^{6}A mutant U87MG cells compared to WT control (**Fig. 6F**). These
392 results support that m^{6}A modifications around start codon mediate repression of NMD
393 in GBM.

394 YTHDC1 has been reported as an m^{6}A modification reader that mediates mRNA
395 splicing, and mutating either W377 or W428 to alanine completely disrupts its
396 binding to m^{6}A RNA(15). KO of *YTHDC1* reduced sphere number substantially in
397 METTL3 overexpression cells but not in control cells (**Supp. Fig. 7G**).
398 Overexpressing mutant YTHDC1 (m^{6}A binding activity loss) failed to enhance the
399 sphere formation capacity of U87MG cells (**Supp. Fig. 7H**), suggesting that
400 YTHDC1 contributes to the GBM phenotype (e.g. sphere formation) dependently on
401 its m^{6}A binding activity. Moreover, RIP-qPCR assay results showed that YTHDC1
402 binds to *SRSF3*, *SRSF6*, and *SRSF11* mRNA when compared to negative control (**Fig.**
403 **6G; Supp. Fig. 7I**). In addition, by analyzing PAR-CLIP-seq data from GSE74397(7)
404 and GSE58352(2), we found YTHDC1 binds near the start codon region of *SRSFs*
405 mRNAs (**Supp. Fig. 7J**). KD *YTHDC1* led to the accumulation of NMD of *SRSF3*,
406 *SRSF6*, and *SRSF11* mRNAs in GBM cells (**Fig. 6H**). Moreover, KD *YTHDC1* could

affect the luciferase activity of the WT *SRSF6* minigene reporter but not the *SRSF6* reporter with the mutated m^{6}A site (**Fig. 6I**). Together, these data suggest that *YTHDC1* KD mediated NMD is dependent on m^{6}A around start codon of the mRNA in GBM cells.

KD of the m^{6}A methyltransferase *METTL3* results in dysregulation of alternative splicing events in GBM.

We compared the alterative splicing events in *METTL3* KD U87MG cells compared with U87MG control cells. Using the rMATS tool, a total number of alternative splicing events was identified with an obvious change of exon inclusion levels (ψ, $\psi \geq 0.1$). We found that downregulation of splicing factors can affect various types of alternative splicing, including skipped exon (SE), alternative 5' ss exon (A5SS), alternative 3' ss exon (A3SS), retained intron (RI), and mutually exclusive exons (MXE), and in particular, SE events in sh*METTL3* U87MG cells were most affected (**Fig. 7A**). Subsequent analysis indicated that the SE type of alternative splicing was negatively regulated by *METTL3*-KD, whereas A3SS, MXE, and RI were positively regulated by *METTL3*-KD (estimated by changes of ψ after *METTL3*-KD) (**Fig. 7B**). Next, we compared genes that were differentially spliced in *METTL3*-KD U87MG cells to cells with scrambled control shRNA. When analyzing the cellular functions of METTL3-regulated alternative events using gene ontology, we found that METTL3 affected alternative splicing of a number of genes, such as *BCL-X* and *NCOR2*, with functions in cancer cell death and motility (**Fig. 7C; Supp.**

Fig. 8A).

BCL-X is a well-known example of genes critical for cancer that has splicing variants that can function as cancer biomarkers and therapeutic targets. The *BCL-XL* isoform is anti-apoptotic in various cancer types, whereas the *BCL-XS* isoform is pro-apoptotic in cancer. Using semi-quantitative RT-PCR and qPCR, we confirmed that KD of *METTL3* significantly shifted the transcription of *BCL-XL* into *BCL-XS* (**Fig. 7D, E; Supp. Fig. 8B**). The protein levels of *BCL-XL* were also reduced in *METTL3*-KD GBM cells (**Supp. Fig. 8C**). To examine whether the splicing alteration of *BCL-X* was responsible for the *METTL3*-KD phenotypes, we designed shRNAs to specifically target *BCL-XS* in order to inhibit the expression of *BCL-XS* but not *BCL-XL* (**Supp. Fig. 8D**). As shown in **Figure 7F** and **7G**, *METTL3* and *BCL-XS* double-KD GBM cells grew significantly faster with reduced apoptosis than cells with the *METTL3*-KD alone. This phenotypic rescue suggests that *METTL3* maintains the tumorigenicity of GBM cells, at least partially, through the splicing of *BCL-X*.

NCOR2 (also known as *SMRT*) exists in two major splicing isoforms, α and τ, which have different roles in preserving cellular identity and tissue homeostasis. Little is known about potential functional differences between these two isoforms in GBM. Using semi-quantitative RT-PCR and qPCR, we revealed that KD of *METTL3* significantly increased the transcription of isoform α of *NCOR2* (**Fig. 7H, I; Supp. Fig. 8E**). RT-PCR analysis showed that shRNAs targeting isoform α specifically inhibited its expression, but not the τ isoform of *NCOR2* in U87MG cells (**Supp. Fig. 8F**). Furthermore, we demonstrated that KD of the *NCOR2*α isoform partially rescued

METTL3 KD-induced inhibition of U87MG cell growth (**Fig. 7J**). In addition, our neurosphere formation data show that KD of the *NCOR2*α isoform significantly increased the neurosphere formation capacity and stem cell frequency in *METTL3*-KD U87MG cells (**Fig. 7K, L**), and together these data suggest that the NCOR2α isoform may play an important role in the regulation of GSC self-renewal.

Discussion

In this study, we established a novel mechanism for m^6A modifications around start codon of mRNA splicing factors in modulating NMD of these splicing factors. In addition, we found that METTL3 modulated alternative splicing of *BCLX* and *NCOR2*, which leads to GBM tumor outgrowth and self-renewal. Unlike previous studies, reporting that m^6A modifications at 3'-terminal ends are destabilizers of mRNA, our study revealed that m^6A modifications around start codon stabilize the mRNAs of *SRSFs* by preventing NMD. By preventing NMD and promoting mRNA degradation, m^6A modifications act as a molecular rheostat to finely adjust the transcript levels of *SRSFs* in order to influence alternative splicing events.

The role that METTL3 plays in cancer is complex. Two research teams reported opposite conclusions on the role that METTL3 plays in the self-renewal and tumorigenesis of GSCs. The reasons for these opposite conclusions may depend on the patients from whom the GBM cells originated and other compensatory genetic mutations and epigenetic changes in GBM cells. In this study, we chose clinical GBM samples from different stages, knocked down *METTL3* expression using both

sgRNAs and shRNAs in primary GBM cells, and validated our findings using catalytic inactive mutants of METTL3. All of these results consistently demonstrated that METTL3 promotes proliferation and self-renewal of GBM cells. Notably, the oncogenic ability of METTL3 is dependent upon the m^6A methyltransferase catalytic domain. Interestingly, although KD *METTL14* expression reduced mRNA m^6A levels in GSCs(22), KO of *METTL14* has no effect on GBM oncogenicity. A recent study in acute myeloid leukemia cells showed that METTL3 bound the promoter regions of active genes (about 80 genes) independent of METTL14(34). They also showed that CEBPZ is required for recruitment of METTL3 to the promoters. Their results indicate that specialized partner proteins might exist at splicing factor loci in GBM cells which give clues to decipher METTL14 independent METTL3's functions in GBM.

M^6A modifications may play different roles at different developmental stages of GMB tumors. In glioma, the mutation of isocitrate dehydrogenase 1 (*IDH1*) occurs frequently, which results in accumulation of the metabolic by-product 2-hydroxyglutarate (2-HG). The 2-HG could inhibit FTO activity, thereby increasing global m^6A modifications and contributing to cancer initiation. In the late stage of glioma, high m^6A modification levels may increase epigenetic reprogramming of non-GSCs into GSCs, whereas KD *METTL3* may reduce the proportion of GSCs in GBM. This hypothesis was indirectly verified by the observation that KD of *METTL3* in pluripotent stem cells, at naïve or primed states, resulted in different cell fate transitions(35). Thus, strategies designed to reduce levels of m^6A modifications may

provide a means to target malignant GBM and to develop more effective therapies.

The prevailing goal of understanding the regulatory roles of m^6A modifications in RNA processing has been mainly focused on the regulation of mRNA translation or mRNA stability. Indeed, we found that METTL3 regulates the stability of a specific set of transcripts, such as apoptosis pathways and glial differentiation genes, in GBM. The m^6A-binding protein YTHDF2 may recognize these methylated mRNAs, leading to their decay and subsequently to decreased cell apoptosis and differentiation, thereby promoting GBM tumor growth and dedifferentiation. Another m^6A modification reader, YTHDC1, is involved in the process of alternative splicing through recruitment and modulation of splicing factors to their targeted RNAs(36). We have presented a number of findings supporting the notion that m^6A modifications modulate the NMD of splicing factors. The NMD pathway protects eukaryotic cells by reducing the production of harmful truncated proteins translated from PTC-bearing mRNA transcripts. In our study, the reduced m^6A modifications by KD *METTL3* consequently led to the degradation of *SRSFs* transcripts via triggering NMD, and thus, control of GBM initiation and progression. It should be noted that KD *METTL3* affected not only YTHDC1 mediated NMD, but also the m^6A mediated mRNA degradation. Therefore, the effect of KO *YTHDC1* on GBM phenotype was not as significant as that of KD/KO *METTL3*.

SRSFs proteins are known for their ability to promote exon inclusion and exon-skipping events, suggesting that the regulatory role of SRSFs proteins in alternative events. Brain tissue has been found to have particularly high levels of

alternative splicing(37, 38). Consistently, a large number of cancer-relevant genes have undergone splice alterations in GBM(39-41). The importance of alternative splicing in the development of GBM was further reinforced by the findings that a large number of splicing factors were overexpressed in GBM(42, 43), yet the mechanisms responsible for this upregulation and its clinical relevance remain to be fully addressed. Our results support a model where METTL3 controls the cancer-relevant phenotypes of GBM cells by promoting the expression of SRSFs. This subsequently results in the creation of cancer-specific alternative splicing patterns, such as the preferential expression of the anti-apoptotic transcript variant of *BCL-X* and the GSC-promoting transcript variant of *NCOR2* (**Fig. 7M**). It is worth noting that analysis of clinical outcomes revealed significant relationships between combined expression of METTL3 and splicing factors with GBM patient prognosis.

Taken together, this study provides an important mechanistic insight into how m^6A methyltransferase METTL3 serves as an NMD regulator of splicing factors with potential clinical implications of alternative splicing events of *BCL-XS* and *NCOR2*. Our study also demonstrates that expression of METTL3 can be used to dissect the molecular differences between histologically similar GBM entities and to help predict GBM prognosis.

Acknowledgements

This work was supported by National Natural Science Foundation of China (81572766, 81702784, 81972651, 31771630, 81802974, 31771462, 81772614, 31471252, and 31500813), Guangdong Innovative and Entrepreneurial Research

539 Team Program (2016ZT06S029), the Natural Science Foundation of Guangdong
540 Province (2017A030312009, 2017A030310228, 2014TQ01R387, 2017A030313134
541 and 2016A030313238), the Special funds for Dapeng New District Industry
542 Development (KY20160309). Q.C. is supported by U.S. Department of Defense
543 (W81XWH-15-1-0639 and W81XWH-17-1-0357), American Cancer Society
544 (TBE-128382) and NIH/NCI (R01CA208257).

545

References

1. Desrosiers R, Friderici K, Rottman F. Identification of methylated nucleosides in messenger RNA from Novikoff hepatoma cells. Proceedings of the National Academy of Sciences of the United States of America. 1974;71:3971-5.
2. Dominissini D, Moshitch-Moshkovitz S, Schwartz S, Salmon-Divon M, Ungar L, Osenberg S, et al. Topology of the human and mouse m6A RNA methylomes revealed by m6A-seq. Nature. 2012;485:201-6.
3. Meyer KD, Saletore Y, Zumbo P, Elemento O, Mason CE, Jaffrey SR. Comprehensive analysis of mRNA methylation reveals enrichment in 3' UTRs and near stop codons. Cell. 2012;149:1635-46.
4. Zhao X, Yang Y, Sun BF, Shi Y, Yang X, Xiao W, et al. FTO-dependent demethylation of N6-methyladenosine regulates mRNA splicing and is required for adipogenesis. Cell research. 2014;24:1403-19.
5. Bartosovic M, Molares HC, Gregorova P, Hrossova D, Kudla G, Vanacova S. N6-methyladenosine demethylase FTO targets pre-mRNAs and regulates alternative splicing and 3'-end processing. Nucleic acids research. 2017;45:11356-70.
6. Fustin JM, Doi M, Yamaguchi Y, Hida H, Nishimura S, Yoshida M, et al. RNA-methylation-dependent RNA processing controls the speed of the circadian clock. Cell. 2013;155:793-806.
7. Zheng G, Dahl JA, Niu Y, Fedorcsak P, Huang CM, Li CJ, et al. ALKBH5 is a mammalian RNA demethylase that impacts RNA metabolism and mouse fertility. Molecular cell. 2013;49:18-29.
8. Meyer KD, Patil DP, Zhou J, Zinoviev A, Skabkin MA, Elemento O, et al. 5' UTR m(6)A Promotes Cap-Independent Translation. Cell. 2015;163:999-1010.
9. Wang X, Zhao BS, Roundtree IA, Lu Z, Han D, Ma H, et al. N(6)-methyladenosine Modulates Messenger RNA Translation Efficiency. Cell. 2015;161:1388-99.
10. Wang X, Lu Z, Gomez A, Hon GC, Yue Y, Han D, et al. N6-methyladenosine-dependent regulation of messenger RNA stability. Nature. 2014;505:117-20.
11. Wang Y, Li Y, Toth JI, Petroski MD, Zhang Z, Zhao JC. N6-methyladenosine modification destabilizes developmental regulators in embryonic stem cells. Nature cell biology. 2014;16:191-8.
12. Jia G, Fu Y, Zhao X, Dai Q, Zheng G, Yang Y, et al. N6-methyladenosine in nuclear RNA is a major substrate of the obesity-associated FTO. Nature chemical biology. 2011;7:885-7.
13. Liu J, Yue Y, Han D, Wang X, Fu Y, Zhang L, et al. A METTL3-METTL14 complex mediates mammalian nuclear RNA N6-adenosine methylation. Nature chemical biology. 2014;10:93-5.
14. Shi H, Wang X, Lu Z, Zhao BS, Ma H, Hsu PJ, et al. YTHDF3 facilitates translation and decay of N(6)-methyladenosine-modified RNA. Cell research. 2017;27:315-28.
15. Xu C, Wang X, Liu K, Roundtree IA, Tempel W, Li Y, et al. Structural basis for selective binding of m6A RNA by the YTHDC1 YTH domain. Nature chemical biology. 2014;10:927-9.
16. Hsu PJ, Zhu Y, Ma H, Guo Y, Shi X, Liu Y, et al. Ythdc2 is an N(6)-methyladenosine binding protein that regulates mammalian spermatogenesis. Cell research. 2017;27:1115-27.
17. Lin S, Choe J, Du P, Triboulet R, Gregory RI. The m(6)A Methyltransferase METTL3 Promotes Translation in Human Cancer Cells. Molecular cell. 2016;62:335-45.
18. Chen M, Wei L, Law CT, Tsang FH, Shen J, Cheng CL, et al. RNA N6-methyladenosine methyltransferase-like 3 promotes liver cancer progression through YTHDF2-dependent posttranscriptional silencing of SOCS2. 2018;67:2254-70.
19. Vu LP, Pickering BF, Cheng Y, Zaccara S, Nguyen D, Minuesa G, et al. The N(6)-methyladenosine

(m(6)A)-forming enzyme METTL3 controls myeloid differentiation of normal hematopoietic and leukemia cells. 2017;23:1369-76.

20. Li Z, Weng H, Su R, Weng X, Zuo Z, Li C, et al. FTO Plays an Oncogenic Role in Acute Myeloid Leukemia as a N(6)-Methyladenosine RNA Demethylase. Cancer cell. 2017;31:127-41.

21. Visvanathan A, Patil V, Arora A, Hegde AS, Arivazhagan A, Santosh V, et al. Essential role of METTL3-mediated m(6)A modification in glioma stem-like cells maintenance and radioresistance. Oncogene. 2018;37:522-33.

22. Cui Q, Shi H, Ye P, Li L, Qu Q, Sun G, et al. m(6)A RNA Methylation Regulates the Self-Renewal and Tumorigenesis of Glioblastoma Stem Cells. Cell reports. 2017;18:2622-34.

23. Zhang S, Zhao BS, Zhou A, Lin K, Zheng S, Lu Z, et al. m6A Demethylase ALKBH5 Maintains Tumorigenicity of Glioblastoma Stem-like Cells by Sustaining FOXM1 Expression and Cell Proliferation Program. Cancer cell. 2017;31:591-606 e6.

24. Ozawa T, James CD. Establishing intracranial brain tumor xenografts with subsequent analysis of tumor growth and response to therapy using bioluminescence imaging. Journal of visualized experiments : JoVE. 2010.

25. Dominissini D, Moshitch-Moshkovitz S, Salmon-Divon M, Amariglio N, Rechavi G. Transcriptome-wide mapping of N(6)-methyladenosine by m(6)A-seq based on immunocapturing and massively parallel sequencing. Nature protocols. 2013;8:176-89.

26. Alcantara Llaguno S, Chen J, Kwon CH, Jackson EL, Li Y, Burns DK, et al. Malignant astrocytomas originate from neural stem/progenitor cells in a somatic tumor suppressor mouse model. Cancer cell. 2009;15:45-56.

27. Zhang S, Zhao BS, Zhou A, Lin K, Zheng S, Lu Z, et al. m(6)A Demethylase ALKBH5 Maintains Tumorigenicity of Glioblastoma Stem-like Cells by Sustaining FOXM1 Expression and Cell Proliferation Program. Cancer cell. 2017;31:591-606 e6.

28. Schwartz S, Mumbach MR, Jovanovic M, Wang T, Maciag K, Bushkin GG, et al. Perturbation of m6A writers reveals two distinct classes of mRNA methylation at internal and 5' sites. Cell reports. 2014;8:284-96.

29. Murat A, Migliavacca E, Gorlia T, Lambiv WL, Shay T, Hamou MF, et al. Stem cell-related "self-renewal" signature and high epidermal growth factor receptor expression associated with resistance to concomitant chemoradiotherapy in glioblastoma. Journal of clinical oncology : official journal of the American Society of Clinical Oncology. 2008;26:3015-24.

30. Kawaguchi A, Yajima N, Tsuchiya N, Homma J, Sano M, Natsumeda M, et al. Gene expression signature-based prognostic risk score in patients with glioblastoma. Cancer science. 2013;104:1205-10.

31. Linder B, Grozhik AV, Olarerin-George AO, Meydan C, Mason CE, Jaffrey SR. Single-nucleotide-resolution mapping of m6A and m6Am throughout the transcriptome. Nature methods. 2015;12:767-72.

32. Jin S, Zhang X, Miao Y, Liang P, Zhu K, She Y, et al. m(6)A RNA modification controls autophagy through upregulating ULK1 protein abundance. Cell research. 2018;28:955-7.

33. Gaudelli NM, Komor AC, Rees HA, Packer MS, Badran AH, Bryson DI, et al. Programmable base editing of A*T to G*C in genomic DNA without DNA cleavage. Nature. 2017;551:464-71.

34. Barbieri I, Tzelepis K, Pandolfini L, Shi J, Millan-Zambrano G, Robson SC, et al. Promoter-bound METTL3 maintains myeloid leukaemia by m(6)A-dependent translation control. Nature. 2017;552:126-31.

634 35. Zhao BS, He C. Fate by RNA methylation: m6A steers stem cell pluripotency. Genome biology.
635 2015;16:43.
636 36. Xiao W, Adhikari S, Dahal U, Chen YS, Hao YJ, Sun BF, et al. Nuclear m(6)A Reader YTHDC1
637 Regulates mRNA Splicing. Molecular cell. 2016;61:507-19.
638 37. Yeo G, Holste D, Kreiman G, Burge CB. Variation in alternative splicing across human tissues.
639 Genome biology. 2004;5:R74.
640 38. Modrek B, Resch A, Grasso C, Lee C. Genome-wide detection of alternative splicing in expressed
641 sequences of human genes. Nucleic acids research. 2001;29:2850-9.
642 39. Cheung HC, Hai T, Zhu W, Baggerly KA, Tsavachidis S, Krahe R, et al. Splicing factors PTBP1 and
643 PTBP2 promote proliferation and migration of glioma cell lines. Brain : a journal of neurology.
644 2009;132:2277-88.
645 40. Lo HW, Zhu H, Cao X, Aldrich A, Ali-Osman F. A novel splice variant of GLI1 that promotes
646 glioblastoma cell migration and invasion. Cancer research. 2009;69:6790-8.
647 41. Yu Y, Jiang X, Schoch BS, Carroll RS, Black PM, Johnson MD. Aberrant splicing of cyclin-dependent
648 kinase-associated protein phosphatase KAP increases proliferation and migration in glioblastoma.
649 Cancer research. 2007;67:130-8.
650 42. Pavlyukov MS, Yu H, Bastola S, Minata M, Shender VO, Lee Y, et al. Apoptotic Cell-Derived
651 Extracellular Vesicles Promote Malignancy of Glioblastoma Via Intercellular Transfer of Splicing Factors.
652 Cancer cell. 2018;34:119-35.e10.
653 43. Lefave CV, Squatrito M, Vorlova S, Rocco GL, Brennan CW, Holland EC, et al. Splicing factor
654 hnRNPH drives an oncogenic splicing switch in gliomas. The EMBO journal. 2011;30:4084-97.

655

Figure legends

Figure 1. The m^{6}A methylome in neural progenitor cells (NPCs) and glioma stem cells (GSCs)

(**A**) Venn diagrams of m^{6}A modification peaks between NPCs and GSCs.

(**B**) Heatmap and overlaps of m^{6}A MeRIP-seq signals for NPCs (GSE54365) and GSCs (GSE87515). The global m^{6}A modification status was arranged into three groups according to m^{6}A modification enrichment (enrichment score >1.5): shared (genes with m^{6}A modification in both GSCs and NPCs), GSC (genes with m^{6}A modification in GSCs but not in NPCs), and NPC (genes with m^{6}A modification in NPCs but not in GSCs).

(**C**) KEGG analyses of genes with increased m^{6}A modifications in GSCs.

(**D**) The m^{6}A modification status of the represented genes from three groups.

669 **Figure 2. Increased expression of METTL3 in GBM cells and in classical tumors**

670 (**A**) Expression of m^6A modulators was measured by qPCR in GBM specimens (n=35)
671 and compared to normal brain tissues (n=10). N.s., no significant difference.

672 (**B**) Immunohistochemistry (IHC) staining of METTL3 in patients with gliomas
673 (grade 1 to 4) and comparison with normal brain tissue. The statistical results showed
674 the proportion of METTL3 positive cells in each group.

675 (**C**) IHC staining of METTL3 in primary and recurrent GBM tumors from three
676 patients with GBM. The statistical results showed the proportion of METTL3 positive
677 cells in each group.

678 (**D**) The sphere formation efficiency was plotted post inhibition of m^6A modulators
679 using two different sgRNAs in U87MG cells. The number of spheres formed after 7
680 days were counted using Image J software.

681 (**E**) The association between *METTL3* expression in GBM and overall survival time
682 of the selected patients was analysed by Kaplan-Meier analysis.

683 *, $P < 0.05$; **, $P < 0.01$; ***, $P < 0.001$ is based on the Student's *t*-test. All results are
684 from three independent experiments. Values are mean ± SD.

Figure 3. Impairment of GBM proliferation and tumorigenicity by METTL3 inhibition

(**A**) The cell viability tests of U87MG, U251, and primary GBM cells transduced with sh*METTL3* were performed using CellTiter-Glo®.

(**B**) The cell viability tests of U87MG and U251 cells overexpressing wild-type (WT) METTL3 or METTL3 with a mutated catalytic domain (METTL3-MUT) were performed using CellTiter-Glo®.

(**C**) The proportion of apoptotic cells in *METTL3*-KD and control GBM cells were evaluated by flow cytometry. The statistical results showed the proportion of Annexin V^+ PI^- cells, which indicate the amount of apoptotic cells in each group.

(**D**) Sphere formation assay after *METTL3* silencing in U87MG cells compared with control cells. The number of spheres formed was counted after transferring spheres to stem cell culture conditions for 7 days.

(**E**) Limiting dilution assay (LDA) of GSCs transduced with control shRNA or *METTL3* shRNAs.

(**F**) U87MG and U251 cells were transduced with flag-tagged wild-type (WT) METTL3 or METTL3 with a mutated catalytic domain (METTL3-MUT). The number of spheres formed was counted after transferring spheres to stem cell culture condition for 7 days. Representative images of the spheres shown at 10× magnification. Scale bar=100 μm.

(**G**) Xenogen images of brain tumors in GSC-grafted nude mice (n=4) transplanted with U87MG sphere cells that were transduced with control shRNA or *METTL3*

707 shRNA. The scale bar for bioluminescence intensity is shown on the right.

708 *, $P < 0.05$, **, $P < 0.01$, ***, $P < 0.001$ is based on the Student *t*-test. Values are

709 mean ± SD of three independent experiments.

710

Figure 4. Splicing factors are critical target genes of METTL3 in GBM.

(**A**) Motif analysis of m^6A modification peaks in control and *METTL3*-KD MeRIP-seq data .

(**B**) Distribution of m^6A modification peak reads across all mRNAs in control and *METTL3*-KD U87MG cells.

(**C**) Scatter plots showing the increased (red) and decreased (green) m^6A modification enrichment in mRNAs from control and *METTL3*-KD U87MG cells.

(**D**) Gene ontology analysis of mRNAs with decreased m^6A modification in *METTL3*-KD U87MG cells.

(**E**) Heatmap showing the mRNA expression changes in GBM cells depleted of METTL3.

(**F**) Gene Ontology (GO) analyses of the genes differentially regulating genes between *METTL3*-KD and control cells.

(**G**) Gene Set Enrichment Analysis (GSEA) enrichment plots of differentially regulated genes between *METTL3*-KD (*METTL3* shRNA-1) and control cells. Data of *METTL3* shRNA-2 drew same conclusion (data not shown).

(**H**) A qRT-PCR analysis. The mRNA levels were first normalized to the level of β-actin mRNA. The relative ratio (fold change) obtained in the presence of control shRNA was set to 1.

(**I**) U87MG or U251 cells transduced with indicated shRNAs were plated in a 96-well plate for 72 h. Cell viability was assayed using CellTiter-Glo®.

(**J**) Pearson correlation analysis of *METTL3* with *SRSF3*, *SRSF6*, or *SRSF11* based on

733 REMBRANDT data.

734 *, $P < 0.05$, **, $P < 0.01$, ***, $P < 0.001$ is based on the Student *t*-test. Values are

735 mean ± SD of three independent experiments.

736

Figure 5. METTL3-mediated non-sense mediated decay (NMD) of *SRSFs* mRNAs rely on its m^{6}A methyltransferase activity.

(**A**) Genomic visualization of the m^{6}A immunoprecipitation-normalized signal in neural progenitor cells (NPCs) and glioma stem cells (GSCs) of the *SRSFs*. The x-axis represents the genomic position. The y-axis shows normalized reads per million (rpm).

(**B**) Integrative genomics viewer (IGV) plots of m^{6}A peaks and RNA-seq peaks at *SRSFs* mRNAs. The y-axis shows the sequence read number, blue boxes represent protein coding exons, and yellow boxes represent NMD exons.

(**C**) and (**D**) RT-qPCR analysis of the total, protein-coding, or NMD RNA levels of *SRSFs* in U87MG cells transduced with sh*METTL3* (**C**) or METTL3 (**D**).

(**E**) RT-qPCR analysis of the total, protein-coding, or NMD RNA levels of *SRSFs* in U87MG cells transduced with a mutated catalytic domain (METTL3-mut).

(**F**) RT-qPCR analysis of the total, protein coding, or NMD RNA levels of *SRSFs* in U87MG cells treated with indicated shRNA(s).

(**G**) RT-qPCR analysis of the total, protein coding, or NMD RNA levels of *SRSF3*, *SRSF6*, and *SRSF11* in *METTL3*-KD U87MG cells treated with CHX (Cycloheximide).

*, $P < 0.05$, **, $P < 0.01$, ***, $P < 0.001$ is based on the Student *t*-test. Values are mean ± SD of three independent experiments.

Figure 6. The m^{6}A modification around start codon of splicing factors modulates NMD through YTHDC1

(**A**) Schematic illustration of WT *SRSF6* minigene or m^{6}A consensus sequence mutant (A-to-G mutation) reporter constructs. *SRSF6* minigene was fused with Renilla luciferase reporter. NMD splicing of *SRSF6* minigene reporter cannot generate Renilla luciferase. R-luc, Renilla luciferase; F-luc, firefly luciferase.

(**B**) Relative luciferase activity of *SRSF6* minigene with wild-type or mutated m^{6}A sites after co-transfection with control shRNA, or *METTL3* shRNA in U87MG cells. Renilla luciferase activity was measured and normalized to firefly luciferase activity.

(**C**) Relative luciferase activity of *SRSF6* minigene with wild-type or mutated m^{6}A sites after co-transfection with WT METTL3 or METTL3-mut in U87MG cells.

(**D**) Schematic illustration of base editing system.

(**E**) Sequence of *SRSF3* in WT and m^{6}A site edited U87MG cells.

(**F**) RT-qPCR analysis of the total or NMD RNA levels of *SRSF3* in WT and m^{6}A site edited U87MG cells.

(**G**) RIP-qPCR analysis of YTHDC1 in U87MG cells and negative control cells (*YTHDC1*-KD U87MG cells).

(**H**) RT-qPCR analysis of the total, protein-coding, or NMD RNA levels of *SRSFs* in U87MG cells transduced with sh*YTHDC1*.

(**I**) Relative luciferase activity of *SRSF6* minigene with wild-type or mutated m^{6}A sites or *SRSF3* minigene after co-transfection with control shRNA, or *YTHDC1* shRNA in U87MG cells.

780 *, $P < 0.05$, **, $P < 0.01$, ***, $P < 0.001$ is based on the Student *t*-test. Values are

781 mean ± SD of three independent experiments.

782

Figure 7. METTL3 regulates *BCL-X* and *NCOR2* alternative splicing in GBM cells.

(**A**) The amount of changed alternative splicing events in U87MG cells transduced with sh*METTL3*.

(**B**) The relative fraction of each alternative splicing event affected either positively or negatively by METTL3.

(**C**) Representative genes with significantly changed alternative splicing events.

(**D**) IGV plot illustrating the splicing changes of *BCL-X* promoted by METTL3.

(**E**) RT-qPCR analysis of splicing changes of *BCL-X* after *METTL3* KD.

(**F**) The cell viability tests of U87MG cells transduced with sh*METTL3* or/and sh*BCL-XS* were performed using CellTiter-Glo®.

(**G**) The proportion of apoptotic cells in U87MG cells transduced with sh*METTL3* or/and sh*BCL-XS* was evaluated by flow cytometry.

(**H**) IGV plot illustrating the splicing changes of *NCOR2* promoted by METTL3.

(**I**) RT-qPCR analysis of splicing changes of *NCOR2* after *METTL3* KD.

(**J**) The cell viability tests of U87MG cells transduced with sh*METTL3* or/and sh*NCOR2* were performed using CellTiter-Glo®.

(**K**) U87MG cells were transduced with sh*METTL3* or/and sh*NCOR2*. The number of spheres formed was counted after transferring to stem cell culture condition for 7 days.

(**L**) Limiting dilution assay of GSCs transduced with sh*METTL3* or/and sh*NCOR2*.

(**M**) Schematic illustration of the working model.

805 *, $P < 0.05$, **, $P < 0.01$, ***, $P < 0.001$ is based on the Student *t*-test. Values are

806 mean ± SD of three independent experiments.

807

808

Figure 1

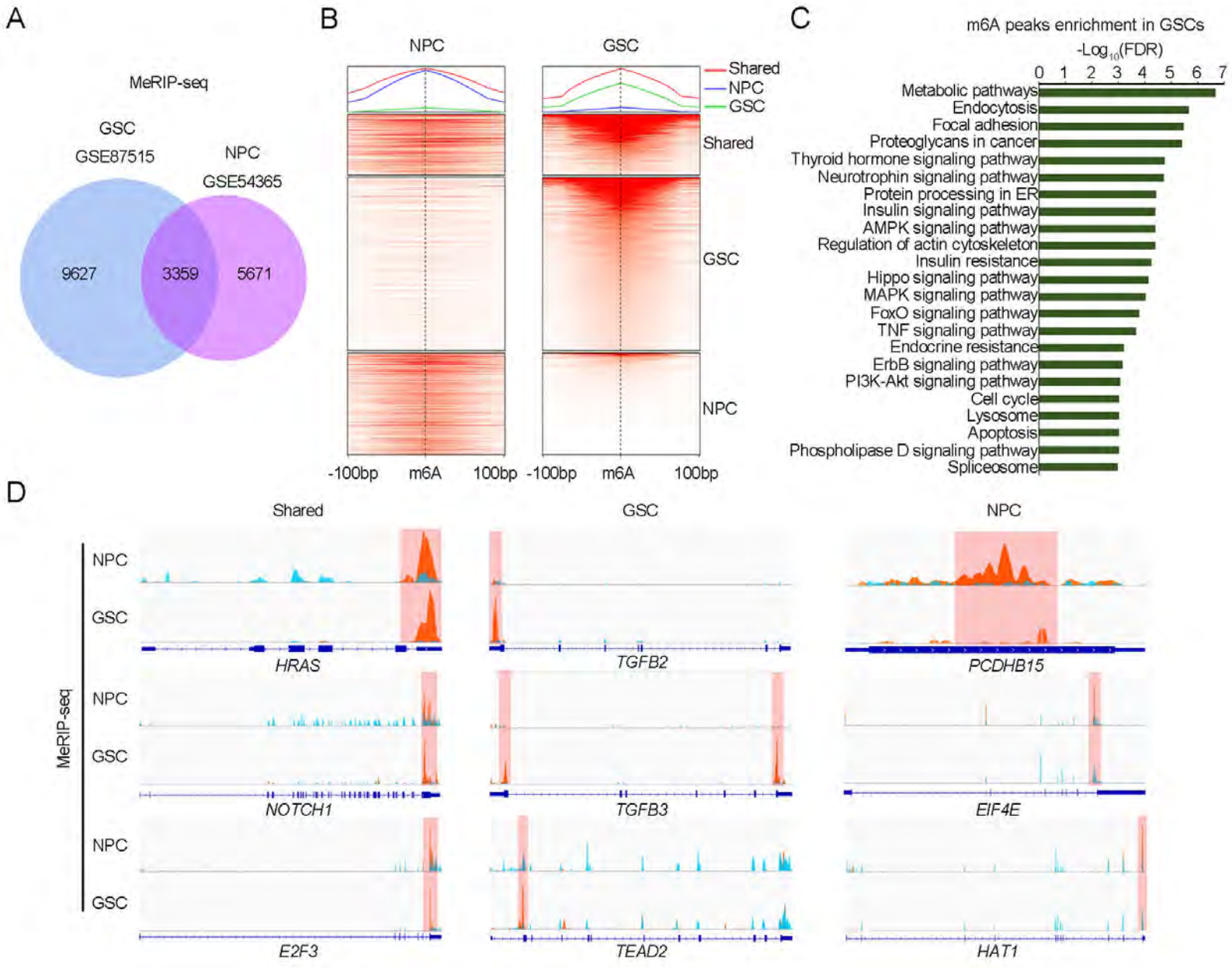

Figure 2

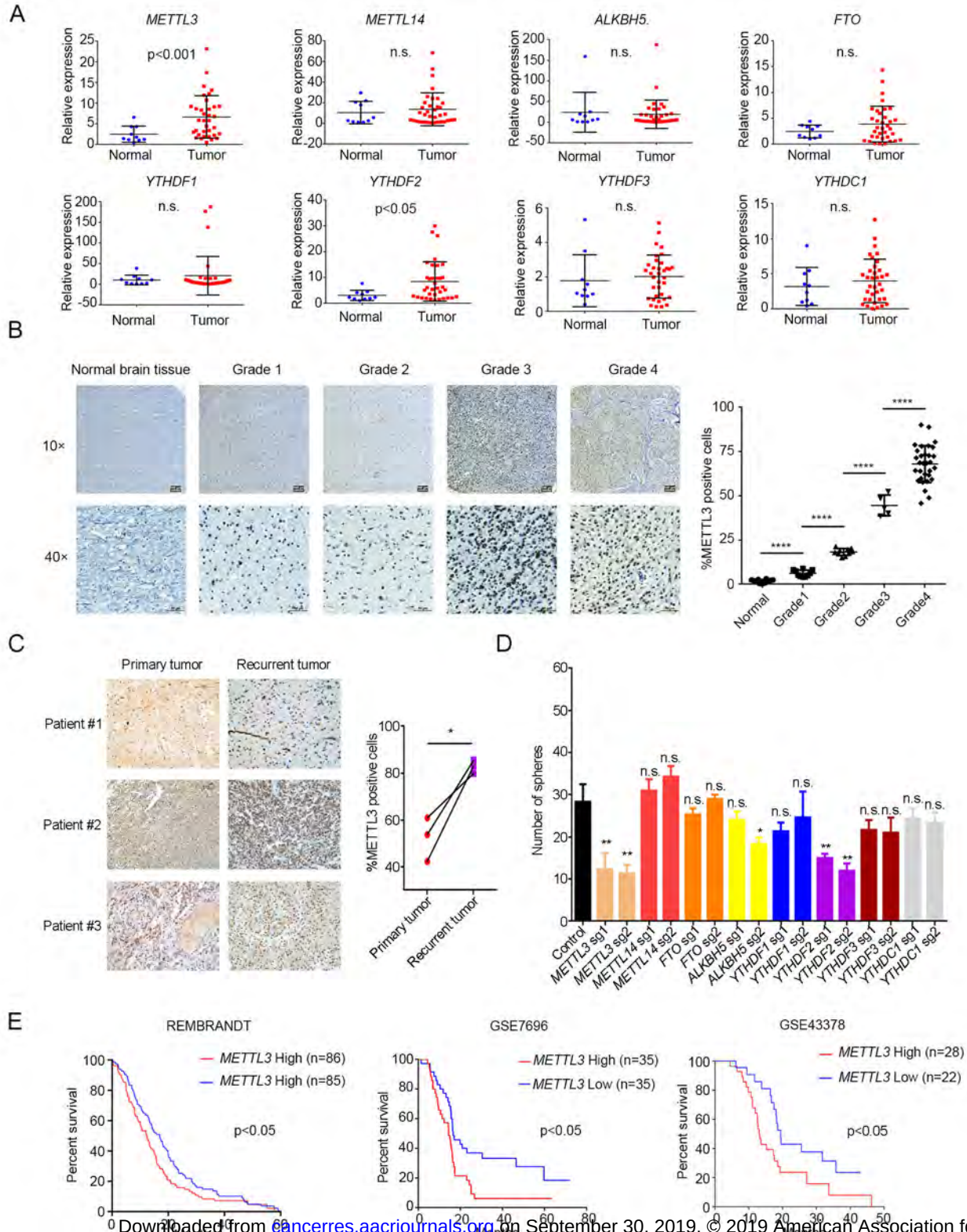

Figure 3

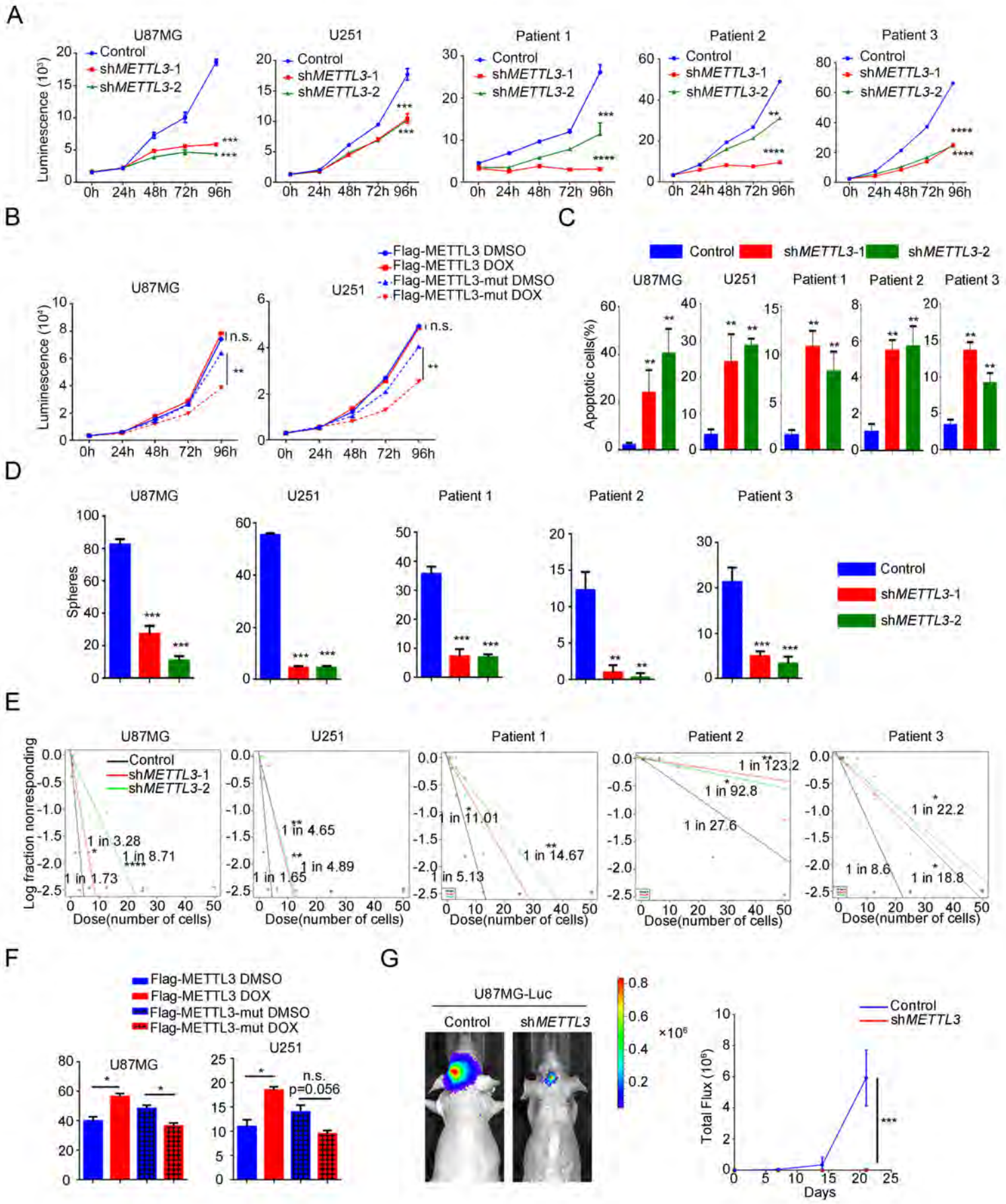

Figure 4

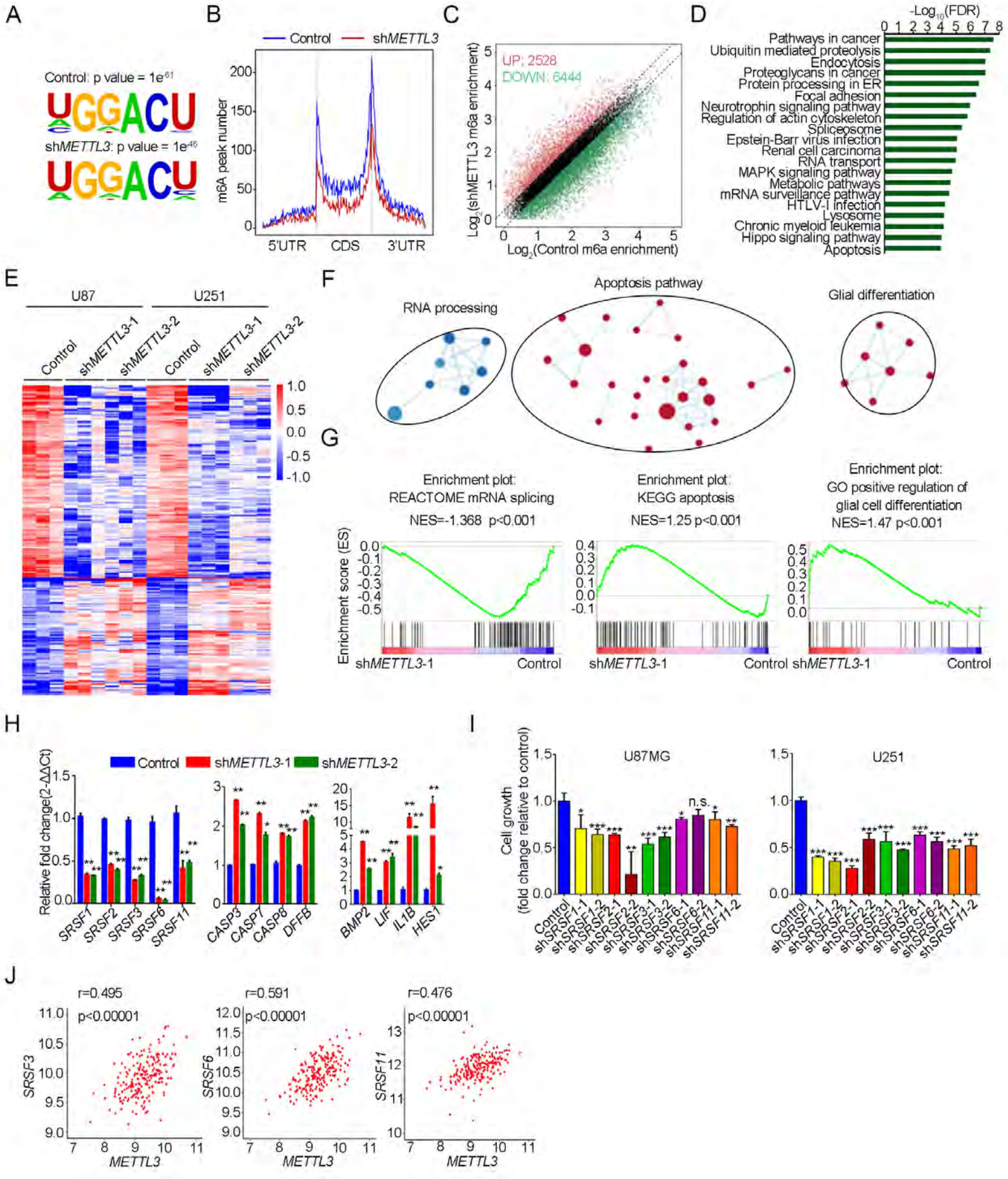

Figrue 5

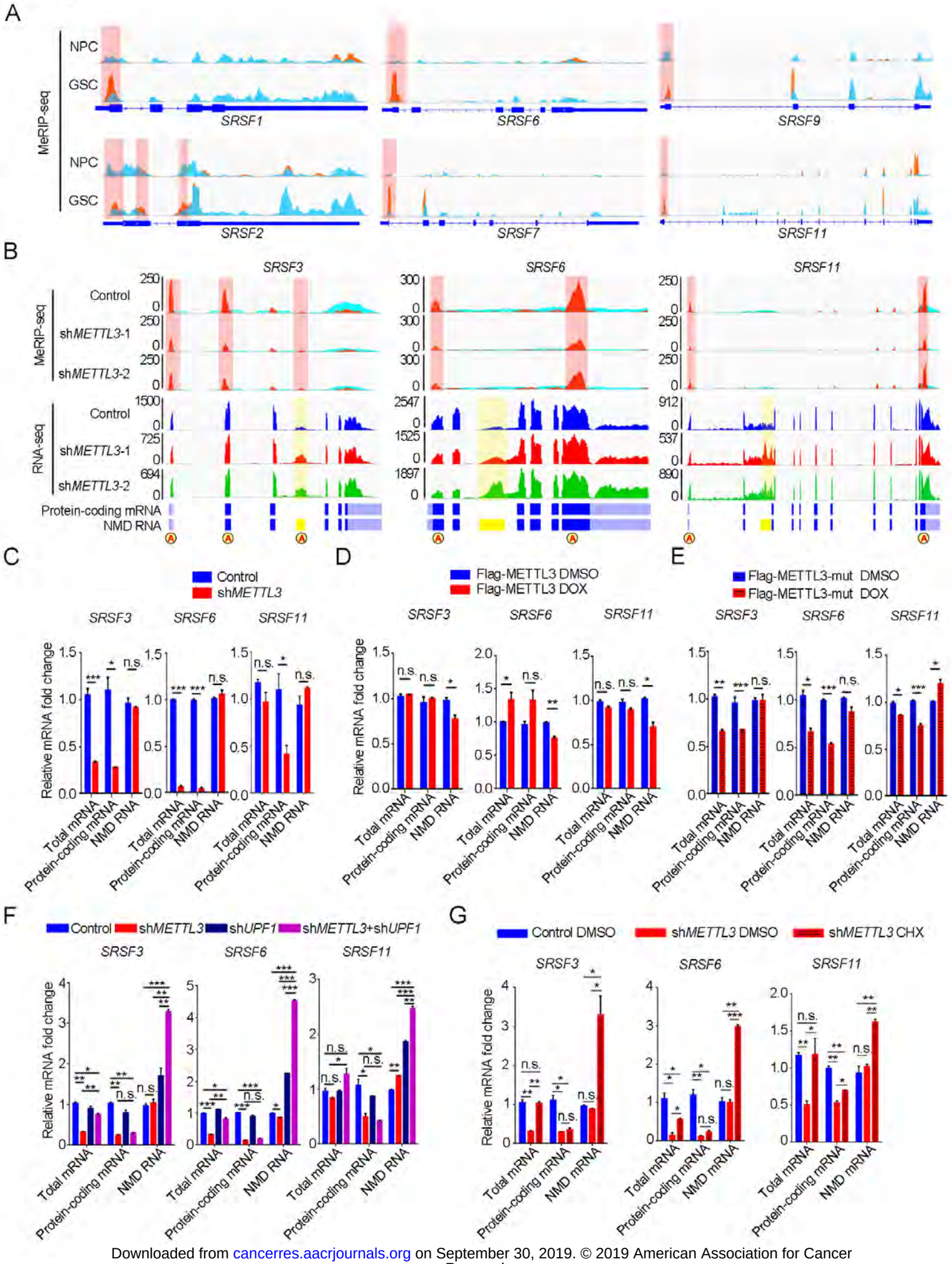

Figrue 6

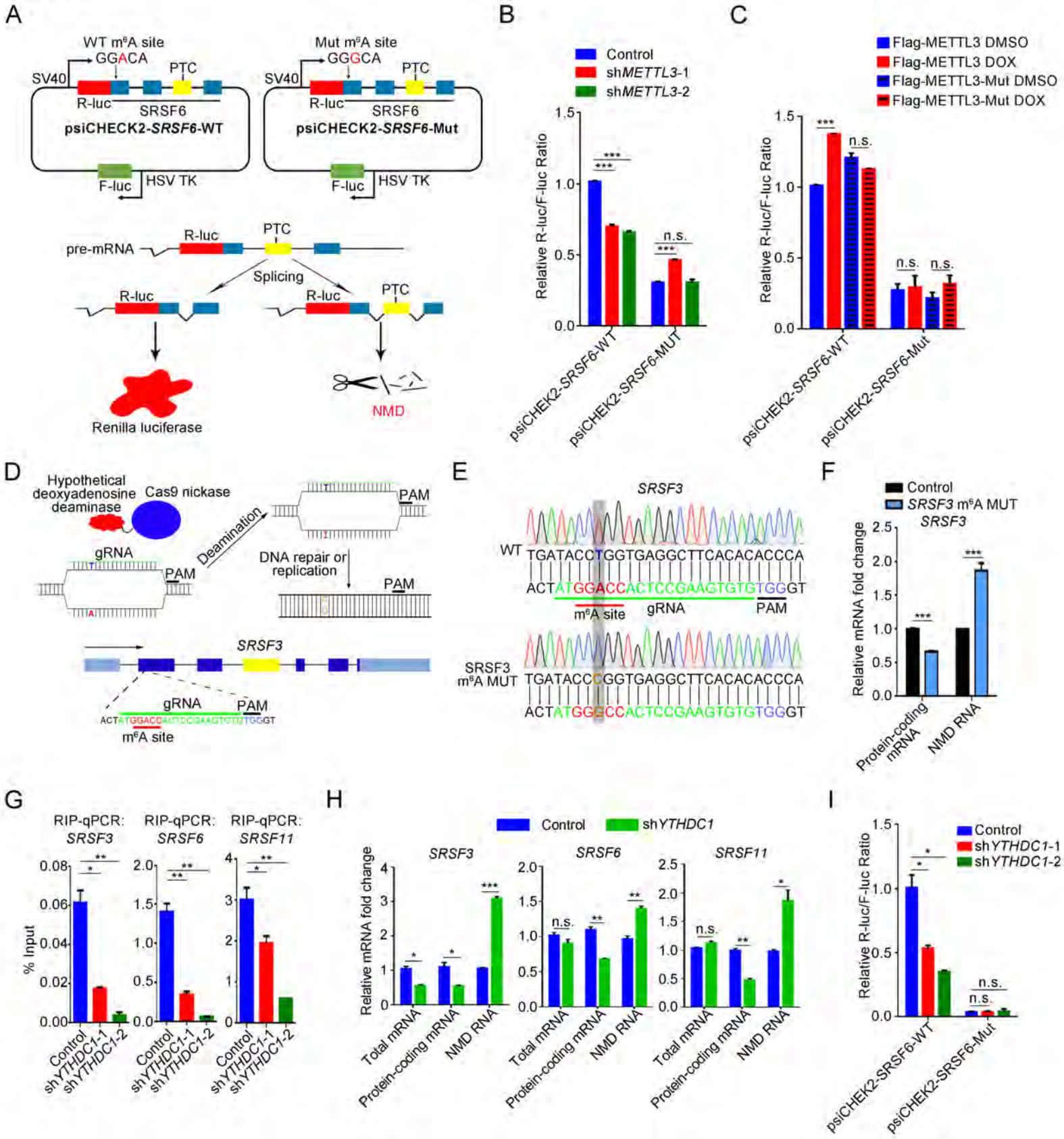

Figure 7

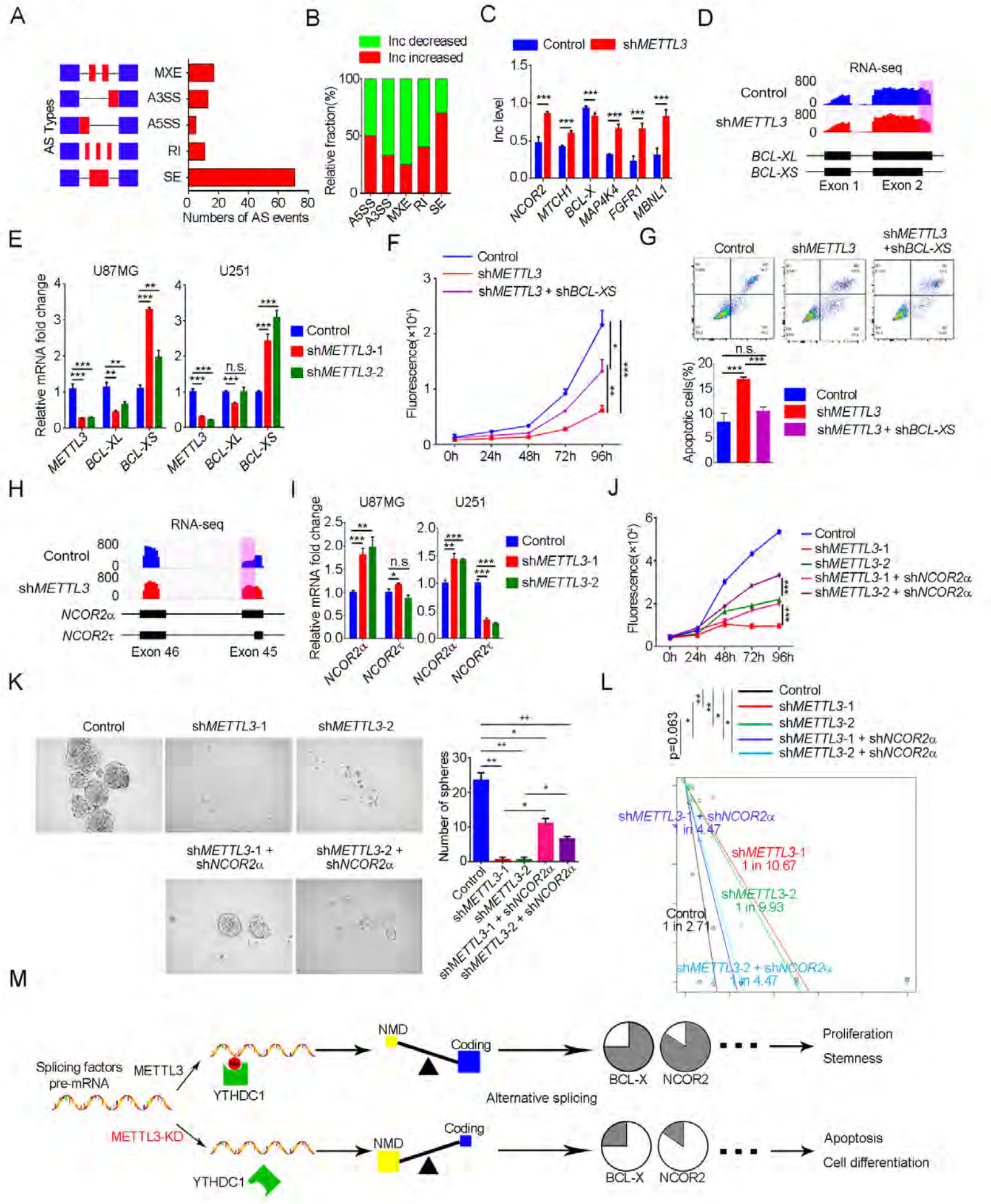

Cancer Research
The Journal of Cancer Research (1916–1930) | The American Journal of Cancer (1931–1940)

AACR American Association for Cancer Research

N6-methyladenosine Modulates Nonsense-mediated mRNA Decay in Human Glioblastoma

Fuxi Li, Yang Yi, Yanyan Miao, et al.

Cancer Res Published OnlineFirst September 17, 2019.